Subsurface Voids and their Sedimentology – Implications for Drilling into Mines for Heat

ADAM GILLETT

Subsurface Voids and their Sedimentology –

Implications for Drilling into Mines for Heat

Adam Richard Gillett

Department of Earth Sciences

Durham University

2024

Thesis submitted in accordance with the regulations for the degree of Master of Science by

Research in Durham University, Department of Earth Sciences, 2024

Abstract

Flooded mine workings across County Durham and the Northumberland coalfields represent potential shallow geothermal aquifers, where groundwater has returned to pre-mining levels to flood the abandoned workings. These provide potentially large aquifers to extract low-enthalpy geothermal heat from, using ground source heat pumps. Heat pumps tapping flooded mine waters have significant potential in the decarbonisation and regeneration of densely populated ex-coal mining areas. Coal extraction largely took place through room and pillar mining, with the majority of flow occurring through residual 'rooms', possessing very high permeabilities and porosities. Pillars left to support the overburden can fail overtime, giving rise to various anthropogenic coal deposits within the workings, which are important to appraise as the heterogeneity of the Carboniferous coal measures will impact the flow properties of the workings. The structure of collapsed workings has been studied previously, but no attention has been paid to the lithologies and highly variable permeabilities and porosities (over several orders of magnitude). This research has investigated anthropogenic coal deposits in the former mine workings at Whitley Bay, and integrated findings with borehole datasets from Bayfield in the local region. Detailed permeabilities, porosities and petrography were collected through extensive fieldwork, focused on the Upper Carboniferous High Main seam. This research demonstrates the negligible permeabilities (<0.01 mD) and low porosities (<8%) of the anthropogenic coal deposits compared to the surrounding lithologies, and may act as flow barriers. Closely associated and laterally connected sandstones and siltstones have much higher permeabilities (~100-300 mD) and porosities (~15-30%). Integration with biostratigraphy and detailed chemostratigraphy from Whitley Bay and Bayfield datasets ~10 km inland enables the sedimentological observations to be more widely correlated, allowing for identification of coal seams. The findings presented establish one of the first data sets that can be used for modelling of geothermal prospects in former shallow coal mine workings.

Table of Contents

Declaration and Copyright

I declare that this thesis has not been previously submitted to this or any other university. The work carried out in this thesis is the solely of that of the author, except where reference is made to previously published or unpublished work.

Adam Richard Gillett

Durham University

March 2024

Acknowledgements

I would like to formally acknowledge and give thanks to my supervisors Stuart Jones and Leigh Sharpe, without whom this research could not have taken place. They have both provided crucial insights throughout the process. Specific thanks to Stuart Jones as my primary supervisor for his guidance, and to Leigh Sharpe and the Coal Authority for providing the data and insights into the Bayfield Housing Estate investigation. A thank you to Alex Finlay for his assistance in using Chemostratigraphy. A great thank you to my family for supporting me throughout the process. Also, a thank you to Durham University for providing the resources for this research.

1. Introduction to Former Coal Mine Workings and their Anthropogenic Nature

Anthropogenic sediments are sediments which have distinct characteristics that have arisen through strong influences from human activity in the past. As the human race has grown and developed through time, the need for resources and materials has also grown, with an increasing population size being the main driver. This has been solved by increasing the magnitude of resource excavation via widespread mining and landscape modification, including the resultant waste and remains of former mining activity (Price et al, 2011). There is a worldwide estimate of 57000 Mt (million tonnes) of deliberately moved sediment annually (Price et al, 2011), showing how humans have become significant geomorphological agents, with the magnitude of these actions increasing to accommodate increasing population. This has led to recent human history being referred to as the Anthropocene, where anthropogenic sediments are widespread and important to understand how they act with the natural environment.

By their nature, many anthropogenic units are strictly allostratigraphical: individual anthropogenic deposits are typically created in a single phase of deposition and their bounding surfaces, including local hiatuses and disconformities, *are* significant to their definition and identification.

With the exception of reworking and slumping (including the failure of engineered slopes in made ground), few immediate processes are likely to significantly disrupt the original superpositional nature of anthropogenic sediments. However, not all anthropogenic deposits conform to the Law of Superposition. Anthropogenic deposits created in the subsurface through activities such as mining, tunnelling and subsequent backfilling, or deposits resulting from the transfer of man-made materials into subsurface for storage or disposal, may exhibit complex relationships similar to natural intrusive rocks. By analogy, 'anthropogenic intrusives' that do not conform to the Law of Superposition may be described as 'lithodemic' and delimited on the basis of their rock characteristics. Such deposits may be hosted by earlier natural or anthropogenic deposits. This is very much the case for subsurface mining of coal and not until subsequent opencast mining displays the remnant coal pillars and rooms (Ford et al, 2014).

Within the UK, there are very few places to investigate the inner workings of coal mines, with no large scale coal extraction taking place since ~2020, and many open pits now shut down. However, due to coastal erosion at Whitley Bay, former room and pillar workings have been exposed, making it an ideal location to look at the inner workings as one of the only places where they have been exposed.

1.1. Aims of Research

The aims of this research are as follows:

- How does coal mine waste influence permeabilities and porosities for fluid flow modelling?
- Can lithological heterogeneities be correlated and, aid predictive hydrogeological modelling for geothermal potential?

Before delving into the specifics about coal mine waste characteristics and the lithologies encountered as part of this research, a background on coal mining history is required.

1.2. Anthropocene – Event vs Epoch Debate

There is an ongoing debate around how the Anthropocene should be defined – either as a new epoch with a defined start date, or as an event within current geological time. Gibbard et al (2022) have proposed that the Anthropocene should be considered as an informal geological event as opposed to a formally defined chronostratigraphic event. In July 2023, the Crawford Lake in Ontario, Canada, was chosen as a site that could formally represent the start of the Anthropocene as a new epoch, with sediment in the lake showing a spike in plutonium from hydrogen bomb tests in the 1950s (Nature, 2023). However, a committee has voted against the proposal of the Anthropocene being an epoch, highlighting the aspect that the impact of humankind on the Earth is far greater than just the nuclear bomb testing residuals (New York Times, 2024).

Any formal definition and creation of a new epoch limits the use of the Anthropocene in other disciplines of social sciences and societal understanding, hence the ongoing debate on how the

Anthropocene term should be used. Delving further into this debate is beyond this project, so for the purpose of this project any anthropogenic sediment or deposit generated forms part of the Anthropocene.

1.3. Anthropogenic Deposit Classifications

Ford et al (2014) determined that anthropogenic sediments that were either created from scratch or from the modification of natural stratigraphy both counted as 'novel sedimentary environments'. They show several of the same traits as natural strata, such as conforming to the Law of Superposition and mainly being allostratigraphical, however the inherent heterogeneity and variation in depth makes it hard to apply standard lithological classification (Ford et al, 2014, Price et al, 2011, Zalasiewicz et al, 2011).

Table 1 - Artificial Ground Classification as of 2010. From Ford et al, 2010.

MADE GROUND	Areas where material is known to have been placed by man on the pre-existing natural land surface (including engineered fill).
WORKED GROUND	Areas where the pre-existing land surface is known to have been excavated by man.
INFILLED GROUND	Areas where the pre-existing land surface has been excavated (WORKED GROUND) and subsequently partially or wholly backfilled (MADE GROUND).
DISTURBED GROUND	Areas of surface or near-surface mineral workings where ill-defined excavations (WORKED GROUND), areas of subsidence caused by the workings and spoil (MADE GROUND) are complexly associated with each other.

LANDSCAPED GROUND	Areas where the pre-existing land surface has been extensively remodelled but where it is impracticable to delineate separate areas of MADE GROUND, WORKED GROUND or DISTURBED GROUND.

The British Geological Survey (BGS) classify anthropogenic sediment as a type of geology, termed 'Artificial Ground' to join Bedrock Geology, Superficial Geology and Mass Movement Geology in the BGS Lexicon of Named Rock Units (Ford et al, 2014). As described by Table 1 and Figure 1, the range of deposit that Artificial Ground spans is quite varied. The classification is good for the purpose created, where the ability to distinguish anthropogenic sediment based on the influence of the pre-existing land surface is key.

The classification of former mine workings within the lithology of an area is highly complex, as the widespread variation makes it hard to confine any workings into one type of deposit. This variation exists due to how the mines have changed over time, with some workings having the mine tailings moved to an external dump while others have the anthropogenic waste sediments contained within the workings themselves formed through pillar spalling, roof collapse and backfilling. There are several different types of anthropogenic sediment classification, and while most are designed for a specific location or type of deposit, an official classification for different types of mine sediments does not currently exist.

Applying this to former coal mine workings can be difficult, as Disturbed Ground is the umbrella term for anything related to former shallow mine workings. However, former shallow workings can consist of a wide variety of anthropogenic deposits, meaning that one overarching description is not sufficient when looking in detail.

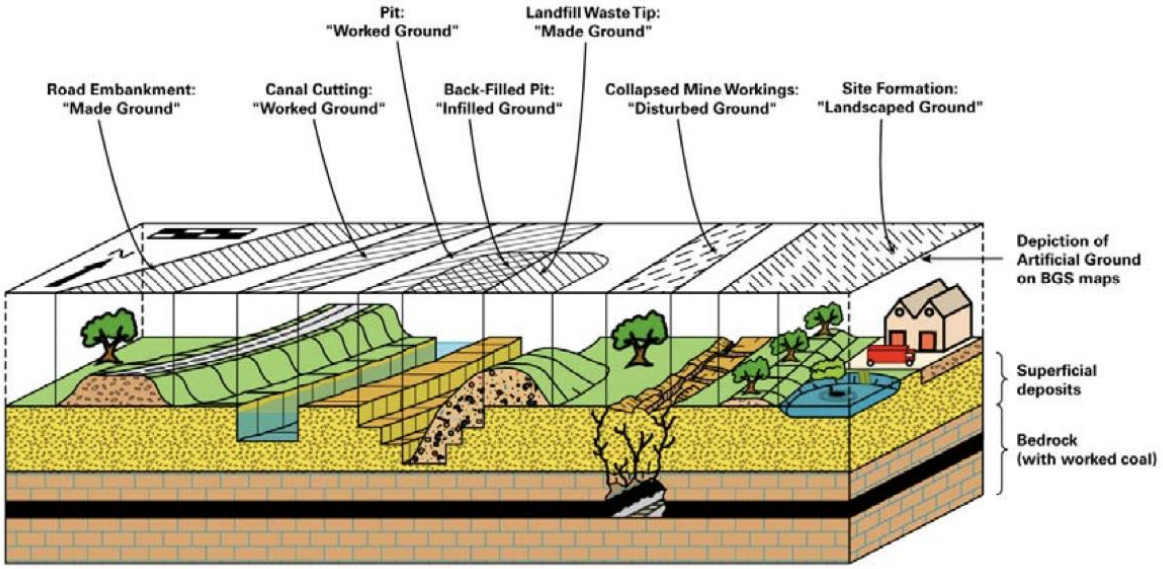

Figure 1 - Examples of the different types of Artificial Ground and how they are shown on a geological map. From Ford et al, 2010.

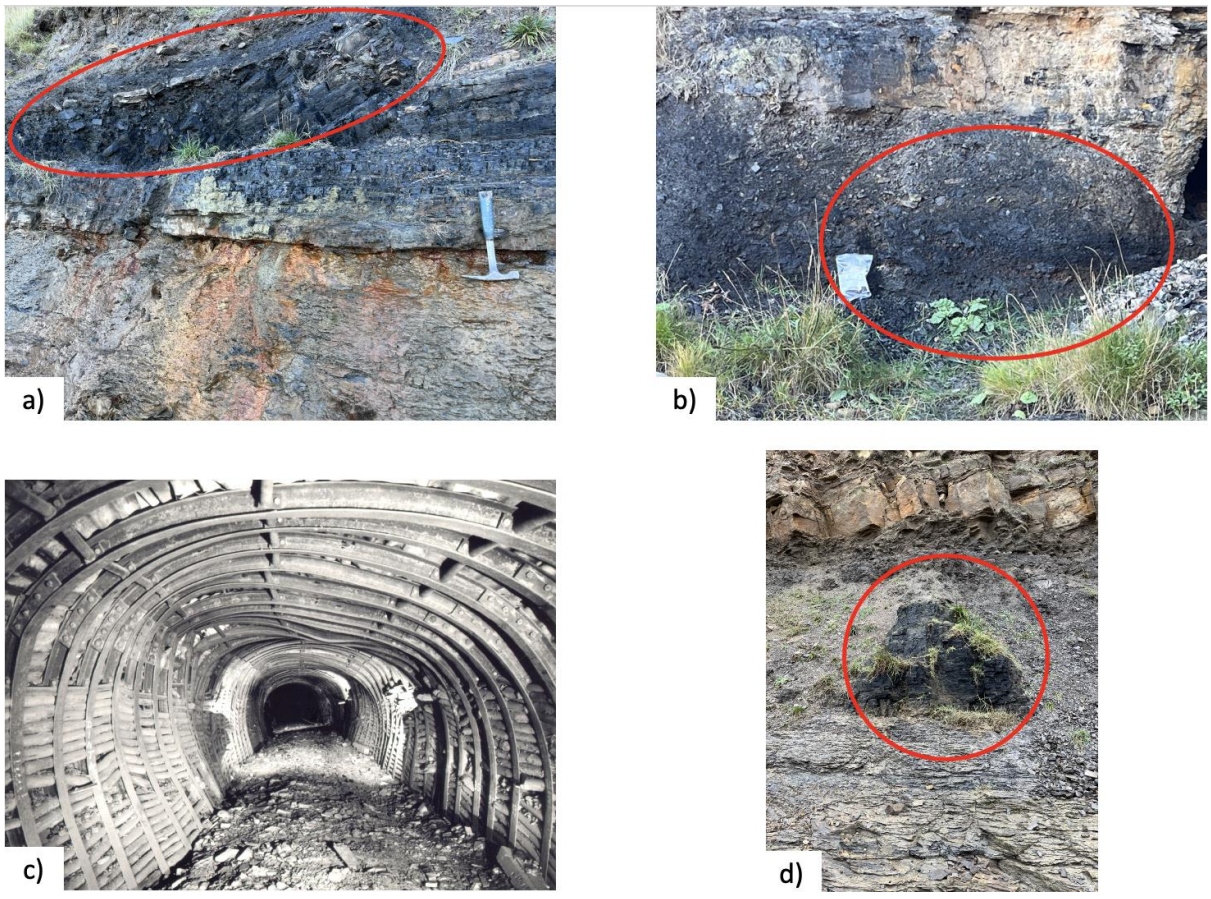

Figure 2 - Four main types of anthropogenic coal deposits, with red shapes outlining the deposit where needed. (a) is roof collapse; (b) is backfill; (c) is open roadway; (d) is in-situ *pillar. (a)(b)(d) are photographed at Whitley Bay, County Durham. (c) is provided by The Coal Authority.*

Figure 2 shows the 4 main types of anthropogenic deposit found in former coal mine workings – roof collapse, backfill, open roadways and coal pillars. Based on the classifications already covered, all four occurrences of anthropogenic coal would be grouped together as Artificial Ground. Where backfill could be classified as Made Ground or Infilled Ground, both roof collapse and the coal pillars have no class to fit into, as they consist of *in-situ* coal that has been transformed by anthropogenic activity but occur quite differently (see Figure 2). The roadways found within former coal mines could be argued to fit into Worked Ground, however they are distinctly different from the example of 'canal cuttings' from Ford et al (2011).

For the purpose of this project, the definitions of the terminology used for anthropogenic coal deposits are found in Table 2.

Table 2 – Types of deposits found in former room and pillar coal mine workings.

IN-SITU COAL (natural)	Coal that is still located where it was initially deposited.
PILLAR (anthropogenic)	Coal purposefully left behind by miners to act as support pillars for the overburden.
ROADWAY/VOIDSPACE (anthropogenic)	Areas within former coal mine workings where the coal located there was excavated, and an open space was left – i.e space not filled by other material.
BACKFILL (anthropogenic)	Sections of former coal mine workings where the material is made up of a heterogenous mix of clay, mud, and coal. Pieces of coal within this tend to be very small (centimetre scale), with the mud and clay tightly packed around it.
ROOF COLLAPSE (anthropogenic)	Parts of former coal mine workings where the overburden strata have collapsed and filled in the voidspace that was previously beneath, as a result of the supporting material no longer able to

[redacted]	support the overburden. Also encompasses ‘goaf’ and ‘gob’ for the purpose of this project.

1.4. Coal Mining during the Industrial Revolution

The Industrial Revolution saw a major increase in global population and productivity as a result of increased mineral extraction through widescale exploitation of the subsurface (Price et al, 2011). From Clark and Jacks (2007), it’s known that coal was a major part of the Industrial Revolution by being a cheap and efficient way to smelt iron ore into iron, as well as being used in steam engines at the time. It was also found that the impact of coal on the Industrial Revolution was felt more in the UK than elsewhere, for example China, due to the population centres being located near coal deposits (Clark and Jacks, 2007).

As the global population increased throughout this time, the need for resources increased, so the rate of mineral extraction from the subsurface increased in order to cope (Price et al, 2011). This is especially prevalent in the extraction amounts for coal, where the extraction totals of coal can be used as a proxy for population growth, as well as for economic growth and stress (Cooper et al, 2018, Price et al, 2011). As such, the amount of anthropogenic sediment generated as a by-product of the increased extraction also increased, as well as changing with the various types of coal mining methods used over time (Cooper et al, 2018).

The British Geological Survey (BGS) has estimated a total of 24700 Mt of coal has been extracted since 1850 (Price et al, 2011). Price et al (2011) estimated that the amount of anthropogenic sediment generated as a result of coal extraction as up to 6800 Mt and can be found as a range of different forms depending on which type of coal mining method was used at the site in question. The main types of coal extraction through the Anthropocene (within the UK) are **Bell Pit, Opencast**, **Room and Pillar**, and **Longwall**, which will all be covered in the following sections.

1.4.1. Bell Pit Mining

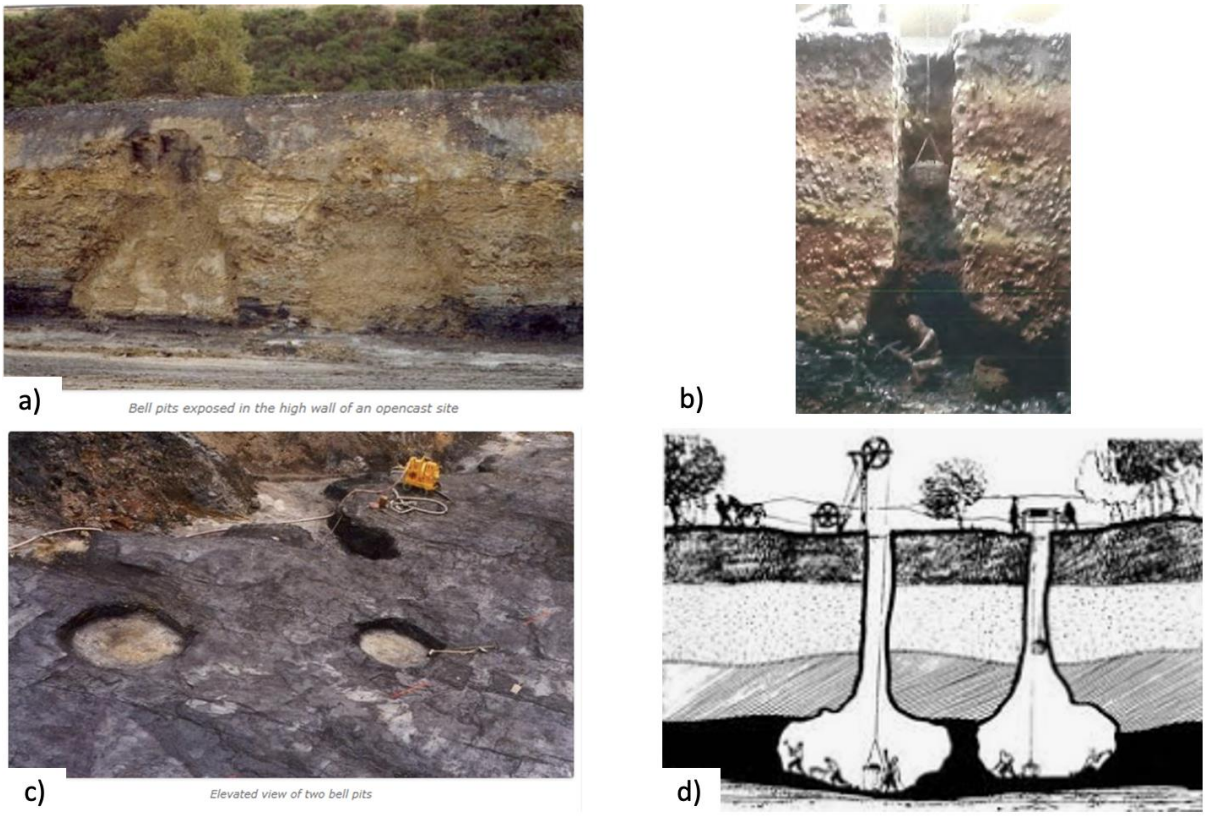

Figure 3 - Images of the bell pit mining method - (a) and (b) are side-on views, while (c) is an elevated view of where coal was extracted from the seam. (d) is a cross-section diagram of how bell pit mines were operated. Provided by The Coal Authority.

Bell Pit mining is a primitive form of mining that focuses on shallow coal seams, and usually limited to around 12 m in depth (Donnelly, 2020). The large difference between the bell pit and opencast mining methods is the amount of anthropogenic sediment produced. Bell pit mining eliminates the necessity of removing the overburden strata, therefore reducing the amount of waste generated (see Figure 3). They were mined without the use of wooden pillar supports, so would continue until the overburden roof collapsed in on itself (Durham Mining Museum, 2017). As found by Donnelly (2020), they became popular in the 14th century, and can be found along the coal seam outcrop as a series of crownholes – an anthropogenic sediment formed as the voidspace in the subsurface migrates to the surface.

During early stages of the Anthropocene Event and coal mining, records of mine plans were not regularly kept, until the *Inspection of Coal Mines Act* was put into legislation in 1850. This means

that there are very few plans that recorded the locations of bell pits prior to 1850, leaving anthropogenic deposits in the form of crownholes and mine tail dumps as the main indicators (Durham Mining Museum, 2017). Bell pits were not an efficient way of extracting minerals as they only partially exploited the resources and were soon abandoned for more efficient methods from the mid-1800s.

1.4.2. Opencast Mining

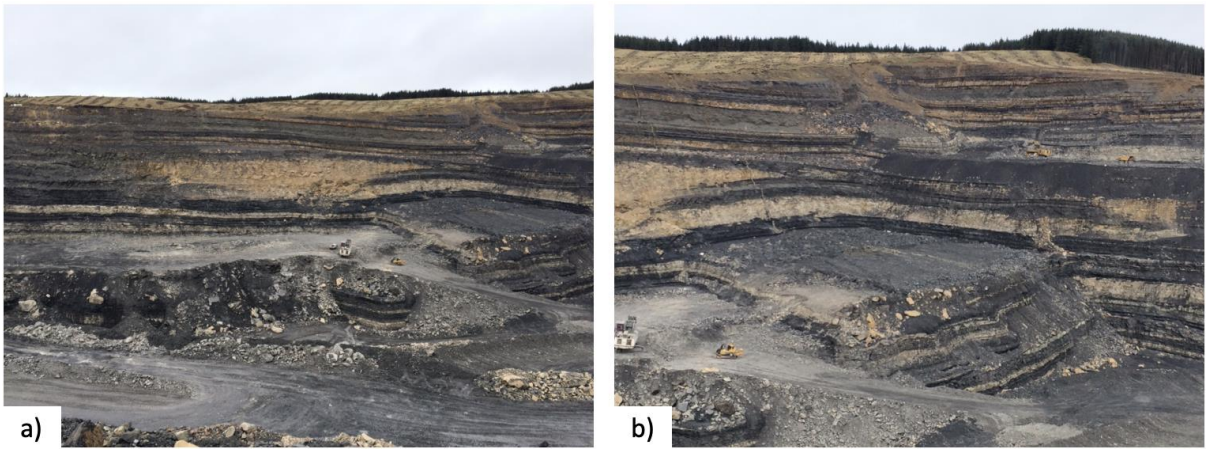

Figure 4 - Images of an opencast coal mine from House of Water surface mine, Scotland. Closed in July 2020 (East Ayrshire Council Planning Committee, 2020). Provided by The Coal Authority.

Opencast coal mining was one of the earliest forms of coal mining (Price et al, 2011). To extract coal seams that appeared at the surface, the coal itself and the surrounding material was excavated as a whole (Figure 4). While this mining method ensures that a high recovery rate of coal is achieved, it also produces a significant amount of mining waste, as the overburden strata must also be extracted (Scott et al, 2010). Scott et al (2010) found that this was the main drawback of opencast coal extraction, as to efficiently remove the overburden strata in present-day comes with high economic costs, making opencast extraction viable only when the coal seam is in the shallow subsurface (usually <100 m). This was the main method of coal extraction within the UK for a period, with opencast coal mining in Britain peaking at 14 Mt in 1958 (Durham Mining Museum, 2022). Within

the North East, there are many former opencast coal pits, such as Stobswood Opencast, which was in operation from 1990-2005.

Due to the extraction of large amounts of overburden strata, opencast mining produces large amounts of anthropogenic sediment, which are mainly deposited or relocated in the form of mine tailing dumps or landfills, either onsite (internal anthropogenic deposits) or offsite (external anthropogenic deposits) (Verma et al, 2013). External anthropogenic deposits come with more drawbacks than internal, as the economic costs of waste transport and external land acquisition can be extensive (Verma et al, 2013). The alternative to this is in-pit dumping (IPD), which entails the generation of anthropogenic waste deposits on-site by infilling unused pits concurrent with the continued extraction of coal (Verma et al, 2013).

1.4.3. Room and Pillar Mining

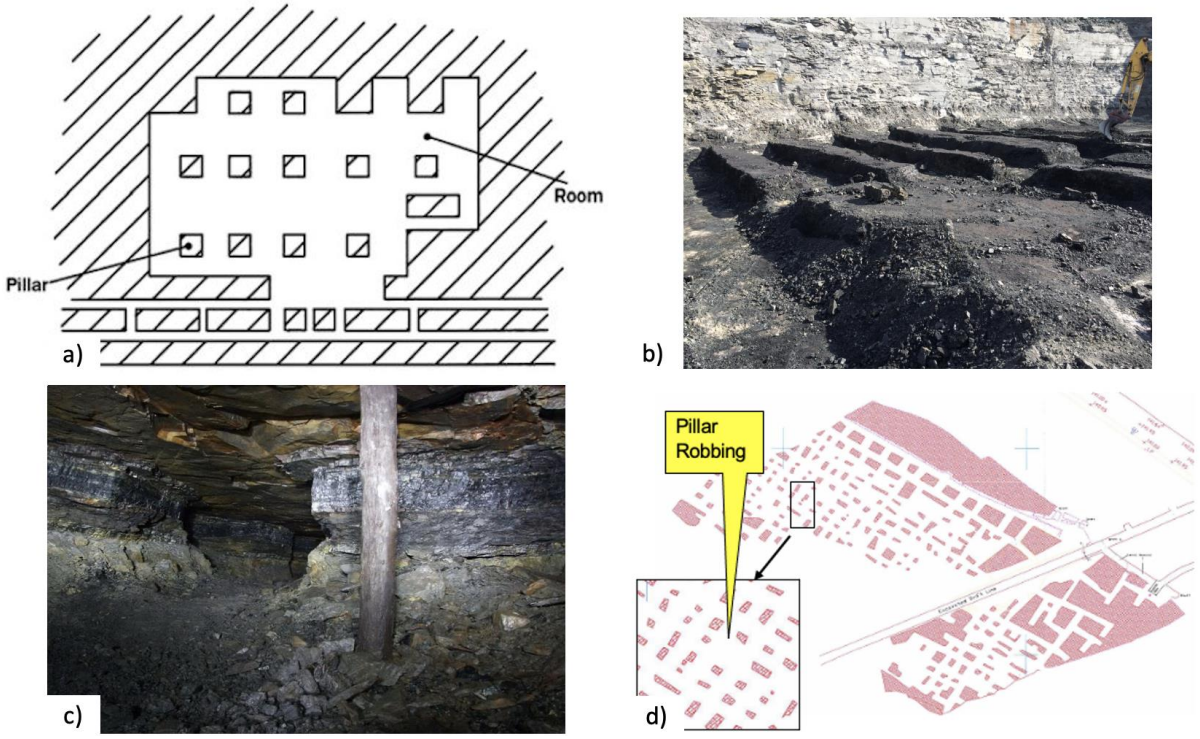

Figure 5 - Room and pillar mining images. (a) and (d) are both schematic diagrams. (b) shows exposed workings at the Field House Surface Mine, County Durham, while (c) is an underground view of former workings. Provided by The Coal Authority.

Figure 6 – Room and pillar coal workings uncovered by opencast mining at Blindwells, East Lothian. The two men give an idea of the scale of the rooms left behind. Photo © British Geological Survey GeoScience Ref P001520 – Blindwells Opencast Site, Tranentt, East Lothian.

Room and pillar mining became widely used between the 14th and early 20th century, and while more efficient than bell pits, it does not possess as high an extraction rate as opencast mining (Andrews et al, 2020, Donnelly, 2020, Scott et al, 2010). It could be considered an extension of bell pit mining, as the introduction of wooden roof supports and coal pillars acted as a framework to reduce the likelihood of roof collapse (Andrews et al, 2020, Daunton, 1981, Donnelly, 2020). The area between the *in-situ* coal pillars was excavated, leaving empty 'rooms' behind, as shown in Figure 5 and Figure 6. This meant that extraction rates of room and pillar mines were dependent on the size of the pillars left to support the overburden, with the dimensions of pillars and rooms found to vary in the available literature.

Donnelly (2020) found that room dimensions ranged between 1.8-4.2 m wide, Younger and Adams (1999) sized the pillars in Carboniferous Coal Measures at 9-30 m wide with the rooms at 6-9 m wide, and Todd et al (2019) finding that old mine plans had the pillars and anywhere between 5x5 m to >30x15 m. This leads to a range of extraction rate values, with literature stating that extraction rates

could range anywhere from 15% to 90% (Donnelly, 2020, Edmonds, 2018, Gee et al, 2019, Wardell and Wood, 1965).

This inherent variability between the pillars and rooms is found in the flooded abandoned mines, with several factors contributing to the generation of a non-homogeneous artefact of mining (Lawrence et al, 2023). As time has passed, the pillars within the abandoned mines have been degraded by a variety of factors with a range of results. These factors have been listed by Donnelly (2020), with pillar spalling, pillar robbing, roof support degradation and groundwater rebound all contributing to the destruction of coal pillars – elaborated in Table 3. The destruction of the coal pillars increases the instability of the overburden, until the roof between the pillars – above the rooms – collapses (Andrews et al, 2020, Donnelly, 2020, Edmonds, 2018, Gee et al, 2019). This will occur at differing speeds due to inherent differences in conditions between locations, so each mine can be very different from another.

To add to the unknown state of the abandoned mines, it is complicated further by the appearance of mine waste within the mine workings, in the form of backfill. Backfilling the areas of the mines that have been extracted is an alternative method for mine waste disposal that also increases the stability of the overburden (Sloss, 2013). As outlined by Sloss (2013), the backfilling of mine workings has several benefits, where the waste generated from the coal extraction is returned to the subsurface with no expenditure to dispose of the waste to an external site, while also replacing some of the voidspace created, aiding the stability of the workings, and reducing the likelihood of void migration and subsidence.

Table 3 – List of the factors affecting the stability of in situ *coal pillars in pillar-and-room workings.*

Degradation Factor	**How it affects pillar stability**
Depth and thickness of extraction	Greater depths of extraction and thickness of coal extracted increases the amount of overburden stress put through the pillars, decreasing stability.
Pillar geometry	Thicker pillars are more stable than thinner pillars, due to an increased volume of material to support the roof of the extraction area.
Pillar robbing	Pillar robbing took place as mines were abandoned and consisted of miners taking extra material from existing pillars, reducing the integrity of the pillar.
Degradation of timber roof supports	The use of timber roof supports aided the *in-situ* pillars in preventing roof collapse, but over will have degraded over time to an unknown state, leaving more emphasis on the pillars to take the bulk of the overburden stress.
Presence of minewater	The presence of minewater can accelerate the weathering of the coal pillars (eg. wetting and drying cycles, seasonal changes), increasing the likelihood that a pillar may fail.

1.4.4. Longwall Mining

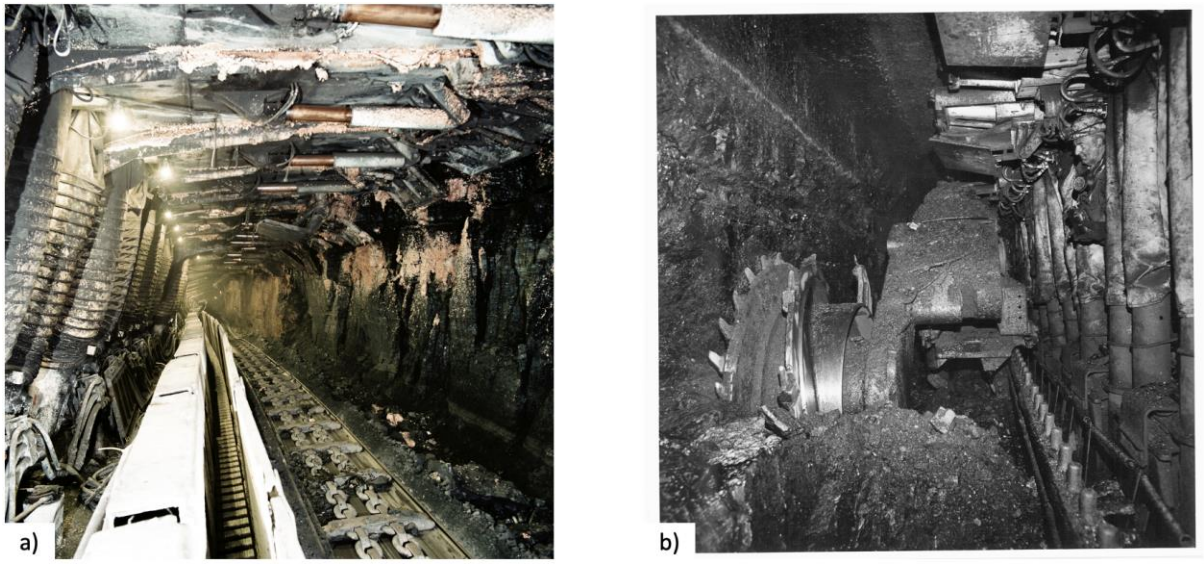

Figure 7 - Images of longwall mining machinery. (b) is a 'radio-controlled shearer' from Daw Mill Colliery, Warwickshire, in 1978. Images provided by The Coal Authority.

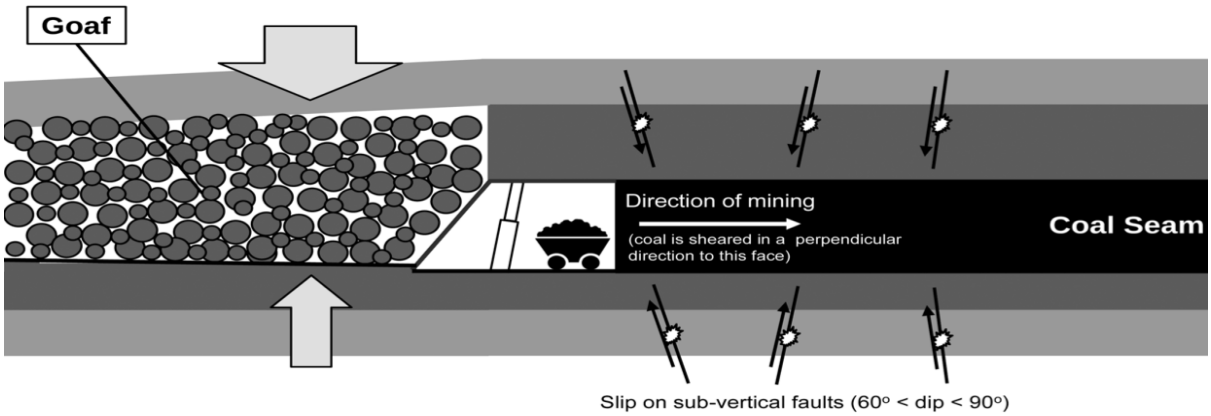

Figure 8 - Schematic cross-section diagram of longwall mining operations. Adapted from Bischoff et al, 2010.

Longwall mining is the most modern technique for the mining of coal seams, coming into popularity in the 20th century (Donnelly, 2020). The advancement of technology allowed for the mechanisation of coal extraction, increasing the yield to a higher level. This took place in the US following the 1972 'Energy Crisis', with the adoption of UK and German longwall mining techniques, allowing for 'high efficiency high production longwall mining system(s)' (Peng et al, 2019). By having hydraulic roof supports included as part of the machinery that operates on the longwall face (Figure 7), the need for *in-situ* coal pillars to be left behind is removed, increasing the yield (Donnelly, 2020, Peng et al,

2019). Seen in Figure 8, as the machinery moves forward, the overburden behind is allowed to collapse, creating an anthropogenic sediment referred to as 'goaf', or 'gob' – otherwise known as roof collapse (Donnelly, 2020). While longwall mining was an uncommon method within the County Durham and Northumberland coalfields, the method is one of the most common in Present-day coal extraction and has been carried out in the UK, including former coal mine workings encountered by the UKGEOS site in Glasgow (Monaghan et al, 2022).

1.5. Carboniferous Stratigraphy

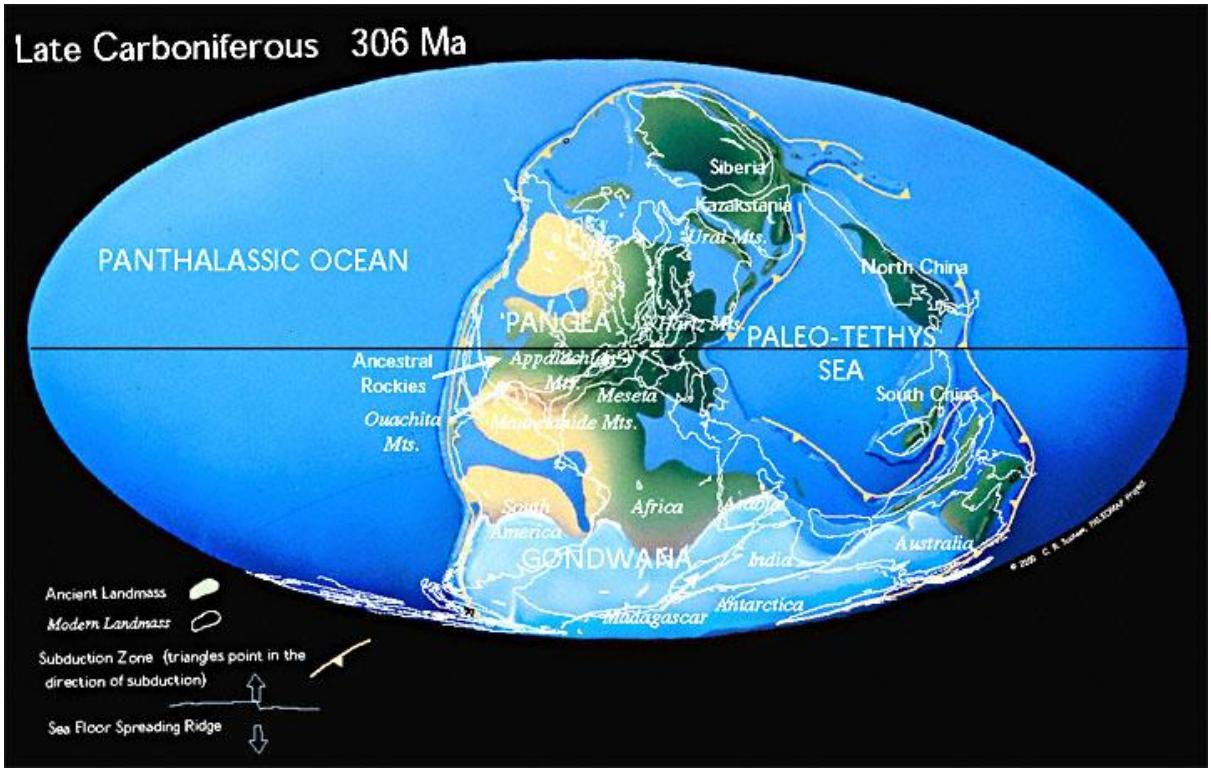

Figure 9 - Palaeomap of the Earth during the Late Carboniferous (306 Ma). From scotese.

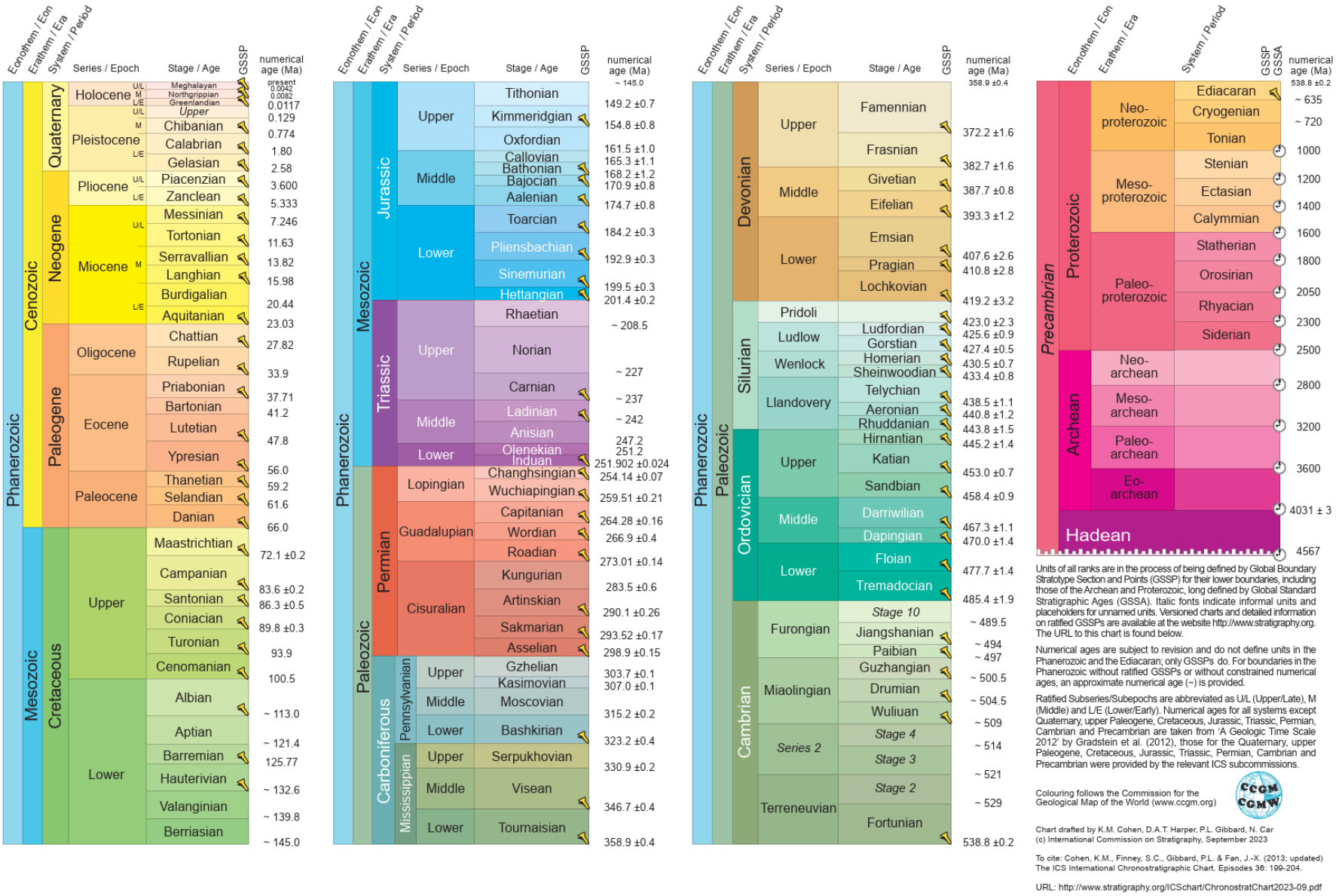

Figure 10 – Geologic Time Scale according to the International Commission on Stratigraphy, 2023.

The coal measures within the UK are contained within the Late Carboniferous stratigraphy, being deposited around 306 Ma – during the Kasimovian Stage of the Late Pennsylvanian Epoch (see Figure 9 and Figure 10). This was around the period where the global landmasses started to collide to form the supercontinent Pangea, with Europe situated on the equator. Gondwana was situated over the Southern Pole, and with ice covering lots of the Southern Hemisphere this meant that much of Gondwana was covered by ice sheets (see Figure 9).

The rise of plant life throughout the Devonian led to global oxygen levels rising, which was the driver of larger forest regions developing in the equatorial regions of the period. The decay of the large volumes of plant matter accumulated and was buried within what is now known as the Carboniferous Coal Measures, with several regions within the UK being large producers of coal during the Industrial Revolution (see Figure 11).

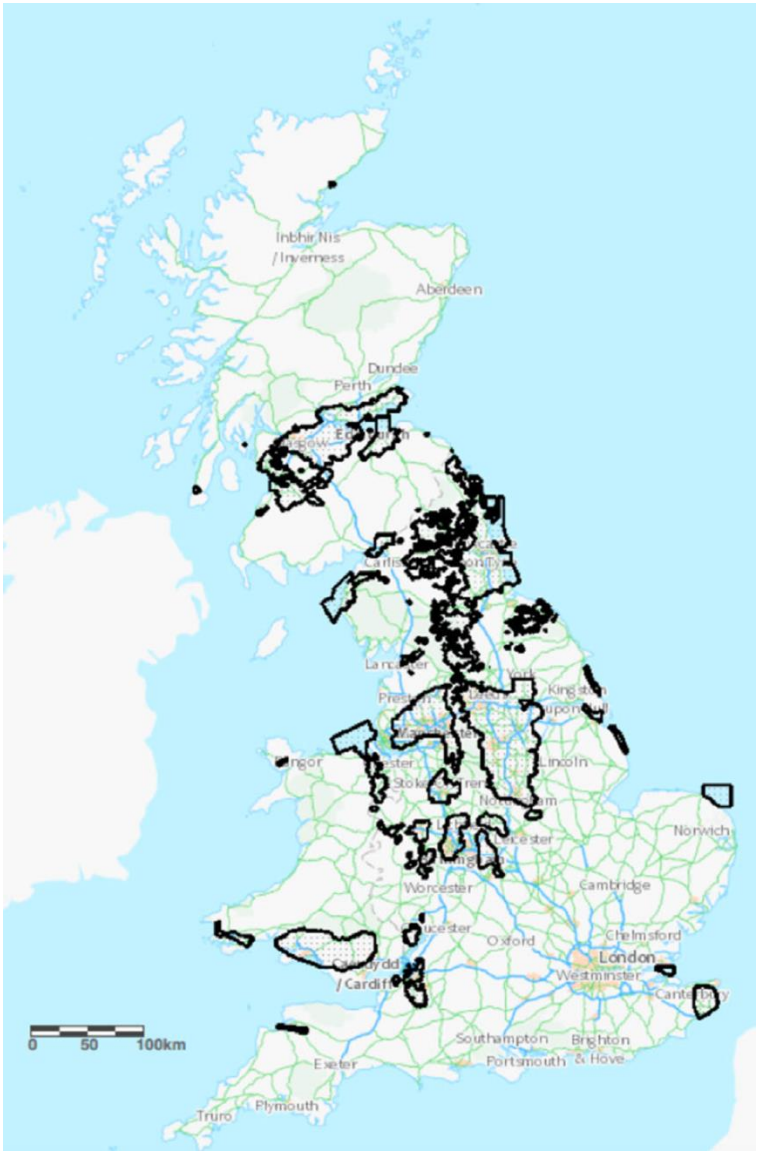

Figure 11 – Polygon map of areas explored for coal extraction – not all areas necessarily exploited for coal extraction. From The Coal Authority Interactive Map.

The low-elevation landmass around the equator during the Carboniferous was repeatedly flooded by the eustatic sea level changes driven by the waxing and waning of the Gondwanan ice sheet, leading to the cyclic marine sequences contained within Carboniferous strata seen in present-day. During periods of low sea level, deltas developed out into shallow coastal areas, giving rise to large areas of swampy conditions and vegetation (O'Mara and Turner, 1999). River channels washed in mud, which hardened into mudstone, while the sand deposited above gave rise to sandstones. The swampy vegetation accumulated and was buried, developing into coals. Once sea levels began to

rise again, the swamps and deltas became flooded, resulting in the deposition of limy marine muds, developing into the limestone bases at the base of Carboniferous stratigraphy (see Figure 12).

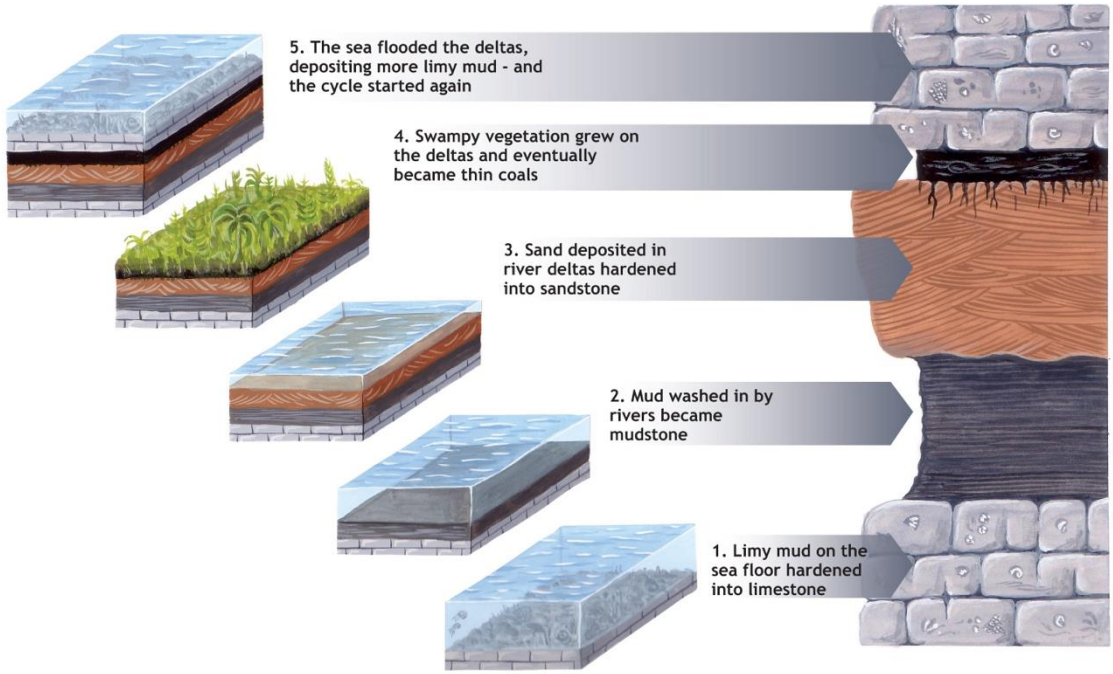

Figure 12 – Diagram showing the formation of a typical cyclothem sequence. © Elizabeth Pickett, 2022.

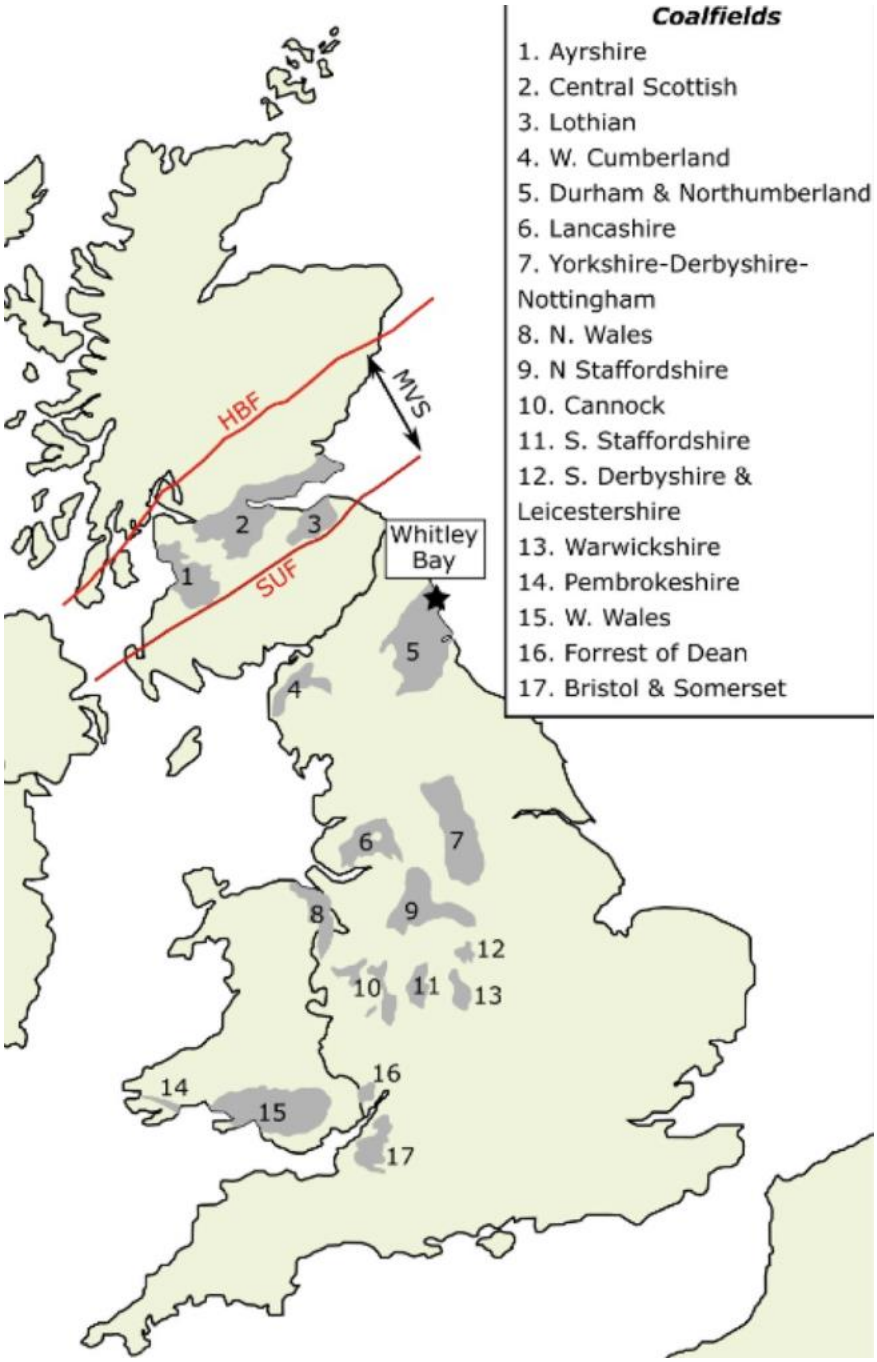

Figure 13 – Map of UK coalfields, with Whitley Bay located by the star. From Billy Andrews et al, 2020.

The focus of this project is within the Northumberland Coalfield, with the High Main coal seam being the most productive and exploited coal seam in the region, rarely being less than 1.5 m in thickness and often exceeding 2 m thicknesses (Fielding, 1984, Smailes, 1935). Whitley Bay is one of the only places in the UK to see exposed coal workings, with room and pillar workings for the High Main seam being exposed at the coast due to coastal erosion (see Figure 13). As well as the former coal

workings, part of the Carboniferous stratigraphy below the High Main coal seam is also exposed. The area is part of the Northumberland Basin, which was a low relief, humid coastal fluvio-deltaic environment during the Carboniferous (O'Mara and Turner, 1999). The High Main is visibly underlain by the stratigraphy that is typical of a deltaic depositional environment, which is further explained in the next section.

1.6. Deltaic Facies

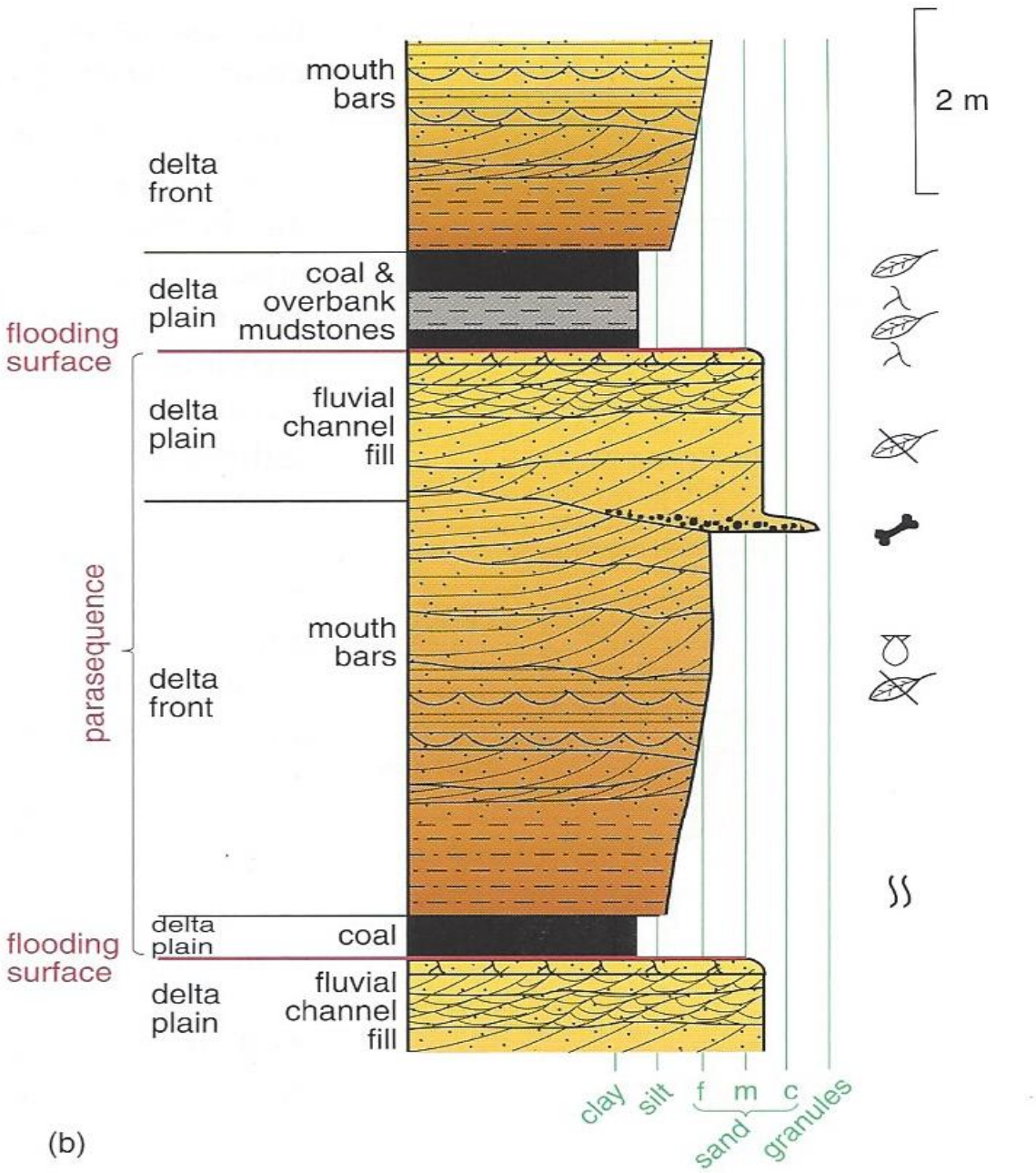

Figure 14 - Sketch graphic log of a typical succession resulting from deltaic progradation. From Tucker and Jones, 2023.

The start of the sequence consists of a limestone base containing marine fossils, formed from an offshore marine shelf. Above this limestone base comes a section of coarsening-upward mudstones, with fewer marine fossils found as the sequence progresses upwards. This comes from the deposition of sediments from out-flowing distributary river channels. The finer sediment is carried further out from the delta plain, hence the sequence coarsening upwards. This part of the sequence also commonly contains laminations and bioturbation. The mudstones continue coarsen upwards and change to cross-bedded sandstones from the delta front, from the deposition of coarser sediment closer to the distributary channel mouths.

The mudstone strata are overlain by thick, coarse sandstone beds, deposited by the in-filling of the distributary channels from the sediment of more major channels. This process can repeat several times, creating several strata of thin, fining-upwards sandstone beds. The infilling of the channels and bays gives rise to peat and swampland, where the decomposition of the resident plant life results in coalification. This is found in the deltaic sequence as a layer of seatearth overlain by the coal seam itself. Deeper repetitions of the sequence contain thicker coal seams, whereas the shallower sequences contain thinner coal seams (Fielding, 1982, Smailes, 1935).

1.7. Coal Petrography

As mentioned previously, coal originated from the decay and burial of vegetation in swampy regions during the Carboniferous. It can be separated out into two different types; ‘humic’ coals developed from woody material and peatfication and ‘sapropelic’ coals developed from non-woody sources like algae, pollen, or leaf wax (O’Keefe et al, 2013). Coal found in the UK is 86-88% carbon, making it ‘bituminous’ coal, a subset of humic coals.

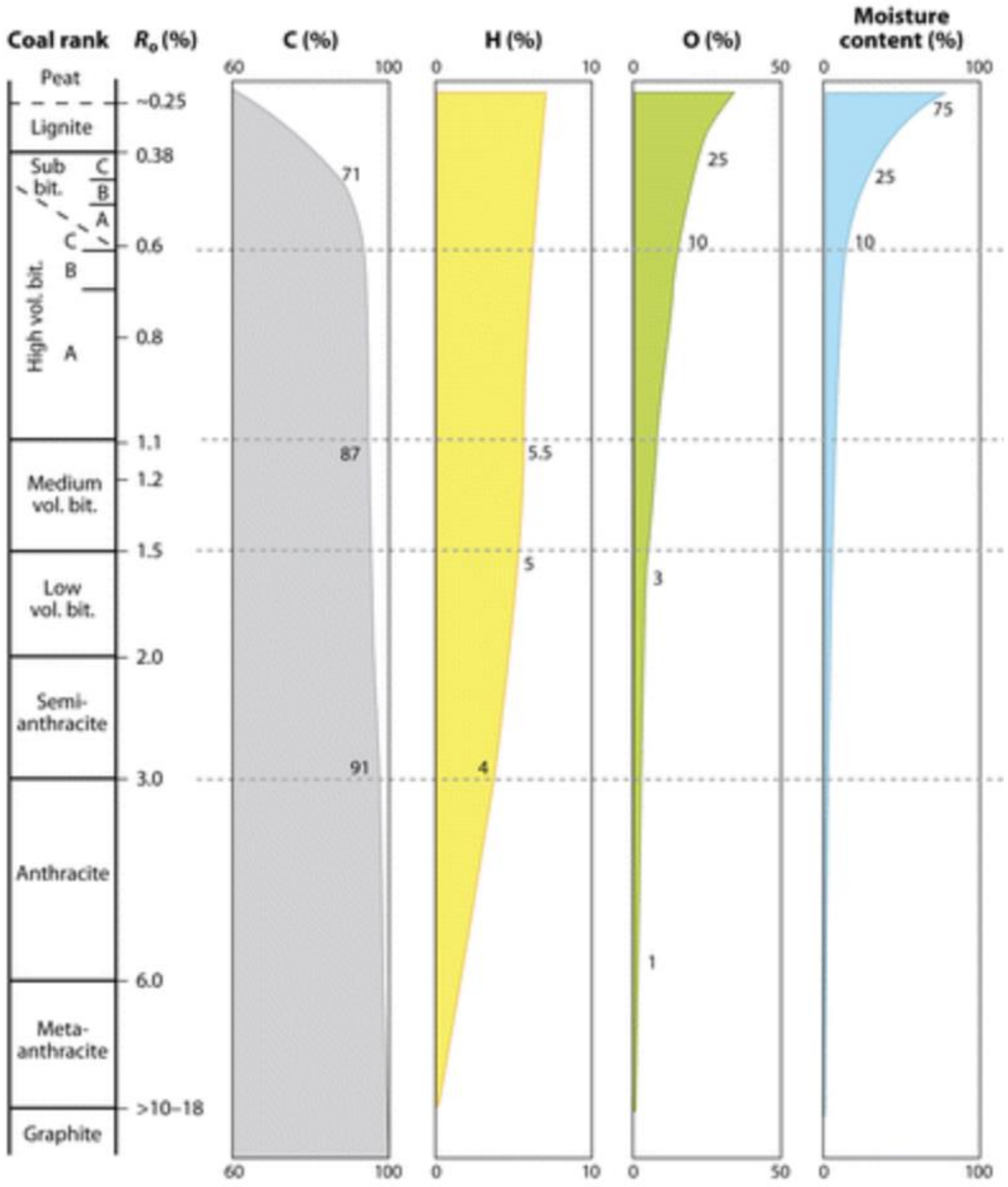

Figure 15 - Coal rank and changes in coal properties with increasing coalification. Adapted from Strąpoć et al, 2011. Abbreviations - vol. = volatile; bit. = bituminous; R_0 = vitrinite reflectance; C = carbon; H = hydrogen; O = oxygen.

Coal rank is a scale to differentiate between humic coals based on the degree of coalification that they have undergone (O'Keefe et al, 2013, Tucker and Jones, 2023). *Anthracitic* coals contain >90% carbon, while *bituminous* coals contain 75-90% carbon (Tucker and Jones, 2023). There are also subclasses within these two ranks, as shown in Figure 15, which can be seen as arbitrary due to the

gradual change from bituminous to anthracitic. The increase in rank from bituminous coal to anthracitic coal sees the carbon content increase and the volatile content decrease (Figure 16). During the formation of sub-bituminous coals, *vitrinite* is formed, which is one of the main components of bituminous coals (Tucker and Jones, 2023).

Vitrinite is one of the three maceral groups that forms the basic constituents of coal, along with inertinite and liptinite. Vitrinite forms from the coalification of woody material – leading to humic coals developing, as covered previously – while inertinite forms from fungi, and liptinite is formed from the coalification of algae and spores (Tucker and Jones, 2023). These maceral groups combine to give rise to four different lithotypes that form coal seams and are visible in hand-specimen. *Vitrain* layers appear bright and glassy, *fusain* is soft and charcoal-like, *durain* is dull and possesses no lustre, while *clarain* is laminated with a silky lustre (Tucker and Jones, 2023).

As coalification takes place, the pressure that compresses the decaying plant matter and macerals results in the formation of 'cleats', a form of internal fracture network within coal seams. Cleats form an important part of coal structure, as they have been found to be a major part of how permeable and porous a coal seam can be (Gao et al, 2022, Song et al, 2022, Pan et al, 2019, Zeng et al, 2011, Jing et al, 2017, Mukherjee et al, 2021, Harpalani, 1995). With the cleat network acting as a fracture network, the storage capacity of a coal is directly influenced by the capacity of the cleat network. For clarification, the 'storage capacity' of a coal is how much fluid or gas can be held within the coal itself, whether in the micro- or macro-porosity and cleat network. Gao et al (2022) found that 5% of the total storage capacity of coal was found within the cleat network as 'macroporosity', while the remaining 95% was stored within the matrix of the coal in the 'microporosity'. The storage capacity of coal is variable due to the storage within the cleats, as they have been found to be influenced by directional stresses (eg. Gao et al, 2022, Song et al, 2022, Zeng et al, 2011, Palmer, 2009). Overburden pressure can force the cleat network to close up, reducing the storage capacity (Gao et al, 2022, Zeng et al, 2011, Robertson, 2005).

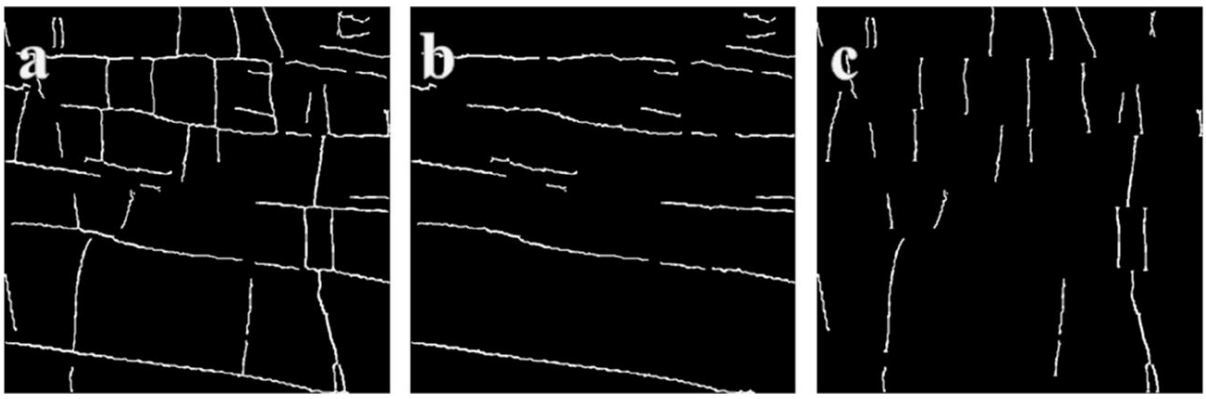

Figure 16 - Diagrams of a cleat network. (a) full network (b) only face cleats (c) only butt cleats. From Mostaghimi et al, 2017.

1.8. Current Research on Coal

Much of the current research into coal permeability and porosity, and how these values change due to the cleat system and varying overburden pressures, has been done for coalbed methane (CBM). CBM is generated within coal seams either through devolatilization (thermogenic CBM) or through microbial-driven decomposition of the plant matter within the seams (biogenic CBM) (Moore, 2012). When CBM is generated, it is stored in the cleat system until the seam degasses and releases the methane. By harnessing the release of CBM it can be used as a 'clean' source of natural gas, and with the cleat systems being the main control of the quantities of CBM and fluid flows through the coal seams, lots of research has been done on how permeable and porous they are (Warmuzinski, 2008, Karacan et al, 2011, Moore, 2012, Flores, 1998, Zhou et al, 2016, Su et al, 2005, Bibler et al, 1998). While CBM operations have been explored in the UK, they have not shown as much promise as opportunities being explored in Australia and China (eg. Ham and Kantzas, 2008, Lau et al, 2017). Several studies have explored how the cleat system – and therefore the permeability and porosity of coal – changes with conditions, with increasing pressure forcing the cleats to close up, decreasing permeability (eg. Gao et al, 2022, Song et al, 2022, Zeng et al, 2011, Palmer, 2009). The amount of gas sorption has also been found to influence the permeability of coal, with molecules within the cleat system also causing partial closure of cleats (Zeng et al, 2011). Table 4 shows the range of current research into the permeability and porosity of coal.

Table 4 – Dataset of permeability and porosity test results of coal seams globally, compiled from available literature.

Sample Location	Coal Type	Pressure Conditions	Porosity (%)	Permeability (mD)	Reference
Dalong Mine, China - #13	-	-	0.8235	0.022	
Dalong Mine, China - #14	-	-	0.8448	0.021	
Dalong Mine, China - #15-1	-	-	0.8341	0.014	Gao et al, 2021
Dalong Mine, China - #16-1	-	-	0.8519	0.012	
Dalong Mine, China - #13 (after artificial cleating)	-	-	0.8235	22.5	
Dalong Mine, China - #14 (after artificial cleating)	-	-	0.8448	17	
Dalong Mine, China - #15-1 (after artificial cleating)	-	-	0.8341	4.8	Gao et al, 2021
Dalong Mine, China - #16-1 (after artificial cleating)	-	-	0.8519	2.4	
Bulli Seam, Southern Sydney Basin, Australia	Bituminous	3.0 Mpa He	-	0.9 - 1.0	
Bulli Seam, Southern Sydney Basin, Australia	Bituminous	2.0 MPa methane	-	0.4 - 0.85	
Bulli Seam, Southern Sydney Basin, Australia	Bituminous	4.0 MPa methane	-	0.35 - 0.6	
Bulli Seam, Southern Sydney Basin, Australia	Bituminous	6.0 MPa methane	-	0.3 - 0.45	Pan, Connell, Camilleri, 2010
Bulli Seam, Southern Sydney Basin, Australia	Bituminous	2.0 MPa co2	-	0.25 - 0.6	
Bulli Seam, Southern Sydney Basin, Australia	Bituminous	4.0 MPa co2	-	0.15 - 0.4	
Bulli Seam, Southern Sydney Basin, Australia	Bituminous	6.0 MPa co2	-	0.05 - 0.3	
Cahn Seam, San Juan Basin, USA	-	6.9 Mpa He-water	-	0.44 - 2.6	
Ignacio Seam, San Juan Basin, USA	-	3.1 Mpa He-water	-	0.04 - 0.13	
Seam No.1, Sundance Pit, LaPlata Mine, San Juan Basin, USA	-	3.1 Mpa He-water	-	0.04 - 0.78	Gash, 1991
Blue Creek Seam, Warrior Basin, USA	-	3.1 Mpa He-water	-	1.4 - 4.6	
Ignacio Seam, San Juan Basin, USA	-	7.45 Mpa	-	0.18	
Jagger Seam, Warrior Basin, USA	-	7.45 Mpa	-	0.68	Puri, Evanoff, Brugler, 1991
Lijiacun, South Qinshui Basin, China	-	2.5 Mpa methane	-	0.127	
Qinxin, South Qinshui Basin, China	-	2.5 Mpa methane	-	0.205	
Changcun, South Qinshui Basin, China	-	2.5 Mpa methane	-	0.0293	Shen et al, 2011
Wangyun, South Qinshui Basin, China	-	2.5 Mpa methane	-	0.329	
Chengzhuang, South Qinshui Basin, China	-	2.5 Mpa methane	-	5.707	
Schwalbach Seam, Ensdorf Colliery, Saarland, Germany	Bituminous	6.9 Mpa He-water	0.63	0.90	
No.1 Seam, Warndt-Luisenthal Colliery, Saarland, Germany	Bituminous	6.9 Mpa He-water	1.76	0.52	
Splint Seam, Watson Head, Lanarkshire, Scotland	Bituminous	6.9 Mpa He-water	1.80	0.73	
Tupton Seam, Carrington Farm, Derbyshire, UK	Bituminous	6.9 Mpa He-water	1.35	2.15	Durucan et al, 2014
Dora Seam, Rumeaux Colliery, Lorraine, France	Semi-Anthracite	6.9 Mpa He-water	1.38	5.52	
9ft Seam, Selar, South Wales	Anthracite	6.9 Mpa He-water	0.96	9.51	
7ft Seam, Tower Colliery, South Wales	Anthracite	6.9 Mpa He-water	0.12	2.93	
Sijiazhuang Mine, Jinzhong City, Shan'xi Province, China	-	2 Mpa He-water	9.1	0.031	
Sijiazhuang Mine, Jinzhong City, Shan'xi Province, China	-	3 Mpa He-water	8.8	0.027	
Sijiazhuang Mine, Jinzhong City, Shan'xi Province, China	-	4 Mpa He-water	8.7	0.026	Zhang, Wu, Liu, 2017
Sijiazhuang Mine, Jinzhong City, Shan'xi Province, China	-	5 Mpa He-water	8.7	0.023	
Sijiazhuang Mine, Jinzhong City, Shan'xi Province, China	-	6 Mpa He-water	8.6	0.022	
Qinshui Basin, China	Anthracite	4.3/8.3 Mpa	3.105	0.015	
Ordos Basin, China	Bituminous	4.3/8.3 Mpa	2.323	0.128	Sun et al, 2018
Sihe Mine, South Qinshui Basin, China	-	2.5 Mpa methane-brine	-	0.052	
Chengzhuang Mine, South Qinshui Basin, China	-	2.5 Mpa methane-brine	-	0.262	
Chengzhuang Mine, South Qinshui Basin, China	-	2.5 Mpa methane-brine	-	0.216	
Gushuyuan Mine, South Qinshui Basin, China	-	2.5 Mpa methane-brine	-	0.510	Zhang et al, 2018
Gushuyuan Mine, South Qinshui Basin, China	-	2.5 Mpa methane-brine	-	0.690	
Wangtaipu Mine, South Qinshui Basin, China	-	2.5 Mpa methane-brine	-	0.950	

1.9. Using Shallow Coal Mines for Geothermal Energy

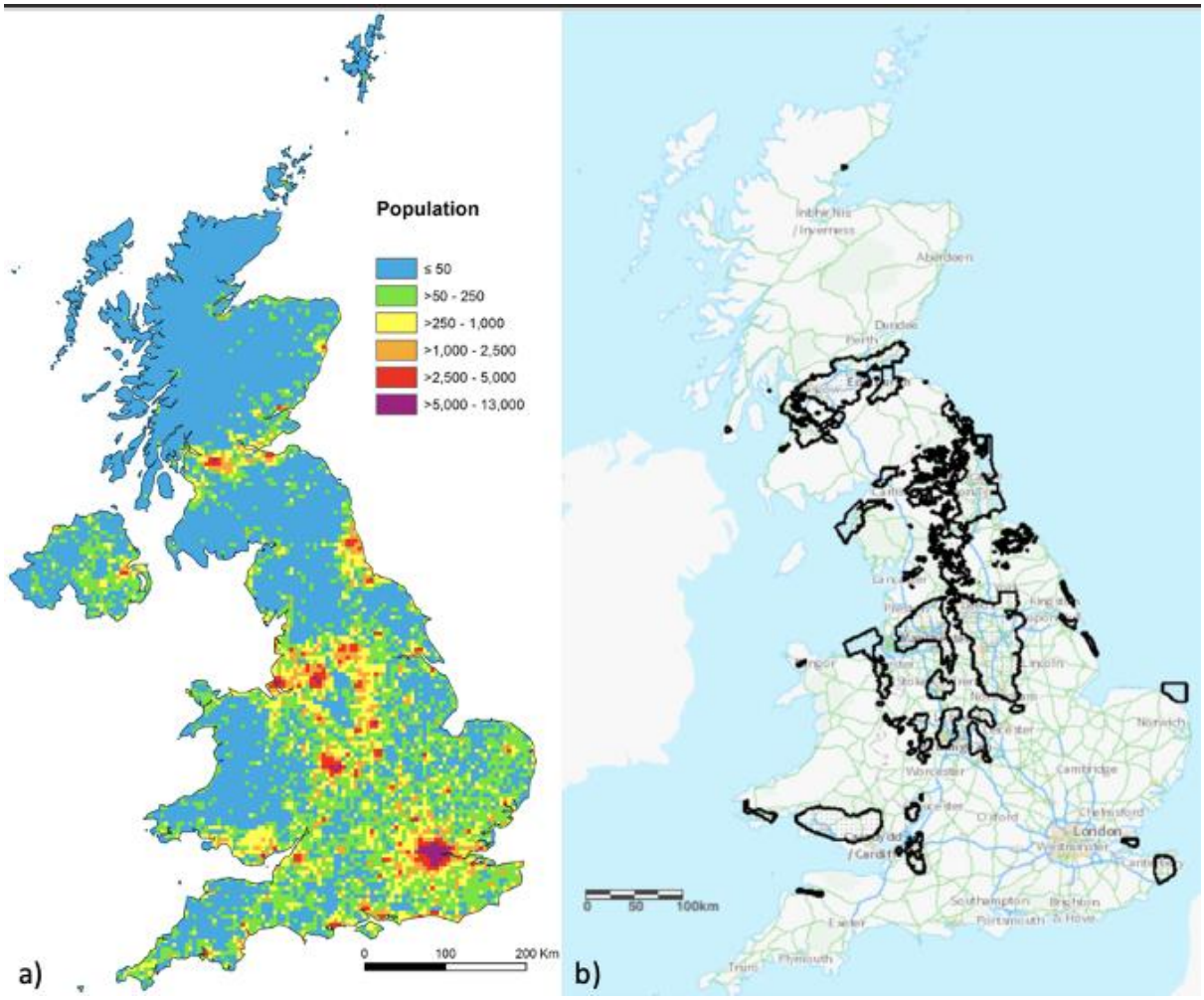

Figure 17 – Maps to show the link between UK population density and areas of coal mining. (a) UK population density. From Vieno et al, 2016. (b) Polygon map of areas explored for coal extraction – not all areas necessarily exploited for coal extraction. From The Coal Authority Interactive Map.

As well as using coal seams for their generation of CBM and utilising them as a source of natural gas, the possibility of using them as a source of shallow geothermal energy has also been explored within the UK (Younger 1995, Andrews et al 2020, Adams, Monaghan and Gluyas, 2019, Monaghan et al, 2022, Gluyas, Adams and Wilson, 2020, Banks, Pumar and Wilson, 2009, Banks et al, 2019). It has been estimated that around 25% of housing and business in the UK resides overtop flooded abandoned mine workings, as can be seen in Figure 17(Banks, Pumar and Wilson, 2009, Banks et al 2019, Gluyas et al, 2020). As the need for decarbonising energy generation increases, it would be

foolish to ignore the vast energy store in the subsurface that is within proximity to a substantial proportion of the UK population. Previous work has been done to investigate the idea of using these flooded mine workings, either as an energy store – such as the 'geobattery' suggested by Fraser-Harris et al (2022) – or for a wider energy generation purpose. In both ideas, the flow of the minewater is an important factor, as the minewater is where the heat is recovered from.

This is where the aspect of variation in the type of anthropogenic waste within the former coal mines becomes of great importance, as they are a factor that should be accounted for when modelling the fluid flow pathways. The occurrence of various anthropogenic deposits found in former coal mines adds much complexity to the task of recovering heat from the minewater, meaning that fluid flow through former coal mines is not simple to understand.

1.10. Thesis Layout

The structure of this thesis is presented as such that Chapter 1 has been an overview on the required context and background for the study, before moving to Chapter 2. Chapter 2, titled '', covers the research carried out at Whitley Bay, the primary study area for this research, where it is the only place in the UK to see the inner workings of a room and pillar coal mine. Chapter 3, titled '', looks at reutilising geotechnical borehole data from a study done by the Coal Authority at the Bayfield Housing Estate, roughly 5-6km inland from Whitley Bay. This study looked at a subsidence issue in that area, which offers an ideal comparison dataset for this study with Whitley Bay, and also provides a second study location to show how the techniques in this study can be reapplied to multiple locations. Chapter 4 is the discussion and conclusions chapter, where the two study locations are compared and contrasted, as well as testing further correlation techniques. This chapter will also cover the basic characterisation and classification of coal mine waste deposits, and how they might be improved moving forward.

2. Characterisation of the Coal Succession at Whitley Bay

2.1. Geological setting and Carboniferous stratigraphy

Northern England is home to several half-graben Basins bounded by faults, developed by crustal extension in the early Carboniferous period, which was possibly caused by the subduction and closure of a back-arc seaway located south of Britain at that time (see Leeder, 1998, O'Mara, 1995, Turner and Smith, 1995, O'Mara and Turner, 1999, Turner and Richardson, 2004). The Northumberland Trough, which is the largest of these Basins, was developed along the line of the closure of the Iapetus Ocean, also known as the Iapetus Suture, and is made up of the Solway Basin in the west and the Northumberland Basin in the east. The Solway Northumberland Basins are separated by a shallow shelf (Figure 18). An early/mid Carboniferous syn-rift phase of subsidence and sedimentation is shown in the Basin-fill, succeeded by a phase of post-rift thermal subsidence in the Moscovian (Leeder and McMahon, 1988). Greater than 4 km worth of predominantly clastic sedimentation in the Northumberland Basin over the course of the Carboniferous period (Turner and Richardson, 2004). The thickest part of this, and thus the deepest part, is in the south of the Basin, adjacent to the Stublick-Ninety Fathom Fault Zone that marks the Basin boundary (see the cross-section of the Northumberland Basin in Figure 18). There were frequent changes to the shoreline of the Northumberland Basin as a result of the interactions between the different environments present, which comprised of a shallow marine shelf in the southwest and the sediment origin terrain to the north and northeast, and as a whole this led to rapid vertical changes in the facies of the Northumberland Basin.

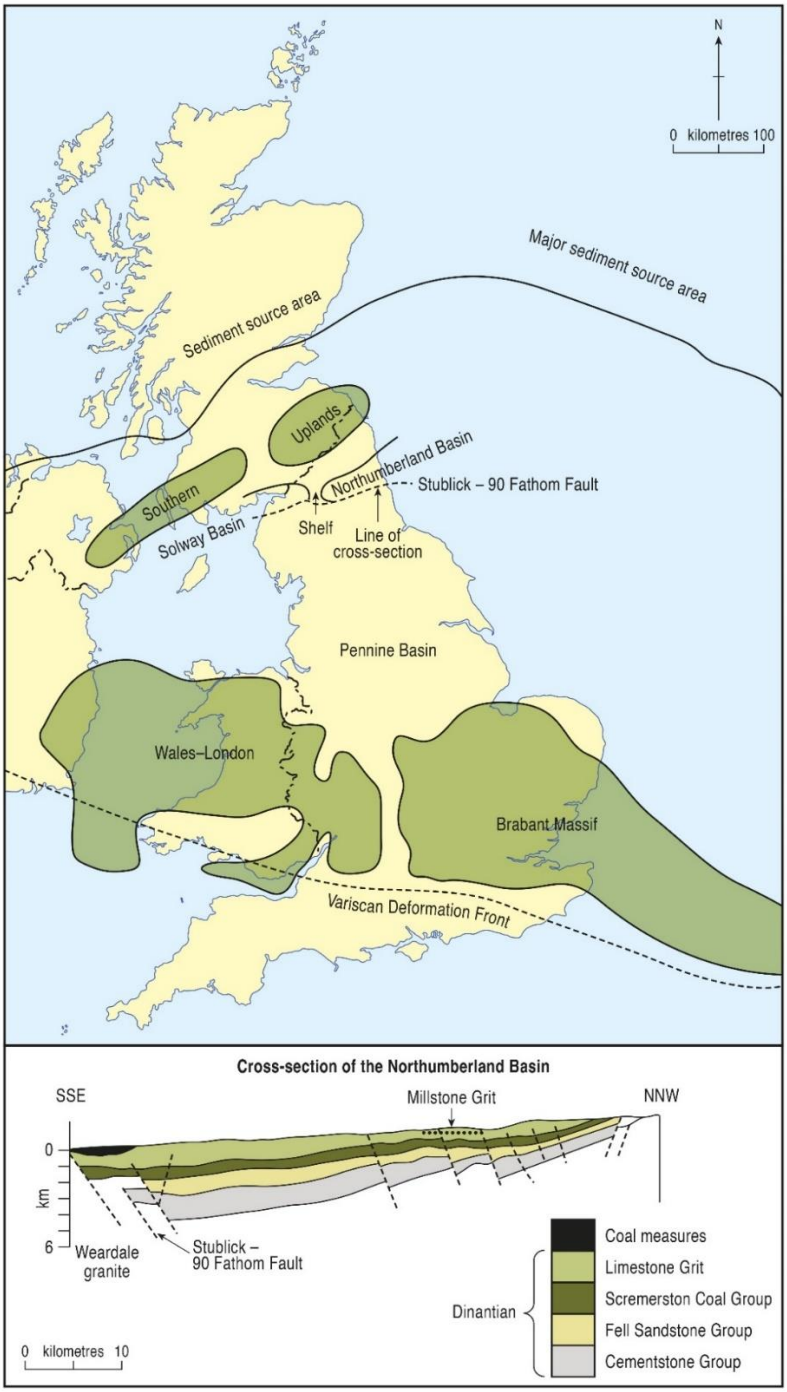

Figure 18 - Palaeographic map of the Pennine Coal Basin, showing the location of the Northumberland Basin. The locations of major sediment source areas and the extent of the Variscan tectonic front are also shown. The diagram in the top left shows the stratigraphy of the Northumberland Basin. Adapted from Turner and Richardson, 2004. The 'Dinantian' is now referred to as the 'Moscovian'.

When the sedimentation of the region began, it started with local alluvial fan conglomerates being deposited, which then give way to strata of the Cementstone Group as you move inwards from the edge of the Basin. There were more arid conditions, with costal alluvial plain channel sandstones

found, as well as floodplain siltstones (see the stratigraphy column in Figure 18). The source region for the sediment underwent a period of tectonic uplift, which resulted in the deposition of the Fell Sandstone Group when this uplift was coupled with increasing humidity levels. This group was deposited from the progradation of sandy, bedload-dominated streams that advanced basinwards. The provenance of the sediment migrated from the northeast to the southwest as the clastic supplies reduced, leading to the influx of marine influence and the deposition of the Scremerton Coal Group, composed of cycles of limestone, shales and sandstones overlain by seatearths and thick coals.

This depositional cycle was succeeded by the deposition of the marine dominated 'Yoredale' cyclothems, made up of limestone, shale and sandstone overlain by seatearth and coal. It can then by separated into the Low/Middle/Upper Limestone Group, with the top of the Middle Limestone Group defined by the Great Limestone, a thick limestone that is found across the region. The Great Limestone also indicates the end of the marine influence on the depositional sequence, with very few limestones found above, indicating the base of a new depositional phase formerly known as the Namurian (Johnson, 1980). The depositional sequence begins to be dominated by fluvial systems, including ~50 m of Millstone 'grit', a group of coarse-grained sandstones deposited in the Carboniferous. This change of depositional influence is also used as a record for the start of renewed tectonism in the hinterland of the basin (Figure 19).

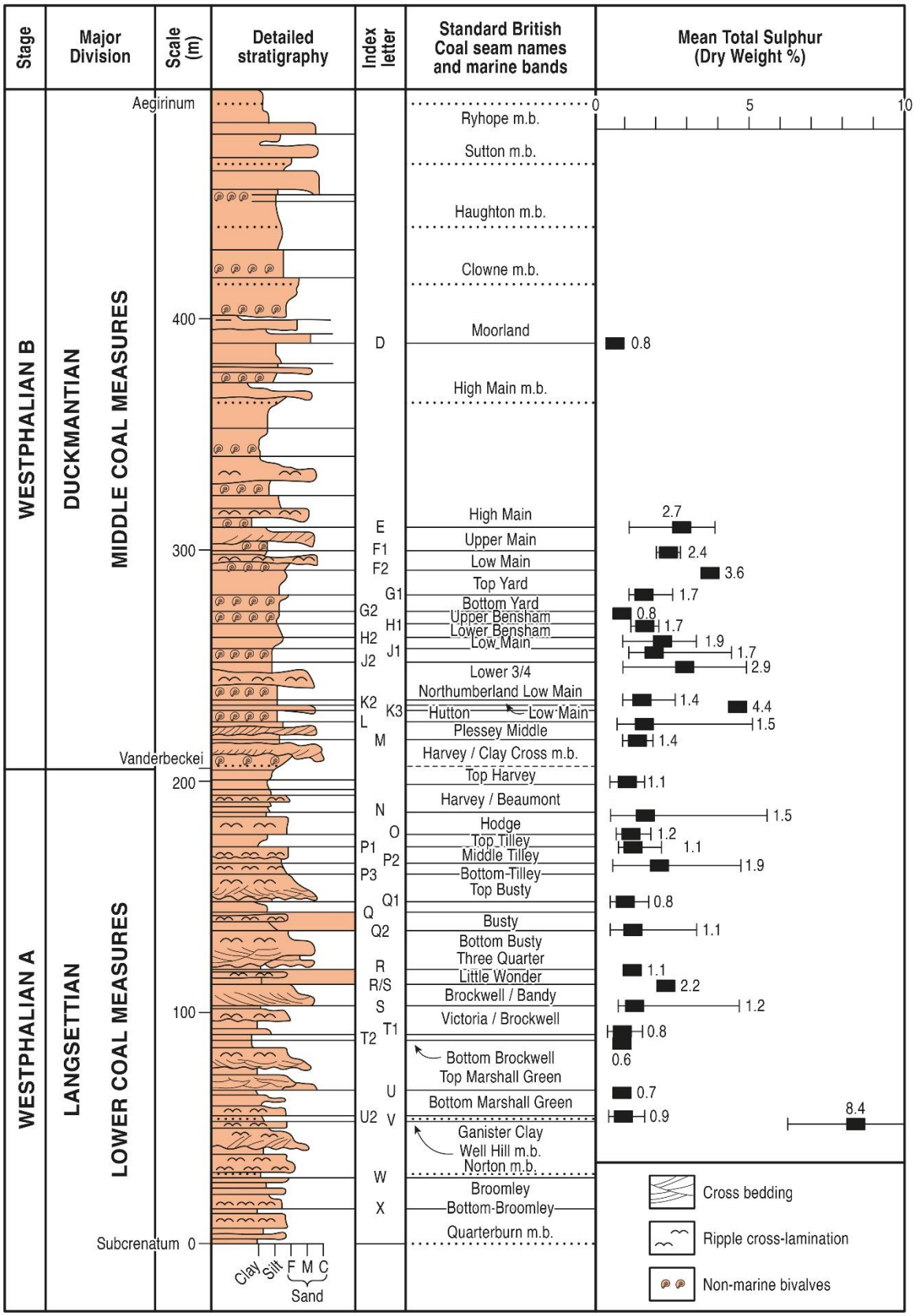

Figure 19 – Detailed stratigraphy of some of the coal seams present in the Northumberland coalfield. Adapted from Turner and Richardson, 2004. The High Main coal seam is located at ~310 m.

Staying with the Limestone Group, it is home to largescale mineral veins throughout the North Pennine Orefield and in other areas within Northumberland, which are comprised of the following – mainly galena (PbS) and sphalerite ((Zn,Fe)S), smaller amounts of pyrite (FeS_2) and marcasite (FeS_2), and then occasional deposits of chalcopyrite ($CuFeS_2$) and pyrrhotite ($Fe_{(1-x)}S$). The valueless minerals, i.e. gangue of the orefield, are zoned with fluorite (CaF_2) and then surrounded by barite/witherite/calcite ($BaSO_4$ / $BaCO_3$ / $CaCO_3$). This zoning was controlled by the temperature of the fluids within the orefield, with higher temperatures in the middle of the orefield and lower temperatures along the margins. A hydrothermal system was set up within the orefield through the intrusion of the Caledonian Weardale granite into the lower Palaeozoic basement rocks, which stripped metals out when migrating into the Carboniferous, lower Palaeozoic and Caledonian Weardale granitic strata by squeezing hot brine out of the shales located in the sedimentary Basin (Dempsey *et al*, 2021). There have been several studies looking at how mineralising fluids can be utilised, as although the main mineralisation phase is thought to be from the Permian at the earliest, potential fluids are still flowing at present day. These fluids have been explored for their potential for geothermal energy, especially in the southern boundary of the Northumberland Basin and along the boundary at the west of the Durham coalfield (see Younger *et al*, 2016; Gluyas *et al*, 2018).

As seen by Figure 20, the Northumberland Basin was situated in the northern part of the larger Pennine Coal Basin during late Bashkirian times. The Pennine Coal Basin is much larger, spanning across central England and into the south of the North Sea into Europe. The formation of the basin has been related to the Variscan orogen, either through reginal strike slip (De Paola *et al*, 2005) or through north-south extensional stress. The Pennine Basin formed to the north of the Variscan mountain front, therefore meaning that the material that infilled the basin is undeformed (Besly, 1988). As seen in the stratigraphic column in Figure 18, only the Moscovian is found in Northumberland, comprised of 750 m of the lower and middle Coal Measures. This section of the stratigraphy is dominated by alluvial influences, with the succession having been deposited atop a

coastal, low-lying alluvial plain, which then turns into environments with more marine influences in the south/southwest. The coastal plain was located >200 km from the coastline, and despite being this large distance from marine influence, relative fluctuations and changes in sea level still influenced the coastal plain.

The drainage of the plain occurred mainly through south-westerly river drainage which flowed into small deltas. These deltas were comprised of shallow interdistributary lakes, often shallower than 20m (Fielding, 1984, Turner and Smith, 1995, O'Mara, 1995). This was then followed by the colonisation of the alluvial plain by vegetation before being flooded by lake waters. This caused the sediment base layer to rise, and therefore the corresponding accommodation space also increased, while the flooding also preserved the peat layer. Over time, this transitioned to become a thin sequence of coarsening-upwards deltaic strata, consisting of sandstone, siltstone and shales, before being topped by the coalified peat in the form of a thin coal bed (see log in Figure 20). Figure 20 shows that crevasse-splays were commonplace in the area, which when paired with relatively straight river channels and frequent flooding of the river banks can imply that the crevasse-splays were perennial, rather than annual.

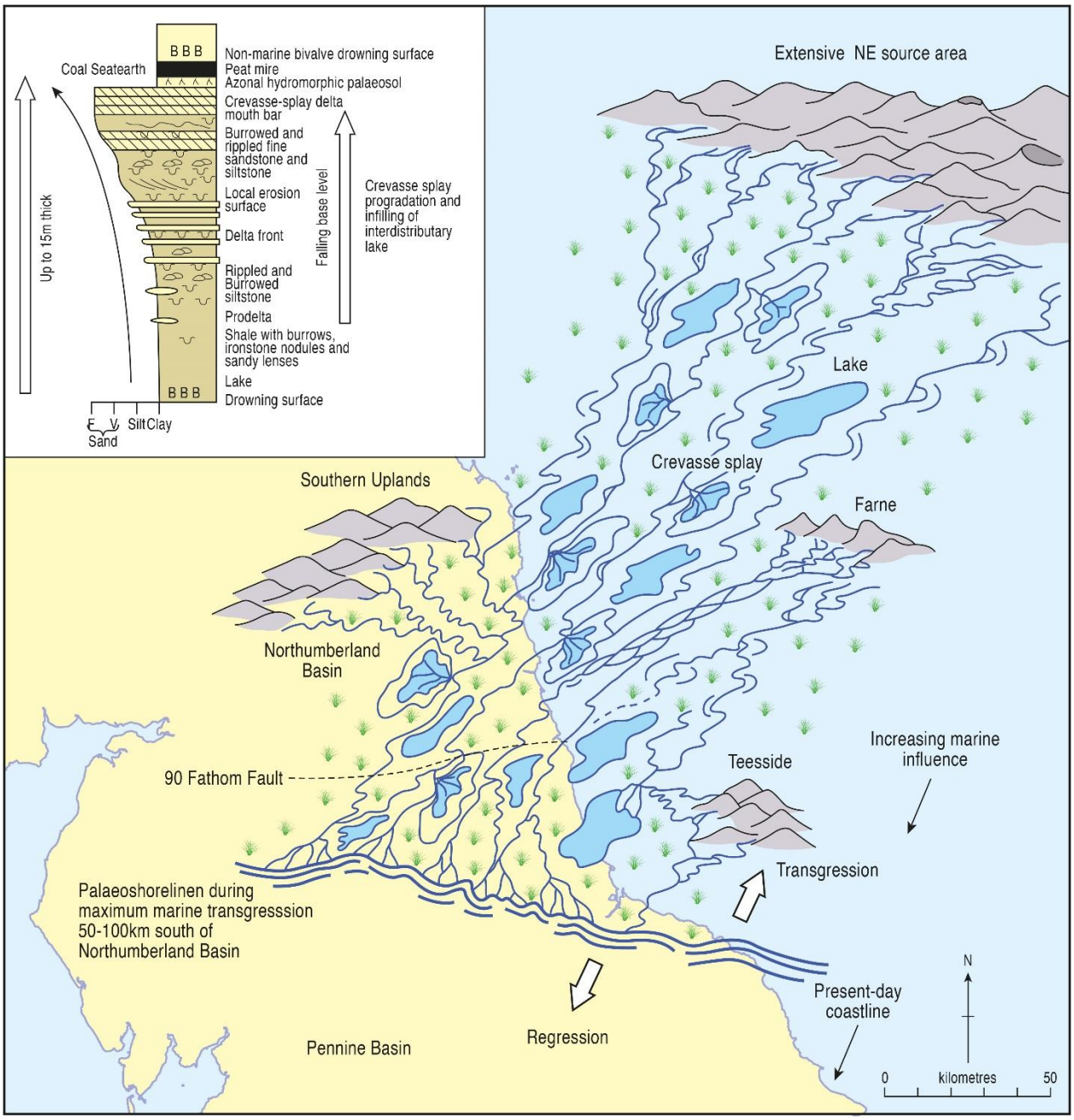

Figure 20 – Map of the northern parts of the Pennine Basin, namely the coal measures located in Northumberland. The main features include showing the location of the sediment source area in the northeast, bringing increasing marine influences on the region. The graphic log in the top left section shows the typical succession expected in an interdistributary lake, as is found in the Northumberland Basin. Adapted from Turner and Richardson, 2004.

Throughout the late Bashkirian and the Moscovian, the depositional environment stayed consistent, with equal rates of sedimentation and subsidence taking place in fluvio-deltaic conditions. During this period, there were also several thin marine bands deposited, as a result of marine transgressions interrupting the previously detailed deposition sequence. As found by Flint *et al* (1995), these thin

marine bands are indicators of the maximum marine flooding surface of the time, with different magnitudes of marine flooding event linked with the *subcrenatum*, *aegiranum*and *vanderbeckei* marine bands. As opposed to being fully developed marine environments, these thin bands are majority *Lingula*-rich mudstones, even though they evolution under mostly marine conditions. These marine flooding surfaces developed in this way because of the low prevalence of total marine conditions in Northumberland, which was due to the northwards shallowing of the marine transgressions and furthered by being diluted with freshwater as the fluvial systems drained towards the south. This meant that Northumberland never underwent a period of total marine conditions, with this being the reason that the marine bands in the depositional sequence are only thin. However, even though these marine influences are minimal, they represent an important part of the depositional sequence, and have been linked to be part of the reason for variable sulphur content across the region (see Figure 21; Turner and Richardson, 2004).

Turner and Richardson (2004) found that the Northumberland Basin had variable sulphur content within the coal seams, with secondary epigenetic pyrite indicating that sulphur was an addition to the coal seams post deposition, potentially originating from the southern boundary of the Northumberland coalfield. The mineralisation of the North Pennine Orefield took place in late Carboniferous to early Permian times, with the sulphide and sulphate mineralisation due to the expulsion of sulphur-rich fluids into the coalfields. This fluid expulsion has been linked to Variscan tectonism, due to the fluid flowing northwards from the Variscan orogen front, at around 280 Ma. When putting this enhanced sulphur content in the coals into the context of this project, the potential for higher concentrations of pyrite has implications when using the coal seams for geothermal projects. Excessive pyrite oxidation can lead to the evolution of ferrous/ferric sulphate from iron sulphide, potentially leading to ferric hydroxide and sulphuric acid (see Equation 1). Considering the amount of piping that geothermal projects require, large amounts of pyrite

generation can lead to increased levels of ochre in the mine waters being used for their geothermal potential, having the potential to corrode the engineering infrastructure of the system (Steven, 2021, Walls *et al*, 2021).

$$2FeS2 + 2H2O + 7O2 = 2Fe2 + 4SO2{-}4 + 4H + (aq)$$

Pyrite + water + oxygen= ferrous iron+ sulphate+ acid Eq. 1

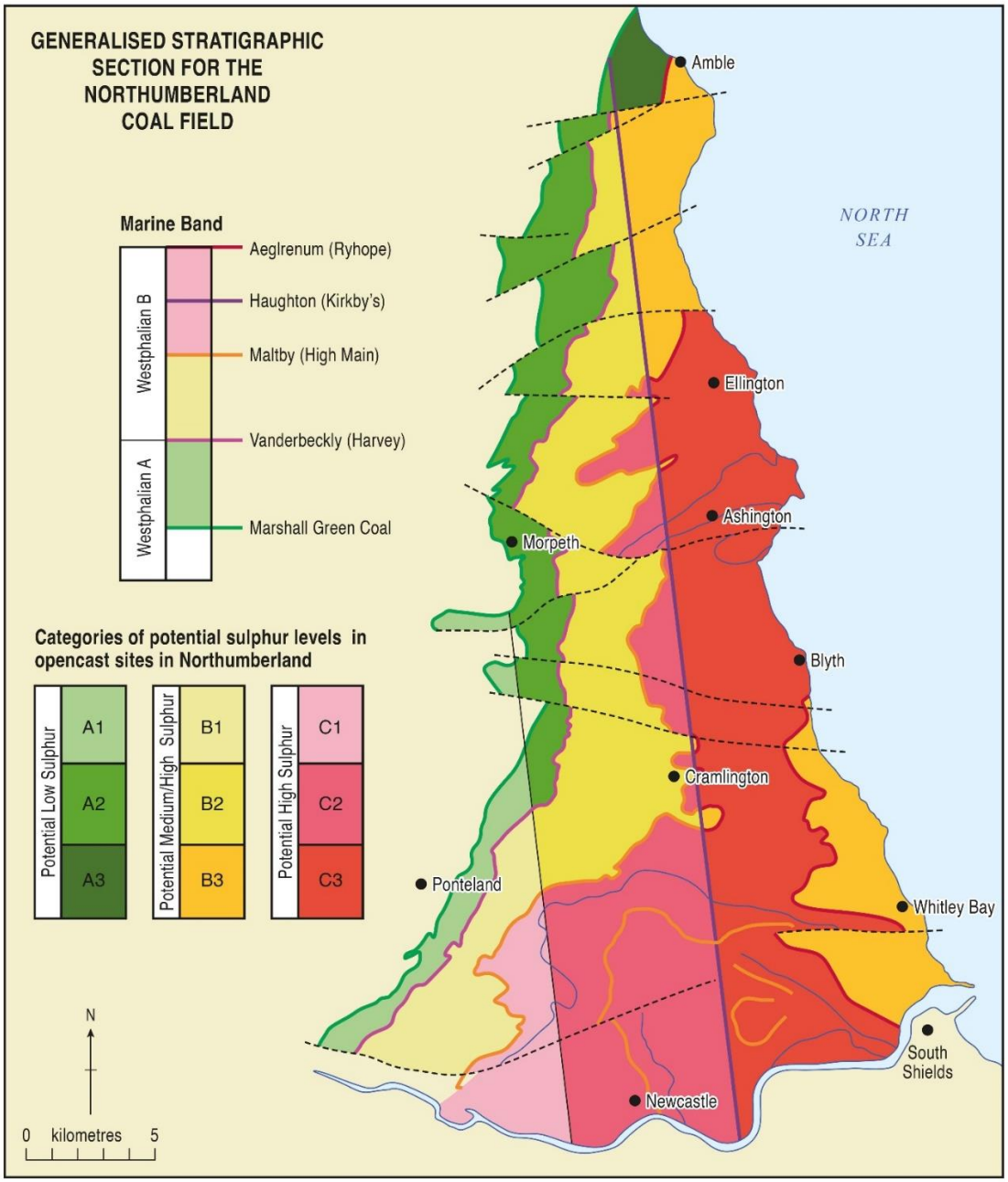

Figure 21 – Map of the Northumberland coalfield categorised by the potential sulphur levels present. The stratigraphy of the region is overlain by a colour scheme for the sulphur levels, leading to the 'zonal' classification of the coalfield. Whitley Bay has Kasmovian stratigraphy (shown in old naming criteria as early Westphalian B stratigraphy), with the coal present being potentially medium/high in sulphur content. Adapted from Turner and Richardson, 2004.

2.2. Coals found in the Northumberland Coalfield

Much like the rest of the coal found in the UK, coals within the Northumberland coalfield are high volatile bituminous coals, increasing in coal rank towards the southern part of the coalfield. The coals developed in this manner as a result of thermal gradients from shallow basement strata, with this gradient being higher in the south and decreasing towards the east, hence the lower ranked coals being found in the easterly parts of the coalfield. The majority of the coals have low ash yields, mainly <10% yield, but they can range from 2.2% to 17%. As found by Turner and Richardson (2004), the sulphur content of these coals ranges between 0.6% and 8.4% S_{TOTAL}, which is found in several different forms. The sulphur can largely be found as cleat infills within the coal, as well as in cubes of sulphate and pyrite, as purely organic sulphur and sulphur nodules, and then also being found as veinlets and bedding-parallel lenses (Turner and Richardson, 2004). In the context of this research, investigating the sulphur content and different forms will be part of the characterisation of the High Main Coal Seam.

2.3. Mine Water Chemistry

Groundwater rebound is what causes the refilling of subsurface mines, and there is extensive documentation on the processes within mines that affect the mine water chemistry within coal mines (eg. Banks *et al*, 1997, Younger and Robins, 2002, Burnside *et al*, 2016, Banks *et al*, 2019). These processes dictate the state of the discharge water leaving the mines, rendering it in various states, such as alkaline, acidic, saline, reducing/oxidising, or uncontaminated mine waters. As mentioned previously, the characteristics of mine water can have impacts on the ability to reutilise the former coal mines for shallow coalmine geothermal, with sulphurous waters leading to increased pyrite and ochre concentrations potentially leading to the clogging up and corrosion of the pipe infrastructure (Steven, 2021, Walls *et al*, 2021). For example, pyrite is one of several sulphide minerals that are vulnerable to being oxidised when exposed to air, and with the coal seams in the

Northumberland coalfield being known to contain sulphide, this can lead to widescale sulphate evolution within reflooded coal mines (eg. Turner and Richardson, 2004).

The mine water that drains out of the Northumberland coalfield has been found to contain increased concentrations of Ca, HCO_3^-, SO_4^{2-}, Fe, and Mn (Turner and Richardson, 2004), which is an indication that there are elevated levels of carbonate dissolution taking place within the former coal mines, mainly as a result of acid production seen in Equation 1. Carbonate minerals within the coal seams, such as calcite, dolomite, siderite and ankerite, can undergo dissolution to give rise to higher base concentrations of cations, potentially adding dissolved iron to the mine water discharge. While this is a process that directly affects the chemistry of the discharged mine water, changes to the pH level of the mine workings can cause calcite precipitation, which can be seen leaving the subsurface directly beneath the coal seams of the Northumberland coalfield, potentially exposing fluid pathways through the strata that were not considered previously. This is seen to occur at Whitley Bay, and shall be discussed later in this chapter.

While this research is focused on characterising the sedimentological and physical properties of the different lithologies, which can have positive implications for improving geothermal energy project models, a study by Bullock *et al* (2018) found that as well as the Northumberland coalfield having variable sulphur content, the coal seams are also significantly enriched in selenium compared to the UK and global coal seam averages. The study found that the selenium enrichment was due to the pyritic nature of the coal seams, meaning that it can be linked to the high sulphur content of the coalfield, especially where epigenetic pyrite has formed as cleat infills. On a wider scope, as the demand for trace metals has increased due to the increased E-tech requirements, this shows that Northumberland also has the potential to be utilised as a potential source of selenium, and possibly other Rare Earth Elements (REE). The research into characterising the strata at Whitley Bay can help REE investigation research, as there will be a better base understanding of the properties of the different lithologies.

2.4. The Carboniferous Stratigraphy of Whitley Bay

Coal mining in the UK was a major industry in the past, but has declined since the 1980s peak, with the last deep coal mine – Kellingley Colliery, North Yorkshire – closing in December 2015. This has been exacerbated by the drive to decarbonise the energy grid and society as a whole, with the aims of all coal-fired power stations to cease by 2025 as part of the transition to net zero by 2050. While NE England was once the powerhouse of UK coal extraction, Shotton Surface Mine – the last open pit in the region – was closed in February 2020, leaving little to no remains of the once extensive industry. However, groundwater rebound, and the subsequent flooding of the former coal mines has provided an opportunity for the heritage to be reutilised for shallow coal mine geothermal projects, and the exposed former room and pillar coal workings at Whitley Bay provide one of the only places in the UK where the inner workings of former coal mine workings can be investigated.

Coastal erosion at Whitley Bay has driven the coastline far enough inland to expose the former room and pillar coal mines that were once operational in the area, exposing the High Main coal seam (see Figure 21). As well as the coal seam being exposed, several metres of the underlying Carboniferous cyclothems have been uncovered, consisting of barren mudstones and mussel bands, siltstones and sandstones, with the bituminous coal above the seatearth that separates the coal from the rest of the lithologies. As well as the natural strata, there are several occurrences of anthropogenic coal deposits (eg. roof collapse, pillars, backfill, roadways) within the former coal mine. The sections at Whitley Bay provide one of the only locations in the UK where one of these cyclothems can be investigated, making it one of the few places where this investigation can be done.

2.5. Methods

2.5.1. Sampling and Stratigraphic Logging

The site at Whitley Bay was visited, and the three sections containing the former coal workings were identified as the **Roadway Section**, the **Roof Collapse Section,** and the **Pillar Section** (see Figure 22).

The sections are within ~107 m stretch (above the high water mark (HWM)) of the beach, with the stratigraphy able to be visually followed along the rock face between the sections. Each section was measured at a 10 cm scale. With the exposures being located at the coast, a rock hammer was used to collect samples from slightly inward of the rock face, in order to try and avoid contamination from groundwater flow and sea spray from the ocean.

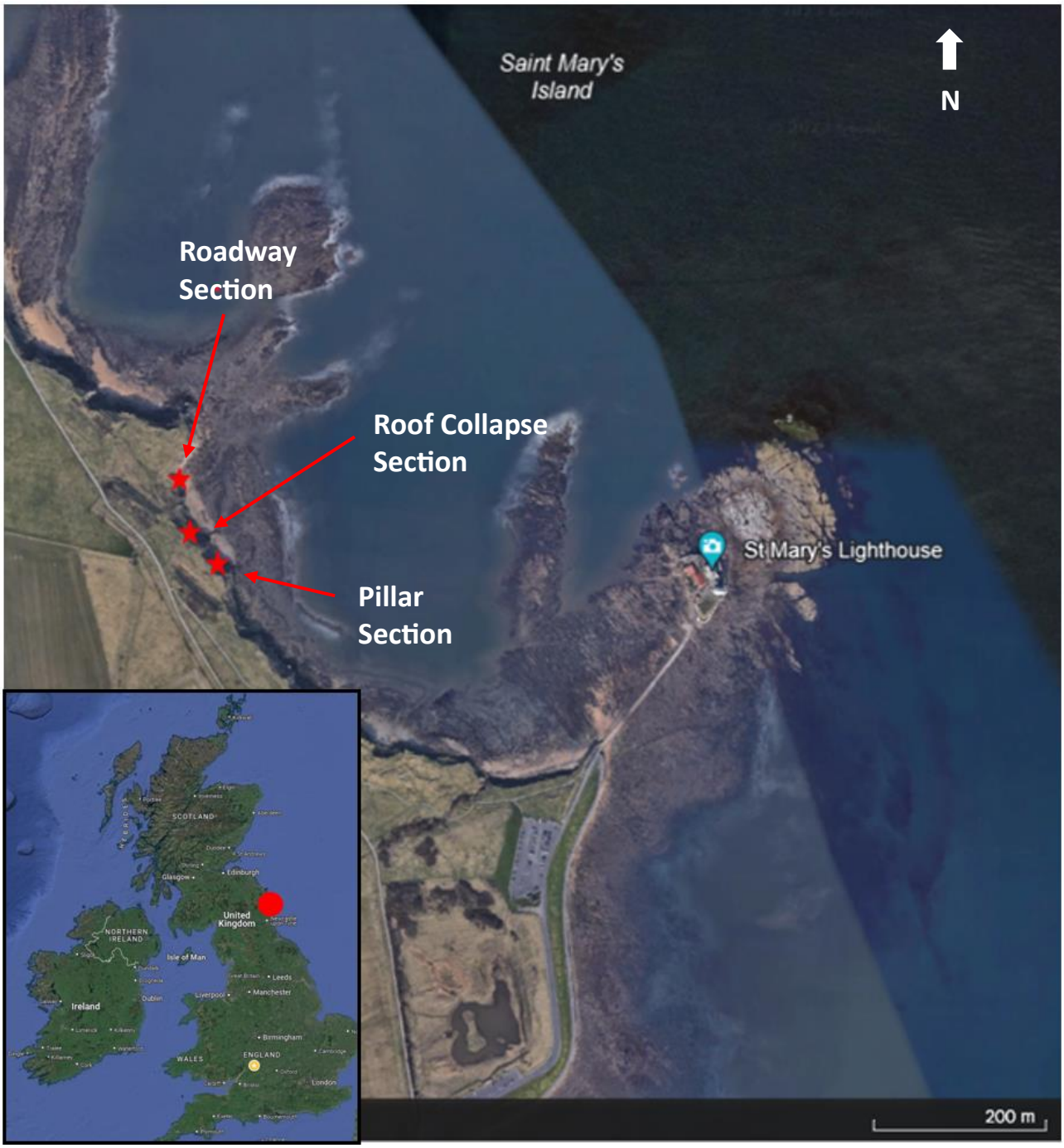

*Figure 22 – Google Earth map to locate the three sections identified for this chapter (red stars). Moving south, the sections are the **Roadway**, the **Roof Collapse**, and the **Pillar** sections (top of map in North). Inset map to show location of site with red circle.*

2.5.1.1. Roadway Section

The Roadway Section is the north-most section at Whitley Bay, and a total of 18 samples were taken through the 6.7 m section. They were taken throughout the section, initially with a sample taken from each different lithology, but repeated samples were taken on subsequent fieldwork days where it was determined that a better-quality sample was desired. The section consists of thick beds of sandstone, moving upwards into a siltstone and then a mudstone layer, overlain by the coal-containing portion of the section. This portion of the section is made up of an anthropogenic deposit, identified as backfill, and the overlying *in-situ* HMS. For this part of the section, more samples were taken with the intention to use them to differentiate the anthropogenic deposits between sections. For the Roadway Section, where the anthropogenic deposit found was backfill, samples were taken from the base/middle/top of the anthropogenic deposit, as there were visual differences, as seen in Figure 23.

Figure 23 - Image of backfill (left, boxed in red) present at Whitley Bay. Visual differences within the backfill can be seen, with the bottom section appearing blacker and becoming more dominated by brown colours as you move up through the red box.

2.5.1.2. Roof Collapse Section

The Roof Collapse Section is the central section of the three, with 12 samples taken from it. The section is 4.8 m in height, consisting of a thick sandstone bed overlain by a thinner siltstone layer, before moving upwards into an *in-situ* coal bed overlain by the anthropogenic deposit that occurs. The anthropogenic deposit, identified as roof collapse, is a layer of coal slumped to the south (see Figure 24), and several samples were taken from this in order to differentiate between the roof collapse and the backfill in the Roadway Section.

2.5.1.3. Pillar Section

The Pillar Section is the southern-most exposure at Whitley Bay and consists of fining-upwards sandstone overlain by siltstone and mudstone before the occurrence of the HMS above this. The section is 7.5 m in height, and seven samples were taken from the Pillar Section, with no need for extra samples in the coal portion due to the coal pillar consisting of natural coal, as seen in Figure 25.

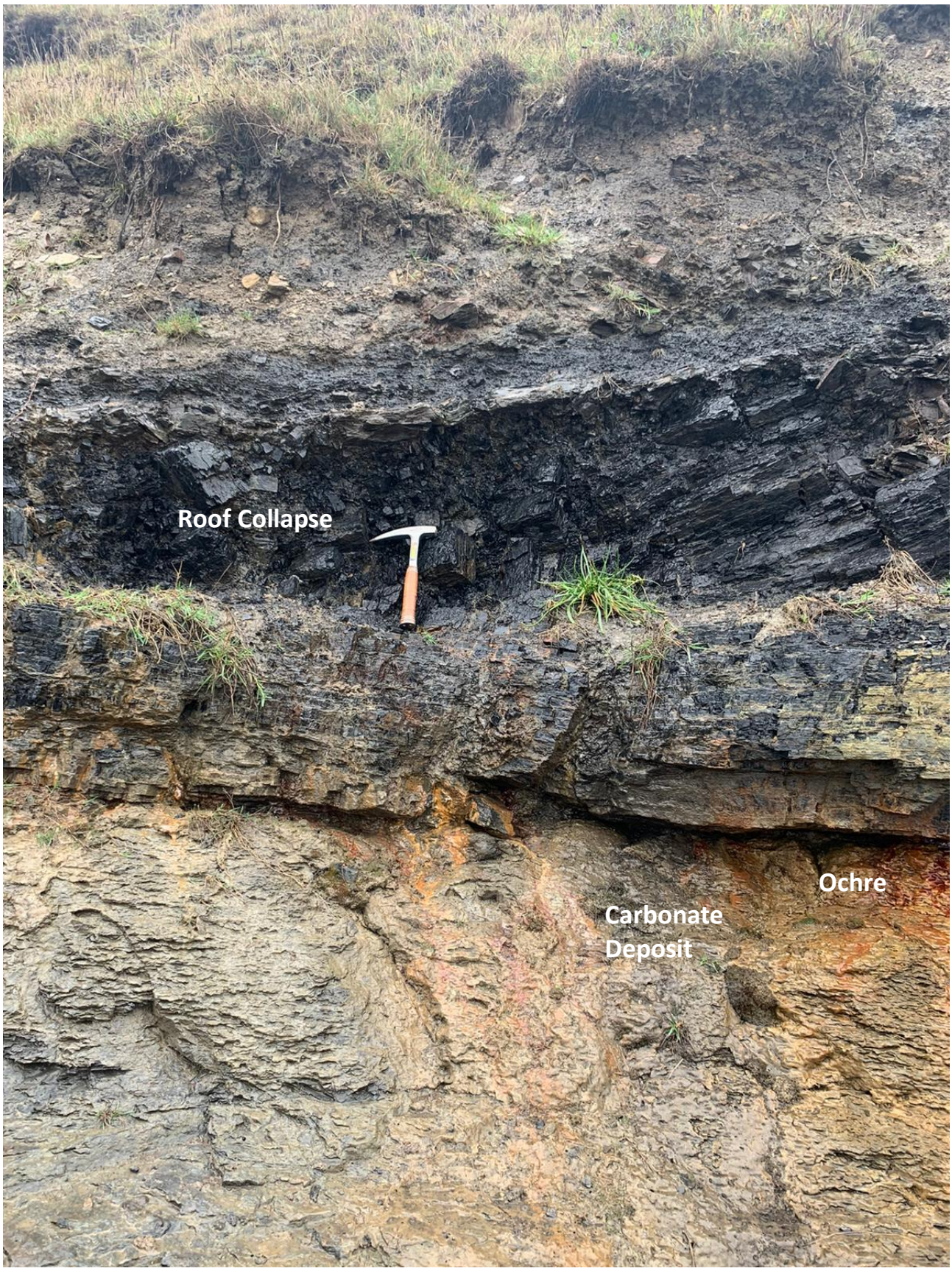

Figure 24 - Image of roof collapse present at Whitley Bay. The roof collapse can be seen to be sloping down to the left (south), atop the in-situ *coal seam. Rock hammer for scale.*

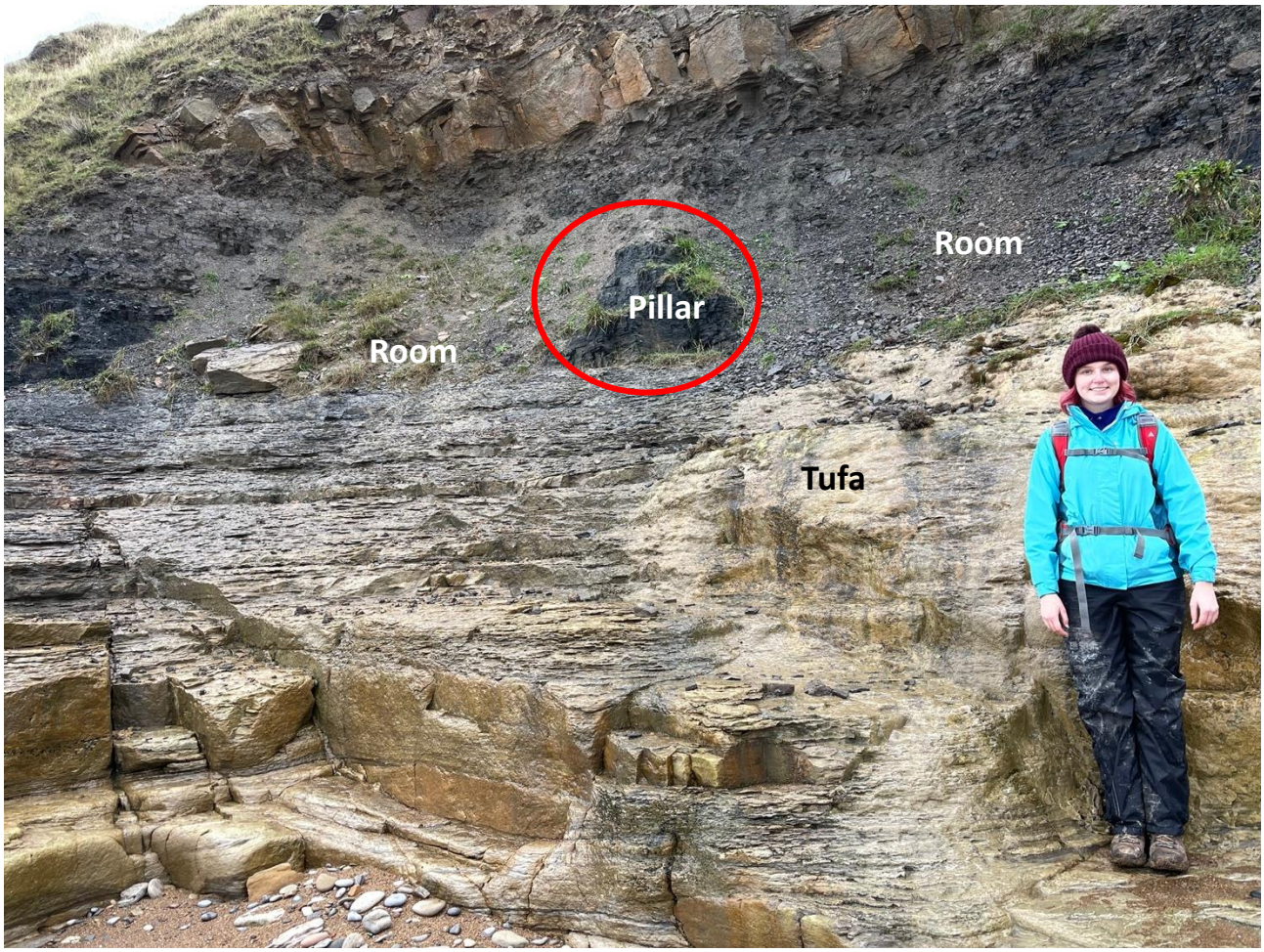

Figure 25 - Image of coal pillar present at Whitley Bay (middle). The pillar can be identified by the lack of coal either side, indicating that coal was extracted from these areas when the coal mine was operational. Part of an additional coal pillar can be seen at the left of the image. Person for scale.

2.5.2. Petrographic Analysis

Several thin sections were cut from the samples collected from the Roadway Section in order to carry out petrographic analysis with a light microscope. All thin sections cut were impregnated with blue dye to highlight porosity. The purpose of this was to estimate porosity and the quantities of each mineral found in the thin sections. The thin sections were viewed under viewed under a Leica DM2500P microscope, using the PETROG software and PETROG stepping stage. Minerals within the thin sections, as well as porosity, were identified with 300 point counts per thin section.

Two other thin sections were made from the same locations as TS1 and TS2 and analysed on a scanning electron microscope (SEM), in order to look at the exact elemental makeup of the thin sections (see Figure 28 for thin section locations on graphic logs). This analysis was carried out to produce detailed elemental analysis of the thin sections, in order to back up any assumptions made from the optical light microscope analysis. Four broken rock surfaces were also examined in an SEM, broken off from samples RS1, RS5, RS6, and RS9 (see Figure 28 for locations on graphic logs). The purpose of analysing the broken rock surfaces was to examine how the pore spaces of the samples were infilled, in order to get a better understanding of the samples.

2.5.3. Field Permeability

To obtain permeability values for the three sections at Whitley Bay, the *TinyPerm II* from New England Research was used. The *TinyPerm II* is a hand-held air permeameter, with a rubber nozzle being pressed against the sample to create a seal before removing air via the syringe. The volume of the syringe and the transient vacuum pulse that is created at the sample surface are both monitored by a microcontroller unit, which in turn returns a response function. By using the theoretical relation between the response function of the *TinyPerm II* and permeability, the matrix permeability of the sample can be determined.

Figure 26 - Image of TinyPerm II handheld air permeameter. From New England Research systems website - accessed 03/08/2023.

For this project, the *TinyPerm II* was taken out into the field at Whitley Bay, and the three sections were tested *in situ* at the outcrop. For the rubber nozzle of the equipment to produce a good enough seal to produce a result, a flat surface was needed, meaning that it was hard to take measurements at consistent intervals. It was also found during measurement collection that the *TinyPerm II* could not take values for the coal or shale strata, only giving permeability measurements for the sandstones below. Measurements were taken three times, and then averaged to give the final permeability value.

The *TinyPerm II* control box records an arbitrary value as the permeability, so the following equation was used to convert these values into permeability in mD, where T is the arbitrary permeability value, and k is the permeability in mD:

$$k = 10^{(T - 12.8738) / -0.8206} \quad \text{Eq. 2}$$

2.5.4. Laboratory Permeability

2.5.4.1. Concept Explanation

As explained above, the *TinyPerm II* cannot be used to obtain a permeability measurement for the coal samples, as the permeability will be too low for the equipment to detect. Due to this, a different method was used to record the measurements for the coal samples – the use of a **tri-axial pressure vessel**. By using Darcy's law of fluid flow through porous media – which relates fluid flow and pressure difference (Escoffier *et al*, 2005) over a defined length of porous medium – the permeability of a porous sample can be determined. Samples had to be cut to cylindrical dimensions of 50x20 mm and were then placed in the pressure vessel. Various methods can be used from this point onwards, but due to the coal samples expected to have low permeability values, the transient **pulse decay method** was used.

First introduced by Brace *et al* (1968), a cylinder of Westerly granite was subjected to confining pressures inside a pressure vessel. Both ends of the sample were capped by pore fluid reservoirs, where the pressures could be varied, making it possible to change the pressure of the pore fluid within the sample. The pressures of both pore fluid reservoirs was initially increased together, allowing the increased pore pressure to settle before any permeability measurements were taken at the new constant confining pore pressure. By introducing a small increase to one of the reservoirs, the pressure difference imposed across the sample initiated an equilibrium process, where the pressures of the reservoirs increased and decreased accordingly until a new common value was achieved. Recording the pressures of the two reservoirs showed that they approached the new common value with an exponential curve, showing exponential decay of pressure with time, which was related to a constant α:

$$\Delta P_t = \Delta P_0[(V_2/V_1) + V_2]e^{-\alpha t}; \quad \text{Eq. 3}$$

where ΔP_0 and ΔP_t are the pressure difference at time 0 and the pressure difference at time t respectively, V_1 and V_2 are the upstream and downstream reservoir volumes of the experimental assembly and t is the time since the application of the initial pressure difference. α is also able to be related to several characteristics from the sample, fluid and assembly:

$$\alpha = (kA/\mu\beta L)(1/V_1 + 1/V_2); \qquad \text{Eq. 4}$$

where k is permeability, A is the cross-sectional area of the sample, L is the length of the sample μ is the dynamic viscosity of the pore fluid and β is the compressibility of the pore fluid. The above two equations show that the volumes of the pore fluid reservoirs is what determines the time required for equilibrium. For the same sized sample and same pore fluid, larger reservoir volumes results in longer times before equilibrium is reached.

2.5.4.2. Procedure

The coal sample was cut to the required size, and the ends smoothed with sandpaper. The sample was then secured in the sample assembly, before being placed into the pressure vessel and connected to the pipes that carry the upstream and downstream pore fluid reservoirs.

The sample was pressurised to a confining pressure of 10MPa, as this was the lowest confining pressure that would give a usable result when the pore pressure of the sample was varied. The sample was left at this level overnight to become fully saturated, at which point there should be a pressure communication between the pore fluids at each end of the sample. This is where an increase in pressure of one of the pore fluid reservoirs should initiate the equilibrium response, and measurements for sample permeability can be started. Measurements were taken by initially closing the pipeline for the downstream pore fluid, causing an increase in pore pressure for both pore fluid reservoirs. The closing of the upstream pipeline followed this, resulting in an increase of the upstream pore pressure. This process created ΔP_0 and isolated the sample from the pore reservoirs, meaning that the changes in pore pressure are a result of the equilibrium process. The exponential

pressure decay was recorded by LabView software, which was then able to be imported into MatLab for data processing.

The code used for the data processing can be found in APPENDIX. The code was designed by Akos Kiss, a PhD student in the Department of Earth Sciences, Durham University, and built for a much more in-depth use of the triaxial pressure rig, but for the purpose of this project the use of the code was purely for the conversion of the LabView data into permeability.

2.5.5. X-Ray Diffraction (XRD)

Eight samples from the Roadway Section were sent to X-Ray Mineral Services for XRD analysis (see results in Appendix 9), in order to determine the crystalline makeup of the samples, as outlined by Chauhan and Chauhan, 2014. By powdering some of a material and passing it through an x-ray, differing atoms will cause x-rays to diffract by different amounts.

The sample is disaggregated by using a pestle and mortar, before splitting 2 g of the sample to be micronized into an x-ray diffraction powder with a mean particle diameter of 5-10 microns. Each sample was analysed between 4.5^{o} and 75^{o} 2 theta, with a step size of 0.013 and nominal time per step of 0.2 s and carried out using the x-ray radiation from a copper anode at 40 kV, 40 mA. The x-ray diffraction patterns of the sample are then compared with the 'International Centre for Diffraction Data PDF-4 Minerals' database, in order to determine which patterns match up with the known intensity for a pure sample of a material. By using 'Rietveld analysis', first published in 1967 (), the phases in the samples tested can be quantified (Post and Bish, 1989).

The XRD analysis also included the analysis of <2 micron clays within the samples, to quantify the proportion of each clay within a sample (i.e. illite+mica, kaolinite, chlorite). The <2 micron fraction of the sample is achieved through the use of ultrasound and centrifugation. By filtering the clay suspension through a Millipore glass microfibre filter and drying on filter paper, the clay XRD mount is obtained. This is then analysed as an untreated clay after overnight saturation with ethylene glycol

vapour and heating at 380 ^{o}C for two hours, followed by further heating to 550 ^{o}C for one hour. The sample is then scanned between 3^{o} and 35^{o} 2 theta at a step size of 0.05^{o} per second, again with x-ray radiation from a copper anode at 40 kV, 40 mA. To define peaks from kaolinite and chlorite, the untreated sample is also analysed between 24-27^{o} 2 theta, with a step size of 0.02^{o} per second. The intensities of different peaks are measured and incorporated to be quantified with respect to the whole rock.

2.5.6. Inductively Coupled Plasma Mass Spectrometry (ICP-MS) and Inductively Coupled Plasma Optical Emission Spectroscopy (ICP-OES)

Like the XRD analysis previously covered, samples collected from the outcrops at Whitley Bay were sent to X-Ray Mineral Services to carry out ICP-MS and ICP-OES, to understand how different elemental components change through each of the sections and could help identify any lithology that could not be visually identified in the field. 20 total samples were analysed, with 10 from the Roadway Section and five from each of the Roof Collapse and Pillar Sections. The methodology followed is outlined by Finlay *et al* (2023) but is given below.

Following the samples being crushed into a fine powder via pestle and mortar, the samples were prepared for ICP analysis using lithium metaborate (alkali) fusion, the method promoted by Jarvis and Jarvis (1992), before being analysed by ICP-MS and ICP-OES equipment. ICP-MS and ICP-OES analysis obtains quantitative data for 48 different elements, split between 10 major elements (Al, SI, Ti, Fe, Mn, Mg, Ca, Na, K, P), 24 trace elements (Ba, Be, Co, Cr, Cs, Cu, Ga, Hf, Mo, Nb, Ni, Pb, Rb, Sc, Sr, Ta, Tl, Th, U, V, W, Y, Zn, Zr), and 14 rare earth elements (REE) (La, Ce, Pr, Nd, Sm, Eu, Gd, Tb, Dy, Ho, Er, Tm, Yb, Lu). Through the use of replicate analyses of multiple preparations of certified rock standard reference materials (SRMs), the accuracy of the ICP data is considered to be within the error range achieved for multi-determinations of the same sample.

For the purpose of this study, several element ratios were chosen to be analysed in detail (K/Ta, Zr/Cr, Sc/Lu, K/Cs, Na (wt %)). As explained by Alex Finlay (*pers comms*), these elemental ratios are likely to demonstrate changes found in the mineralogy of the rock. Clays and feldspar-containing sandstones can be associated with showing trends in K, Ta, Cs and Na. Zr and Cr are likely to show variations of heavy minerals in the detrital fractions of samples, therefore showing changes in sediment origin (provenance). From Finlay *et al*, 2022, K commonly has a mineralogical control for clay minerals, interpreted as detrital input and depositional energy, while Zr is a control for heavy minerals interpreted as depositional energy and grain size, and Na controls Halite, being a designator for the salinity of the sample. The purpose of plotting the elemental ratios is to compare the data across the Whitley Bay site, as this will allow for comparisons in geochemical trends – similarities in the trends can be an indication of correlatable horizons.

2.5.7. Grain Size Determination

2.5.7.1. Field Measurements

As outlined above, extra samples were taken from the **Roadway** and **Roof Collapse** sections, in order to determine the grain sizes of the anthropogenic coal deposits found in those sections. Due to the **Pillar** section not having an anthropogenic deposit, only an *in-situ* coal pillar, this was not included in the grain size determination. For the anthropogenic coal deposit found in the **Roadway Section**, three samples were taken at different heights through the deposit, as there was a visible difference within this part of the section (see Figure 23). The process was different for the **Roof Collapse** section, with the size of the grains within the anthropogenic deposit visually much larger than found at the **Roadway** section. Because of this, a 1 m x 1 m quadrat was used to measure the longest axis of the larger grains before samples were collected, as seen in Figure 27 below. 2 quadrat counts were taken, from the left and right sections of the anthropogenic coal deposit.

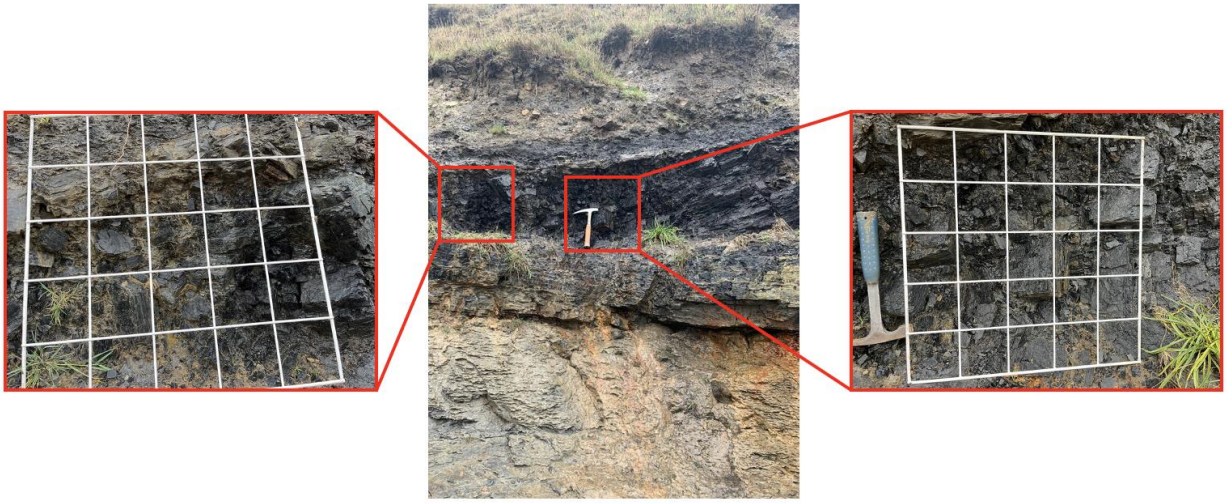

Figure 27 - Locations of quadrat counts in the Roof Collapse section. Quadrats are 1m x 1m.

Once the samples from both sections were collected, they were put through two methods of grain size determination to attempt to quantify the distribution of grain sizes – dry sieving and laser diffraction.

2.5.7.2. Dry Sieving

The samples were dry sieved using metal sieves and a shaker plate for 10 minutes per. sample, resulting in 9 different size fractions as follows - >16 mm, >8 mm, >4 mm, >2 mm, >1 mm, >0.5 mm, >0.25 mm, >0.125 mm, <0.125 mm. Sieving the samples down to the scale of microns is hazardous, with the health implications associated with inhaling coal dust being well documented (eg. Liu and Liu, 2020, Ishtiaq *et al*, 2018, Zhang *et al*, 2021). To avoid inhalation of the smaller coal dust particles, the sieving of the samples was carried out under a Local Exhaust Ventilation (LEV) hood. Because of the minimum exhaust speeds required, a small amount of the smaller fractions was lost, but this was below 5% for all samples. The fractions in each of the sieves were then weighed with a mass balance, before the size fractions smaller than 2 mm in size were recombined to be analysed using a Beckman Coulter LS 13 320 Laser Diffraction Particle Size Analyser.

2.5.7.3. Laser Diffraction

The size fraction <2 mm was then analysed using a Beckman Coulter LS 13 320 Laser Diffraction Particle Size Analyser, which allowed for finer size fractions below 2 mm to be represented, by putting ~2 g of sample into the machine. By using a combination of light scattering and Polarisation Intensity Differential Scattering (PIDS), the range and proportion of particle sizes within the ~2g sample can be represented from 2000 microns (2 mm) to 0.017 microns. This allows for the smaller grain size fractions of the anthropogenic deposits found in the **Roadway** and **Roof Collapse** sections to be included.

2.6. Results

2.6.1. Stratigraphic Correlation

Graphic logs were measured at three separate locations on the beach at Whitley Bay (see Figure 22 for locations, and Figure 28 for the logs side by side). All three sections record the classic cyclothem stratigraphy with sandstones, siltstones, mudstones and coals. All sections record part of the High Main Coal Seam. Seven different lithologies were identified, with four of these containing coal, either *in situ* or as an anthropogenic deposit (Table 2).

The High Main Coal Seam was present in all of the sections, and the thickness was consistent between them at 1-1.5 m. However, the coal appeared in different forms and structures in each section. The **Pillar** section contained an *in situ* coal pillar, a remnant of the former room and pillar coal workings, where the cleats of the coal seam could be seen to be more open than would be expected of *in situ* coal – possibly from interactions with a larger overburden as the supporting coal around the pillar was extracted. The **Roof Collapse** section contained a portion of *in situ* coal, with a ~1 m thick anthropogenic deposit of roof collapse, containing large, unsorted clasts of coal with varying orientation. The **Roadway** section also contained *in situ* coal, but also recorded ~50 cm of

anthropogenic coal in the form of backfill, where very small coal fragments and dust were mixed with mud and clay to help support the overburden and/or seal the workings.

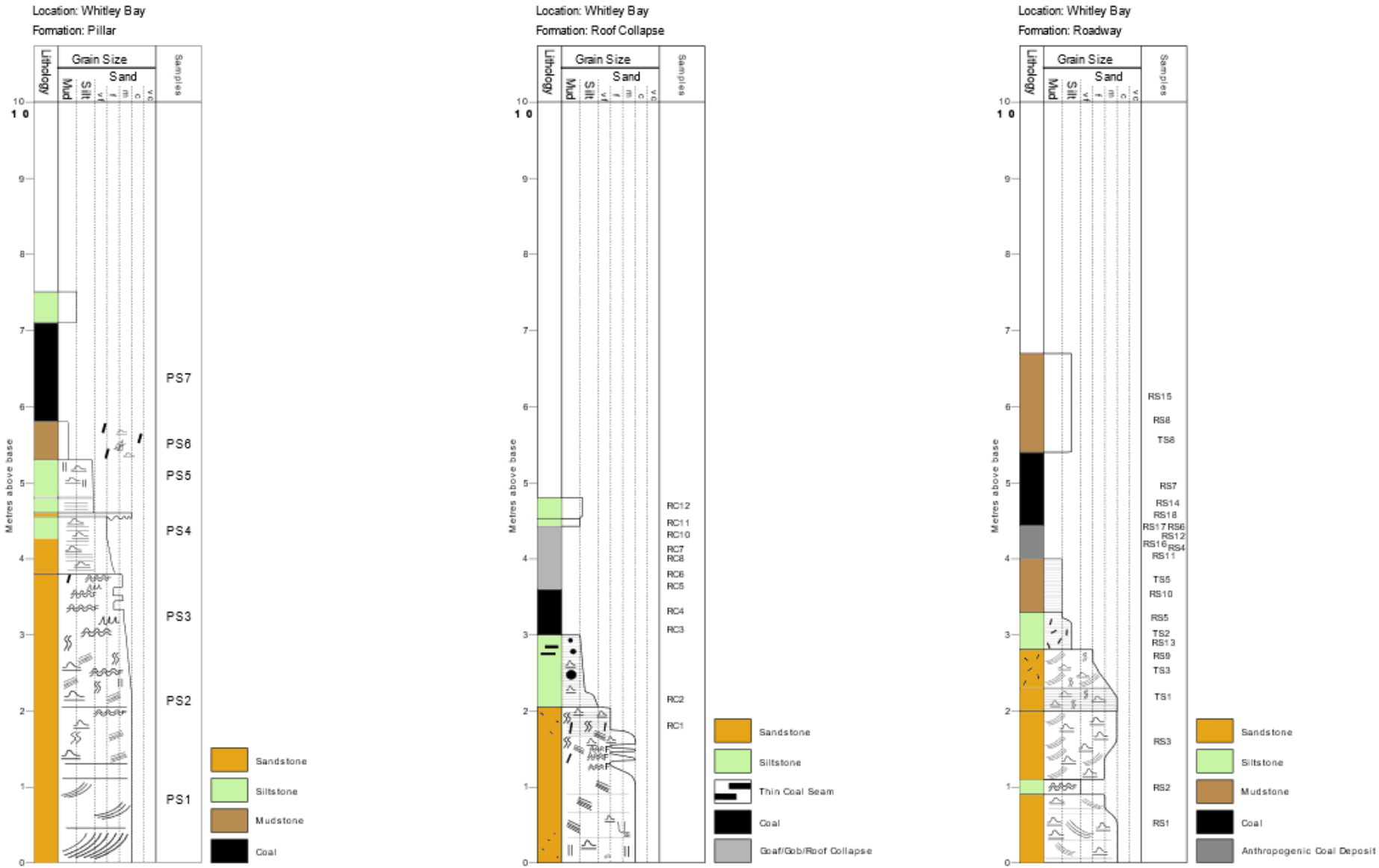

Figure 28 – Detailed stratigraphic logs of the three identified sections at Whitley Bay. See locations of samples on each log.

Table 2 – Facies descriptions of lithologies found at Whitley Bay.

Facies	Description
Sandstone Thickness 0.8-3.8 m	Medium grained, upwards-fining sandstone that is laterally extensive across all sections. Evidence of fluvial structures, such as ripple marks, low/medium angle crossbedding and flaser bedding. Fossiliferous material is also present, such as woody fragments, *Palaeophycus* and *Skolithos*.
Siltstone Thickness 0.2-1 m	Extremely laminated, fine grained siltstone, with evidence of woody material and ripple markings. One section had a thin, laterally extensive clay laminate, while another had thin coal lenses and coal modules.
Mudstone Thickness 0.4-1 m	The vegetation-dominated mudstone is found directly above and below the High Main Coal Seam, but not in all sections. Where found, it is extremely laminated, and contains evidence of woody fragments and other plant material.
In situ High Main Coal Seam Thickness 0.5-1 m	The High Main Coal Seam in found *in situ* in two of the sections. Andrews et al (2020) identified 16 separate coal beds within the 1 m of High Main Seam at Whitley Bay.
Coal Pillar Thickness 1.3 m	Anthropogenic remnant of the former room and pillar coal workings, found with evidence of extracted coal either side of the pillar. Cleats are more visible than found *in situ*, with the sides of the pillar appearing to slump slightly.
Coal Roof Collapse Thickness 1 m	Anthropogenic coal deposit, consisting of large (up to 200 mm in diameter) coal clasts and a clay matrix. Little to no orientation of clasts, with no sorting.

Coal Backfill Thickness 0.4 m	Anthropogenic coal deposit, with small, regularly sized clasts (<16 mm in diameter) supported by a clay matrix. Slight variations in colour, from black to grey and brown.
Roadway	Area of voidspace, left over from where *in situ* coal was excavated during mine operation.

2.6.2. Grain Size Determination of Anthropogenic Coal Deposits

2.6.2.1. Roof Collapse Deposit

As mentioned in the Methodology, extra samples were taken from the anthropogenic coal deposit found in the **Roof Collapse** section, with two quadrat counts also taken from the deposit (see Figure 24 for an image of the anthropogenic coal deposit, and Figure 27 for the quadrat locations). A total of 49 and 44 clasts were identified for the left and right quadrats respectively, and the size distributions are shown in Figure 29 below.

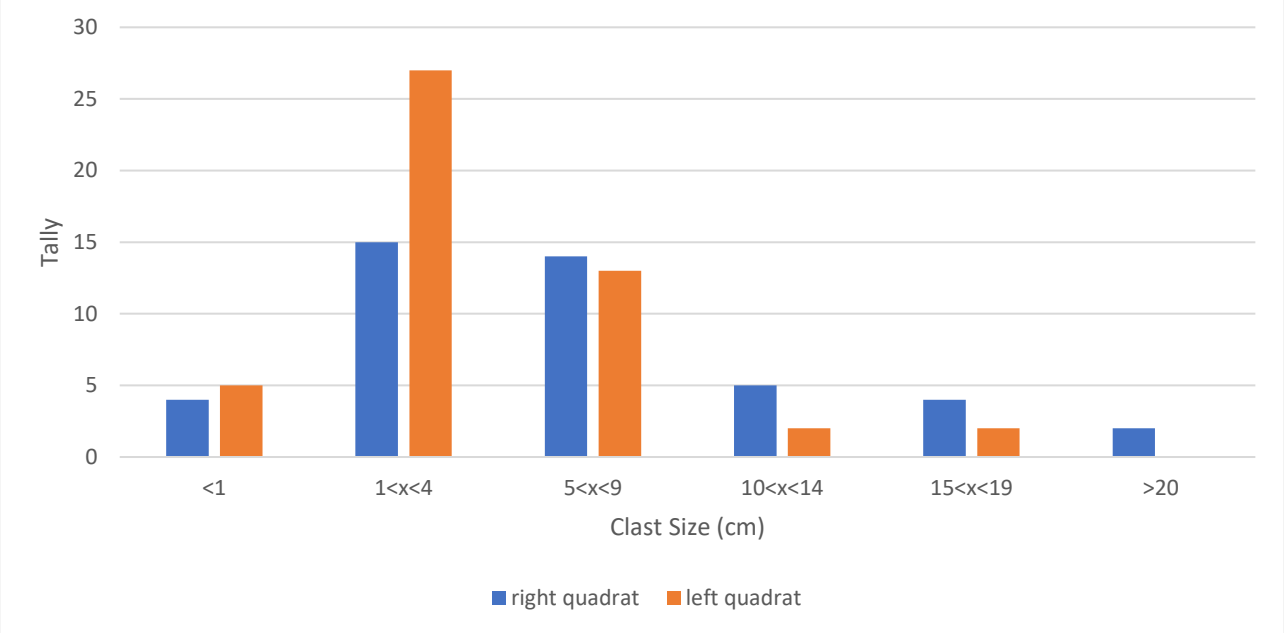

*Figure 29 – Bar chart showing the quadrat counts for the left and right sides of the anthropogenic coal deposit in the **Roof Collapse** section. 'Clast Size' is the length of the longest axis of the selected clast.*

Both counts have a positively skewed size distribution, with a higher count for clasts 1-4 cm. As well as this trend being shown in both sides of the anthropogenic coal deposit, they both show a drop off in occurrence of the larger clast sizes, with the left quadrat having no clasts larger than 20 cm along the largest axis.

The combined results of the dry sieving and the laser granulometry for the sides of the anthropogenic coal deposit can be seen in Figure 30, Figure 31 and Figure 32, and it is important to note the change in scale due to the differences in methodology. Each of the samples were dry sieved, hence the values being provided as a percentage of the total sample weight, whereas the laser granulometry was done to a ~1 g sample that was representative of the sample fraction <2000 microns. For the dry sieved fraction of the samples, it is fairly similar between the sides, with the weight % of both decreasing from 8000 µm to 4000 µm and then to 2000 µm. The major difference between them is the 16000 µm fraction, which comprised >30% of the right quadrat and only ~15% of the left quadrat. The laser granulometry is also similar between the two samples, both skewed towards the larger end of the spectrum, with the left side being a much smoother curve towards the finer fractions compared to the right. The variation becomes much smoother when the data for the left and right samples are combined for a total roof collapse grain size distribution, as seen in Figure 32.

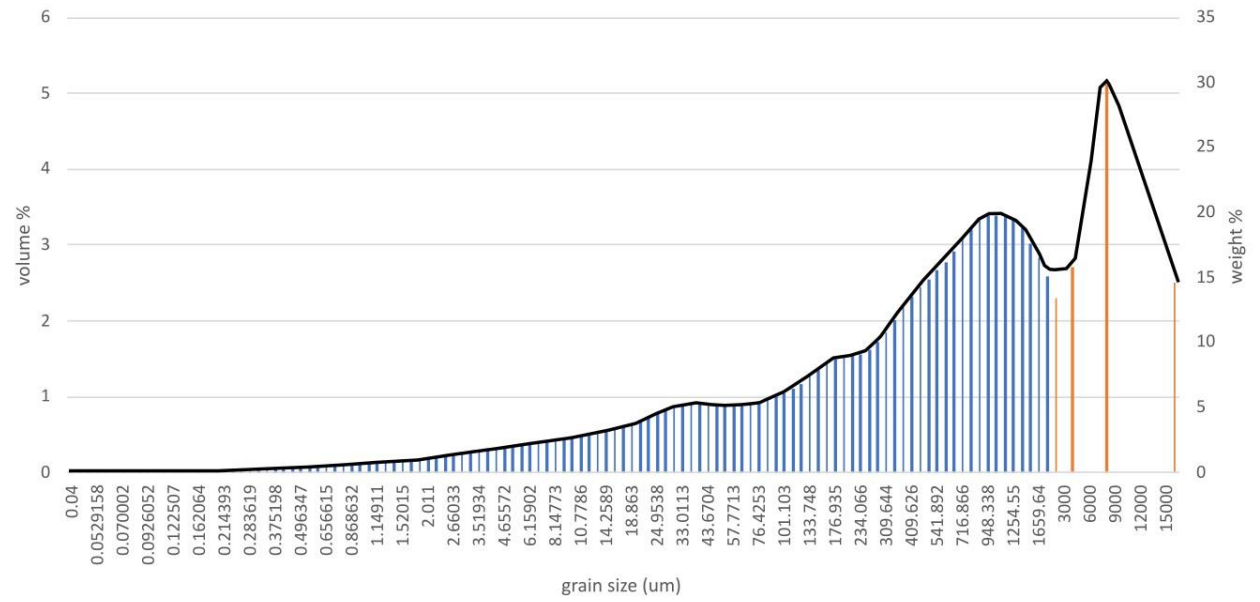

*Figure 30 – Grain size distribution of the sample taken from the left side of the anthropogenic coal deposit found in the **Roof Collapse** section. The blue indicates laser granulometry and the orange indicates dry sieving – note the change in scale for each.*

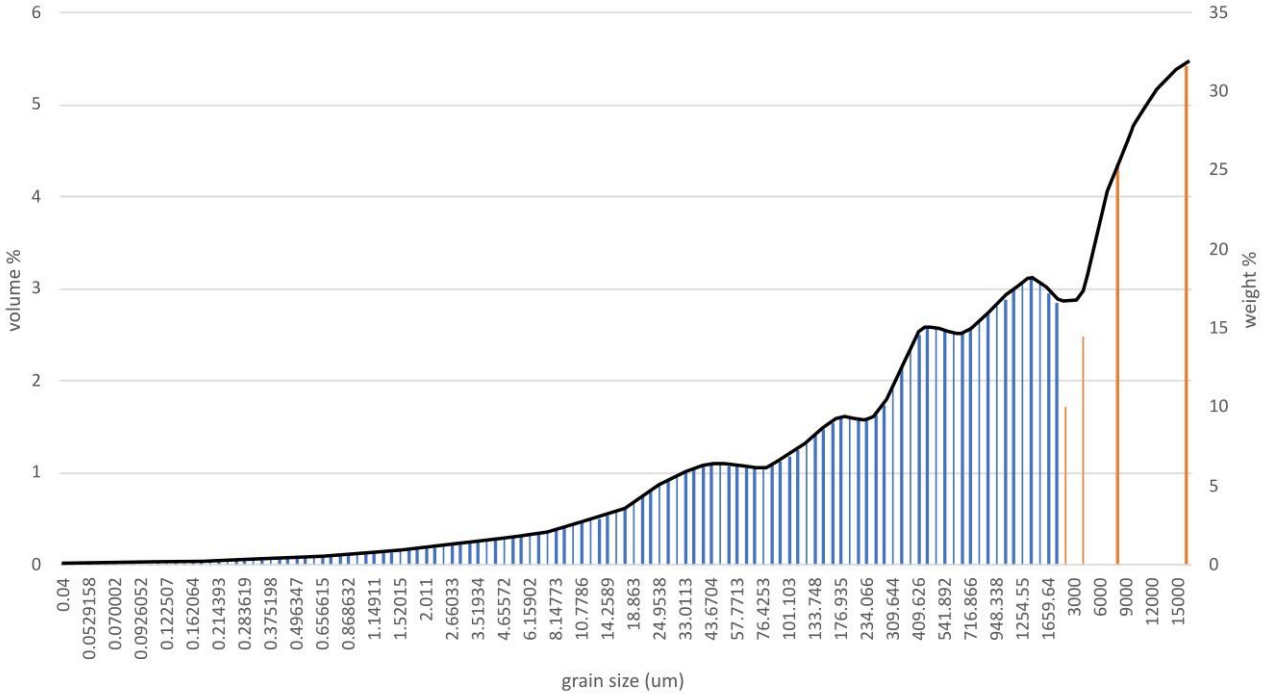

*Figure 31 - Grain size distribution of the sample taken from the right side of the anthropogenic coal deposit found in the **Roof Collapse** section. The blue indicates laser granulometry and the orange indicates dry sieving – note the change in scale for each.*

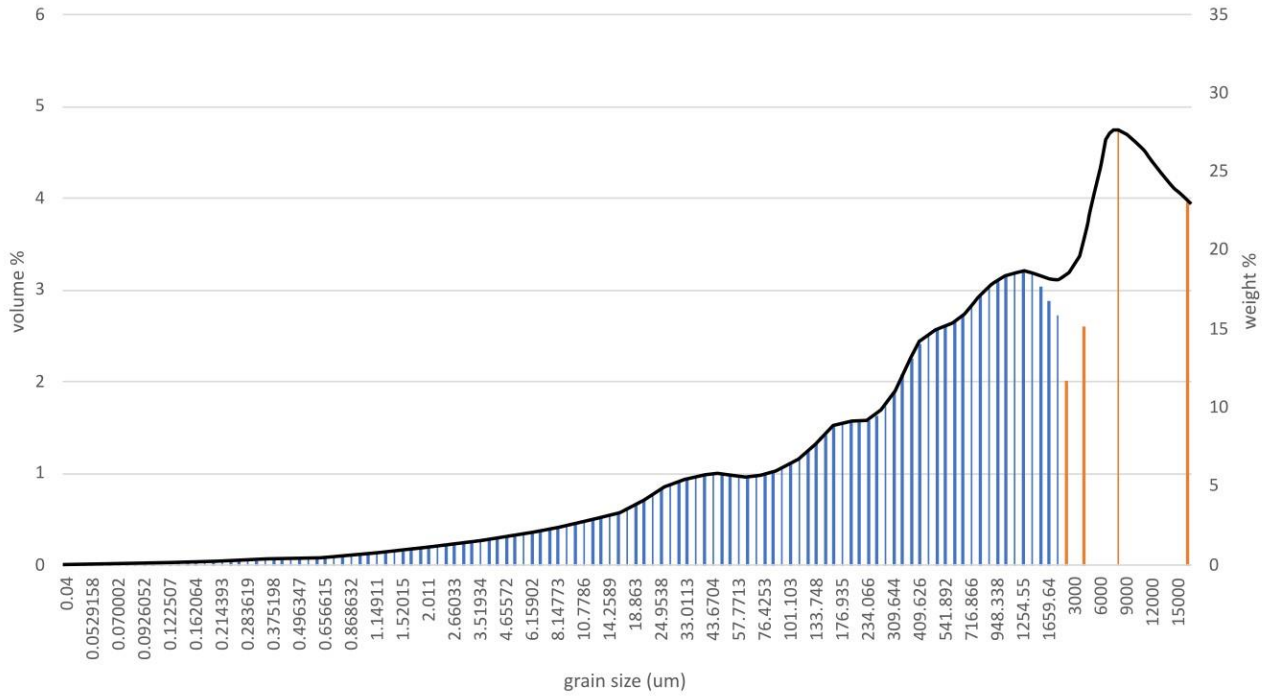

*Figure 32 – Averaged grain size distribution for the anthropogenic coal deposit in the **Roof Collapse** section. The blue indicates laser granulometry and the orange indicates dry sieving – note the change in scale for each.*

2.6.2.2. Backfill Deposit

The anthropogenic coal deposit form the **Backfill** section is easier to look at in terms of scale changes, as the clasts were too small to differentiate using the quadrat, so are only differentiated between via dry sieving and laser granulometry. As mentioned previously, there were visual changes as you move vertically through the anthropogenic coal deposit, with the colour becoming more brown/muddy towards the top and more black towards the bottom (see Figure 23). Due to this, three samples were taken – one from the bottom, one from the middle and one from the top of the backfill. Compared to the roof collapse in the previous section, the sample fractions from the dry sieving are generally more varied between the top/middle/bottom of the backfill (see Figure 33, Figure 34, and Figure 35). Within the middle sample, the dry sieve fractions are more equal than the others, with the smaller three fractions being between 15-20 weight %, while the 16000 µm fraction is larger at ~25 weight %. This is in contrast to the bottom and top samples, where the 16000 µm fraction is the smallest of the dry sieving, at 12 and 3 weight % respectively. The bottom sample is

majority 8000 µm at ~34 weight % and the smaller two fractions at <25 weight %. This is slightly different to the top sample, where the 4000 µm size fraction makes up the largest proportion of the sample at ~31 weight %, and then the remaining 2000 µm and 8000 µm size fractions are both ~21 weight %.

The laser granulometry data for all three sections of the anthropogenic coal deposit shows some similarities, while also showing that each sample is clearly distinct from the others. They all show a negative skew towards the coarser size fractions and extended 'tails' to the finer fractions, with over 50% of the laser granulometry size fractions recorded at <1 volume %. They all show an increase in the volume % for the coarser size fractions, and this is most pronounced in the middle sample, with the largest size fraction (1821 µm) recorded at >5 volume % of the representative sample. While the bottom and top samples display smaller increases at the coarser end of the laser granulometry, they also both show a decrease at the very top end while the middle sample does not, showing that the grain size for these samples is slightly bimodal between the laser granulometry and the dry sieving size fractions.

To get a full view of the grain size distribution for the anthropogenic coal deposit in the **Backfill** section, the three samples were averaged (see Figure 36). This total overview shows that the grain size is skewed towards the larger size fractions, also showing that it is centred around ~3000 µm.

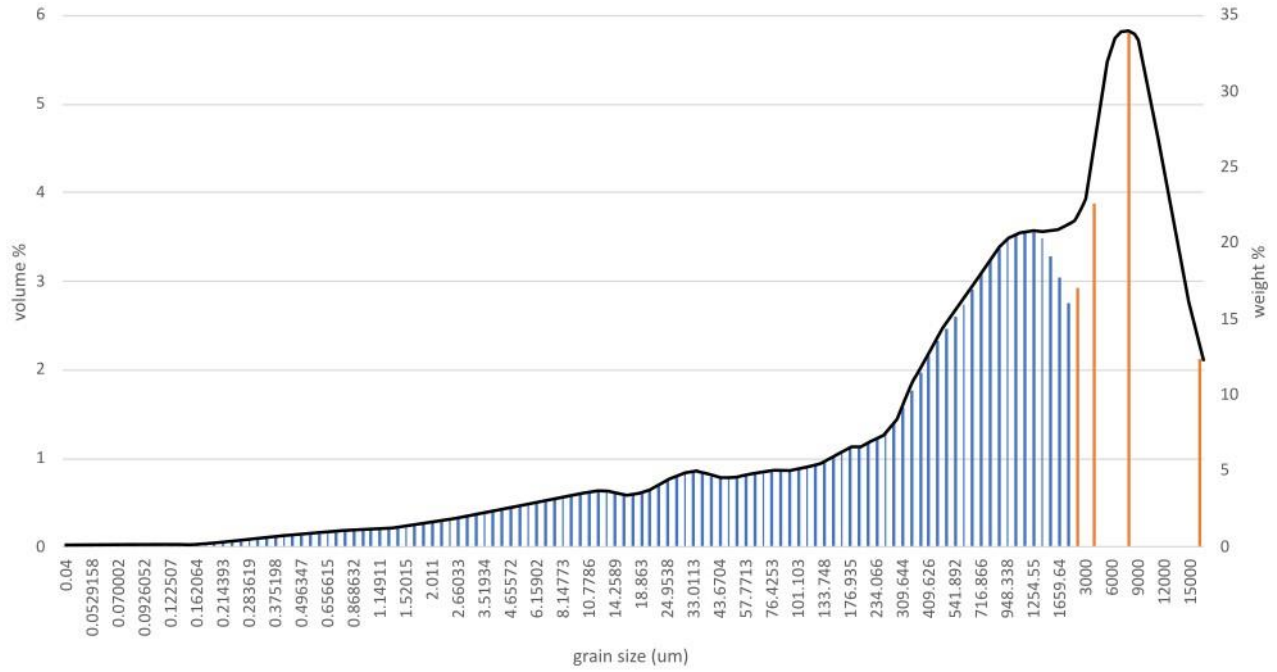

*Figure 33 – Grain size distribution for the lower portion of the **Backfill** section. The blue indicates laser granulometry and the orange indicates dry sieving – note the change in scale for each.*

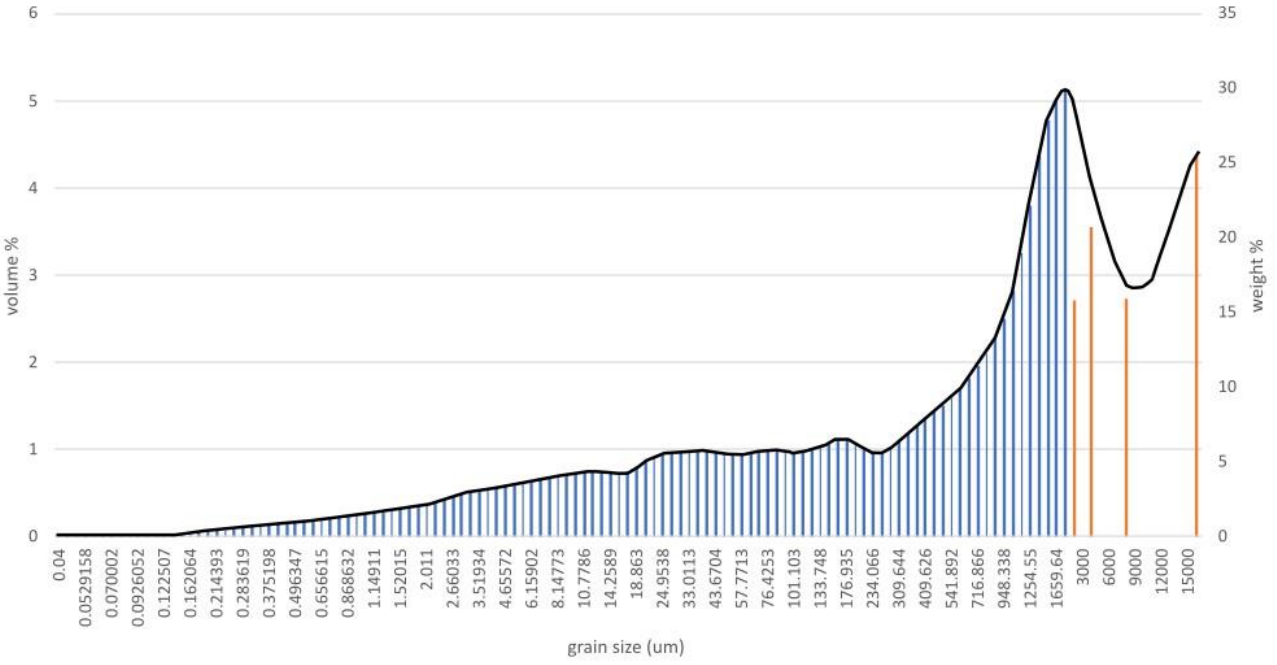

*Figure 34 - Grain size distribution for the middle portion of the **Backfill** section. The blue indicates laser granulometry and the orange indicates dry sieving – note the change in scale for each.*

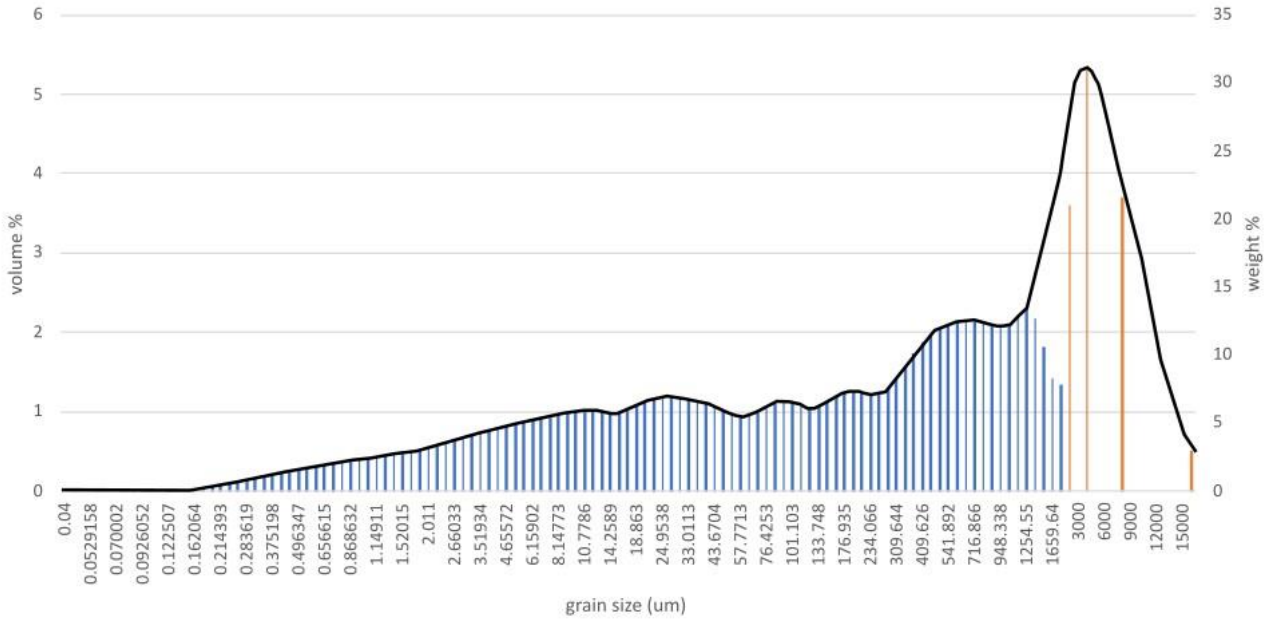

*Figure 35 - Grain size distribution for the upper portion of the **Backfill** section. The blue indicates laser granulometry and the orange indicates dry sieving – note the change in scale for each.*

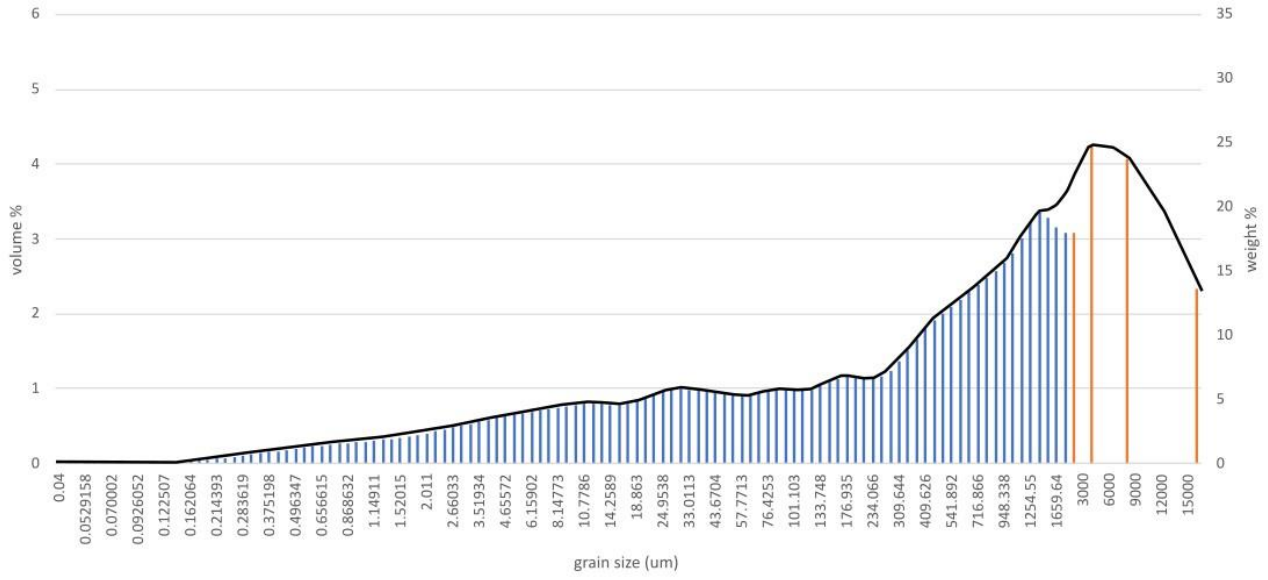

*Figure 36 – Average grain size distribution for the **Backfill** section. The blue indicates laser granulometry and the orange indicates dry sieving – note the change in scale for each.*

2.6.3. Petrography and Porosity

2.6.3.1. Thin Section Micrographs

Thin sections were made from several of the samples in the **Roadway** section, and Figure 37 shows a selection of micrographs from the sandstone package at ~2.5 m. The images are mostly comprised

of detrital medium-fine quartz grains, with smaller proportions of other minerals such as feldspars and micas. The light blue colouring indicates pore space in the PPL images, which is very low at 2% and 2.7% in TS1 and TS3 respectively (see Table 3). The low levels of porosity may be explained by the high proportions of kaolinite in the samples, at 19% and 13% in TS1 and TS3 respectively. Kaolinite is an authigenic, pore-filling clay, so may be contributing to low porosity. Figure 37 highlights the presence of feldspars in the samples, which can undergo dissolution to form the pore-filling kaolinite also present in the samples. While the kaolinite content was picked up by point counting, the feldspar content in the samples was not (see Table 3), hence highlighting the occurrence of them in the micrographs. The limited feldspar content of the sandstones shown in Table 3 means that they plot on Figure 38 as 'litharenite' and 'sublitharenite' sandstones, which is a stark contrast to where they would be expected to plot.

Table 3 also shows the point counting data for TS2 and TS8, which are the underlying siltstone and overlying mudstone (to the coal seam) respectively. TS2 has a much lower porosity than the sandstones, which would be expected, as well as slightly higher kaolinite content and incorporates more mica. The same can be said for TS8, with roughly three times as much mica than TS2, but this is the only similarity. TS8 has a very small proportion of quartz grains compared to the other lithologies, and nearly wholly comprised of mud and mica (55% and 30% respectively). Table 3 shows TS8 having 3.7% porosity, making it the most porous of the samples, but this was due to a fracture appearing during sample preparation as opposed to true porosity.

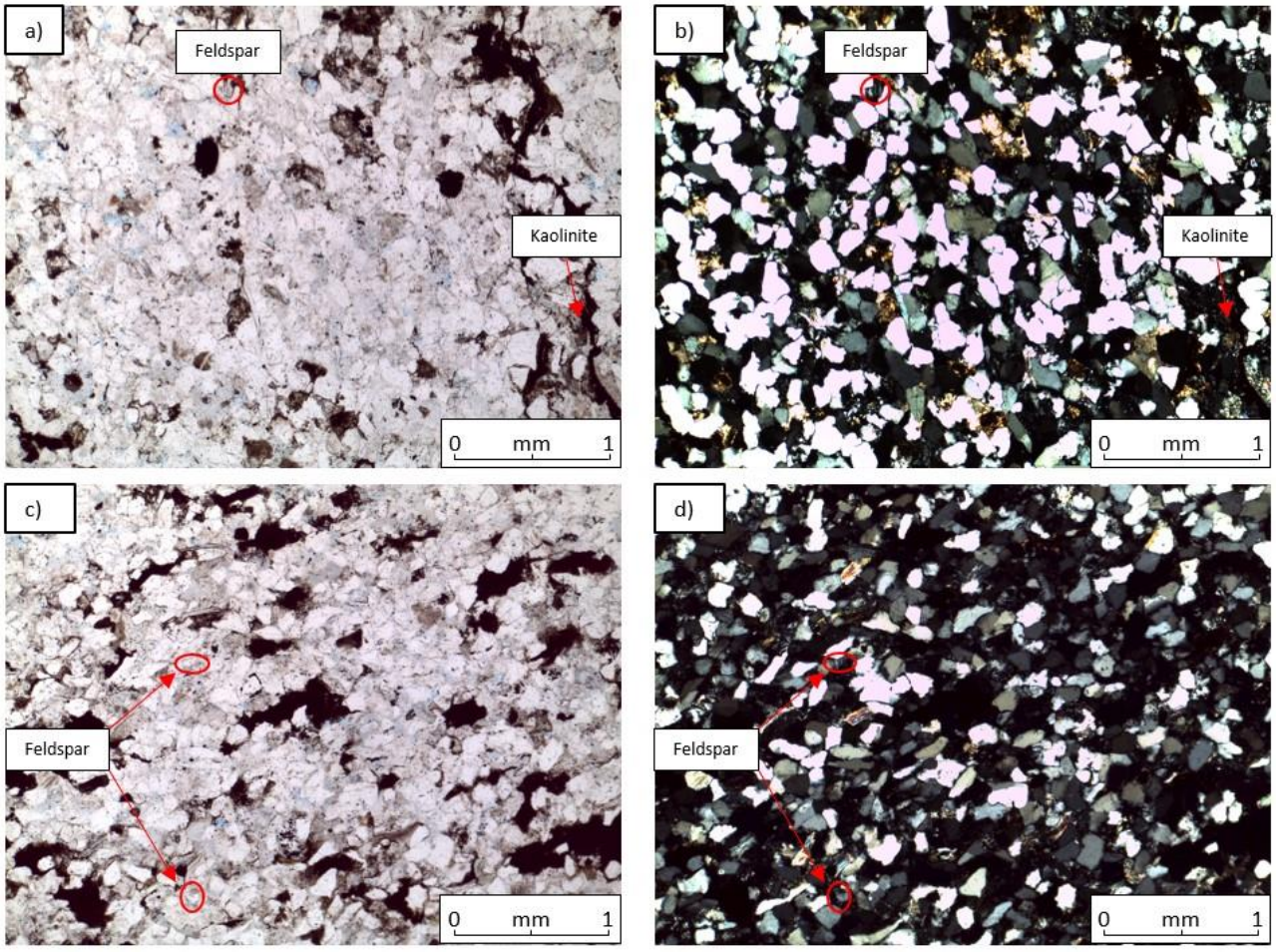

*Figure 37 – Thin section micrographs from the TS1 and TS3 samples in the **Roadway** section (see Figure 27 for locations within section). (a) and (b) are from TS1, while (c) and (d) are from TS3, with (b) and (d) being the corresponding XPL images to (a) and (c). The presence of lamellae-twinning feldspar in both samples has been highlighted, as this is a contributing factor to the occurrence of authigenic, pore-filling kaolinite in the samples, as well as it being present in the images but not highlighted in the point counting data in Table 3. Light blue colouring in PPL indicates porosity.*

Sample Name	Detrital Mineralogy					Authigenic Clay		Mud	Porosity
	Monocrystalline Quartz	Polycrystalline Quartz	Plagioclase	Total Mica	Garnet	Kaolinite	Illite		
TS1	65.0	1.0	0.0	3.3	2.0	19.0	0.0	7.7	2.0
TS2	41.7	11.3	0.0	10.6	0.3	19.7	0.0	16.0	0.3
TS3	31.0	29.7	0.0	9.0	0.3	13.0	0.0	14.3	2.7
TS8	5.0	0.0	0.0	30.0	0.0	6.3	0.0	55.0	3.7

*Table 3 – Petrographic point counting of thin sections made from samples within the **Roadway** section at Whitley Bay (in percent). 'Total Mica' is > 95% muscovite with trace biotite.*

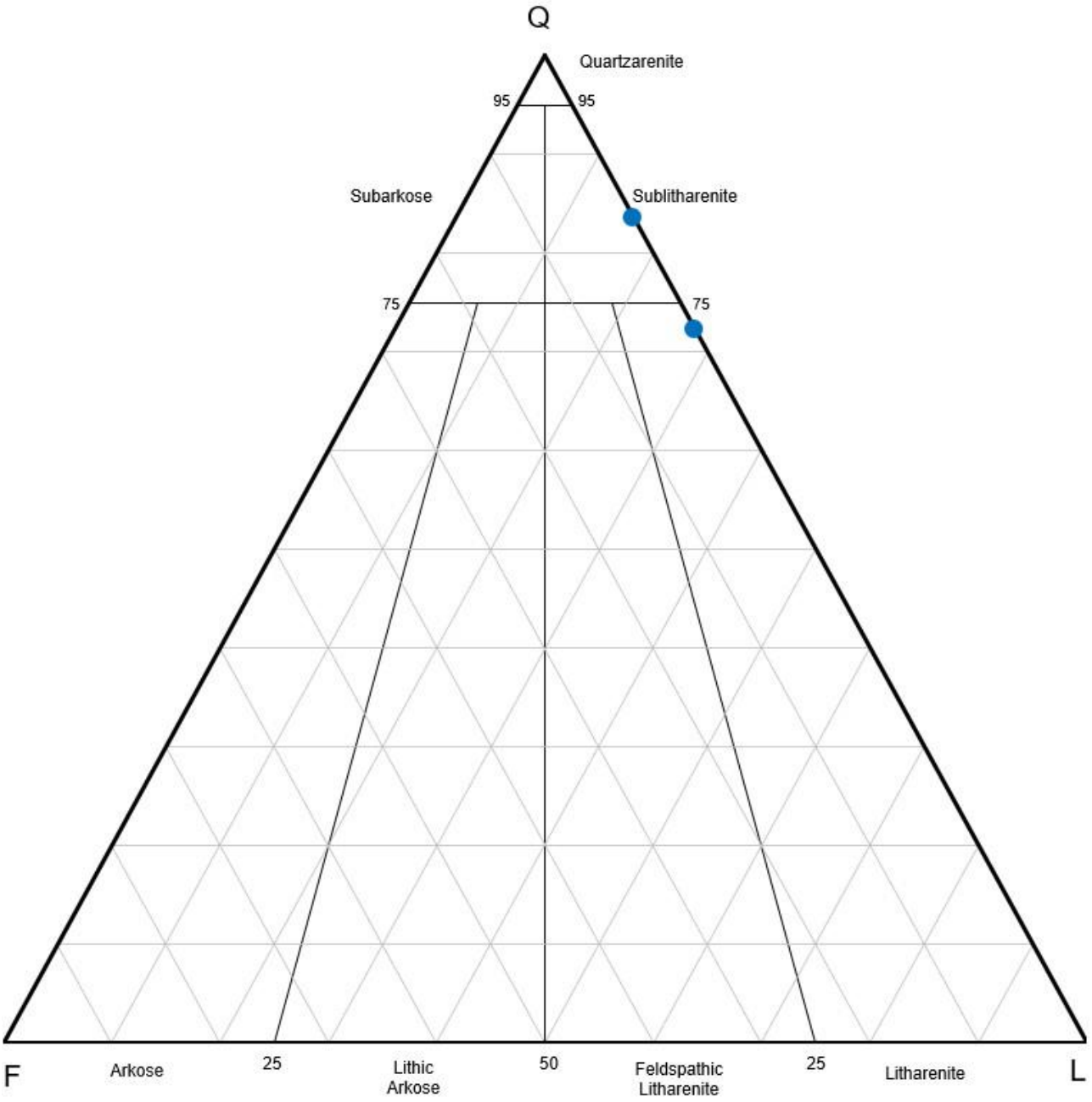

Figure 38 – Folk's (1974) Classification QFL plot with the TS1 and TS3 sandstone samples plotted on the diagram.

2.6.3.2. SEM and SEM EDX Analyses

The SEM and SEM EDX analyses focused on the sandstone and siltstone lithologies, to reveal the main mineral components of the samples, and to aid characterisation of the strata, with the characterisation of the sandstones and High Main Coal Seam supplemented by coal chip analysis.

2.6.3.3. Sandstones

Figure 39 shows that, as expected of a sandstone, it is predominantly detrital quartz grains, with a host of other minerals that comprise the remainder of the rock, such as K-feldspar and plagioclase. Figure 39 shows how some of the pore spaces between the quartz grains are quite large, and this could possibly be due to dissolution of the quartz during rock formation. These large pore spaces were then filled in by authigenic minerals and clays, and Figure 39 shows how it was found that these infilling minerals were mainly K-rich. The green colouring indicates the appearance of smectite-chlorite, derived from the mineral breakdown of detrital mica and other silicates within the sandstones. As shown in Figure 40, these minerals mainly consist of K-rich feldspars and plagioclase, and a large amount of pore-filling kaolinite (also indicated in Figure 39 by the light blue colouring).

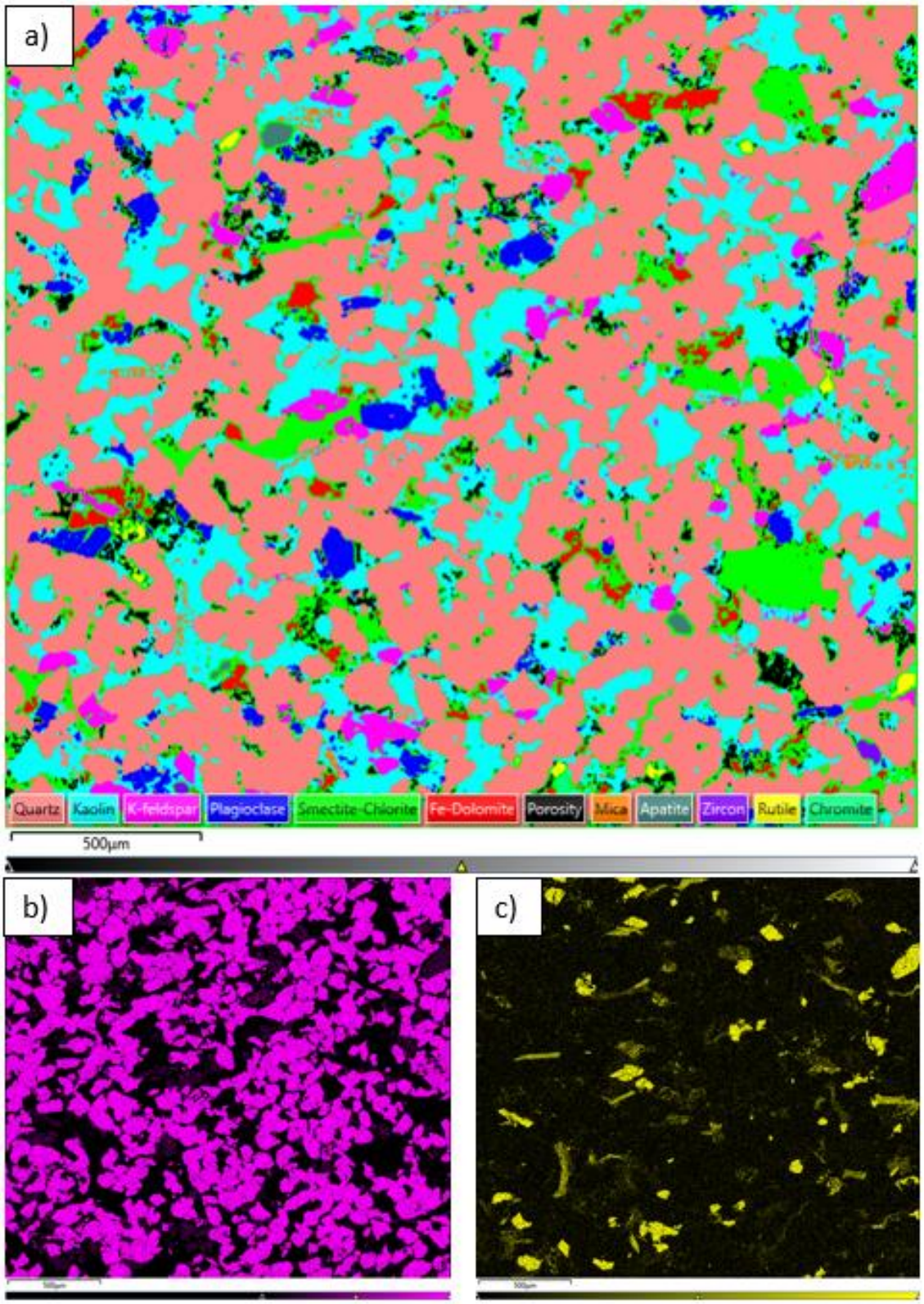

Figure 39 – a) SEM-EDS image of the Carboniferous sandstone beneath the High Main coal seam at Whitley Bay. The light blue colouring indicates the presence of pore-filling kaolinite clays, precursor plagioclase and K-rich feldspars. There is also some occurrence of pore-filling smectite-chlorite, indicated by the green colouring. b) and c) are the individual element mappings of Si and K respectively. They show how there are large pore spaces between the quartz grains of the sandstone, and how they have been infilled by pore-filling authigenic kaolinite, possibly from the dissolution of K-rich feldspars.

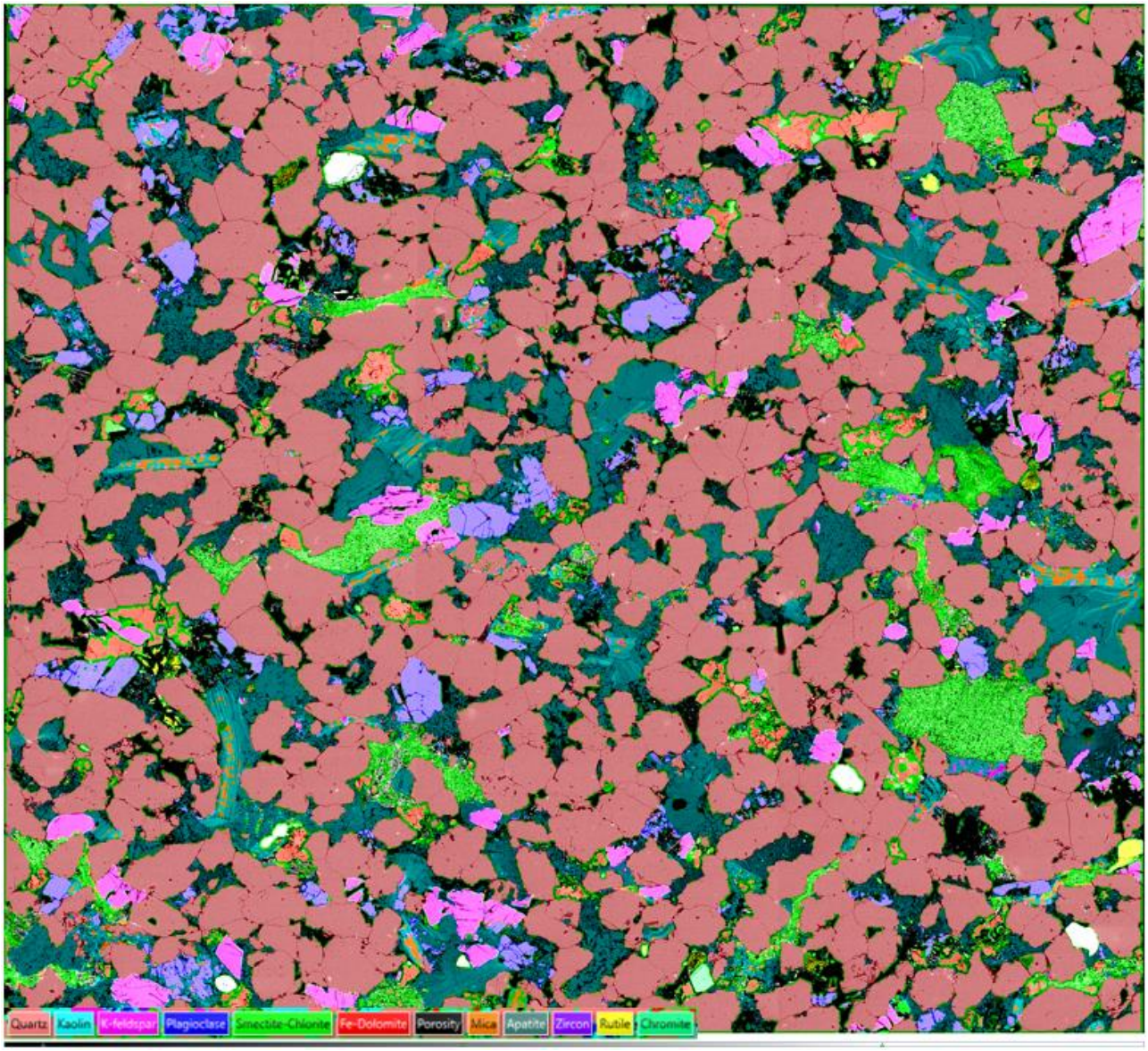

Figure 40 – High resolution SEM-EDS image of the Carboniferous sandstone beneath the High Main coal seam at Whitley Bay. The image shows how the large pore spaces are infilled by authigenic kaolinite, most likely as a result of the dissolution of K-rich feldspars. Due to the majority of the pore spaces being filled, there is a lack of 'free' pore space available for fluid pathways through the sandstone.

The previous elemental maps of the sandstone displayed how the pore spaces are filled with an abundance of kaolinite, and this is also seen in the 3D imaging (see Figure 41). The heart-shaped 'book' is an exceptional image of how kaolinite is filling the pore space between two quartz grains, with several smaller fragments of kaolinite also in the image. Combining the elemental maps showing the kaolinite abundance and the 3D image, it can be understood that the sandstone is extremely full of kaolinite, which will have an impact on the permeability and fluid flow pathways. Covered previously, kaolinite is an authigenic clay that forms as a result of the dissolution of potassium-rich minerals, such as K-feldspar, of which there are several occurrences. This dissolution can be seen in Figure 41, which shows a K-feldspar mineral breaking down into the pore-filling kaolinite. As well as kaolinite clays, smectite-chlorite clays are also present in both the sandstone and the siltstone. Smectite-chlorite is shown in SEM imagery by 'platey' shapes, and this is demonstrated in Figure 41, where several plate-like shapes show how smectite-chlorite surrounds the quartz grains in the sample, as well as fibres of illite on the edges of the smectite plates.

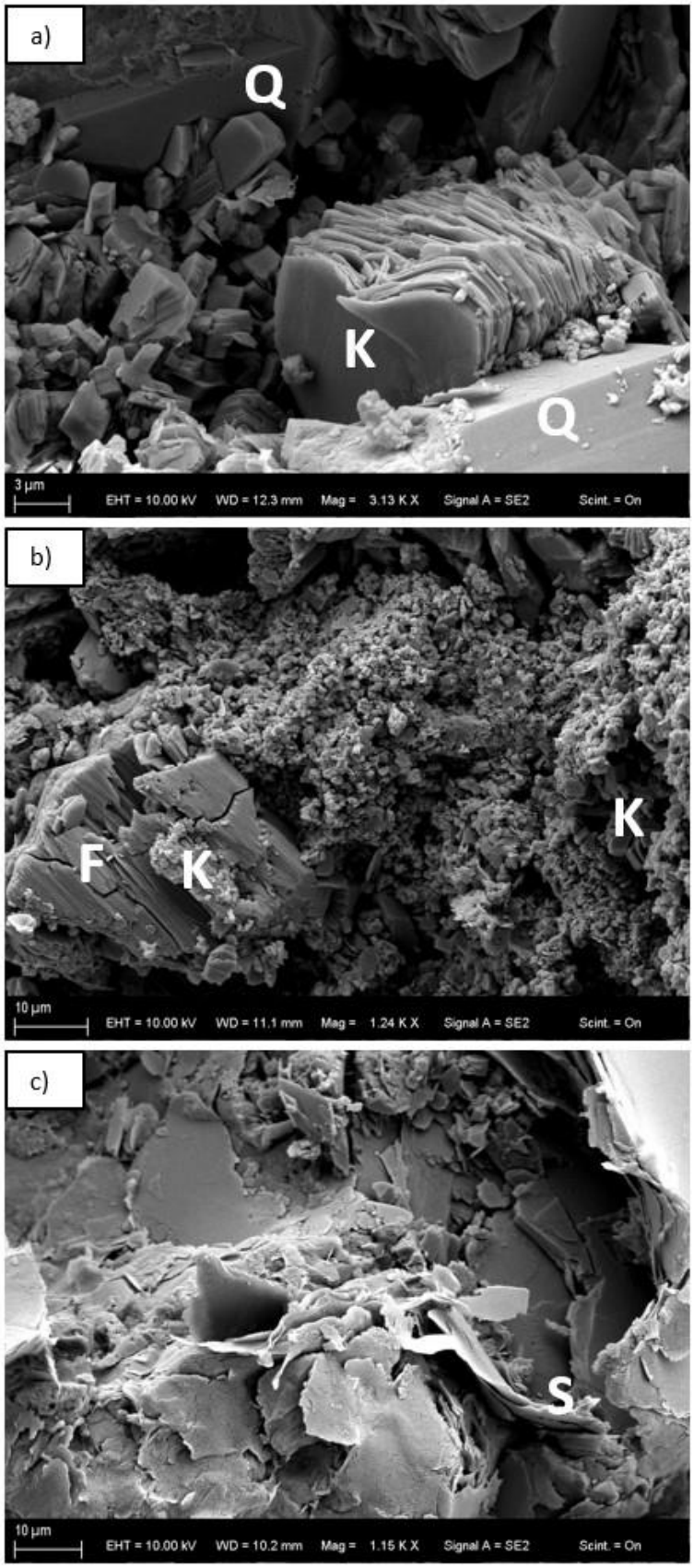

Figure 41 – SEM images of a chip of the RS1 sandstone sample. (a) shows authigenic, pore-filling kaolinite (labelled K) between two quartz grains (labelled Q). (b) shows how feldspar minerals (labelled F) in the sandstone undergo dissolution, giving rise to kaolinite. (c) shows how the sandstone contains multiple types of clay, namely smectite (labelled S) in this case.

2.6.3.4. Siltstones

A thin section of the siltstone underlying the High Main coal seam at Whitley Bay was also analysed using SEM techniques (see Figure 42). There is a large proportion of the section comprised of quartz grains, highlighted by Figure 42 representing the presence of silica in the section. As well as this high amount of quartz, there is very little pore space within the section, and any available pore space has been infilled by clay minerals. There is a high proportion of smectite-chlorite in the siltstone, dominating the pore space infill, as seen in Figure 43. It can also be seen that the siltstone is more tightly packed than the sandstone, and the smectite-chlorite content within the thin section shows less mineral breakdown than in the sandstone. There are also no large portions of smectite-chlorite within the images, meaning that there is very little pore space in the siltstone, and any pore space within the rock is largely unconnected. Lesser pore space than the underlying sandstone, as well as this pore space being disconnected, indicates that the siltstones will be poor for any fluid flow pathways. However, as can be seen in Figure 43, the section is host to two major fractures, one large vertical fracture in the right portion of the image, and a smaller diagonal fracture in the bottom left of the image. These fractures present a much less tortuous fluid flow pathway than through the pore space of the bulk rock, which would greatly increase the permeability of the siltstones. The caveat of this is that these fractures were not seen in the field or in any of the hand samples so may be artefacts of the preparation of the thin section, therefore applying the knowledge of these fractures to the permeability of the siltstone is unadvised and would need further investigation before being utilised.

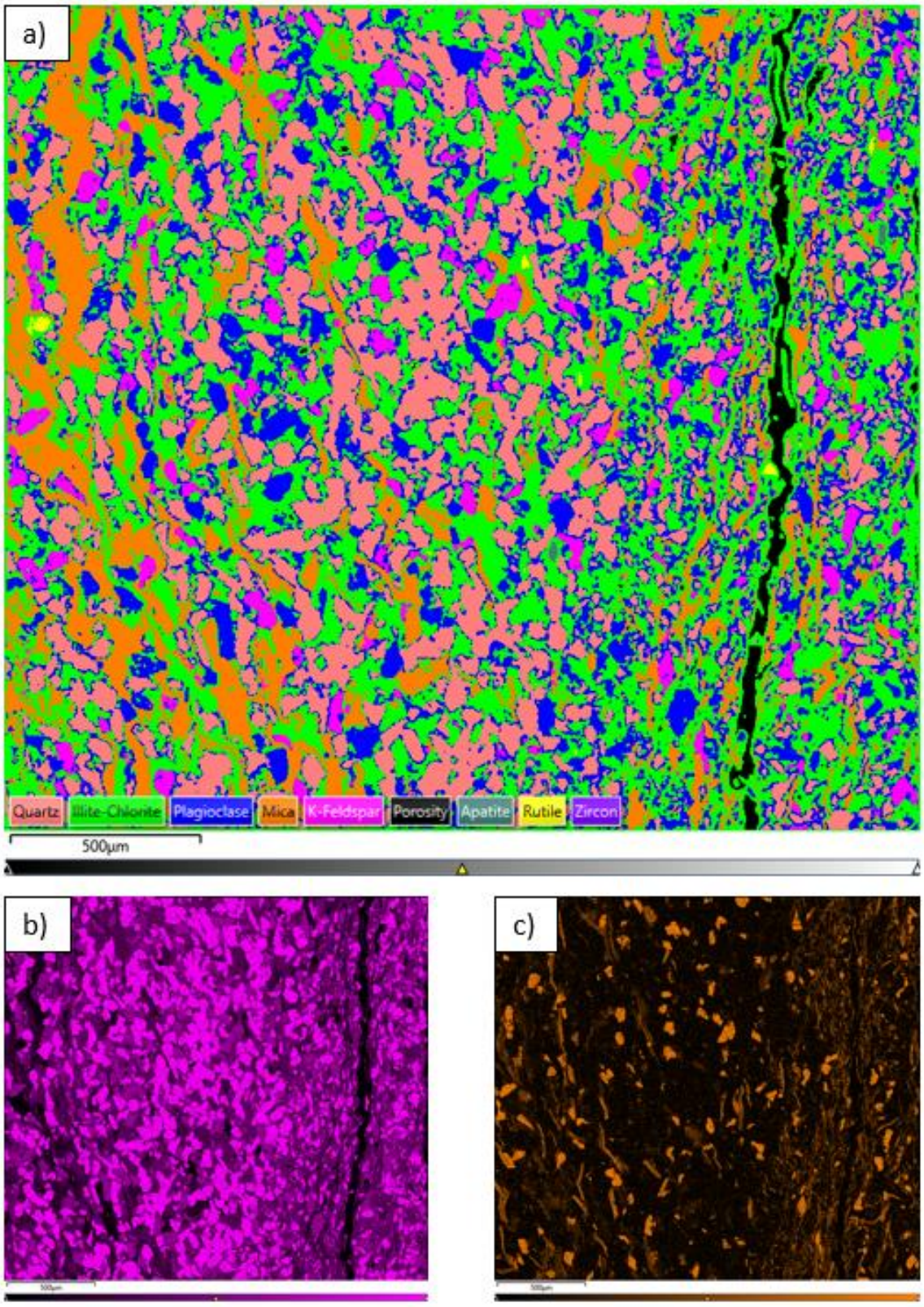

Figure 42 – a) SEM-EDS image of the siltstone below the High Main coal seam at Whitley Bay. Where 'Illite-Chlorite' is present in the key, this actually indicates the occurrence of 'Smectite-Chlorite'. The green colouring shows the presence of this smectite-chlorite clay, which is present over much of the image. b) indicates the presence of Si, showing how the siltstone has a high proportion of quartz grains. c) represents the occurrence of potassium, which shows how the siltstone contains an abundance of K-feldspar and plagioclase.

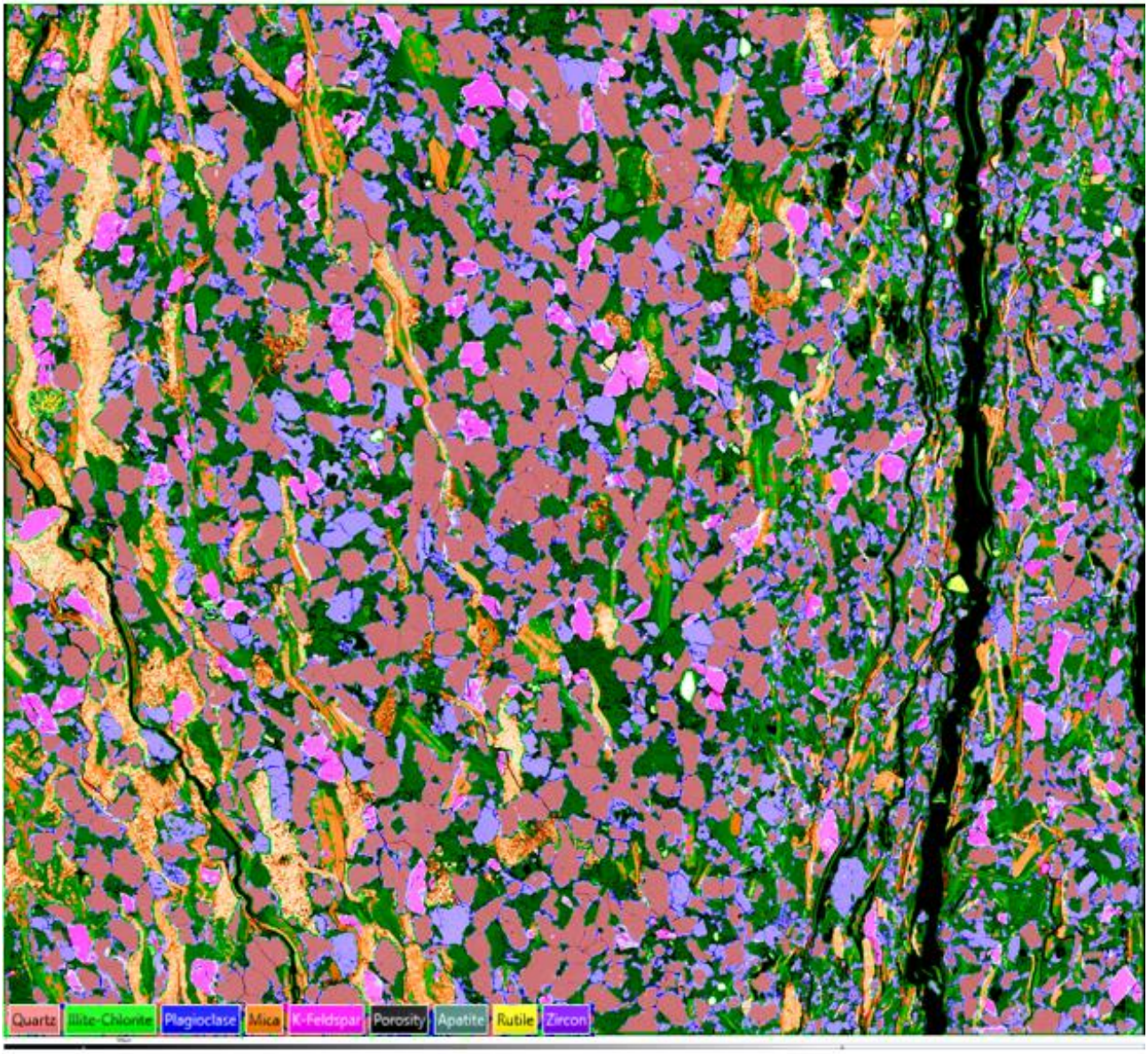

Figure 43 - High resolution SEM-EDS image of Silstone beneath High Main coal seam and coal mine workings, Whitley Bay. In the key where 'Illite-Chlorite' is present, this is actually 'Smectite-Chlorite'. This image reveals the dominance of smectite-chlorite clay minerals across the section. The clay minerals form the dominant infill of porosity in the siltstone. There is also a particular abundance of K-feldspar and Plagioclase feldspar that could degrade further to produce clay minerals such as Kaolinite.

2.6.3.5. High Main Coal

Only 3D sample chips were analysed from the High Main Coal Seam, but the images give valuable insight into the characterisation of the coal. Figure 44 shows SEM imagery of a coal sample from the High Main Coal Seam, and while it shows similar clay content to the sandstone in Figure 41, there are several occurrences of pyrite within the images in the form of bright cubic shapes.

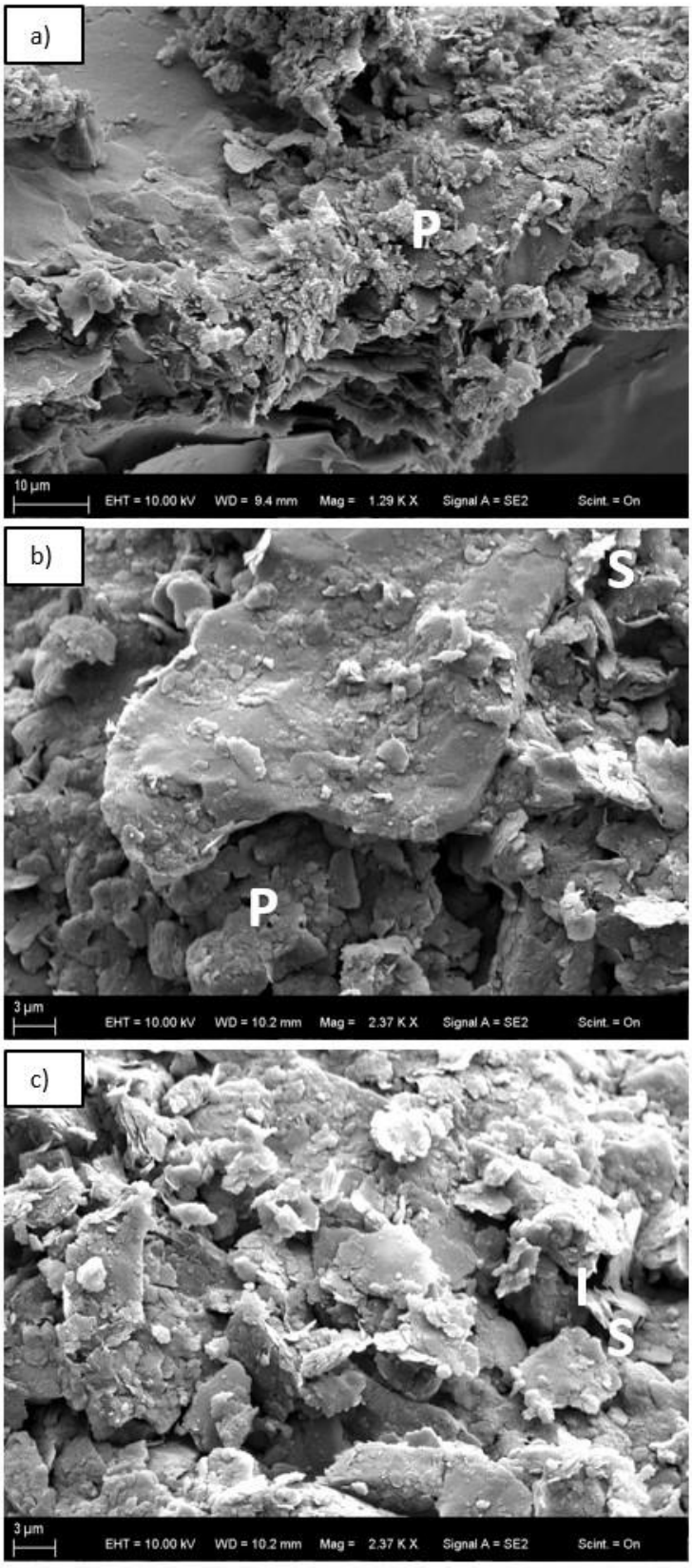

Figure 44 – SEM images of a coal chip taken from the RS6 sample. (a) shows the occurrence of pyrite within the coal, indicated by the small, bright-coloured cubic shapes. (b) shows more occurrence of pyrite cubes, as well as the presence of smectite and chlorite clays. (c) shows another view on the various clays within the sample, with illite, smectite and chlorite shown in this image (indicated by I, S, and C respectively).

2.6.4. XRD

As a preface to the XRD results, it should be noted that the clay content is only representative of the crystalline content in the samples analysed, and does not include or show any representation of any amorphous content. This is important, as all of the samples analysed were found to contain amorphous content (i.e. non-crystalline), with this being particularly significant in samples RS7, RS11, and RS12. These three samples were from the coal-baring portion of the **Roadway** section, with RS7 being from the *in-situ* coal while RS11 and RS12 are both from the anthropogenic backfill deposit.

The clay in the **Roadway** section was found to be dominated by kaolinite (see Figure 45), which indicative of the amount of feldspar contained within the outcrop. Kaolinite originates from the weathering of feldspars, so the high proportion of kaolinite in the **Roadway** section results from there possibly being a high concentration of feldspar. The kaolinite proportion was found to be 70%+ in all roadway samples except RS12, and found to be 100% for samples RS7 and RS11.

Chlorite was the least-prevalent type of clay throughout the section, with only three samples showing evidence of containing chlorite. This was recorded in samples RS13, RS5, and RS8, which were collected from either side of the coal seam. With the exception of RS5, the other two samples showed very similar levels of illite+mica and chlorite content, both around 15% with kaolinite making up the rest. This is seen in Figure 45, where the levels of illite+mica and chlorite follow the same trend of decreasing between ~1 m and ~3 m, which is within the sandstone of the section, before both showing an increase above 3 m when moving into the overlying siltstone. The illite+mica content throughout the **Roadway** section was consistently below 25%, with the exception of sample RS12, which was 59% illite+mica, however this was also located within the anthropogenic coal found in this section (determined to be backfill).

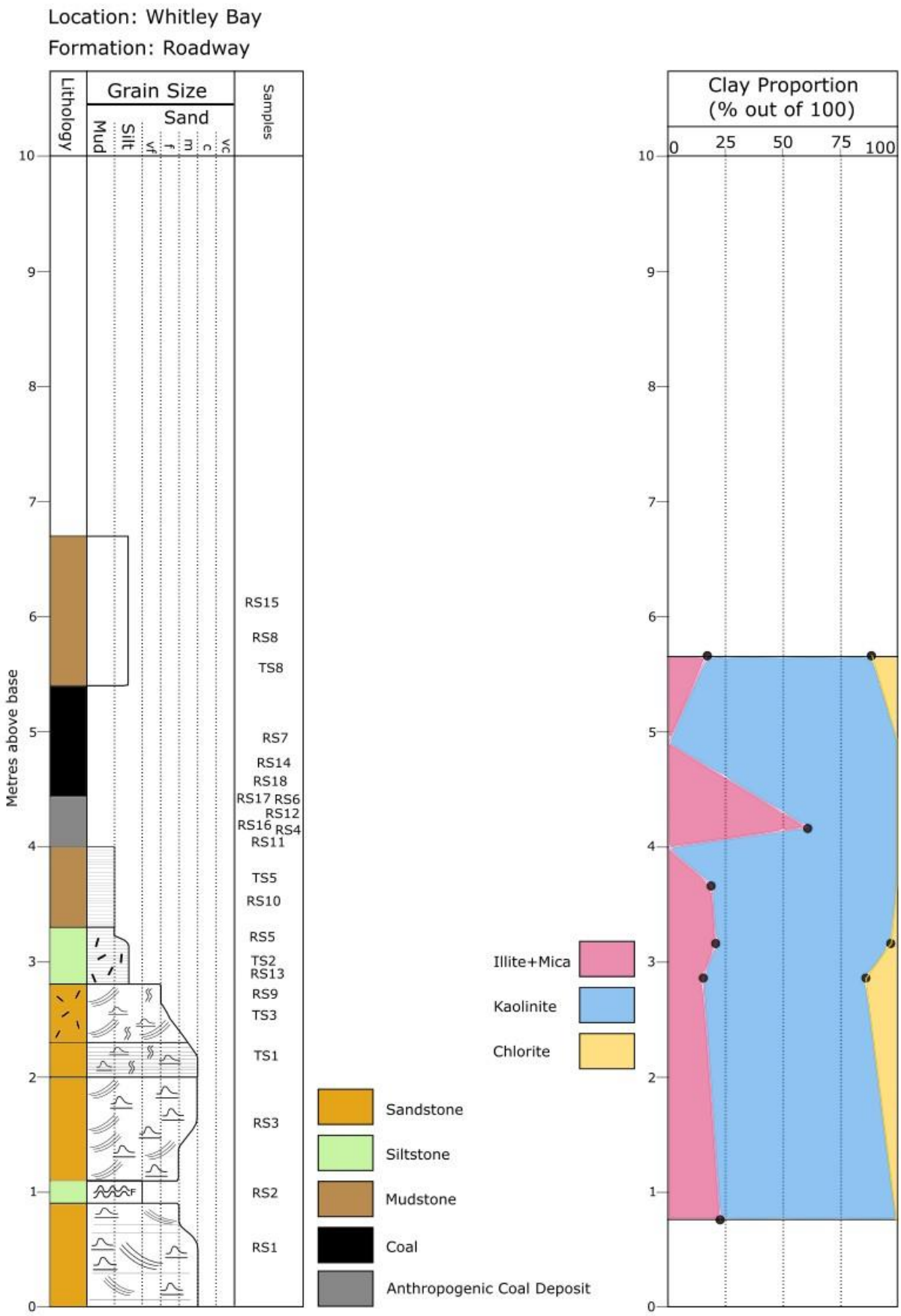

*Figure 45 - graphic log of **Roadway** section, alongside a proportional graph of clay content through the section. The black dots indicate changes between clay type.*

2.6.5. Permeability of Sandstones

As mentioned in the methodology, the *TinyPerm II* is an air permeameter, and as such there needs to be an allowance of air passing through the sample rock for a value to be obtained. This means that it struggles to measure a value for lithologies with very low permeabilities, such as shales and coals. This was the case when collecting the measurements for the outcrops at Whitley Bay, and can be seen in Figure 46, where the field measurements were only able to be collected in the sandstones. The permeability values obtained have some variability across the three sections, as well as within the values obtained for each section independently.

The general character of the sandstone facies consists of moderate permeability, but is several magnitudes greater than subordinate siltstones and coal seams. The sandstones present at Whitley Bay are generally thick (0.8-3.8 m) with many fluvial structures, such as extensive crossbedding, flaser bedding, and thin lenses of clay and coal (Figure 46). The heterogeneity of the sandstones, coupled with their feldspathic and micaceous nature can result in lower permeabilities than may be expected, with the fluvial structures contributing to the variabilities shown in Figure 46.

The **Roof Collapse** and **Roadway** sections show an increase in permeability up-section, while the **Pillar** section shows a decrease over the same height, with all the field measurements recorded between 100-375 mD. The sandstone at the top of the sections with increasing permeability possess finer grains, as well as woody material and extensively laminated beds.

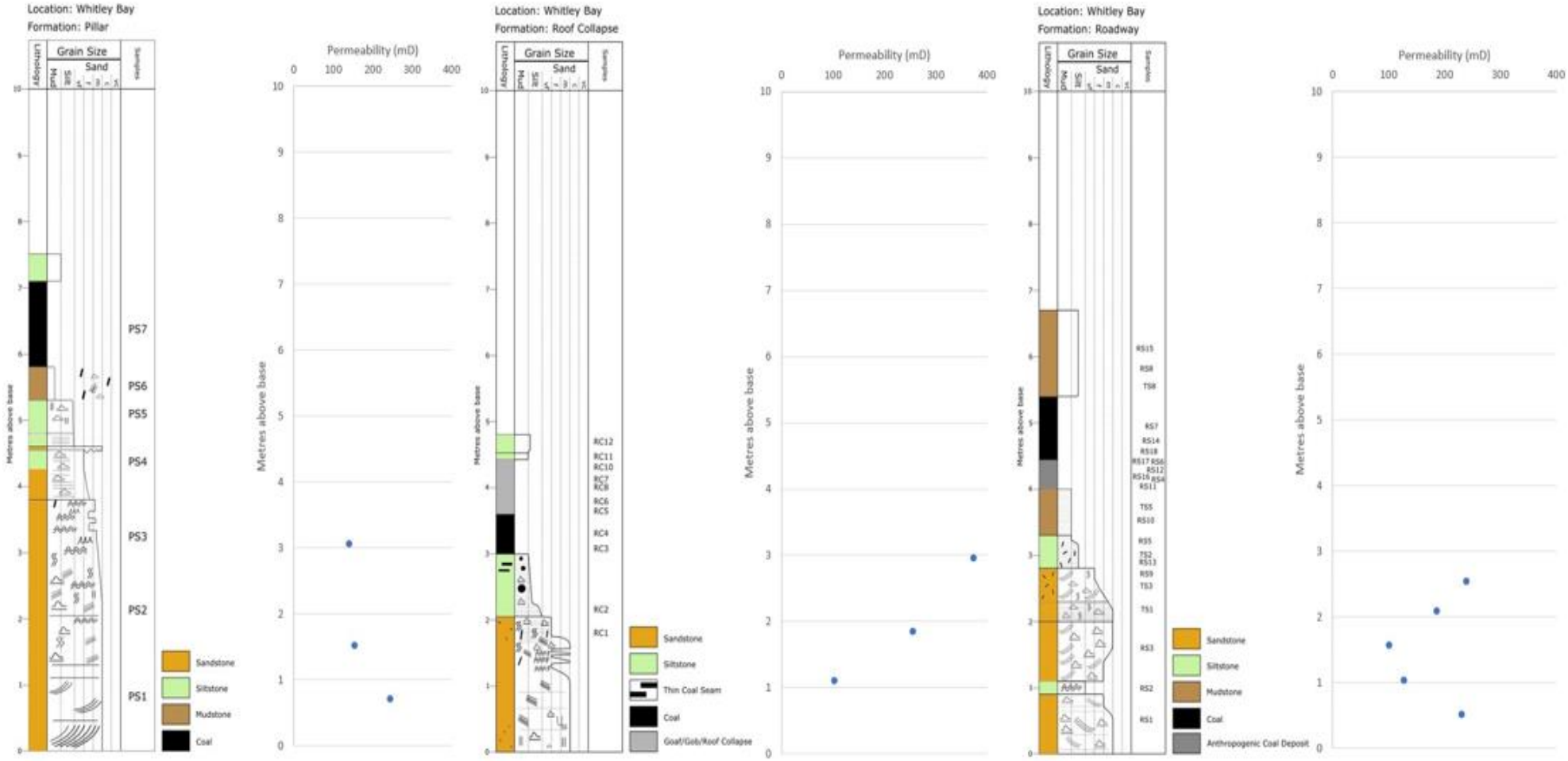

Figure 46 – Field permeability measurements for sandstones at Whitley Bay, alongside the graphic logs for each section.

2.6.6. Permeability of Coal Samples

When samples of the coal from the High Main Coal Seam were attempted to be cut for the tri-axial pressure vessel, the samples proved too friable to give a usable sample of coal. However, Stephan Nielsen, a member of staff within the Durham University Earth Sciences department, made a sample available to us that was taken from a drilling project undertaken by Lanchester Wines. The sample is from the BH1 borehole drilled at Abbotsford Road, Gateshead, from a depth of 150 m – the initial borehole was only drilled to 117 m, but was then continued where they intercepted the coal seam at ~150 m. The data from the tri-axial pressure vessel was processed to determine the permeability of the coal sample from the experiment outlined in the methodology previous, which are several magnitudes lower than the recorded values for the sandstones (see Table 4).

Table 4 - Conditions and resulting permeability of the coal sample tested in the tri-axial pressure vessel.

Confining Pressure (MPa)	Sample Pore Pressure (MPa)	Permeability (mD)
10	2	*negative value, therefore disregarded*
10	5	$7x10^{-8}$
10	5	$1.7x10^{-7}$
10	2	$1.7x10^{-7}$
10	5	$2.2x10^{-6}$
10	5	$1.9x10^{-5}$
10	5	$4.8x10^{-6}$
10	5	$5.5x10^{-6}$
10	2	$9.5x10^{-6}$
10	2	$6.3x10^{-6}$

2.6.7. ICP-MS and ICP-OES

Figure 47, Figure 48, and Figure 49 show each of the graphic logs for the three outcrops at Whitley Bay lined up alongside the selected chemical element ratios mentioned in the methodology – Ka/Ta, Zr/Cr, Sc/Lu, K/Cs, and Na (wt%). The coal-baring samples (those coloured black instead of blue) have not been linked to the other samples, as they cannot be correlated between sections due to the high organic matter content, and are shown on the figures to show where the coal-baring portions of the sections are. The **Roadway** section has the best data coverage of the three sections as it had the most samples analysed, while the **Pillar** section has the least coverage, with no sample from above the coal being analysed (not safely accessible ay field outcrop). For all of the ratios in the **Roof Collapse** and **Roadway** sections, the API units stay consistent either side of the coal-bearing strata. Due to the nature of using geochemical analysis for correlation, the absolute values should not be looked at, but instead analyse the trends of the elemental ratios. The **Pillar** section does not show as pronounced trend changes as much as the other sections, where the ratio is consistent or records a gradual change through the whole section. Figure 48 and Figure 49 show distinctive trend changes in most of the ratios, with the changes directly below the High Main Coal Seam being due to lithology changes from siltstone to sandstone. Zr/Cr is an indication of provenance and sediment origin, with a trend change recording lithology changes, supported by the changes matching with the graphic logs. chemGR API can also be used as a way to record lithology changes via gamma radiation, with the 'high-to-low' trend changes in Figure 48 and Figure 49 supported by the graphic log change from siltstone to sandstone. The Na (wt%) trend changes in Figure 48 and Figure 49 are interesting, recording an increase in the top of the sandstone before showing a decrease at the base of the section, but this is not seen in Figure 47. However, due to the sections being in close proximity to the sea, this could be due to contamination from sea spray.

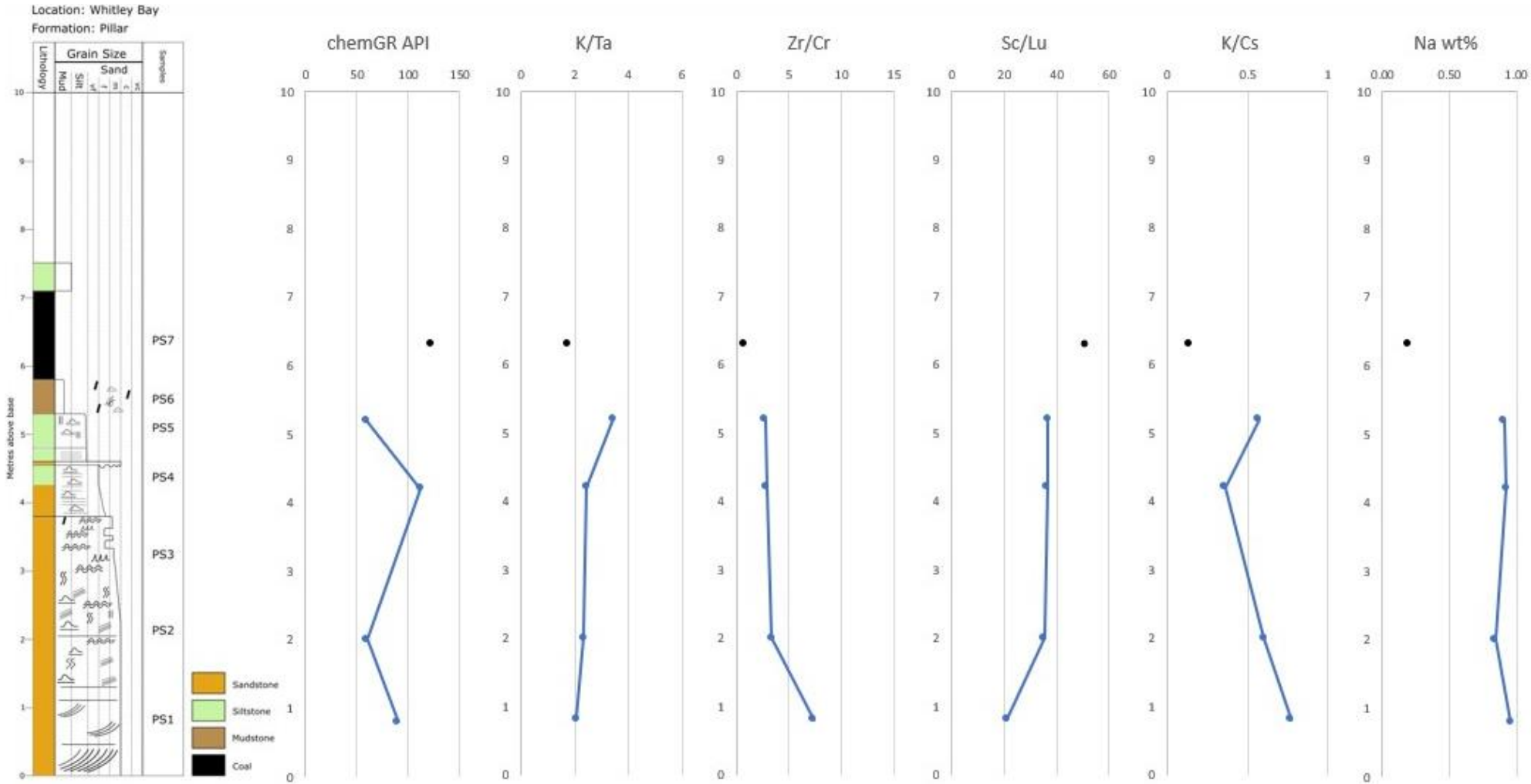

*Figure 47 - graphic log for **Pillar** section alongside selected ICP-MS and ICP-OES ratios. 'chemGR API' is the chemical ga mma radiation value in API units. Black points indicate coal-baring samples.*

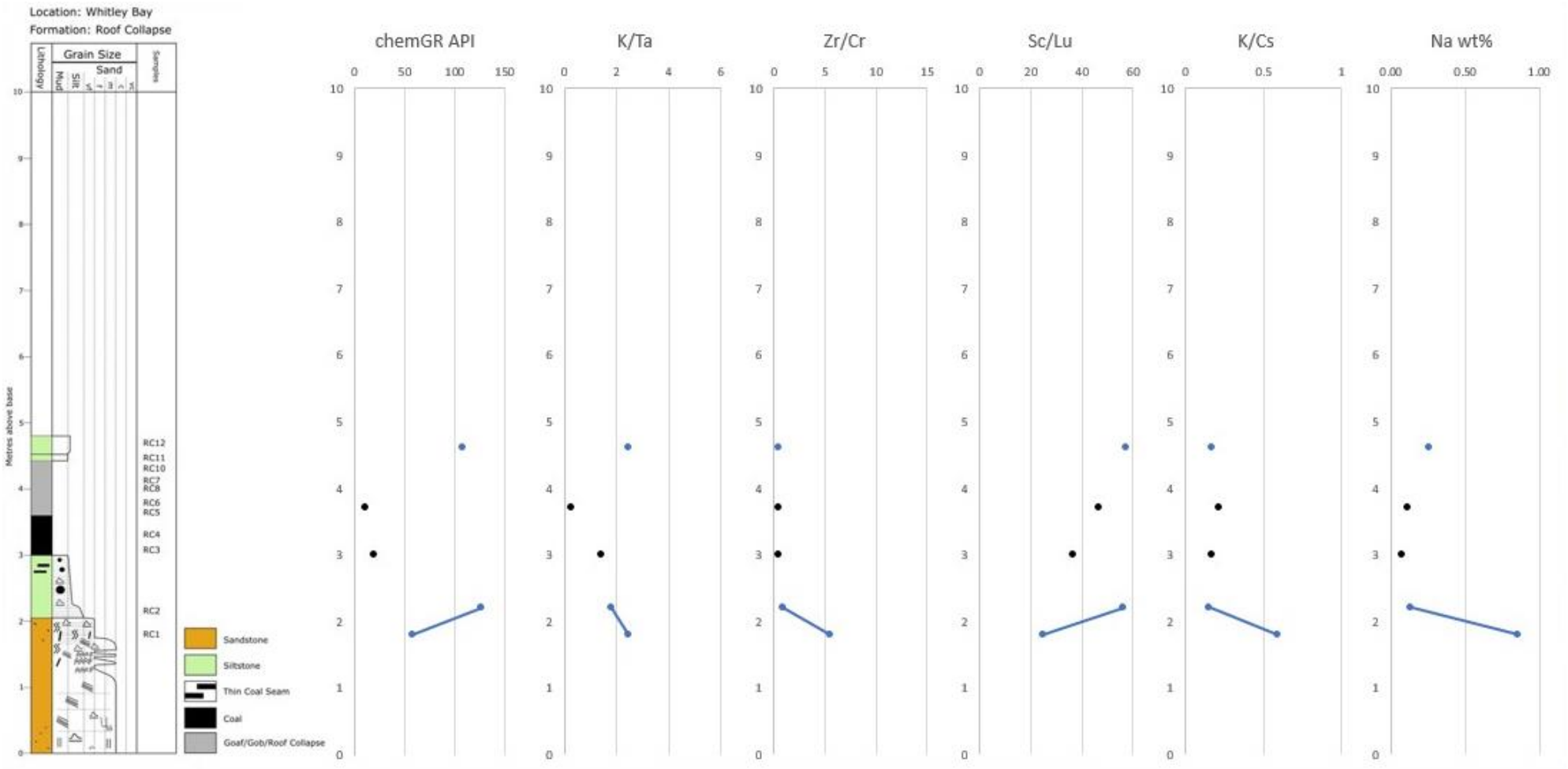

*Figure 48 - graphic log for **Roof Collapse** section alongside selected ICP-MS and ICP-OES ratios. 'chemGR API' is the chemical ga mma radiation value in API units. Black points indicate coal-baring samples.*

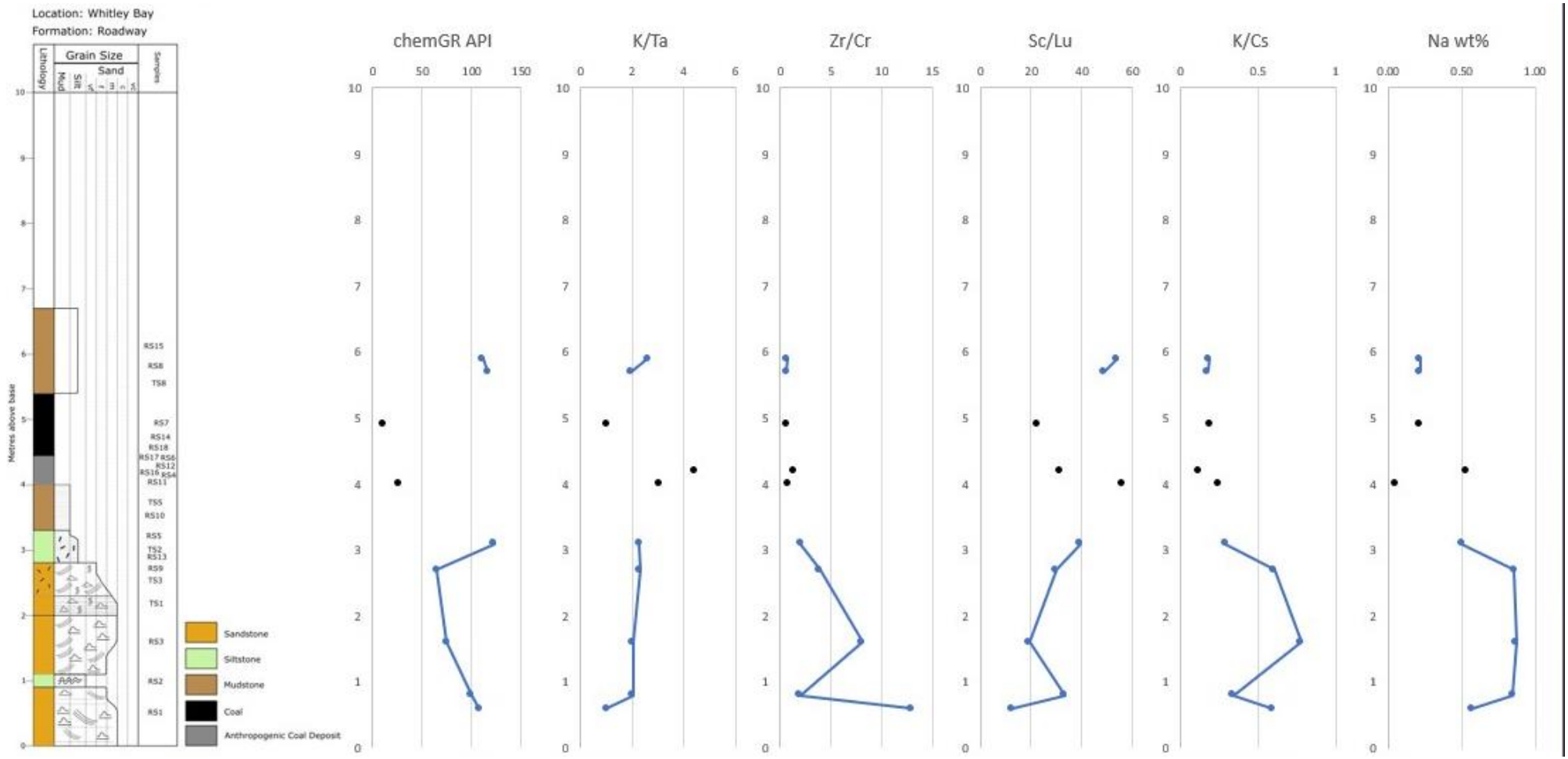

*Figure 49 - graphic log for **Roadway** section alongside selected ICP-MS and ICP-OES ratios. 'chemGR API' is the chemical ga mma radiation value in API units. Black points indicate coal-baring samples.*

The strata can be visually correlated, able to be followed between the sections along the coastline, and overlaying the geochemistry for each section together gives further insight (see Figure 50). The ratio values stay consistent through the coal-bearing strata across the **Roof Collapse** and **Roadway** strata, and this may be the case for the **Pillar** section but is not known as it was not possible to collect samples from above the coal pillar due to the nature of the outcrop. This consistency is highlighted by the pink line being near-vertical for the top portion of all of the graphs in Figure 50. Below this, at ~3 m, is where each ratio starts to deviate, and this is most likely due to the change in lithology. This height level is where the strata changes from either mudstone or siltstone to the base sandstone, which is likely the cause for the changes in elemental ratio data. There are increases in Zr/Cr, K/Cs and Na (wt%), decreases in the chemGR API and Sc/Lu ratio, while the K/Ta ratio sees very little variation at the ~3 m mark for all three sections.

For Na (wt%), the pink line is mainly dependent on the samples from the **Roadway** section, as this dataset has the best coverage, but the initial trend of an increase at ~3 m is also shown in the **Roof Collapse** data. The trend is shown at slightly different heights for the two sections, due to the differences in the total heights of the sections, but the trend is consistent between both of them. While Na (wt%) is impacted by the amount of feldspar in the samples, due to sodium being a key element in the chemical makeup of feldspars, this could also have been affected by the location of the outcrops at Whitley Bay. All of the sections are within close proximity to the sea, being located on the beach coast, so are consistently coated in sea spray via rising tides. If the samples were taken too close to the surface of the rock face, they would be more likely to be more affected by sea spray contamination, which would have an impact on the Na (wt%) data.

The general trend changes at ~3 m are ‘interrupted’ by opposite-trend spikes (zigzags) at around 1 m for the Zr/Cr, Sc/Lu and K/Cs ratios, where this spike is picked up in the **Roadway** samples. Lining up these trends alongside the graphic log for the **Roadway** section shows that this spike lines up with the thin siltstone bed within the largely sandstone base of the outcrop. The takeaway from this

is that the spike can be determined to be due to the siltstone occurrence, as the following datapoint (located at 0.8 m from the base of the section) shows a value that would be expected if it followed the trend above. This sample at 0.8 m is from the sandstone package, so it makes sense that it would follow the trend from the sandstone beds above it.

The similarities in the element ratios across the three sections allows for the determination that it is the same lithology that is outcropping along the rockface of the beach at Whitley Bay. While this was assumed from the viewing the sections in the field, this chemical evidence is a quantitative view of the lithologies that backs up this assumption. For example, Zr/Cr can reflect the nature of the provenance of the samples, so the similarity across the three sections implies that the sediment has the same place of origin. This shows that the stratigraphy at Whitley Bay can be correlated across the ~107 m distance between the three sections.

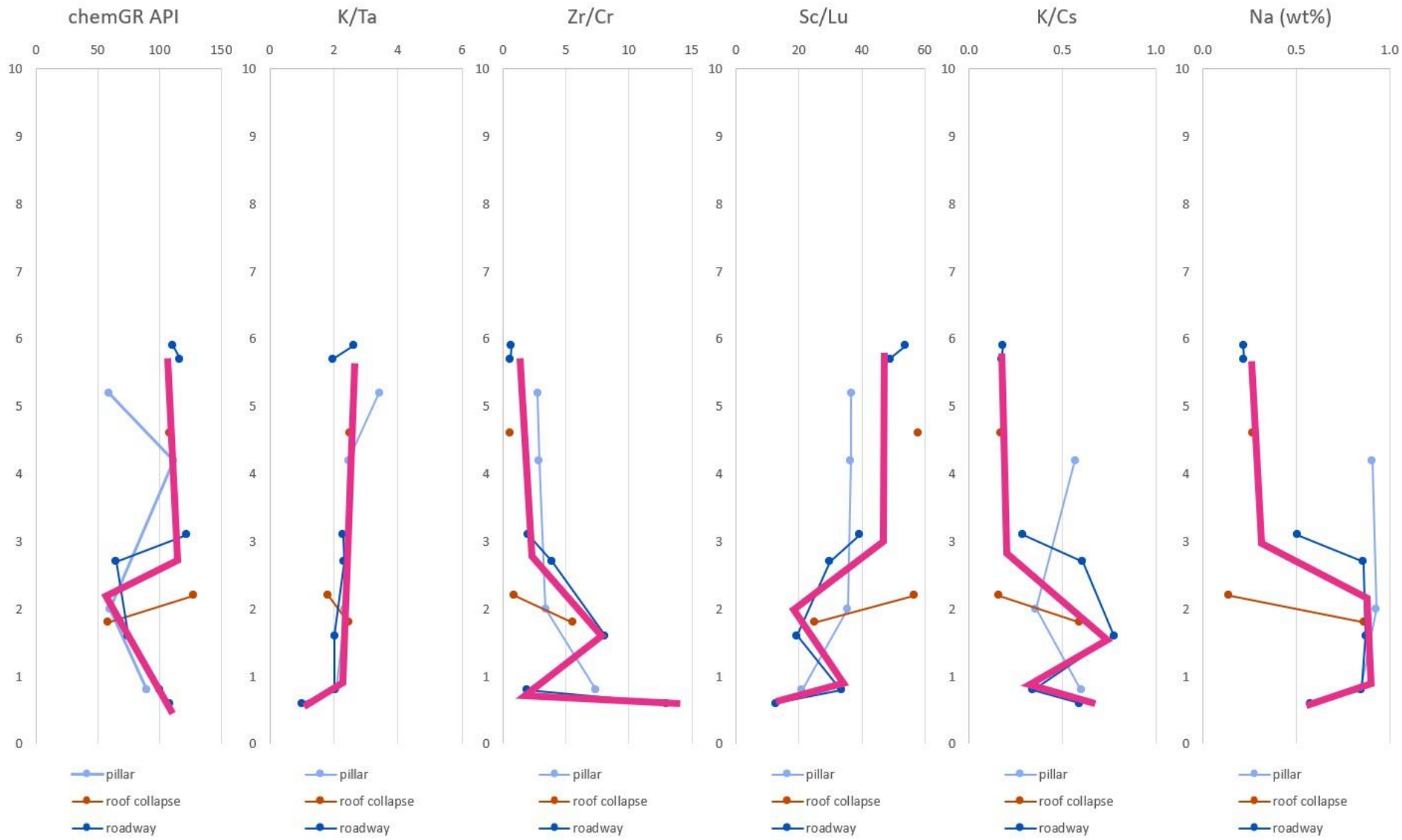

*Figure 50 - Selected elemental ratios for the **Pillar**, **Roof Collapse** and **Roadway** sections at Whitley Bay. The data has been overlain to allow for easy viewing of trends that are consistent across the three sections, and have been highlighted by the pink line. Where the data points within the same section are not connected is where there is the occurrence of coal in between the analysed samples.*

2.7. Discussion

2.7.1. Porosity and Permeability Characteristics of Cyclothems

The field permeability investigation as part of this study has focused on the sandstones, due to limitations with the *TinyPerm II*, while the investigation into the coal permeability was conducting in a laboratory. The cyclothem has a wide range of permeability, from the extremely permeable sandstones to the highly impermeable coal seam. Within the sandstones, there are slight variations due to fluvial structures (see Figure 28), but are overall still the most permeable lithology of the cyclothem. The sandstone was also the most porous lithology, with the siltstone recording 0.3% compared to ~2.5%, with the siltstone pores dominated by smectite-chlorite clay minerals.

An interesting observation was made during the study, where tufa deposits and groundwater was found to be precipitating on the rock face directly below the High Main Coal Seam (see Figure 51). This was consistent across all of the sections at Whitley Bay. The ochre content of the groundwater supports the SEM-EDX analysis of the High Main Coal Seam, where the coal seam contains pyrite, and is further supported by the findings of Turner and Richardson (2004). Their study found that Whitley Bay coal seams possessed medium/high levels of sulphur, which further supports the findings of this study. This observation further shows that the permeability of the coal seam is negligible compared to the surrounding strata, with the tufa and groundwater found beneath the rooms from the former room and pillar coal mine workings, rather than leaving the rock face beneath the coal pillar.

*Figure 51 - Image of the **Pillar** section, with a red line showing the top of the sandstone - which could be seen across the other two sections, and has been used as the central marker for correlation between sections. The area on the right of the image shows how groundwater has left the rock face directly beneath the level of the coal seam, indicated by the tufa deposit comprised of precipitated carbonates. Person for scale.*

While not investigated as part of this project, it is important to highlight that the characteristics of coal within the Northumberland Basin have been looked at in other studies, so should be included here as part of the section characterisation. As a brief repeat from the beginning of this chapter, Turner and Richardson (2004) found that the coal seams within the Northumberland Basin were high volatile bituminous coals that increased in rank towards the south. Coal in itself is comprised of different macerals, and Fender *et al* (2020) used a sample of coal from the Top Plessey seam (within the Northumberland Basin and Pennine Middle Coal Measures) to investigate them. As seen in Figure 52, the sample is rich in vitrinite and inertinite, with millimetre-long bands of bituminite parallel to bedding. This is supported by looking at the level of vitrinite reflectance of the sample, which was found to be 1.56%R_0. This high proportion of organic material in the coal seams can impact the permeability, with the low porosity and low permeability coal seams acting as barriers to subsurface fluid flow.

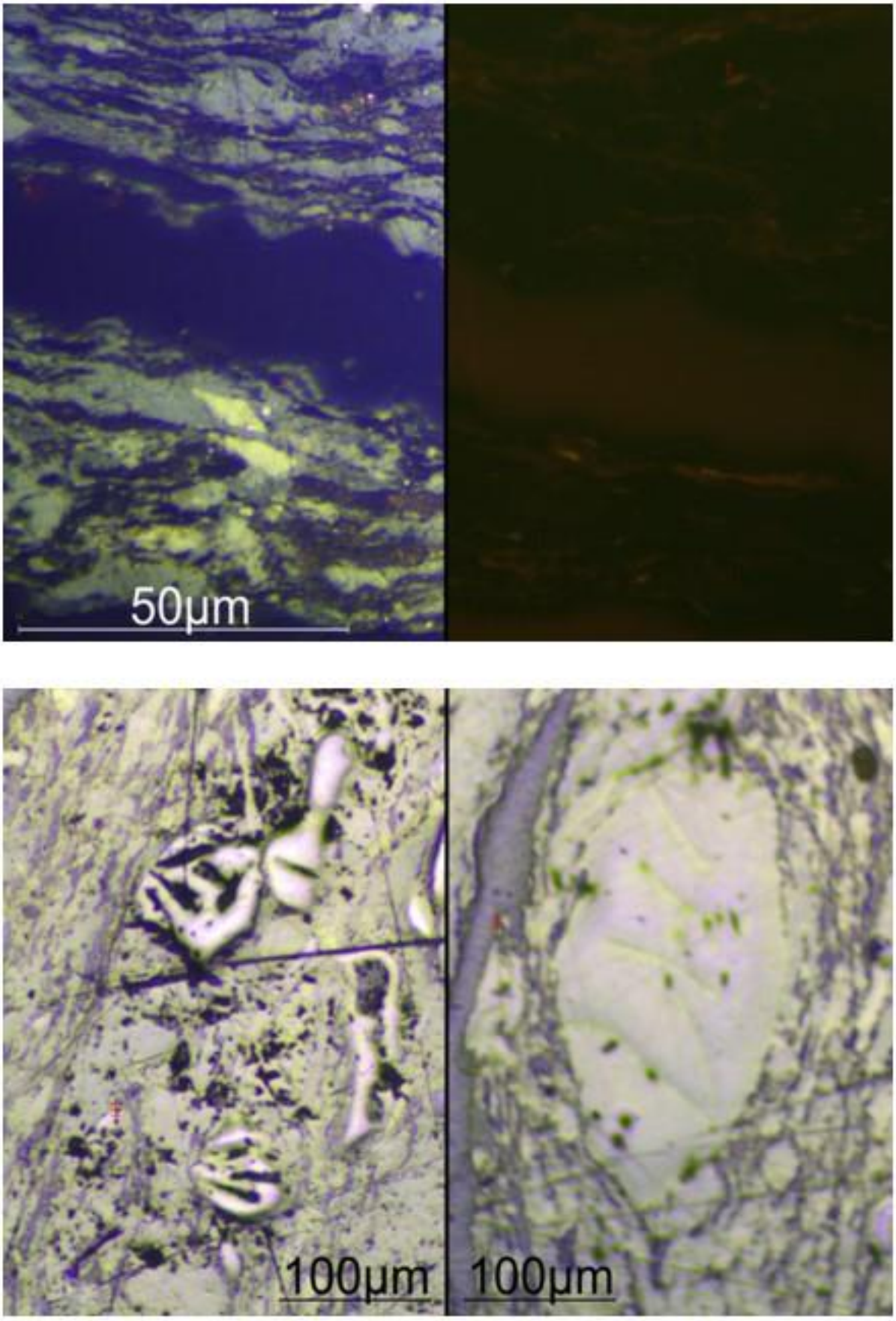

Figure 52 - Cathode luminescence images of a sample of the Top Plessey coal seam, Northumberland Basin. The top image shows bituminite, while the lower image shows inertinite. From Fender et al, 2020.

2.7.2. Anthropogenic Sedimentology of Whitley Bay Coal Succession

Whitley Bay is unique in being one of the only places to investigate the inner workings of former room and pillar coal mines, and this study identified different anthropogenic coal deposits – a coal pillar left to support the overburden roof of the coal mine; a deposit where the coal roof had collapsed; a backfill deposit, where coal had been packed into voidspace to help support the overburden. Each of the deposits are unique in their appearance and characteristics (see Table 2), and this study has identified differences between them, increasing understanding of how these anthropogenic coal mine deposits can be identified and differentiated between.

Presently, former mining activities and anthropogenic sediments are classified as a singular entity, and fall under 'Artificial Ground' (Ford et al, 2010). However, this study has found that the anthropogenic sediments associated with former coal workings are highly variable in manner, with the current classification methods not giving enough detail for suitable use for former room and pillar coal mine workings. By quantifying the difference in grain size between the roof collapse and backfill deposits, this study has increased the understanding of these anthropogenic sediments, which could be used to start to create a new classification framework for anthropogenic sediments associated with former room and pillar coal mines.

2.7.3. Correlation and its Importance

This study has shown that while the strata at Whitley Bay could be visually traced along the coastline to correlate the sections, geochemical correlation techniques using ICP-MS and ICP-OES can correlate the lithologies (Figure 53). The top of the sandstone package is the most consistent horizon across all the sections, so provides the best part to base the stratigraphic correlation - shown in Figure 51. The coal-bearing strata have also been correlated, even though they cannot be correlated geochemically through the methods used in this study.

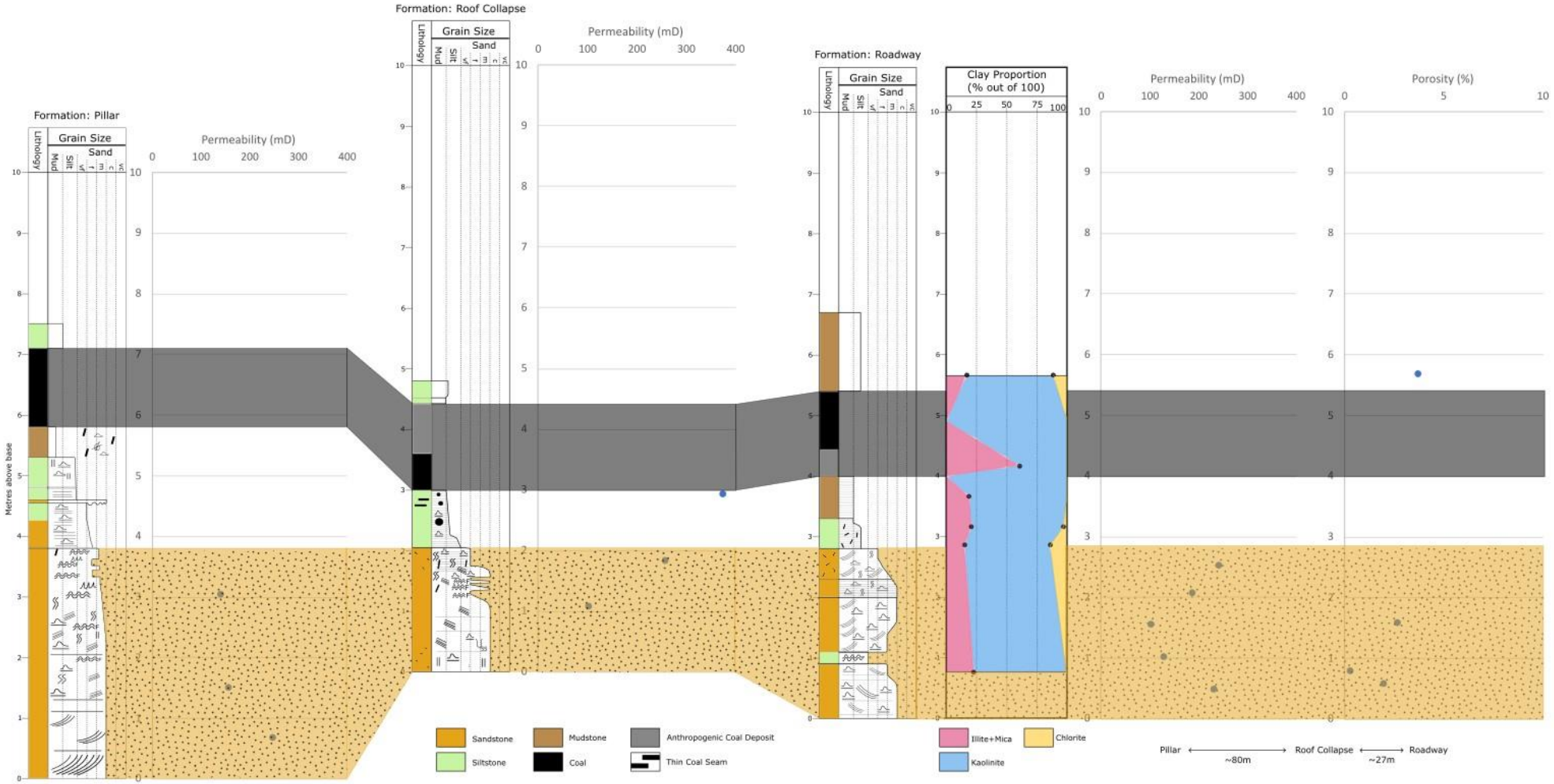

Figure 53 – Correlation panel of the Whitley Bay sections, with the associated field permeability and XRD data alongside the graphic log of each section.

Being able to correlate stratigraphy can have large implications for increasing the understanding of regional stratigraphy, as understanding the underlying geology of a region is a crucial stage of any large development. The knowledge of whether the strata are the same or different in two locations can be invaluable when it comes to geothermal projects, as knowing whether the aquifers are connected or disconnected could have larger implications for a heating network. For laterally extensive strata, such as the thick sandstone package found at Whitley Bay, correlating this in other sections allows for locating which part of the wider stratigraphy is being investigated, which can reduce errors.

2.7.4. Relevance to Room and Pillar Coal Mine Workings

The investigation into the former room and pillar coal mine exposed at Whitley Bay has provided the opportunity to identify some of the different anthropogenic sediments present in former room and pillar mines, giving greater understanding than previous. By identifying the pillar, roof collapse and backfill deposits, and being able to differentiate between them both visually and quantitatively (eg. grain size), a classification framework can start to be formed. On top of this, the three anthropogenic deposits can act as 'end members' of what may be found in former room and pillar coal mines, and can act as a starting point for further investigations.

This study has also highlighted how variable and unknown the inner workings of former room and pillar coal mines are, and that they are not quite the empty pipe lines that can be described in proposed shallow coal mine geothermal projects. As found in this study, they can contain several different types of anthropogenic deposits as artifacts from the mining, which can have unknown implications for fluid flow through the workings. A coal pillar can act as a large barrier for fluid flow, but the increased size of cleats due to increased overburden pressure could act as fluid pathways, while the variable nature of the clay matrix and non-orientated coal clasts could have large impacts

of permeability and fluid flow through the former coal mines. As such, this aspect can be taken forward in further research to continue investigation into these anthropogenic deposits.

2.8. Conclusion

This chapter has covered the detailed study into the Whitley Bay coal succession, able to be investigated due to coastal erosion. The succession provides detailed parameters of deposits associated with former room and pillar coal mine workings, being one of the only places in the UK where the succession and inner workings are exposed. The following points are the key findings of this chapter:

- The coal succession present at Whitley Bay is a classic Upper Carboniferous (Moscovian) sequence, recording sandstones, siltstones, mudstones and a coal seam. The key characterisations of each of the lithologies are as follows:
    - The sandstones are medium grained and fine upwards, with several fluvial structures (eg. flaser beds, ripple markings), and possess high permeabilities of up to 375 mD. The petrography analysis revealed the sandstones contain high concentrations of authiogenic, pore-filling kaolinite.
    - The siltstones and mudstones are both extremely laminated, and much less permeable than the sandstone, with the pore spaces in the siltstones being dominated by infilling smectite-chlorite clay minerals.
    - The High Main Coal Seam outcrops in several forms, either *in situ* or as anthropogenic deposits from the former room and pillar coal workings. From laboratory permeability tests on coal from the Hutton Seam, the coal is extremely impermeable. Turner and Richardson (2004) found that the Northumberland Basin coal seams contained sulphur, and the SEM-EDX analysis revealed pyritic cubes within the *in situ* coal.

- The anthropogenic coal deposits from the former room and pillar coal mine workings were found to be in three forms – a coal pillar; a section of collapsed coal seam roof; a deposit of packed backfill.
    - The coal either side of the pillar had been extracted, leaving the cleated coal deposit behind. The edges of the coal pillar are slumped, due to the increased overburden pressure of the former coal mine working roof.
    - The roof collapse deposit consists of unsorted, irregularly sized coal clasts in a clay matrix, up to 20 cm in diameter. While a large proportion of the deposit is made up of larger clasts, the grain size analysis revealed that the smaller size fractions were highly variable, with the 8000 μm size fraction being the most dominant.
    - The backfill deposit was made up of small, regularly sized coal clasts supported by a clay and mud matrix. The weighting of size fractions is spread more evenly than for the roof collapse deposit, with the largest weighting being ~4000 μm in size.
- The strata in the three sections at Whitley Bay could be visually correlated between all the sections. By using specific element ratios from the ICP-MS and ICP-OES, trends that indicate lithology changes were consistent between the three sections by matching with the graphic logs, meaning that the sections can be geochemically correlated with high confidence.

3. Application of chemostratigraphic techniques at Bayfield Housing Estate

3.1. Introduction

Following on from Chapter 2, the same techniques for characterising and correlating strata surrounding former coal mines should be tested in other locations to trial their viability. The Northumberland Basin has a rich history of coal mining in the past, and as such there were many collieries and coalfields across the region, peaking at over 170,000 coal miners in 1923 according to the Durham Record Office (Durham Record Office, accessed 6/10/2023). As such, the large amount of coal extraction taking place in different parts of the region, combined with the lack of defined stratigraphic correlation, led to discrepancies in the naming of coal seams, with different names being used in several locations for the same coal seams. This was partially due to the lack of legislation and rulings on coal mining, with the *Inspection of Coal Mines Act* coming into effect in 1850, with any plans or records before this time being unreliable and inconsistent. This makes it especially difficult to correlate the different coal seams across different collieries in the region – for example, the coal seam now known as the 'Durham Low Main' has been found to have at least 10 alternative names throughout County Durham and Northumberland ('Geology of the district around Newcastle upon Tyne, Gateshead and Consett', 1998). This is where testing the viability of the techniques displayed in Chapter 2 could be applied, as correlating strata above and below the different coal seams could aid in correlating the coal seams themselves, helping to achieve a stratigraphic control for regional correlation. By using the geochemical data from the samples, Chemostratigraphy could be applied across the three exposed sections at Whitley Bay, allowing for stratigraphic correlation between them. Chemostratigraphy can further the understanding of the underlying stratigraphy, especially in areas of regional subsidence, such as aiding in the identification of unreported or unidentified coal removal.

One of the geohazards that is associated with coal mining is subsidence, where there is infill of the overlying sediments into a void left by coal removal. Coal was originally extracted where it

outcropped on the surface, with mining becoming progressively deeper via shallow workings. These shallow workings were in the form of bell pits, which later became room-and-pillar, as outlined in Chapter 1 and 2. This progressed to larger, open pits as well as more widespread subsurface room and pillar, and often through longwall mining methods. The underground mining of coal can often lead to subsidence at the surface, and this can be seen at Whitley Bay through the infilling of overlying sediments into rooms where the coal has been removed. There are generally two types of subsidence associated with coal mining. Crownholes are the result of the collapse of mine entries, mine roadway intersections, and shallow void consolidation (see Figure 54). The other type of subsidence is part of the longwall mining process, where the roof is encouraged to collapse in order to reduce the stresses acting on the working face, generating a subsidence trough.

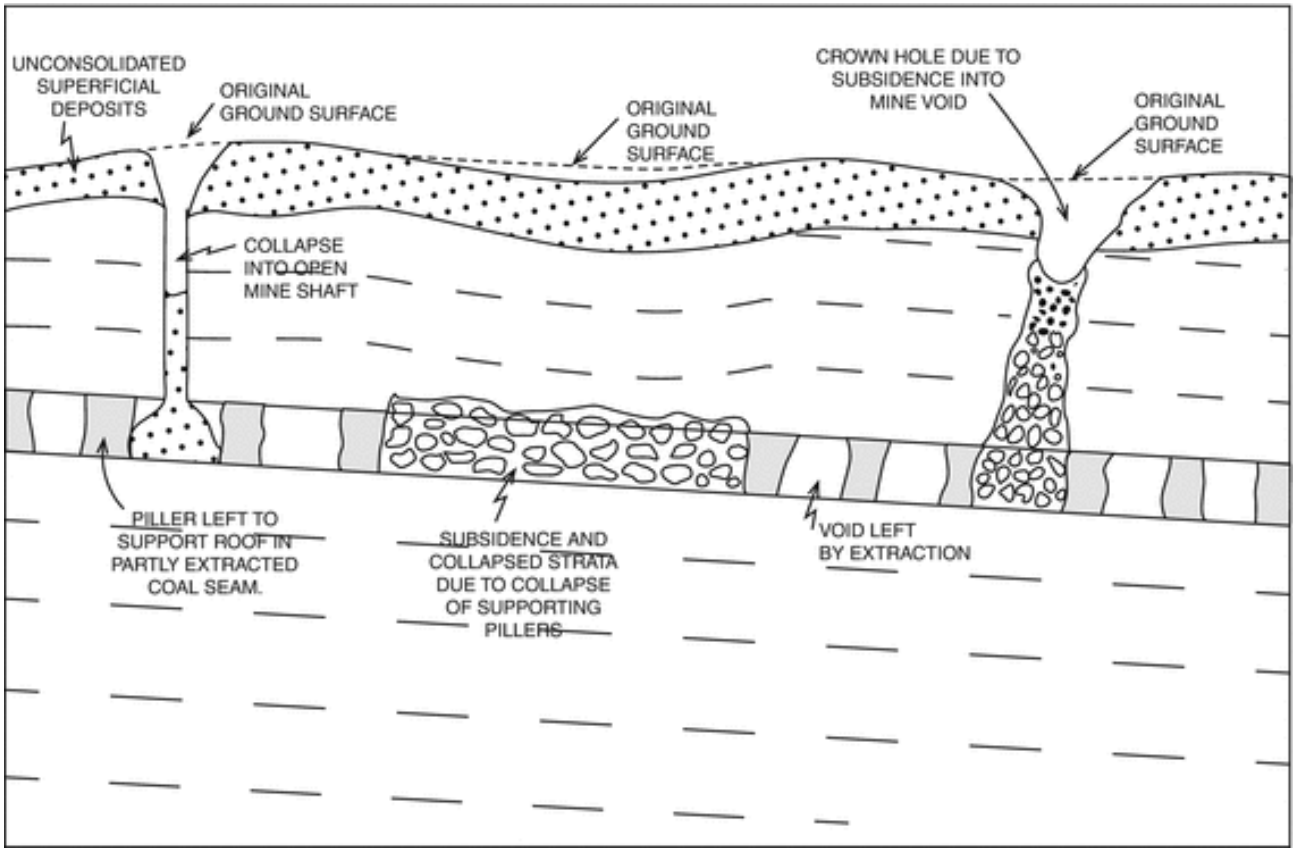

Figure 54 – Diagram showing different examples of land subsidence associated with coal workings, and how they relate to the location of void spaces within the workings. From Marker, 2016.

The issue of coal mine subsidence shows the importance of detailed coal mine plans, as having an understanding of where former room and pillar mines are, as well as the levels of coal extraction – therefore an estimate on the proportion of rooms to stable strata. This is crucial in urban development, as building over an area of potential subsidence could have huge implications for damages should the structure of the subsurface not be understood. One such case of this is at the Bayfield Housing Estate in North Tyneside, where development proceeded with identification and recognition of former coal mine workings.

Bayfield – Location and Geology

Figure 55 - Map showing the location of the Bayfield Housing Estate, West Allotment, North Tyneside. Star to show the location of the exposed former room and pillar coal workings at Whitley Bay for reference. The inset map in the top right is of the UK, with the red circle showing the location of the zoomed in map.

In 2011, the Bayfield Housing Estate was built in West Allotment, North Tyneside (Figure 55). However, just four years post-construction in 2015, five of the houses in the development showed

signs of damage resulting from subsidence, leading to evacuation of families in June 2016 and permanent relocation in January 2017 – with each affected house being worth £130,000 - £150,000, there is a considerable financial cost to the impacts of the subsidence (Geoinvestigate, 15/5/2022). When any new development is proposed, a site check is done to see if the development is in an area of prior coal mining, and if so then The Coal Authority (CA) is in charge of detailed checks for the stability of the workings and subsurface. For the Bayfield Estate, much of the West Allotment falls in a zone defined by the CA as high-risk, therefore requiring a coal mining risk assessment (CMRA) required (ISURV, accessed 16/8/2023). The coal mining records showed that the area had extensive coal mining in the past, with Geoinvestigate finding that letters from historical land owners of 'Prospect Hill Farm' (the former name of the Bayfield Estate in the 1870s) claimed 'surface damage', the Victorian term for ground surface subsidence caused by mining (Geoinvestigate, 15/05/2022).

A 14 month-long investigation was carried out by the CA to determine whether there were any former coal workings below the Bayfield Estate, with six boreholes drilled in the area (see Figure 56). The drilling revealed that two of the boreholes drilled uncovered 'zones of no recovery', inferred to be possible former coal workings or voidspace, around 3 m in thickness. The former coal workings identified were determined to be over-extracted room-and-pillar workings, with extraction rates of over 70% compared to the usual 45-50% extraction rate for the area, resulting in narrow pillars and wide rooms (FutureClimateInfo, accessed 16/8/2023). As detailed in Table 3 (Chapter 1), narrower pillars are directly linked to decreased stability of subsurface room-and-pillar workings, leading to increased likelihood of subsidence issues as seen at the Bayfield Estate. The report written by ISURV, 2017, interpreted evidence of a historical sandstone quarry to the west of the Bayfield Estate, from a combination of different sources (including CA records), which also showed a possible entrance to the former coal workings – further supporting the evidence indicating former coal workings being located directly beneath the Bayfield Estate.

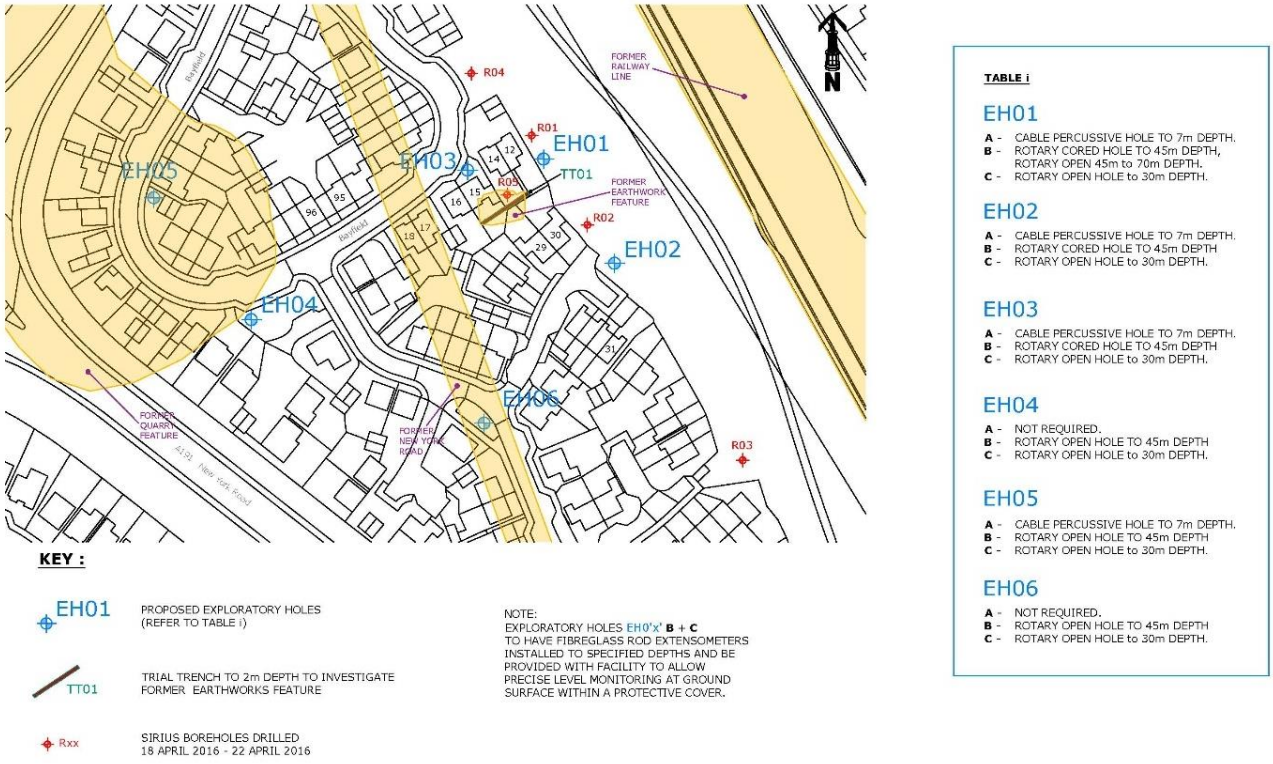

Figure 56 – Detailed map of the Bayfield Housing Estate, and where the 6 boreholes were drilled. Provided by Soil Engineering.

The Bayfield Estate is around 5-6 km inland from the exposed former coal workings at Whitley Bay, and the report by Soil Engineering (2017) found that the strata encountered in the borehole drilling consisted of Upper Carboniferous lithologies – mudstones, siltstones, sandstones, and thin bituminous coal seams. This makes the underlying geology of the Bayfield estate of comparable age to the strata encountered at Whitley Bay, supported by the constraints of marine marker bands and local records. The reports also found that the coal seam intercepted by some of the boreholes was the High Main coal seam, furthering the support that the stratigraphy is comparable to Whitley Bay (see Figure 57 for the location of the HMS within the stratigraphy).

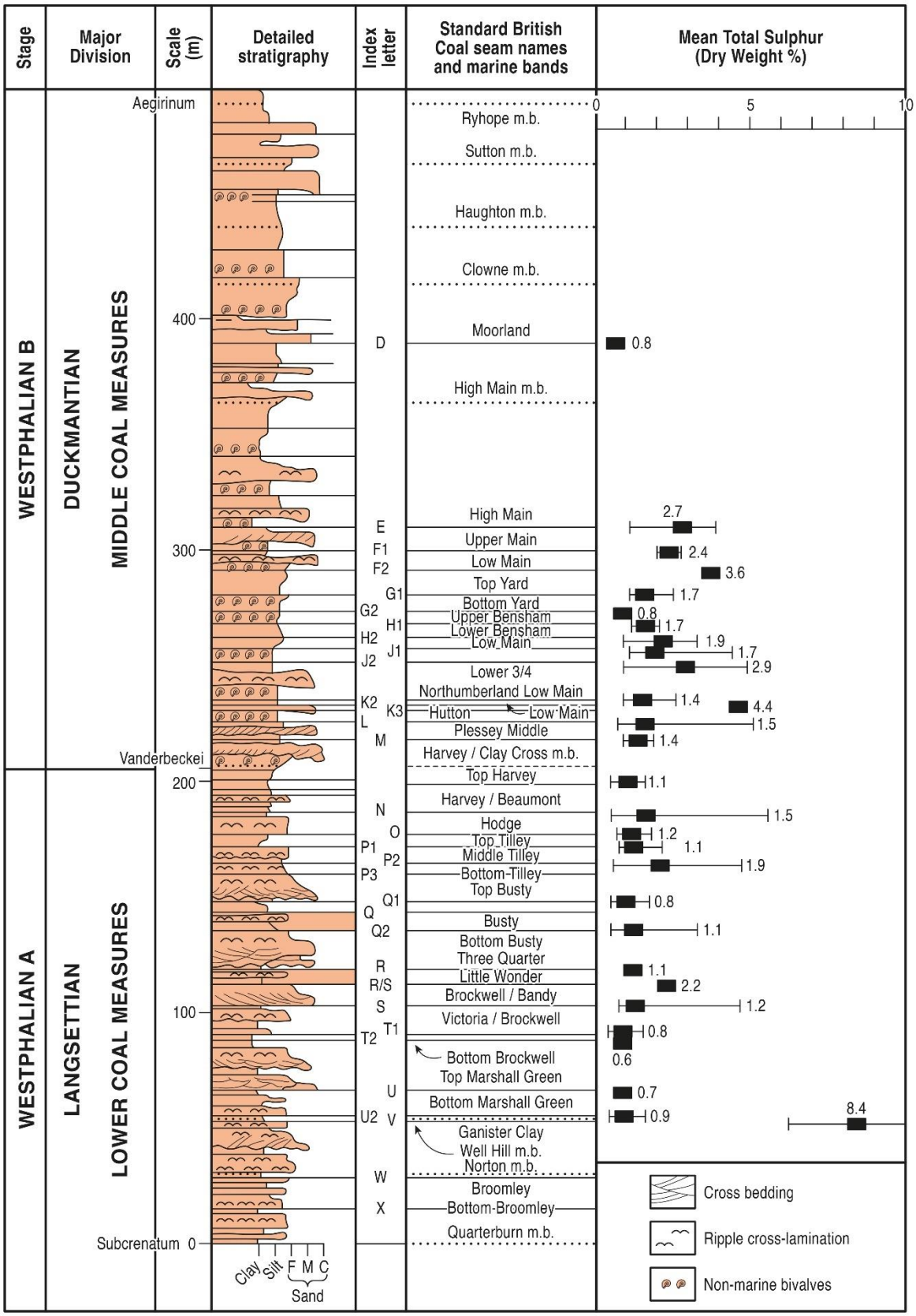

Figure 57 – Detailed stratigraphy of some of the coal seams present in the Northumberland coalfield. Redrawn from Turner and Richardson, 2004. The High Main coal seam can be seen at ~310 m.

3.2. Recognition and correlation of shallow coal mine workings

The investigation into the subsurface of the Bayfield Estate included the drilling of multiple boreholes, with several of the boreholes intercepting the HMS and two of them encountering former room-and-pillar workings, known by the drilling core having a section of voidspace – reflected as core loss in engineering logs of the boreholes. The samples retained from these boreholes were made available for this project, with the intention of correlating the strata between the boreholes. If the strata and the coal seam can be correlated across the Bayfield Estate boreholes, there are wider implications on what this means for regional stratigraphy. The wider region is known to have exploited the HMS, which was done through many shallow room and pillar mines. This has led to a large number of crownholes being able to be identified at surface level, as indicators of possible former workings in the subsurface. By using these indicators as locations for borehole investigations, a better understanding of the subsurface stratigraphy can be gained. Much like two of the boreholes in Bayfield, sections of voidspace within the borehole will likely be where coal has been extracted from mining. Collecting this data, as well as carrying out the techniques used in this study (i.e. ICPMS and Chemostratigraphy), allows for greater understanding of the regional stratigraphy.

Shallow coal mine geothermal projects operate by injecting and abstracting water from the former coal mines, where the rebounded groundwater levels have refilled the mines. This rebounded groundwater is what stores the heat from the subsurface, so abstracting the water through a heat conductor can generate usable energy before reinjecting the water back into the coal seam to be reheated. With the extent of coal seams spanning over the whole Northumberland Basin, it is important for geothermal projects using the coal seams to understand the stratigraphic location of the strata being used, and that the same coal seam is being used for the project in different locations – i.e. injecting/abstracting water from the same reservoir. As such, the techniques used in Chapter 2 for Whitley Bay can be applied to the data provided for the Bayfield Estate boreholes in order to

further test the methodology, and if so, will show how these techniques can be used in other locations.

Coal seams cannot be directly correlated using chemostratigraphic techniques (due to the high organic content of coal), however using the strata around the seams will indicate whether they are the same - i.e. if two coal seams have the same underlying strata, it can then be inferred that the coal seams themselves are the same seam, through the inference that chemically similar strata can be chemostratigraphically correlated. A different correlation method that is widely used is the use of marine bivalve bands, however an issue with solely using marine incursions is that they are not always far-reaching, and can be washed out or reworked – hence the usefulness of utilising chemostratigraphy. While it was possible at Whitley Bay to visually see the strata and follow them between the three sections, this is a particular case and not the normal scenario, as the majority of former coal mines will be in the subsurface where the seams cannot be seen. This is how the Bayfield Estate is an ideal dataset to test the techniques, as the former coal mine found is in the subsurface and cannot be seen, hence the requirement for correlation between the boreholes to determine whether the strata are linked.

By utilising the data available from the Bayfield investigation by the CA, the underlying stratigraphy can be characterised to gain a better understanding of the strata surrounding former room and pillar coal workings, as well as using chemostratigraphy to correlate across the estate.

3.3. Methods

All data collected from the boreholes as part of the Bayfield investigation was provided by the CA for this project (see Table 1), and used primary data collection for this research project.

Table 5 – Database of samples made available for this study, and the scope of relevant data available for each well drilled.

Well	Samples	Sample Type	Core Log	XRD Analysis	FTIR Analysis	ICP-MS and ICP-OES Analysis
Broomlea-1	36	Core	No	-	36	36
EH01	49	Core	Yes	1	49	48
EH02	58	Core	Yes	-	55	55
EH03B	62	Core	Yes	21	56	58
U15	43	Cuttings	No	13	43	39
(EH7B)	16	Core	No	-	11	-
(EH08)	8	Core	No	-	10	-

3.3.1. Sampling and Stratigraphic Logging

Samples taken from the borehole drilling carried out in the Bayfield Estate investigation were provided for the project, with three of the boreholes chosen for a focus – EH01, EH02, EH03B. This was because these three boreholes had the most complete set of data needed for comparison. For these three boreholes, a total of 169 samples were taken from the drilling cores (EH01 – 49; EH02 – 58; EH03B – 62; see Table 1). Through a combination of borehole samples and engineering logs, a stratigraphic log of each of the three boreholes was produced.

The boreholes revealed that the underlying geology of the Bayfield Estate consisted of the HMS incorporated into sandstones, siltstones, and mudstones typical of Upper Carboniferous strata. The HMS being the worked coal seam, placing the strata in the Westphalian B (see Figure 57) – a comparable age to the strata investigated at Whitley Bay.

3.3.2. Petrographic Analysis

To carry out petrographic analysis, two thin sections were cut from sandstone samples from the EH03B borehole, to estimate the porosity and mineral quantities of the samples. This was done via the same method outlined in Chapter 2, through the use of a Leica DM2500P microscope and PETROG software and stepping stage, with 300 point counts per thin section. They were taken from below the upper coal seam encountered in the boreholes, at depths of 24.8 m and 25.9 m. The thin sections were impregnated with blue dye in order to help identify pore space in the samples.

3.3.3. Permeability

The *TinyPerm II* hand-held permeameter from New England Research was used in order to measure the permeability of the samples. By pressing the rubber nozzle of the instrument against a flat surface on the sample, a seal was created. Pressing the syringe in removed air from through the sample, with a microcontroller unit monitoring the volume of the syringe and the transient vacuum pulse, recording a response function. The permeability of the sample can then be calculated using the given theoretical relation between the response function of the microcontroller unit and permeability. Measurements were taken 3 times per sample, and then averaged.

Much like when collecting permeability measurements for Whitley Bay in Chapter 2, the *TinyPerm II* could not withdraw air through the shales or the coal, so permeability measurements for these samples could not be collected.

3.3.4. XRD

XRD analysis was carried out on 21 of the borehole samples from EH03B, carried out by X-Ray Mineral Services by the following process.

The sample is disaggregated by using a pestle and mortar, before splitting 2 g of the sample to be micronized into an x-ray diffraction powder with a mean particle diameter of 5-10 microns. Each sample was analysed between 4.5^{o} and 75^{o} 2 theta, with a step size of 0.013 and nominal time per

step of 0.2 s and carried out using the x-ray radiation from a copper anode at 40 kV, 40 mA. The x-ray diffraction patterns of the sample are then compared with the 'International Centre for Diffraction Data PDF-4 Minerals' database, in order to determine which patterns match up with the known intensity for a pure sample of a material. By using 'Rietveld analysis', first published in 1967 (), the phases in the samples tested can be quantified (Post and Bish, 1989).

The XRD analysis also included the analysis of <2 micron clays within the samples, to quantify the proportion of each clay within a sample (i.e. illite+mica, kaolinite, chlorite). The <2 micron fraction of the sample is achieved through the use of ultrasound and centrifugation. By filtering the clay suspension through a Millipore glass microfibre filter and drying on filter paper, the clay XRD mount is obtained. This is then analysed as an untreated clay after overnight saturation with ethylene glycol vapour and heating at 380 ^{o}C for two hours, followed by further heating to 550^{o} C for one hour. The sample is then scanned between 3^{o} and 35^{o} 2 theta at a step size of 0.05^{o} per second, again with x-ray radiation from a copper anode at 40 kV, 40 mA. To define peaks from kaolinite and chlorite, the untreated sample is also analysed between 24-27^{o} 2 theta, with a step size of 0.02^{o} per second. The intensities of different peaks are measured and incorporated to be quantified with respect to the whole rock.

3.3.5. ICP-MS and ICP-OES

ICP analysis was carried out on the majority of the samples from the EH01 (48 out of 49), EH02 (55 out of 58) and EH03B (58 out of 62) boreholes, undertaken by X-Ray Mineral Services through the following methodology.

Following the samples being crushed into a fine powder via pestle and mortar, the samples were prepared for ICP analysis using lithium metaborate (alkali) fusion, the method promoted by Jarvis and Jarvis (1992), before being analysed by ICP-MS and ICP-OES equipment. ICP-MS and ICP-OES analysis obtains quantitative data for 48 different elements, split between 10 major elements (Al, SI,

Ti, Fe, Mn, Mg, Ca, Na, K, P), 24 trace elements (Ba, Be, Co, Cr, Cs, Cu, Ga, Hf, Mo, Nb, Ni, Pb, Rb, Sc, Sr, Ta, Tl, Th, U, V, W, Y, Zn, Zr), and 14 rare earth elements (REE) (La, Ce, Pr, Nd, Sm, Eu, Gd, Tb, Dy, Ho, Er, Tm, Yb, Lu). Through the use of replicate analyses of multiple preparations of certified rock standard reference materials (SRMs), the accuracy of the ICP data is considered to be within the error range achieved for multi-determinations of the same sample.

For the purpose of this study, several element ratios were chosen to be analysed in detail (K/Ta, Zr/Cr, Sc/Lu, K/Cs, Na (wt %)). As explained by Alex Finlay (*pers comms*), these elemental ratios are likely to demonstrate changes found in the mineralogy of the rock. Clays and feldspar-containing sandstones can be associated with showing trends in K, Ta, Cs and Na. Zr and Cr are likely to show variations of heavy minerals in the detrital fractions of samples, therefore showing changes in sediment origin (provenance). From Finlay *et al*, 2022, K commonly has a mineralogical control for clay minerals, interpreted as detrital input and depositional energy, while Zr is a control for heavy minerals interpreted as depositional energy and grain size, and Na controls Halite, being a designator for the salinity of the sample. The purpose of plotting the elemental ratios is to compare the data across the Bayfield site, as this will allow for comparisons in geochemical trends – similarities in the trends can be an indication of correlatable horizons.

3.4. Results

3.4.1. Logs

The graphic logs from each of the boreholes were produced through the use of engineering logs from the time of drilling and gamma-ray log signatures, combined with the borehole samples provided. All of the boreholes were topped by substantial amounts of top soil/boulder clay, and their locations can be seen in Figure 56. For the ease of comparison between the Bayfield boreholes and the Whitley Bay sections, the depths of the boreholes are from the base of the well, as opposed to depth from the surface.

All the boreholes selected for this study intercepted coal, with EH03B intercepting two at ~15 m and ~32 m above the base of the borehole. For EH01, there is a coal seam marked at 35 m from the base (Figure 59), and there is a section of voidspace below 10 m. This voidspace, or 'zone of no recovery', as mentioned in the introduction to this chapter, was interpreted by the drillers as part of former rom and pillar coal workings that were beneath the Bayfield Estate, specifically a room – where the coal had been extracted, therefore being an anthropogenic deposit. This voidspace was overlain by ~13 m of medium-grained sandstones (see Figure 58). The upper coal seam of the borehole, it is underlain by upward-fining sandstones, typical of being deposited from a fluvial delta plain. The same can be said for the strata underlying the voidspace, albeit consisting of very thin sandstone and mudstone. The lower coal seams in EH02 and EH03B are both underlain by mudstone, which is also to be expected from the background geology of the region and of the Upper Carboniferous, as explained in Chapter 2.

Figure 58 – Image of medium-grained sandstone from EH01, at ~17 m above the base of the borehole.

EH02 shows part of the standard lithology expected from the Upper Carboniferous, comprised of two thick, coarse-grained sandstone packages, with finer strata between them. This finer stratum is made up of a smaller, more fine sandstone package at around 20 m from the base of the borehole, and is overlain by interbedded mudstones and siltstones. This pattern is seen in all three of the boreholes, with <10 m of mudstone confined by two coarser sandstones in EH01, and EH03B also showing mudstones and siltstones confined by sandstone packages.

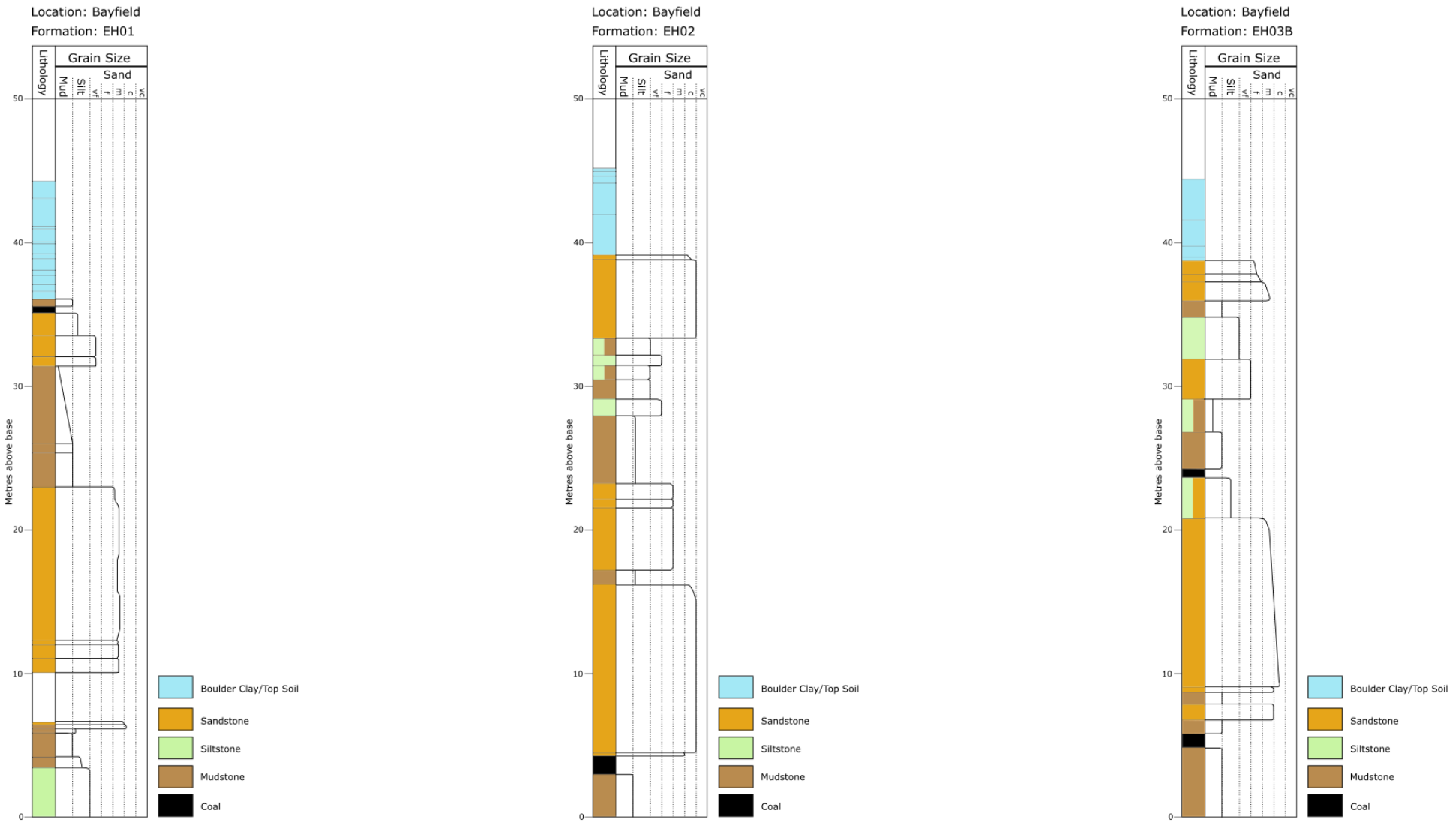

Figure 59 – Graphic logs of the three boreholes selected for this study – EH01, EH02, EH03B.

3.4.2. Petrography

As expected from an Upper Carboniferous sandstone, the two samples from 18.4 m and 19.5 m from the base of the EH03B borehole are both primarily comprised of quartz grains, with other subsidiary fractions of mica, feldspar and authigenic clays. Figure 60 shows that a large portion of the 18.4 m sample is porosity, around 33.7% (see Table 2). While this is a high proportion of the sample, there is no full pore 'network' as such, with the pore spaces visible seen to be disconnected from each other. The connection between pore spaces is partially inhibited from the presence of pore-filling, authigenic kaolinite, derived from the dissolution of feldspar minerals (see Figure 60). (c) and (d) from Figure 60 are from the 19.5 m sample, which has a lower porosity of 13.7% (see Table 1). This is visually evident, with only a few small pore spaces highlighted by the blue dye, and more kaolinite visible in Figure 60 which may have infilled the pore spaces. The 19.5 m samples also has a good example of how the thin sections also have mica present, as highlighted by the long, thin mica in Figure 60. Figure 61 shows how the two samples plot on a Folk classification diagram, both comprised of ~94% quartz and therefore classified as 'subarkosic sandstones'.

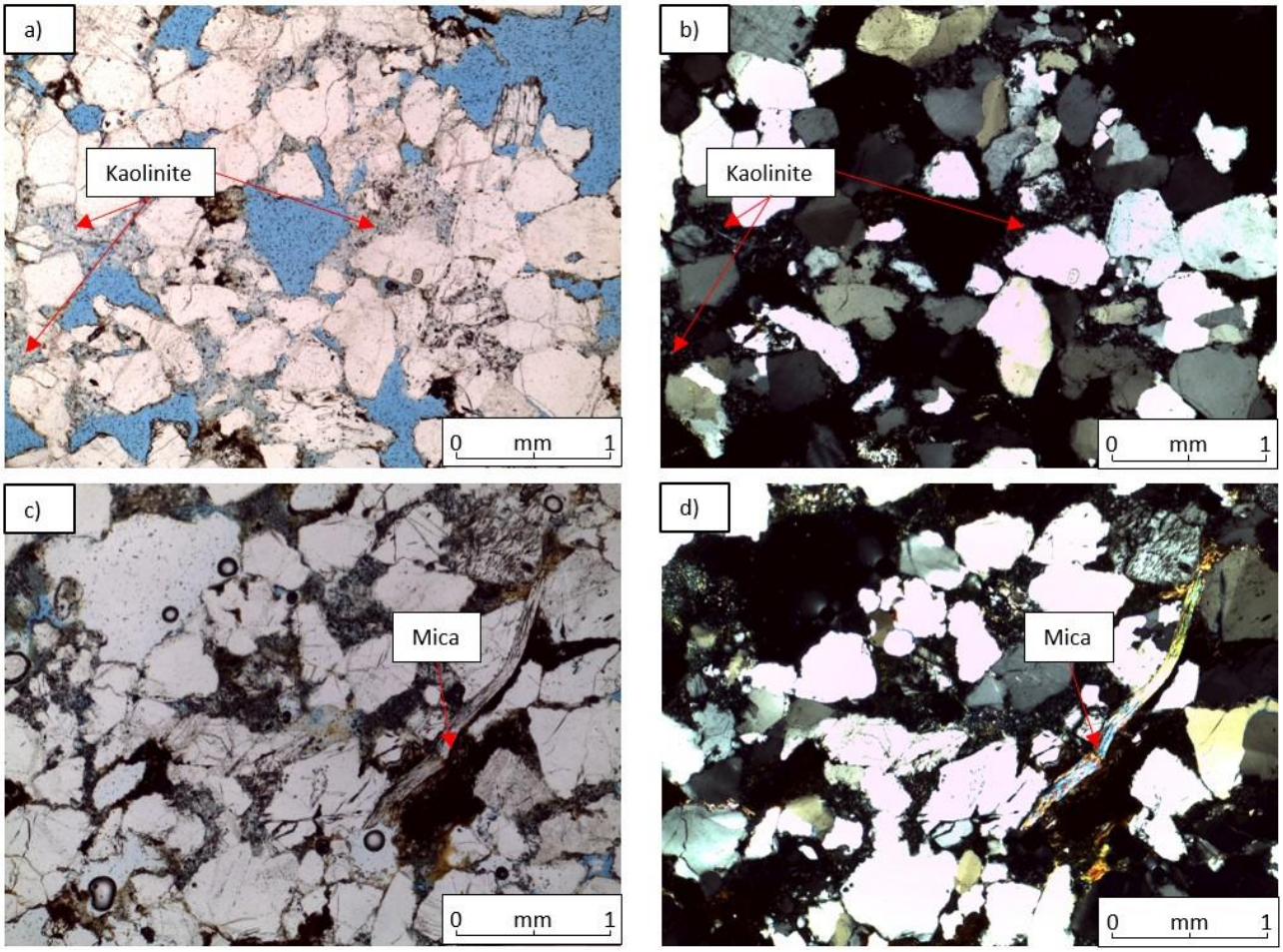

Figure 60 – Thin section micrographs of the sandstone samples from the EH03B borehole – (a) and (c) are in PPL, while (b) and (d) are in XPL. (a) and (b) are at 18.4 m above the base of the borehole, while (c) and (d) are at 19.5 m. (a) shows how there are large pore spaces, although they are disconnected from one another, as well as the presence of pore-filling authigenic kaolinite. Blue dye is used to highlight the porosity.

Table 6 – Petrographic point counts of two thin sections from the EH03B borehole.

Sample Height (m)	Detrital Mineralogy				Authigenic Clay		Porosity
	Monocrystalline Quartz	Polycrystalline Quartz	Plagioclase	Muscovite	Kaolinite	Illite	
19.5	44.3	22.7	2.7	1.0	8.7	7.0	13.7
18.4	41.7	13.7	2.0	1.0	4.7	3.3	33.7

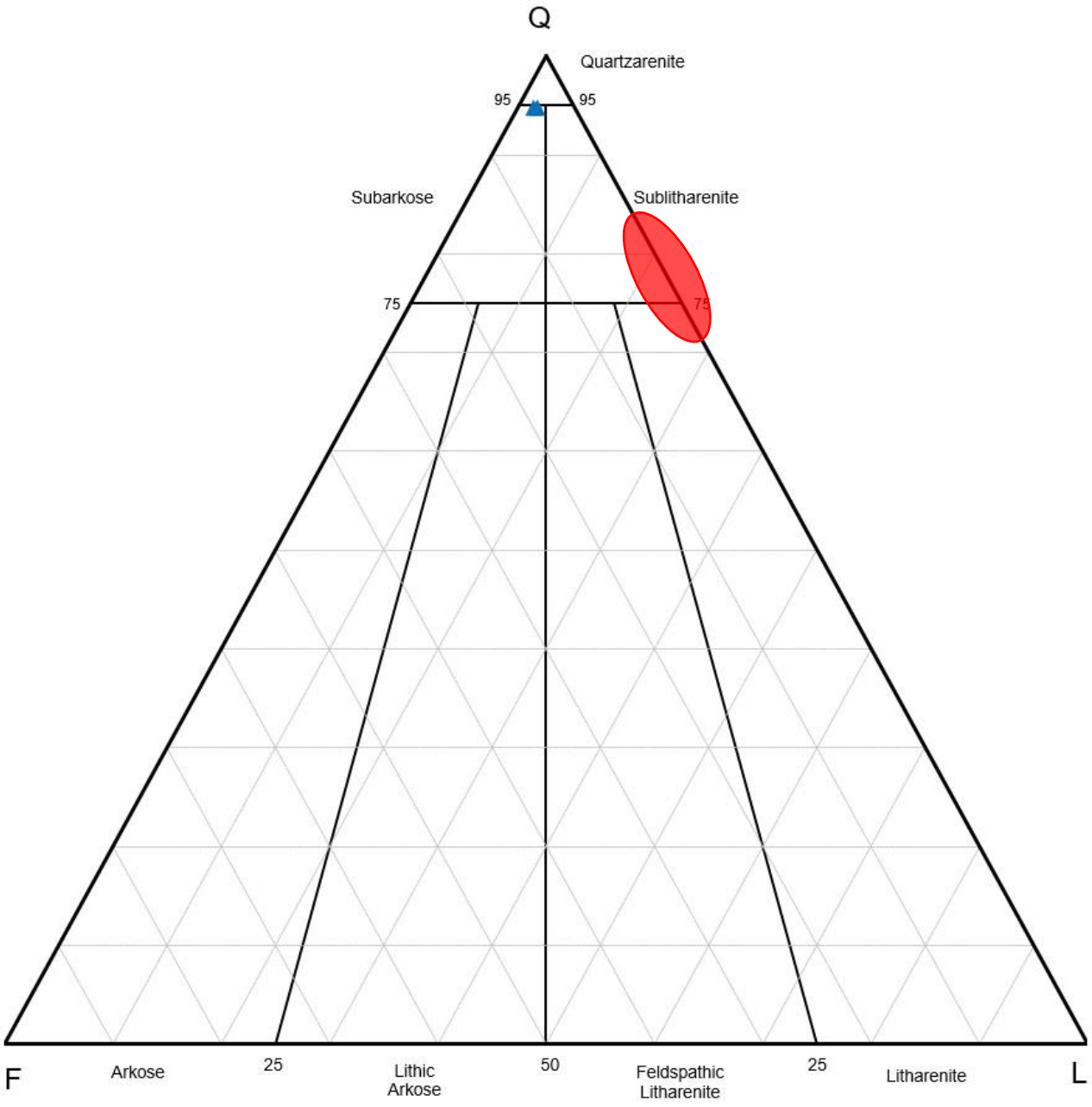

Figure 61 – QFL plot of the two sandstone samples from the EH03B borehole. They both plot very similarly, as subarkosic sandstones, with a high proportion of quartz minerals within the samples, and little feldspathic or lithic fractions. Red data cloud to show where the Whitley Bay sandstone samples plot for reference.

3.4.3. Permeability

There was a lot of difficulty when taking the permeability measurements from the borehole samples, as many of the samples were fragmented or did not possess a flat surface for the *TinyPerm II* to get a seal to record a measurement. As such, there are large portions of the boreholes that have no permeability data, such as the lower 20 m of EH01 being the most noticeable gap (see Figure 62).

This could also have been due to the depth of the strata, meaning that it was much tighter and did not possess enough permeability to be recorded by the *TinyPerm II*.

All three of the boreholes had a wide range of permeabilities, between 80-1800 mD. EH02 had the widest range of the three, ranging from 18 to 1831 mD. As seen in Figure 62, the higher permeability values for EH02 are seen in the thick sandstone layer at ~10 m from the base of the borehole, while the mudstones, siltstones and top sandstones are responsible for the majority of the lower values. Barring one high permeability value from the siltstone bed, recorded at 1202 mD at ~32 m, the rest of the values above 20 m range are all recorded at <600 mD. The lower sandstone is more permeable and also more varied, with a range of permeabilities recorded mainly over 400 mD.

For both EH01 and EH03B, the area between ~20 m and ~35 m contains mostly mudstone and siltstone, and the permeability is more varied than in the rest of the borehole (see Figure 62). EH01 has nearly all of the readings concentrated in this region of the borehole, while EH03B has a more overall assessment of permeability values through the borehole samples, with measurements taken over nearly the whole 45 m. Unlike the thick sandstone found in EH02 at ~10 m, the permeability for the corresponding sandstone in EH03B is less varied, being consistently low at around 30 mD.

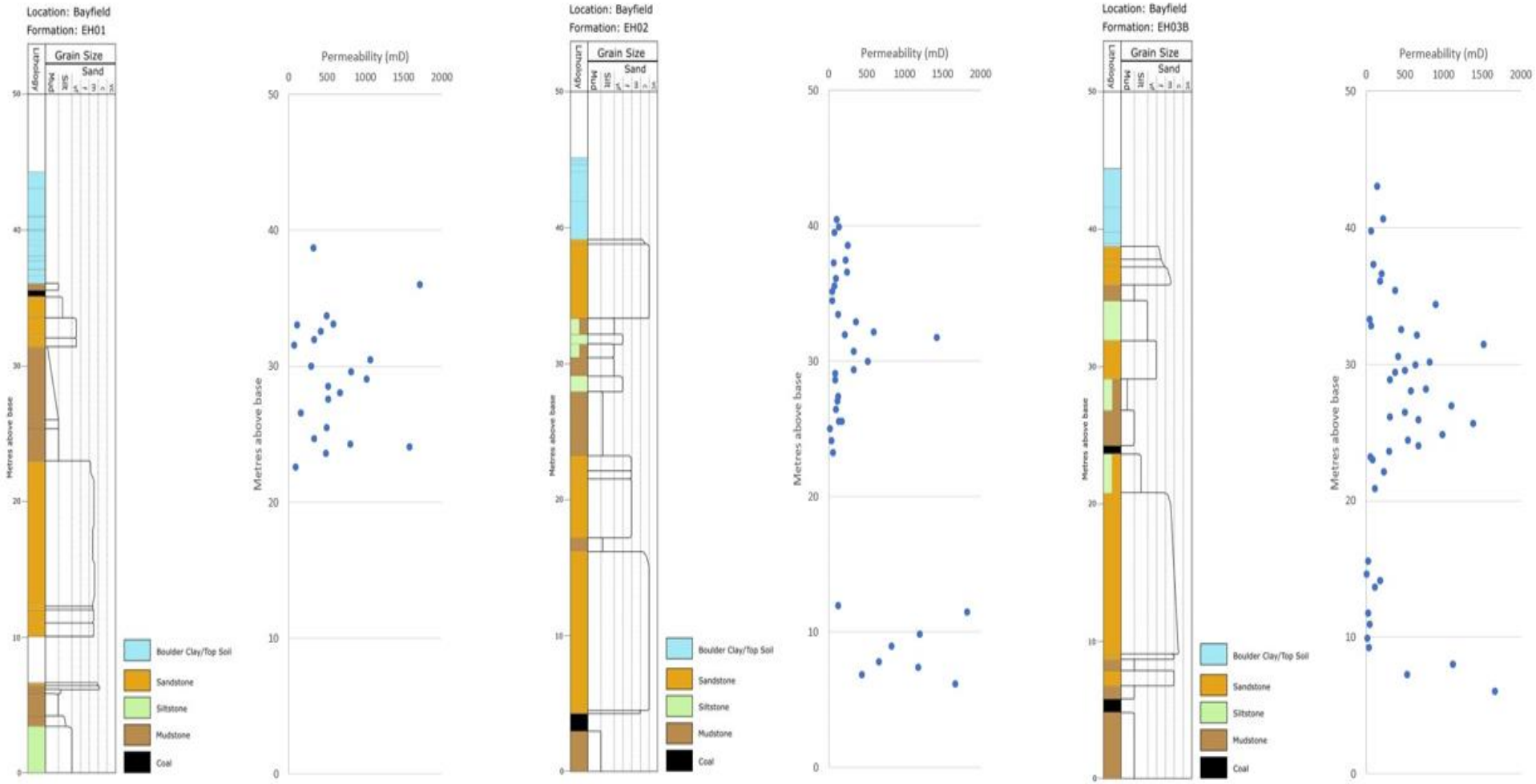

Figure 62 – Permeability measurements of samples from the EH01, EH02 and EH03B boreholes, alongside the graphic logs for each section.

3.4.4. XRD

Figure 63 shows the XRD data for the EH03B borehole alongside the graphic log, and it can be seen that the lower 20 m of the borehole is dominated by kaolinite, while the top portion has more illite+mica. There is very little chlorite throughout the whole borehole, and never exceeds 15% of the total crystalline clay content in the samples analysed. This is highlighted by the lack of chlorite in the thick sandstone that overlies the lower coal seam, where the clay content becomes dominated by kaolinite.

The clay content of the mudstone at the base of the borehole consists of mainly illite+mica, with only ~15% being kaolinite. This is also seen in the mudstones closer to the surface, especially the strata directly overlying the upper coal seam. The mudstones and siltstones located at 15-20 m above the base of the borehole are consistent with the base mudstone, with the clay content comprised of ~13% kaolinite. Again, the mudstones show a move towards the clay content being dominated by illite+mica, reaching a similar level to the base mudstone. The illite+mica peaks at making up 76% of the clay content at ~3 m above the base of the borehole, and again peaks at 75% at 25.8 m.

It can be seen that while the mudstones and siltstones are dominated by illite+mica, the kaolinite dominates the clay content of the sandstone beds within the EH03B borehole data. At ~20 m, the top of the thick sandstone bed (High Main Post), kaolinite makes up the entirety of the clay content within the samples, and the same can be said for the top sandstone at 38.3 m. This is also highlighted around 30 m, where the kaolinite proportion decreases for the sample at 35.1 m by over 50%, due to the sample being mudstone, before then increasing again to 61.7% at 31.6 m.

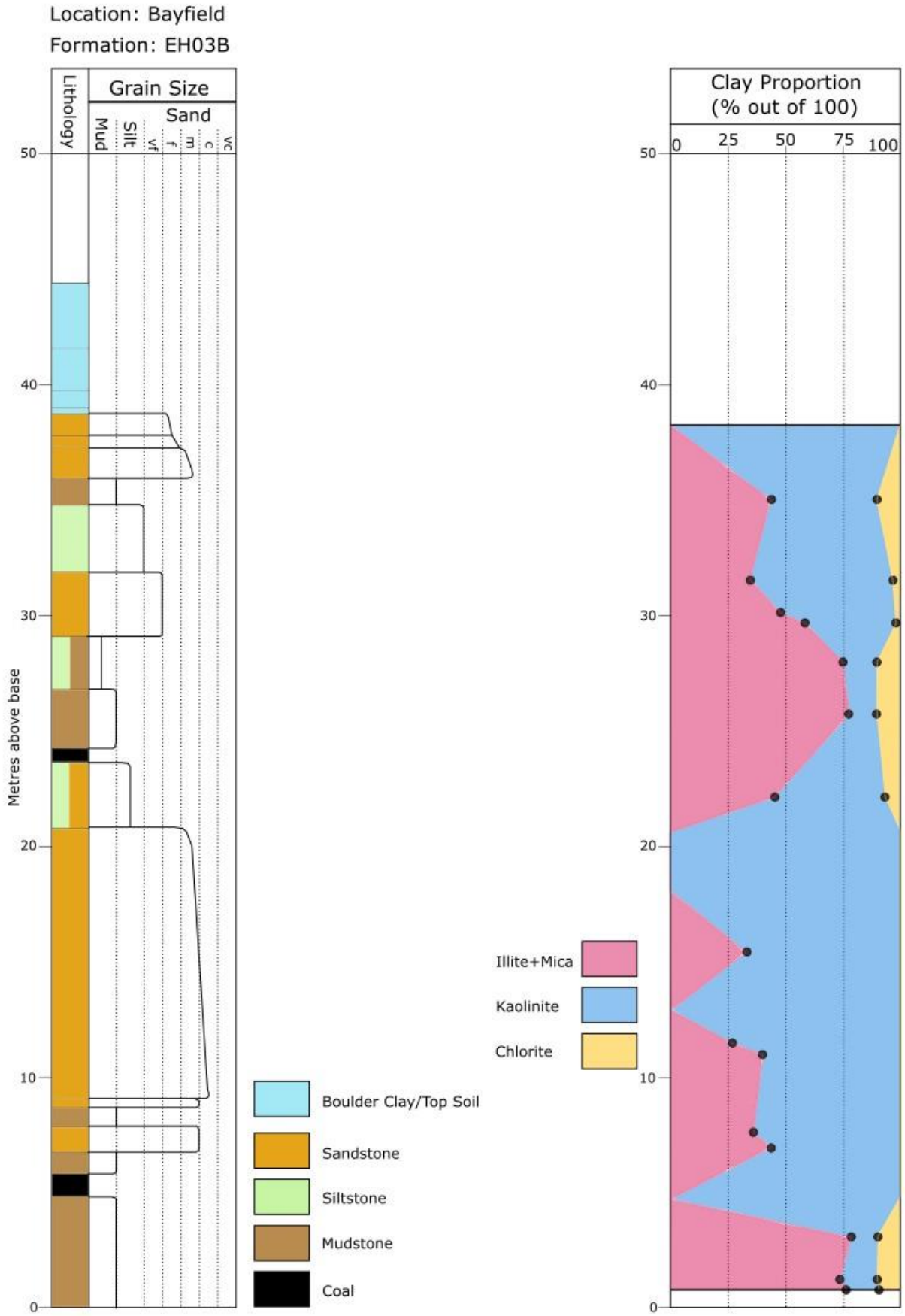

*Figure 63- Graphic log of **EH03B** borehole, alongside a proportional graph of clay content through the section from XRD analysis – does not include clay data from point counting. The black dots indicate changes between clay type.*

3.4.5. Chemostratigraphy (ICP-MS and ICP-OES)

Laying out the graphs of the selected elemental ratios - K/Ta, Zr/Cr, Sc/Lu, K/Cs, Na (wt%) – alongside the graphic logs of the boreholes means that it is easy to pick out certain trends that may be due to lithology (see Figure 64, Figure 65, and Figure 66, and see Figure 56 for the locations of each of the boreholes). Using geochemical analysis for chemostratigraphic correlation relies on looking at the trends of elemental ratios rather than the raw values. For example, all three boreholes show a similar pattern for the chemGR API, where the top portion of the borehole shows low values, before they all show a similar increase from around 20-25 m and below. This is very sudden in EH01 and EH03B, both recording large increases in the space of a metre, while this increase in EH02 is across ~12 m of sandstone stratigraphy. EH01 and EH02 both exhibit a slight spike in chemGR API just below 30 m, but this is more pronounced in the EH02 record. EH02 and EH03B both show a decrease in chemGR API towards the base of the boreholes, just above the lower coal seams, and is more pronounced in EH03B.

It can also be seen that the other elemental ratios show similar trends across all three boreholes, with the Na (wt%), K/Cs and Zr/Cr ratios showing this most prominently. For Na (wt%), it is generally below 0.5% across most of the samples, before showing an increase in the lower samples. The K/Cs trend across the boreholes shows that the portion containing the bulk of the mudstones and siltstones (around 30 m above the base of the borehole) is where the peak is found. The ratio decreases for the sandstone-dominated section of the boreholes below this, before recording an increase in EH02 and EH03B. The ratio of Zr/Cr fluctuates for the mudstone and siltstone-dominated section of all three of the boreholes, before showing a consistent drop at ~20 m, extending down for roughly 6 m. This section of consistently low Zr/Cr is recorded from the thick sandstone package in all of the boreholes.

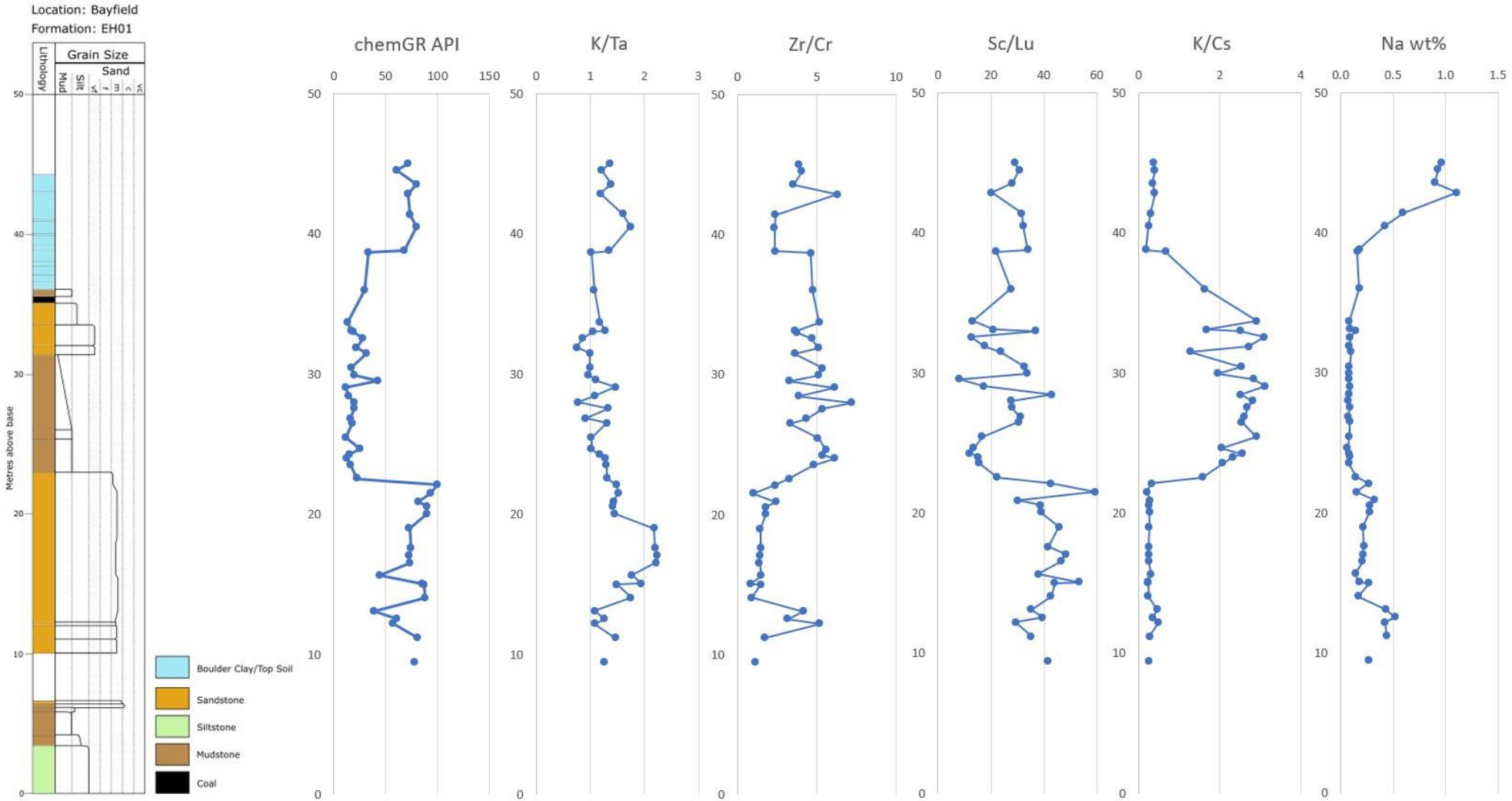

*Figure 64 - Graphic log for **EH01** borehole alongside selected ICP-MS and ICP-OES ratios. 'chemGR API' is the chemical ga mma radiation value in API units.*

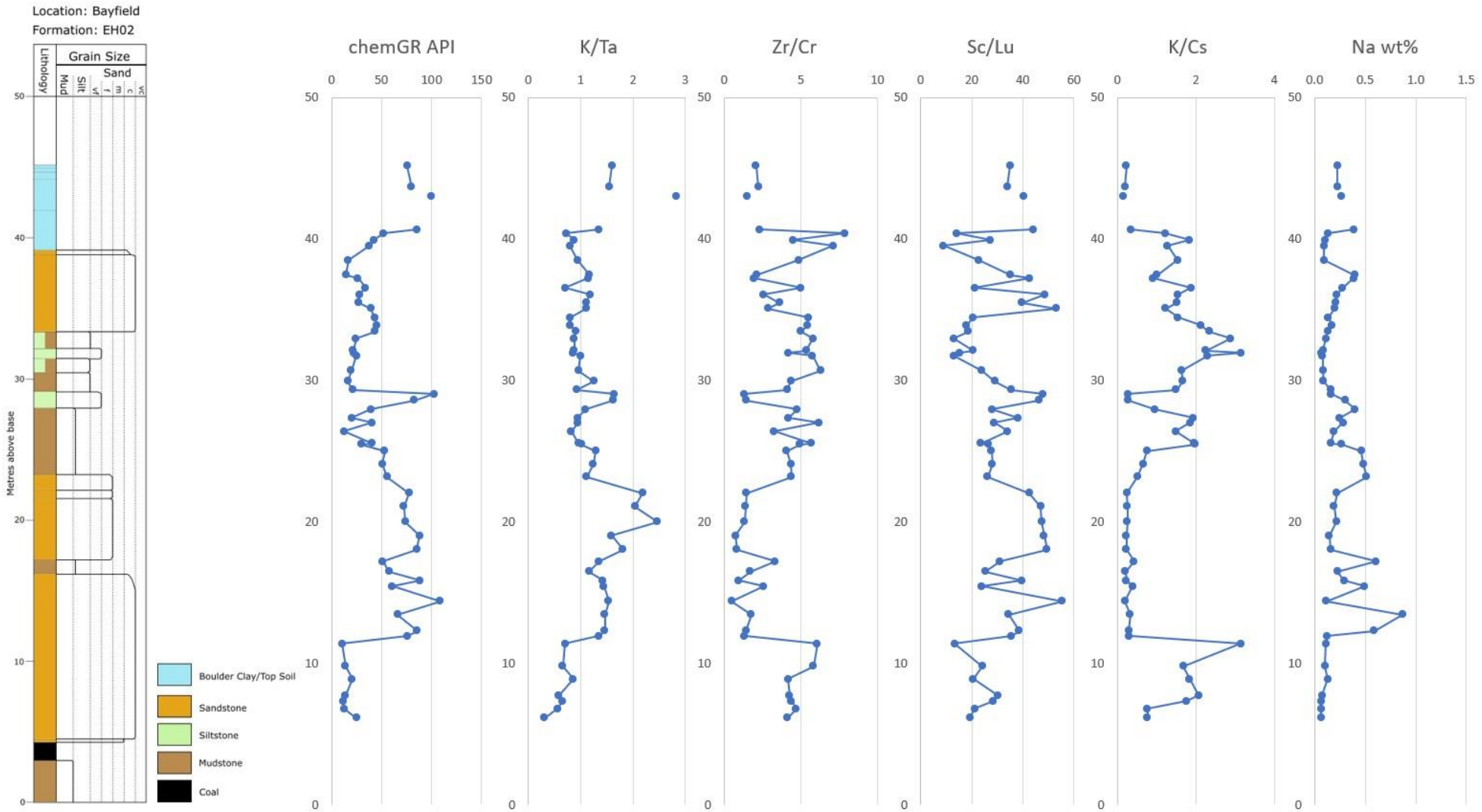

*Figure 65 - Graphic log for **EH02** borehole alongside selected ICP-MS and ICP-OES ratios. 'chemGR API' is the chemical ga mma radiation value in API units.*

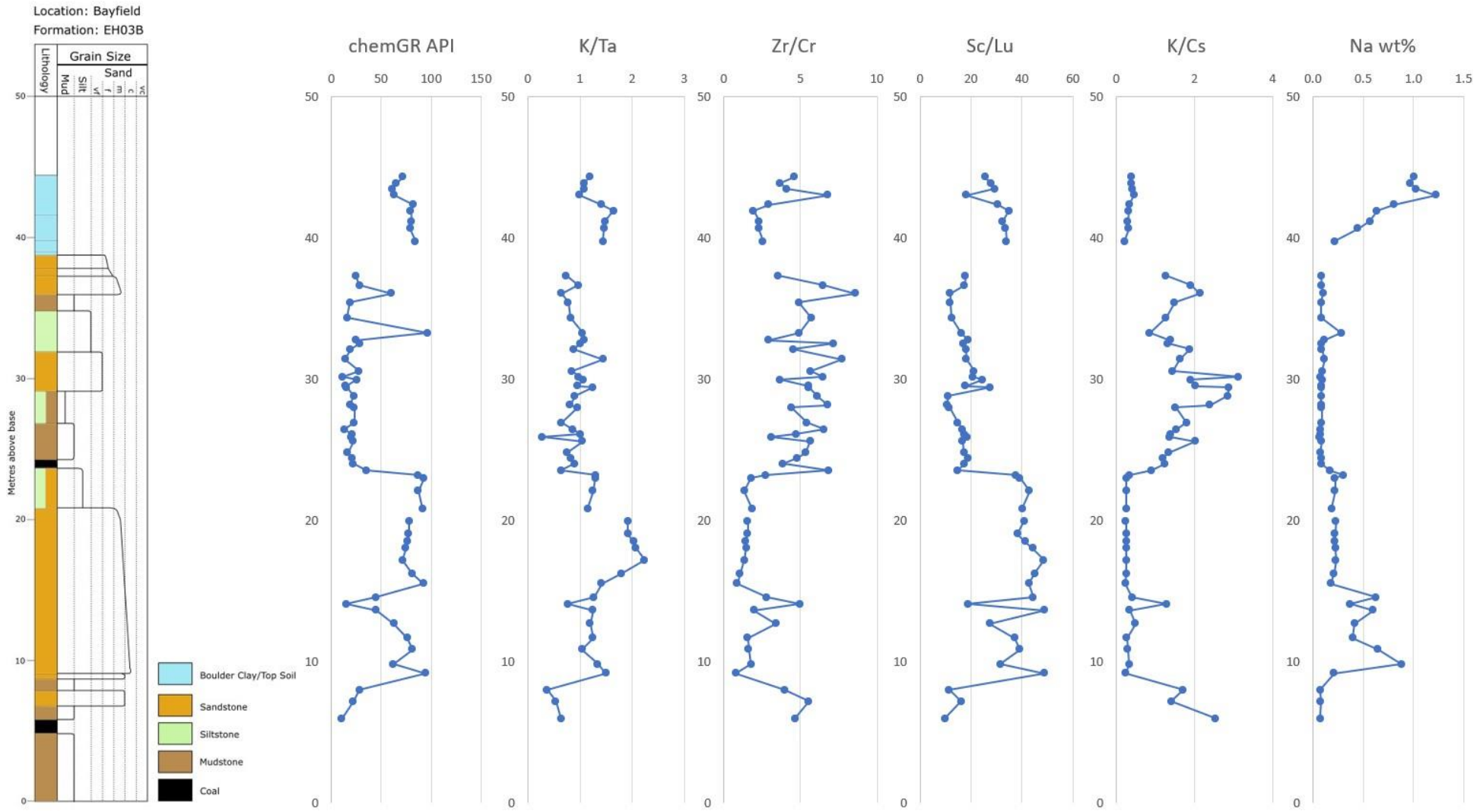

*Figure 66 - Graphic log for **EH03B** borehole alongside selected ICP-MS and ICP-OES ratios. 'chemGR API' is the chemical ga mma radiation value in API units.*

3.5. Discussion

The investigation undertaken by the CA and the geotechnical report that followed revealed that the geology underneath the Bayfield housing estate is that of a typical Upper Carboniferous sequence, and the stratigraphic logs produced for this project confirm this. They also confirm the major difference present at Bayfield compared to the rest of the Northumberland Basin, which is the thicker occurrence of the High Main Seam – up to 3.3 m compared to an average of ~2 m. Combining the report, which contains detailed descriptions of the lithologies encountered, with the samples provided by the CA allowed for the stratigraphic logs to be produced, showing that the geology consisted of upward-fining sandstones, mudrocks, and then a thin coal seam. This sequence can be seen twice in boreholes EH01 and EH03B, with the coal seam at ~24 m found in both, and the seam at ~6 m in EH03B at a similar height of the voidspace in EH01, which was interpreted by the CA report to be extracted coal from former mining operations.

Part of the goal of the project is to characterise the lithologies encountered, and testing the permeability of the borehole samples was part of this process. To briefly repeat, the *TinyPerm II* has a range that it can take measurements from, and the majority of the samples were within this range, however several samples could not produce a permeability reading, mainly some of the mudrock and the coal samples. As such, the recorded measurements have a bias towards the sandstones (see Figure 62). There is a lot of variability in the measurements, but are generally lower than would be expected, and this can be linked to the presence of kaolinite clays, which comprise a higher proportion of the sandstone makeup than expected.

Figure 60 shows how authigenic, pore-filling kaolinite is present in the samples from 18-19 m in the EH03B sandstone, and can be assumed that this continues through the whole bed (from ~9 m to ~21 m). Much like in Chapter 2 with the sandstone samples from the exposure at Whitley Bay, the sandstone is below a coal seam, which have been known to leach acidic fluids into the strata below.

Acidic conditions have been found to accelerate feldspar kaolinization, therefore strata below coal seams will tend to have higher proportions of kaolinite than might be expected. The two samples from the EH03B borehole contain ~5-9% kaolinite and only 2-3% feldspar, showing how this process has taken place in the sandstone (see Table 2). This is further supported by Figure 63, where the clay content in the strata below 20 m is mainly comprised of kaolinite clays, and this becomes apparent again in the sandstone beds at ~38 m as well.

3.5.1. Correlation of boreholes by chemostratigraphy

As covered in the Results section, there are several trends from the ICP-MS and ICP-OES data that is consistent across all three of the boreholes drilled at the Bayfield Estate. By linking trends across the boreholes, it can be determined that the geology found in each of them contain the same lithologies across the Bayfield Estate. Figure 67 shows the ICP-MS and ICP-OES data for EH01, EH02 and EH03B overlaid with each other, with trends consistent across all three boreholes highlighted by the pink line. Each of the boreholes contain slight variations, but generally there is a consistent trend that matches the others.

One of the easiest consistencies to pick out could be the decrease in Zr/Cr at around 24 m from the base of the boreholes, with all three showing the drop from ~5 to ~1.3. The Zr/Cr reflecting changes in the heavy mineral fraction of the samples, and therefore likely to show the provenance and origin of the samples. This means that it can be determined that the consistent drop in Zr/Cr across the boreholes reflects that the lithologies analysed in the three boreholes have the same sedimentary origin location, allowing for the conclusion that the samples are from the same strata, allowing for correlation across the Bayfield Estate.

The K/Cs trend is consistent with the occurrence of mudstone and siltstone in the boreholes, having low values between ~22 m and ~13 m – where all three boreholes are dominated by sandstone – and higher values above and below this range, where the strata mainly consists of mudstone and

siltstone. This could indicate an increase in the amount of clay in the samples, specifically kaolinite. Kaolinite is formed through the dissolution of K-feldspars, so increased K/Cs values could indicate higher levels of K-feldspar and/or kaolinite.

This would also show in the K/Ta values, where the level is fairly consistent for the top portion of the boreholes. There is a decrease in K/Ta from around 20 m and below, and this can be linked to the thin sections from EH03B that were analysed around this height. Between the two thin sections, at 19.5 m and 18.4 m, the amount of feldspar decreases by 0.7%, and the kaolinite content decreases by 4% (see Table 2). This decrease in the amount of potassium-baring minerals could be reasoned to be the cause of the decrease in K/Ta at this height, and can be seen by Figure 67 to be consistent across all three boreholes.

The Na (wt%) is also consistent across the three boreholes, staying low at around 0.1% from 40 m to ~15 m. EH01 and EH03B are more consistent than EH02, which shows slight variations, but they all show the same trend. They all show fluctuating increases at ~13 m, before decreasing back to the previous low value at 10 m. Again, the trend being consistent across the three boreholes implies that the lithologies are the same strata in all the boreholes, which allows for the conclusion that the strata can be correlated across the Bayfield Estate.

While the coal seams cannot be directly correlated, due to the high content of organic matter, the strata above and below them can. This implies that the coal seams are able to be correlated, meaning that the seams found in EH02 and EH03B are likely to be the same seam that was found to have been excavated in EH01, therefore all part of the same room and pillar workings that were found to be beneath the Bayfield Estate, supporting the claims in the CA report.

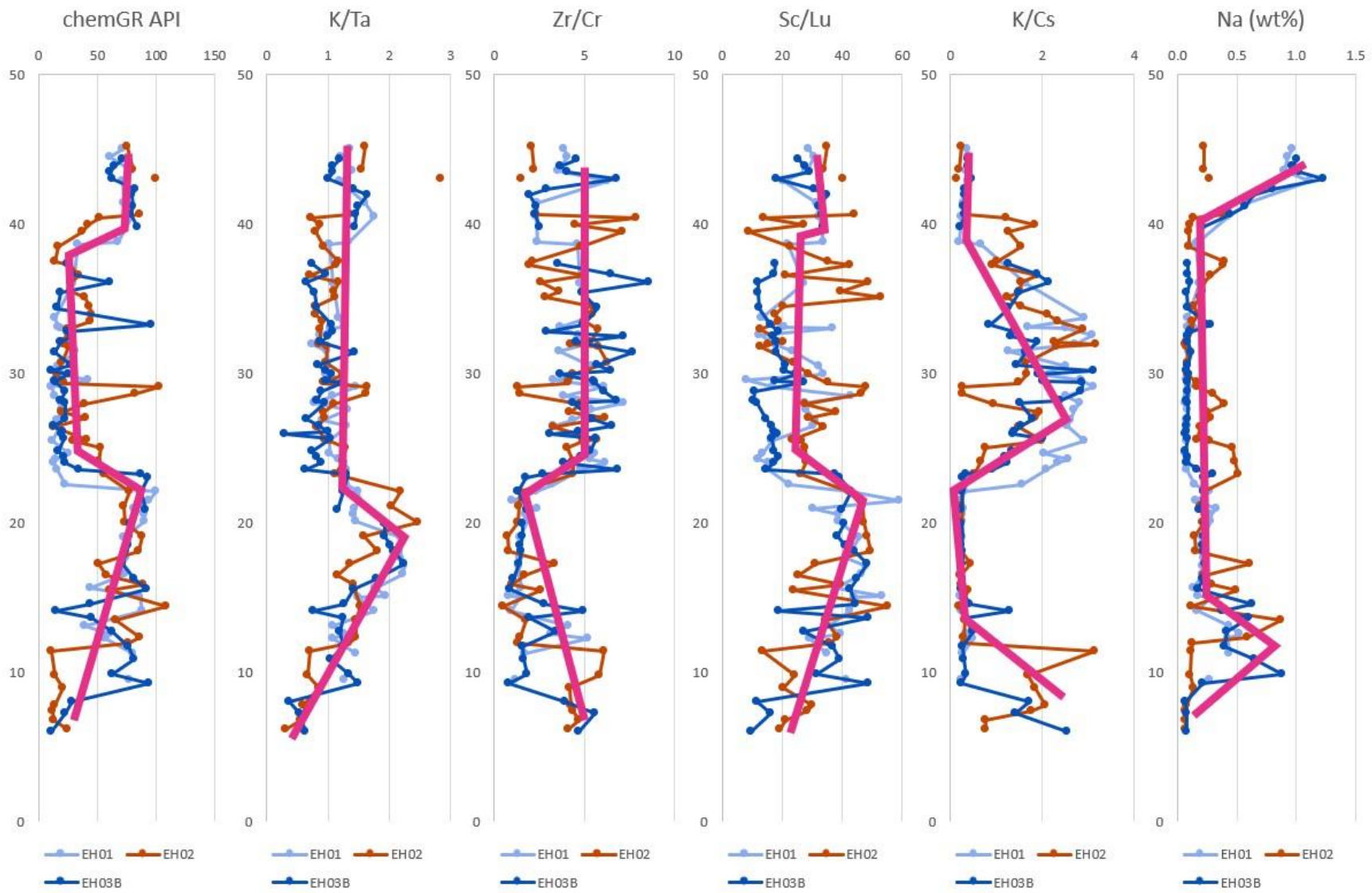

*Figure 67 – Selected elemental ratios for the **EH01**, **EH02** and **EH03B** boreholes at the Bayfield Estate. The data has been overlain to allow for easy viewing of trends that are consistent across the three sections, and have been highlighted by the pink line.*

3.6. Conclusions

The investigation into the boreholes drilled at the Bayfield housing estate by the CA concluded that the subsidence issues with the estate were due to overextraction in a former room and pillar coal mine in the subsurface, with two of the boreholes drilled finding voidspace where other boreholes retrieved coal. As part of this project, the geotechnical data and borehole samples were made available by the CA, allowing for the reapplication of the data in order to characterise the strata and geochemically correlate the boreholes across the estate, which in turn can confirm that the voidspace and coal seams in the different boreholes are connected. The following points are the key findings of this chapter:

- Identification of anthropogenic coal mine workings
    - All of the boreholes drilled as part of the subsidence investigation carried out by the CA intercepted coal, with two of them also intercepting 'zones of no recovery' – i.e. voidspace in the subsurface. This voidspace has been interpreted to be areas where a former room and pillar coal mine had removed parts of the coal seam.
- Comparison of coal-intercepting boreholes to allow for coal seam correlation
    - By applying chemostratigraphic techniques to the data collected as part of the CA investigation, this chapter has shown that boreholes EH01, EH02 and EH03B can be robustly correlated. By using various elemental ratios that are indicative of sediment provenance, the consistent trends across the boreholes show that the sediments are of the same origin, therefore correlatable through chemostratigraphic techniques – the most prominent of these being the trend changes from the interbedded siltstones and mudstones into the High Main Post sandstone.
- Application of chemostratigraphy around recognised coal mine workings

- Even with the voidspace present in EH03B, the geochemical data from the surrounding stratigraphy allows for chemostratigraphic correlation across the Bayfield site. While this shows the robustness of the chemostratigraphy techniques used in this chapter, it also displays how they can be applied to other locations and reutilise already-collected data. By using these techniques in other locations across the Northumberland Basin, a wider understanding of how the regional stratigraphy correlates can be achieved. In the context of shallow coal mine geothermal projects, this holds importance when setting the sites up, as an understanding of how different locations may interact with each other could be gained.

4. Discussions and Conclusions

4.1. Importance of shallow coal mine lithological characterisation and correlation

This study has focused on characterising the Carboniferous sedimentary strata from the Northumberland Coal Measures, building upon the basic understanding of the stratigraphic sequences (eg. see Turner and Richardson, 2004), but also to provide one of the first detailed physical characterisations of the coal measure lithologies and associated anthropogenic deposits. Detailed sedimentological logging and field and lab permeability testing has allowed for an in depth characterisation of the Upper Carboniferous sections, while using chemostratigraphy has allowed for the sedimentary successions at Whitley Bay and Bayfield study sites to be robustly correlated, identifying the potential to correlate coal measure stratigraphy over 10s of kilometres. This is important for identification of subsidence in former coal mined areas, but also offers potential to correlate permeable lithologies and coal seams for prospective coal mine geothermal projects.

4.2. Characterisation of the stratigraphy within Coal Measures

Whitley Bay is one of the few remaining sites in the UK to be able to observe former coal mine room and pillar workings in the field. It provides a unique opportunity to better understand anthropogenic deposits present in former mine workings. Using the Moscovian age sections at Whitley Bay, four different anthropogenic coal mine deposits were identified in this study – a roadway, a backfill section, a coal pillar, and a section of roof collapse. In addition, borehole investigation data at the Bayfield site reveal further anthropogenic coal deposits similar to Whitley Bay, but with significant voidspace found in EH01 confirmed to be a roadway section of the former room and pillar coal mine via down-hole CCTV and a borehole laser scan (Leigh Sharpe, *pers comms*). This research proposes the introduction of a new classification for different anthropogenic deposits commonly encountered

in former room and pillar coal mine workings (see Table 7 and Table 8, which are based on the data gathered as part of the investigation, and presented in this study).

Former room and pillar coal mine workings are host to highly heterogeneous anthropogenic deposits within the variable sedimentary succession of sandstones, mudstones, siltstones and coals. This heterogeneity presents many challenges , with a large difficulty in predictions based on current knowledge of the state of former shallow coal mine workings. While this work has been limited to two study sites, this classification and heterogeneity are likely to be widespread and can be applied to other shallow mine workings as well as deeper workings. This research has significant implications of the shallow mine geothermal sector and any future plans to commission new geothermal heat generation projects. It is obvious from this research , that even when voidspace is encountered, the variability of associated anthropogenic deposits and the stratigraphy of the Carboniferous cyclothem will have significant impacts upon whether flow can be maintained to commission an economic scheme, and therefore whether heat transfer within the system will take place.

Table 7 – Tabulated descriptions, diagrams and images of anthropogenic coal deposits encountered at Whitley Bay. While not investigated as part of this study, it should be acknowledged that longwall deposits would also fit as another category of anthropogenic coal deposits.

***In situ* coal**	**Coal Pillar**	**Roof Collapse**	**Backfill**	**Cleated coal**	**Roadway**
High Main Seam thickness of 1.8-2 m. ~3 m thickness at Bayfield. Very low permeability of $7x10^{-8}$ to $2x10^{-5}$ mD. (grey lines to indicate coal beds)	1.3 m in thickness at Whitley Bay. *In situ* coal with wider cleats due to increased overburden pressure. Slight slumping at pillar sides.	Large, unsorted coal clasts up to 2000 mm in diameter supported by clay matrix. Slight orientation in collapse direction. Average clast size of ~8 mm.	Smaller, regularly sized coal clasts up to 200 mm in diameter supported by clay/mud matrix. Used to increase roof stability. Average clast size of ~4 mm.	*In situ* coal with increased cleat widths due to increased pressure. Permeability of 2 - 24 mD (artificially induced cleating – Gao et al, 2021).	Underground voidspace of extracted coal. Often filled with rebounded groundwater in abandoned mine workings.
	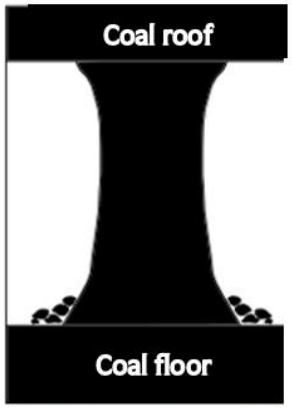	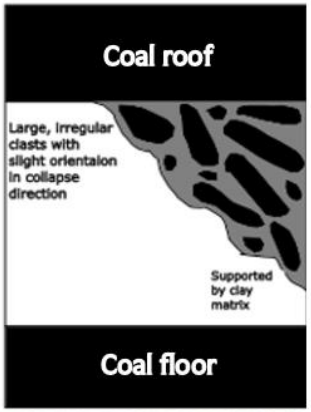	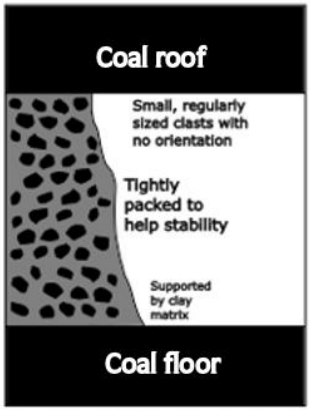	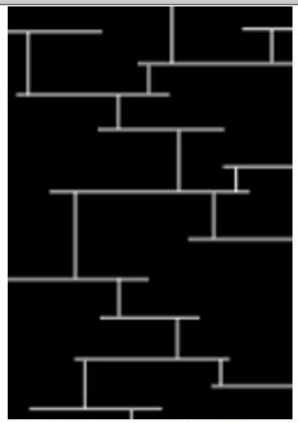	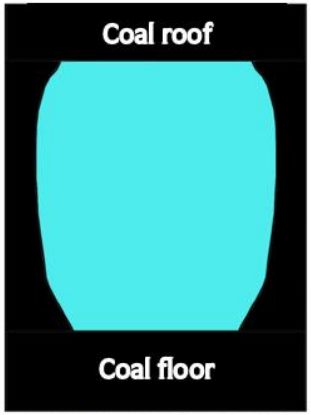
					

Table 8 – Tabulated characterisation of all lithologies encountered in this research. While incomplete, this table can provide a starting point for future discussions, as well as a framework for classifying the stratigraphy.

Lithology	Description	Permeability (mD)	Porosity (%)	Clay XRD	Grain Size	Additional Information
***In situ* coal**	High Main Seam. Average thickness across Northumberland Basin of 1.8 – 2 m, however there are local variations up to 3.4 m.	$7x10^{-8}$ – 9.51	0.6 – 9.1	100% kaolinite clay	-	Varying sulphur content across Northumberland Basin (see Figure 21). Evidence of pyrite cubes in SEM analysis.
Cleated coal	*In situ* coal with increased cleat width.	2 – 24 (from Gao et al, 2021)	-	*Can be expected to be similar to* in situ *coal*	-	-
Coal Pillar	*In situ* coal left by coal mining operations to increase roof stability.	*Can be expected to be similar to cleated coal, as increased overburden pressure leads to increased cleat widths.*	-	*Can be expected to be similar to* in situ *coal*	-	-
Backfill	Small coal clasts supported by a clay matrix, tightly packed by miners to support the mine roof.	*Can be expected to fall somewhere between* in situ *coal and cleated coal.*	-	>50% illite+mica, remainder consists of kaolinite, no chlorite	Average clast size ~4 mm Range up to 16 mm in diameter	Varying clay content may have an impact on permeability
Roof Collapse	Large coal clasts supported by a clay matrix, where the mine roof has collapsed due to instability.	*Can be expected to fall somewhere between* in situ *coal and cleated coal.*	-	*Can be expected to be a mix between Backfill and* In situ *coal*	Average clast size ~8 mm Range up to 200 mm in diameter – concentrated around 10-40	Varying clay content may have an impact on permeability

					mm for larger clasts	
Roadway	Voidspace within former coal mines left from extracted coal. Often filled with rebounded groundwater.	*Extremely high, due to open space filled with water.*	N/A – open voidspace	-	N/A – open voidspace	-
Mudstone	Extremely laminated mudstone, interbedded with the underlying siltstone.	*Can be expected to be more impermeable than both the sandstone and siltstone.*	3.7	<75% kaolinite, little-to-no chlorite, remainder consisting of illite+mica	0.00006 mm	-
Siltstone	Extremely laminated siltstone, interbedded with mudstone. Pore spaces dominated by infilling smectite-chlorite clay.	*Can be expected to be less than the High Main Post sandstone range.*	0.3	>50% kaolinite, equal amount of illite+mica and chlorite	0.0156 mm	Abundance of K-feldspar and plagioclase which could further degrade into kaolinite
Sandstone	Upwards fining sandstone, with several fluvial structures (eg. flaser beds, ripple markings). High concentrations of authigenic, pore-filling kaolinite.	100 - 375	2 – 2.7	~50% kaolinite but multiple occurrences of >50%, very little-to-no chlorite, remainer made up of illite+mica	0.5 mm	Lower porosity than may be expected due to high concentration of pore-filling kaolinite clay

The petrography investigations of the sandstone present in Whitley Bay and Bayfield found that they possess similar characteristics, being medium grained sandstones. The samples in both locations include considerably less feldspar than would be expected of Moscovian (formerly Westphalian B) sandstones. Due to the acidic leaching of mine water from the coal seam into the underlying strata, the feldspar minerals in the sandstones have undergone feldspar kaolinization, reducing the amount of feldspar in the samples, but also increasing the amount of kaolinite. With it being well documented that mine water leaching is highly acidic (eg. Turner and Richardson, 2004), this is a key characteristic of sandstones that underlie a coal seam, and is the case in both Whitley Bay and Bayfield. Additionally, the proportion of clay types is highly variable throughout the section (see Table 2), which may be due to this acidic leaching, and could possibly impact porosity and permeability.

The well-connected deltaic sandstone channels, with excellent permeabilities and porosities (see Table 8) could potentially enhance fluid flow, through increased flow pathways and better transmissivity. However, the well-connected sandstones could equally degrade coal mine workings through sandstone communication, with shallower or other stratigraphic levels introducing cooler waters. However, a complication with this is that the introduction of these cooler waters when starting fluid pumping may modify the hydrogeological flow of the system, creating a mix of natural and anthropogenic deposits within the system. Another potential complication of this may be mining-induced fracturing, which could have potentially significant implications for future projects, though this study has not directly investigated this. The detailed sedimentological approach to characterise the full sedimentary succession and anthropogenic coal mine deposits is an essential approach to classify and grade similar successions and deposits elsewhere and for shallow coal mine geothermal projects.

4.3. Importance of different lithologies for shallow geothermal prospecting

The heterogeneity of former room and pillar coal mine workings make it extremely difficult to appreciate and model fluid pathways through former shallow and deep coal mine workings. This study has investigated the complete Upper Carboniferous cyclothemic sequence of the coal measures in the Northumberland coalfield and identified how the interbedded sandstone lithologies (eg. High Main Post sandstone) could act as suitable targets for mine water heat extraction. This is due to their excellent porosity and permeability characteristics.

The negligible permeability of the coal sample tested (see Table 7) shows that *in situ* coal would make an extremely poor lithology to target individually, even before considering the different types of anthropogenic deposits from former mining operations. Shallow coal mine geothermal projects actually target the minewater-filled rooms, which will have extremely high fluid flow. However, as highlighted by this study, former mines are not solely minewater-filled rooms and *in situ* coal pillars, but instead host to a variety of anthropogenic deposits. This is one of the main issues when targeting the former workings, as it can be near-impossible to accurately predict whether anthropogenic deposits exist within the mine workings and in what forms they are in, which may be further compounded by unreliable and undetailed mine plans. Another factor to the unpredictability of the state of former room and pillar coal mine workings is that a very common way to increase roof stability was to use wooden support beams, which will have degraded at unknown speeds due to different factors – eg. moisture content, overburden pressure. This means that roof collapse can be present in a number of different states and places, adding to the heterogeneity of former coal mine workings.

Because of this, the underlying sandstones may act as a better target for shallow geothermal projects. This study has shown that they are much more permeable that the *in situ* coal, ranging between 100 – 400 mD (see Figure 3), meaning that they would be much more favourable for fluid flow. The sandstone is also very porous in comparison to coal, with Table 2 in Chapter 3 showing porosities of 13.7% and 33.7%, as well as being much more laterally extensive than a coal seam. Coal seams can display coal seam splits (eg. Fielding, 1984), with the different types of branching furthering the idea of the sandstone possibly being a better target for geothermal projects. Albeit much deeper than the strata investigated, over 3 km in depth, the Carboniferous strata of the Northumberland Trough has been found to have a geothermal gradient of 35°C km^{-1} (Gluyas et al, 2018). On top of the already-mentioned factors and characteristics that make the sandstones a potentially better geothermal target than, the geothermal gradient is much higher than could be reached through using shallow former coal mine workings.

Younger et al (2016) investigated the geothermal potential of the Fell Sandstone Formation beneath Newcastle, finding an estimated heat flow of 88 mW m^{-2} and a temperature of 73 °C at 1740 m, which is much hotter than could ever be reached by shallow coal mine geothermal projects in the region. Further adrift from the Northumberland Basin, Raine and Reay (2019) investigated geothermal reservoirs in Northern Ireland. While the Carboniferous sandstones present – namely the Lough Allen Basin and the Slieve Beagh Basin – recorded limited permeabilities of <1 mD, they could produce fluid flow to show that a potential geothermal reservoir exists. These studies further support the notion that the sandstone groups below the coal measures may be better targets for geothermal projects, with larger fluid reservoirs and less heterogeneity than former room and pillar coal mine workings.

4.4. Importance of Regional Stratigraphic Correlation

The previous chapters have touched on the lack of detailed records of coal mining activities from the past, with the subsidence issue at the Bayfield Housing Estate (Chapter 3) being one of many events that have caused property damage as a result of unclear mining records. In the case of Bayfield, there was a lack of detailed mapping of the coal mine in the subsurface, as well as the mining having a higher-than-expected excavation rate, with ~70% of the coal seam exploited as opposed to 30-40% that is the norm. The *Coal Mines Inspection Act 1850* brought in legislation requiring coal mine owners to produce detailed maps of their mines, with future acts increasing the amount of detailing required by such maps. However, this means that many coal mines that were active before 1850 are either unknown or have mining plans that lack the required accuracy when looking to develop structures on the surface.

This is where the importance of this research study is highlighted, as there is a gap in the literature for larger regional correlation of stratigraphy. By using the chemostratigraphic techniques outlined, a first look at how two locations can be robustly correlated via this method has been produced.

4.5. Correlation between Whitley Bay and Bayfield

As shown in Chapter 2, the strata in the three sections identified at Whitley Bay were visually correlatable across the ~107 m stretch of beach, and geochemical data was able to support the visual correlations of worked coal and corresponding stratigraphy. Figure 2 shows how the different elemental ratios show similar trends at various heights through the samples, which are indications of lithology changes. This showed that the technique was able to be used across small distances, which was then applied to the data collected from the Bayfield Housing Estate investigation by the CA. As part of their own investigation, in a geotechnical focus, they collected ICP-MS and ICP-OES data for a selection of the samples, which were able to be utilised for geochemical correlation between the three boreholes selected for this project. Much like the Whitley Bay sections, there

were ratio trends that were consistent between the three boreholes, indicating that the stratigraphy was consistent across the Bayfield Estate.

Wherein some of the elemental ratios have been selected to show the similarities in trends between the two locations, there are obvious robust correlations (see Figure 68). The chosen ratios – chemGR API, Zr/Cr, Sc/Lu, K/Cs – all show a trend in the ratios that can be picked out and highlighted from the overall dataset, and the trend is present in both locations. The chemGR API data shows a large trend change towards lower values at ~23 m at Bayfield and ~2.8 m at Whitley Bay, before moving towards higher values for both datasets. The second ratio chosen, Zr/Cr, shows a thinning of the stratigraphy between Bayfield and Whitley Bay, where the trend in an increasing ratio between ~21-35 m at Bayfield is shown over ~1 m at Whitley Bay. There is then a decreased spike before another increase in the values, which is found in both locations. The thinning effect is also seen in the K/Cs datasets, where the trend between ~21-30 m is found over a ~1 m stretch of stratigraphy at Whitley Bay. Much like the chemGR API trends, the Sc/Lu datasets show that the thinning effect is less prominent than in the Zr/Cr and K/Cs ratios, but is still present, with the second correlatable trend (increase in ratio value shaded in lime) found to be ~1 m at Whitley Bay, but around 8 m at Bayfield. It can also be seen that there is a thinning effect, where the correlatable portions of the sections in Whitley Bay are much thinner than in Bayfield. For example, the dark blue correlatable portion in the Zr/Cr graphs spans ~15 m of section at Bayfield, whereas it only covers ~1.5 m at Whitley Bay (see Figure 2). It must be noted that geochemical correlation is a tentative method, and cannot be used as an exact way to see if two samples are of the same origin, as many factors come into effect. For example, the Na (wt%) data shows no correlation between Bayfield and Whitley Bay, but this can be put down to a variety of reasons. The strata at Whitley Bay is exposed due to coastal erosion and weathering, and while there was an attempt to collect samples that would be unaffected by prolonged exposure to the air, sea spray and groundwater flow, these would all have an impact on the Na (wt%) values. This is one of the reasons why analysing the trends found in the geochemical

datasets is important, rather than the absolute ratio values. Another important point to consider is the scaling between the two locations, as the boreholes drilled at Bayfield extended ~50 m into the subsurface, while the datasets from Whitley Bay used the outcrop exposures, which were ~7 m in height, making any correlation between the two locations tentative. However, with this said, the consistency in the trend changes between Bayfield and Whitley Bay is enough to present the idea of both locations having the same stratigraphy, albeit a condensed sequence found at the Whitley Bay exposures. As mentioned in previous chapters, the coal seams present in Bayfield and Whitley Bay cannot be directly correlated together, as coal contains too much organic matter for the techniques used in this study. However, by correlating the strata surrounding the coal seam, it can be inferred that the seam at Whitley Bay is the same seam found to be present at Bayfield, namely the High Main coal seam.

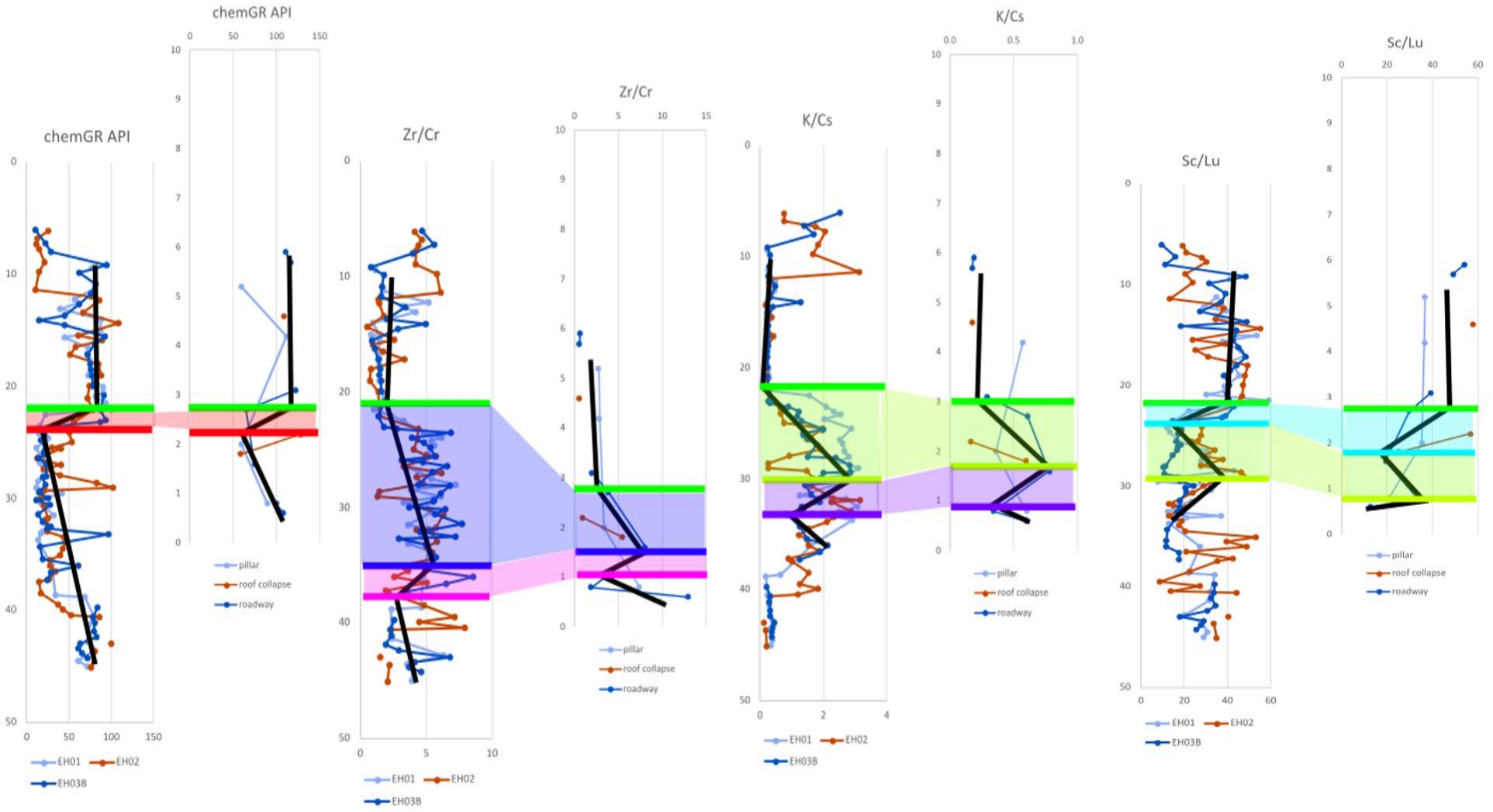

Figure 68 – Geochemical correlation between Bayfield Housing Estate (left datasets) and Whitley Bay (right datasets). The thick black lines highlight the overall element ratio trends, while the different colours are used to indicate different correlatable horizons within the stratigraphy. For the Whitley Bay dataset, the ~2 m horizon is the top of the sandstone, but refer back to Chapters 2 and 3 for more detail. The two locations are ~6 km apart, and the difference in scale between the two locations should be noted.

4.6. Wider Implications for Regional Stratigraphic Correlation

In Chapter 2, the three outcrops identified at Whitley Bay were geochemically correlated, with the distance between them covering ~107 m of the coastline. The boreholes drilled as part of the Bayfield Housing Estate investigation by the CA were all contained within the housing estate, and Chapter 3 correlated the strata found in each of them together, showing that the underlying geology of the whole estate was the same. By utilising chemostratigraphic techniques used in this research, the two locations can be correlated over the ~6 km distance, with potential for this technique to be viable for even larger distances. This also shows the potential applications to other shallow or deeper workings, as well as in other industries where widescale stratigraphic correlation is essential.

Increasing the understanding of regional stratigraphy as a whole can only be viewed as positive, especially for shallow coal mine geothermal projects, and this research has shown and proved that robust regional stratigraphic correlation is possible through the use of chemostratigraphic techniques.

4.7. Conclusions

- Detailed petrographic analysis and sedimentary logging of the exposed former room and pillar coal mine workings located at Whitley Bay, in order to give unique insight into coal mine strata. The strata is of Moscovian age (Upper Carboniferous), made up of fluvial deltaic facies – medium-grained, upward-fining sandstone, mudstone, siltstone and a bituminous coal.
- The sandstones are highly permeable (100 – 400 mD), with high kaolinite content and low feldspar content due to feldspar kaolinization from acidic mine water leaching from the overlying former coal mine. From lab testing of *in situ* coal, the permeability is extremely low ($7x10^{-8}$ – $2x10^{-5}$ mD) and negligible when compared to the High Main Post sandstone below. The implications are that the sandstones may provide a much more favourable fluid reservoir

target in certain scenarios when compared to the impermeable, heterogeneous former mine workings.

- The exposed former room and pillar coal mine at Whitley Bay is host to different anthropogenic coal deposits that were investigated – backfill, roof collapse, a coal pillar, and a roadway. The Bayfield investigation also hosted further anthropogenic coal mine deposits in the form of a roadway/room. The characterisation of the coal measure stratigraphy can act as a classification that can be applied elsewhere for shallow coal mine geothermal projects and anthropogenic coal mine deposits. This has been carried out to a level of detail unseen anywhere else, and as such provides a new form of classification framework for other localities, and a set of key findings from this study.
- The robust correlation of the two study sites shows that Chemostratigraphy is a valuable technique for regional stratigraphic correlation, which is essential for shallow coal mine geothermal projects. It also reveals how there are well-connected sandstones with excellent permeabilities and porosities beneath the High Main Seam, which offer a different geothermal reservoir to be explored. The implications of this is that the higher-permeability sandstones may be of greater significance in locations where longwall mining has been undertaken, although this would require further investigation.

4.8. Future Work

- To further understanding of regional stratigraphy across the Northumberland Basin, more sites should be investigated to test chemostratigraphic correlation to Whitley Bay and Bayfield. Even if they do not correlate to the sites in this study, it will still increase understanding of how the stratigraphy behaves across a wider area, and could potentially become a better way to understand regional stratigraphy as a whole.

- While this study has given valuable insight into the different anthropogenic coal deposits encountered at Whitley Bay, this is only one site, and the next steps of characterisation and classification of these deposits would be to investigate them at other sites, following the same framework methodology. This would add robustness to the differentiators put forward in this study, and reveal other types of anthropogenic deposit that may not be present at Whitley Bay.
- The heterogeneity of the former coal mine workings, with the addition of the highly permeable sandstones, makes them complex targets for geothermal projects. Following this, more focus should be put on these sandstones, as they may provide a more favourable target for such projects. However, it should be noted that this is not always the case, so should be considered per location. This may also bring in debate around regulatory scenarios, hence the requirement for further investigations.
- The robustness of the regional stratigraphic correlation across ~6 km of the Northumberland coalfield opens the door for other potential uses of the chemostratigraphic techniques used in this study. They have potential applications in deeper geothermal projects, where understanding and knowledge of how different lithologies interact is essential.

References

- Adams, C., Monaghan, A. and Gluyas, J., 2019. Mining for heat. *Geoscientist*, *29*(4), pp.10-15.
- Andrews, B.J., Cumberpatch, Z.A., Shipton, Z.K. and Lord, R., 2020. Collapse processes in abandoned pillar and stall coal mines: implications for shallow mine geothermal energy. *Geothermics*, *88*, p.101904.
- Banks, D., Athresh, A., Al-Habaibeh, A. and Burnside, N., 2019. Water from abandoned mines as a heat source: practical experiences of open-and closed-loop strategies, United Kingdom. *Sustainable Water Resources Management*, *5*, pp.29-50.
- Banks, D., Athresh, A., Al-Habaibeh, A., and Burnside, N. (2019). Water from Abandoned Mines as a Heat Source: Practical Experiences of Open- and Closed-Loop Strategies, United Kingdom. *Sustain. Water Resour. Manag.* 5 (1), 29–50. doi:10.1007/s40899-017-0094-7
- Banks, D., Fraga Pumar, A., and Watson, I. (2009). The Operational Performance of Scottish Minewater-Based Ground Source Heat Pump Systems. *Q. J. Eng. Geology. Hydrogeology* 42 (3), 347–357. doi:10.1144/1470-9236/08-081
- Banks, D., Younger, P.L., Arnesen, R.T., Iversen, E.R. and Banks, S.B., 1997. Mine-water chemistry: the good, the bad and the ugly. *Environmental Geology*, *32*, pp.157-174.
- Besly, B.M., 1988. Palaeogeographic implications of late Westphalian to early Permian redbeds, central England. In: Besly, B.M., Kelling, G. (Eds.), Sedimentation in a Synorogenic Basin Complex: The Upper Carboniferous of Northwest Europe. Blackie and Sons, Glasgow, pp. 200–221.
- Bibler, C.J., Marshall, J.S. and Pilcher, R.C., 1998. Status of worldwide coal mine methane emissions and use. *International Journal of Coal Geology*, *35*(1-4), pp.283-310.

- Bullock, L.A., Parnell, J., Perez, M., Armstrong, J.G., Feldmann, J. and Boyce, A.J., 2018. High selenium in the carboniferous coal measures of Northumberland, North East England. *International Journal of Coal Geology*, *195*, pp.61-74.
- Burnside, N. M., Banks, D., and Boyce, A. J. (2016a). Sustainability of Thermal Energy Production at the Flooded Mine Workings of the Former Caphouse Colliery, Yorkshire, United Kingdom. *Int. J. Coal Geol.* 164, 85–91. doi:10.1016/j.coal.2016.03.006
- Clark, G. and Jacks, D., 2007. Coal and the industrial revolution, 1700–1869. *European review of economic history*, *11*(1), pp.39-72.
- Cooper, A.H., Brown, T.J., Price, S.J., Ford, J.R. and Waters, C.N., 2018. Humans are the most significant global geomorphological driving force of the 21st century. *The Anthropocene Review*, *5*(3), pp.222-229.
- Daunton, M.J., 1981. Down the pit: work in the Great Northern and South Wales coalfields, 1870-1914. *The Economic History Review*, *34*(4), pp.578-597.
- De Paola, N., Holdsworth, R.E. and McCaffrey, K.J.W., 2005. The influence of lithology and pre-existing structures on reservoir-scale faulting patterns in transtensional rift zones. *Journal of the Geological Society*, *162*(3), pp.471-480.
- Dempsey, E.D., Holdsworth, R.E., Selby, D., Bird, A., Young, B. and Le Cornu, C., 2021. A revised age, structural model and origin for the North Pennine Orefield in the Alston Block, northern England: intrusion (Whin Sill)-related base metal (Cu–Pb–Zn–F) mineralization. *Journal of the Geological Society*, *178*(4).
- Donnelly, L., 2020. Chapter 11 Coal mining subsidence in the UK. *Geological Society, London, Engineering Geology Special Publications*, *29*(1), pp.291-309.
- Durham Mining Museum, 2017. Early Coal Mining History, http://www.dmm.org.uk/pitwork/html/history1.htm, accessed 22/08/2023.

- Durham Mining Museum, 2022. Opencast Coal, http://www.d mm.org.uk/history/ocast00.htm, accessed 23/08/2023.
- Durham Record Office, Coal mining and Durham collieries. https://durhamrecordoffice.org.uk/our-records/coal-mining-and-durham-collieries/, accessed 22/10/2023.
- East Ayrshire Council Planning Co mmittee, 2020. Revised Restoration Plan – House of Water Opencast Coal Mine – New Cumnock, https://docs.east-ayrshire.gov.uk/crpad mmin/2012%20AGENDAS/PLANNING%20CO MMITTEE/12%20JUNE%202020/Revised%20Restoration%20Plan%20-%20House%20of%20Water%20Opencast%20Coal%20Mine%20-%20New%20Cumnock.pdf, accessed 23/08/2023.
- Edmonds, C., 2018. Five decades of settlement and subsidence. *Quarterly Journal of Engineering Geology and Hydrogeology*, *51*(4), pp.403-416.
- Fender, T.D., Rouainia, M., Van Der Land, C., Jones, M., Mastalerz, M., Hennissen, J.A., Graham, S.P. and Wagner, T., 2020. Geomechanical properties of coal macerals; measurements applicable to modelling swelling of coal seams during CO2 sequestration. *International Journal of Coal Geology*, *228*, p.103528.
- Fielding, C.R., 1984. A coal depositional model for the Durham Coal Measures of NE England. *Journal of the Geological Society*, *141*(5), pp.919-931.
- Fielding, C.R., 1984. A coal depositional model for the Durham Coal Measures of North East England. Journal of the Geological Society of London 141, 917–931.
- Flint, S., Aitken, J. and Hampson, G., 1995. Application of sequence stratigraphy to coal-bearing coastal plain successions: implications for the UK Coal Measures. *Geological Society, London, Special Publications*, *82*(1), pp.1-16.

- Flores, R.M., 1998. Coalbed methane: from hazard to resource. *International journal of coal geology*, *35*(1-4), pp.3-26.
- Ford, J.R., Price, S.J., Cooper, A.H. and Waters, C.N., 2014. An assessment of lithostratigraphy for anthropogenic deposits. London: The Geological Society of London.
- Fraser-Harris, A., McDermott, C.I., Receveur, M., Mouli-Castillo, J., Todd, F., Cartwright-Taylor, A., Gunning, A. and Parsons, M., 2022. The Geobattery Concept: A geothermal circular heat network for the sustainable development of near surface low enthalpy geothermal energy to decarbonise heating. *Earth Science, Systems and Society*, p.3.
- FutureClimateInfo, Newcastle: New Build Property demolished after Coal Mine Discovery, https://futureclimateinfo.com/case-studies/newcastle-new-build-property-demolished-after-coal-mine-discovery/, accessed 15/10/2023.
- Gao, Q., Liu, J., Huang, Y., Li, W., Shi, R., Leong, Y.K. and Elsworth, D., 2022. A critical review of coal permeability models. *Fuel*, *326*, p.125124.
- Gee, D., Bateson, L., Sowter, A., Grebby, S., Novellino, A., Cigna, F., Marsh, S., Banton, C. and Wyatt, L., 2017. Ground motion in areas of abandoned mining: Application of the intermittent SBAS (ISBAS) to the Northumberland and Durham Coalfield, UK. *Geosciences*, *7*(3), p.85.
- Geoinvestigate, 2022. Draft West Allotment Bellway Homes, https://geoinvestigate.co.uk/2022/05/15/draft-west-allotment-bellway-homes/, accessed 20/01/2024.
- Gibbard, P., Walker, M., Bauer, A., Edgeworth, M., Edwards, L., Ellis, E., Finney, S., Gill, J.L., Maslin, M., Merritts, D. and Ruddiman, W., 2022. The Anthropocene as an Event, not an Epoch. *Journal of Quaternary Science*, *37*(3), pp.395-399.
- Gluyas, J.G., Adams, C.A. and Wilson, I.A.G., 2020. The theoretical potential for large-scale underground thermal energy storage (UTES) within the UK. *Energy Reports*, *6*, pp.229-237.

- Gluyas, J.G., Adams, C.A., Busby, J.P., Craig, J., Hirst, C., Manning, D.A.C., McCay, A., Narayan, N.S., Robinson, H.L., Watson, S.M. and Westaway, R., 2018. Keeping warm: A review of deep geothermal potential of the UK. *Proceedings of the Institution of Mechanical Engineers, Part A: Journal of Power and Energy*, *232*(1), pp.115-126.
- Ham, Y. and Kantzas, A., 2008, June. Development of coalbed methane in Australia: unique approaches and tools. In *SPE Unconventional Resources Conference/Gas Technology Symposium* (pp. SPE-114992). SPE.
- International Co mmission on Stratigraphy, 2023. International Chronostratigraphic Chart, https://stratigraphy.org/chart#latest-version, accessed 15/03/2024.
- ISURV, 2017. Subsidence and old mine workings: underground dangers, https://www.isurv.com/info/390/features_archive/11463/subsidence_and_old_mine_workings_underground_dangers, accessed 15/10/2023.
- Johnson, G.A.L., 1980. Dinantian stratigraphy. In: Robson, D.A. (Ed.), The Geology of Northeast England. Natural History Society of Northumbria, Newcastle upon Tyne, pp. 11 – 22. Special Publication.
- Karacan, C.Ö., Ruiz, F.A., Cotè, M. and Phipps, S., 2011. Coal mine methane: a review of capture and utilization practices with benefits to mining safety and to greenhouse gas reduction. *International journal of coal geology*, *86*(2-3), pp.121-156.
- Lau, H.C., Li, H. and Huang, S., 2017. Challenges and opportunities of coalbed methane development in China. *Energy & Fuels*, *31*(5), pp.4588-4602.
- Lawrence, S., Davies, P., Hil, G., Rutherfurd, I., Grove, J., Turnbull, J., Silvester, E., Colombi, F. and Macklin, M., 2023. Characterising mine wastes as archaeological landscapes. *Geoarchaeology*.

- Leeder, M. R. and M cmahon, A. (1988) Upper Carboniferous (Silesian) basin subsidence in northern Britain. In: Sedimentation in a Synorogenic Basin Complex (Eds. B. Besley and G. Kelling), Blackie, Glasgow, pp. 43-52
- Leeder, M.R., 1988. Recent developments in Carboniferous Geology: a critical review, with implications for the British Isles and NW Europe. Proceedings of the Geologists Associa- tion 99, 73–100.
- MacKenzie, M.R., 2022. Modelling Mine Energy Systems: A Feasibility Study of the Implementation of a Minewater Heating System on the University Estate. Unpublished MScR Thesis, Durham University.
- Mills, D A C, and Holliday, D W. 1998. Geology of the district around Newcastle upon Tyne, Gateshead and Consett. *Memoir of the British Geological Survey*, Sheet 20 (England and Wales).
- Monaghan, A.A., Starcher, V., Barron, H.F., Shorter, K., Walker-Verkuil, K., Elsome, J., Kearsey, T., Arkley, S., Hannis, S. and Callaghan, E., 2022. Drilling into mines for heat: geological synthesis of the UK Geoenergy Observatory in Glasgow and implications for mine water heat resources. *Quarterly Journal of Engineering Geology and Hydrogeology*, *55*(1).
- Moore, T.A., 2012. Coalbed methane: A review. *International Journal of Coal Geology*, *101*, pp.36-81.
- Mostaghimi, P., Armstrong, R.T., Gerami, A., Hu, Y., Jing, Y., Kamali, F., Liu, M., Liu, Z., Lu, X., Ramandi, H.L. and Zamani, A., 2017. Cleat-scale characterisation of coal: An overview. *Journal of Natural Gas Science and Engineering*, *39*, pp.143-160.
- New York Times, 2024. Are We in the 'Anthropocene', the Human Age? Nope, Scientists Say. https://www.nytimes.com/2024/03/05/climate/anthropocene-epoch-vote-rejected.html, accessed 15/03/2024.

- O'Mara, P.T., 1995. Correlation, facies distribution and sequence stratigraphic analysis of the Westphalian B Coal Measures in Quadrant 44 of the southern North Sea. Unpublished MSc Thesis, University of Durham.
- O'Keefe, J.M., Bechtel, A., Christanis, K., Dai, S., DiMichele, W.A., Eble, C.F., Esterle, J.S., Mastalerz, M., Raymond, A.L., Valentim, B.V. and Wagner, N.J., 2013. On the fundamental difference between coal rank and coal type. *International Journal of Coal Geology*, *118*, pp.58-87.
- O'Mara, P.T. and Turner, B.R., 1999. Sequence stratigraphy of coastal alluvial plain Westphalian B Coal Measures in Northumberland and the southern North Sea. *International Journal of Coal Geology*, *42*(1), pp.33-62.
- Palmer, I., 2009. Permeability changes in coal: analytical modeling. *International Journal of Coal Geology*, *77*(1-2), pp.119-126.
- Peng, S.S., 2019. *Longwall mining*. CRC Press.
- Price, S.J., Ford, J.R., Cooper, A.H. and Neal, C., 2011. Humans as major geological and geomorphological agents in the Anthropocene: the significance of artificial ground in Great Britain. *Philosophical Transactions of the Royal Society A: Mathematical, Physical and Engineering Sciences*, *369*(1938), pp.1056-1084.
- Prillaman, M., 2023. Are we in the Anthropocene? Geologists could define new epoch for Earth. *Nature,* 613, 14-15 (2023)
- Raine, R. and Reay, D.M., 2019. A review of geothermal reservoir properties of Triassic, Permian and Carboniferous sandstones in Northern Ireland.
- Robertson, E.P., 2005. Measurement and modeling of sorption-induced strain and permeability changes in coal. *2000-2009-Mines Theses & Dissertations*.

- Scott, B., Ranjith, P.G., Choi, S.K. and Khandelwal, M., 2010. A review on existing opencast coal mining methods within Australia. *Journal of Mining Science*, *46*(3).
- Sloss, L., 2013. Coal mine site reclamation. *IEA Clean Coal Centre*, p.978e92.
- Smailes, A.E., 1935. The development of the Northumberland and Durham coalfield. *Scottish Geographical Magazine*, *51*(4), pp.201-214.
- Soil Engineering, 2017. *Report on a Ground Investigation at Bayfield, West Allotment*.
- Song, Z., Zhang, J., Zhang, L., Dong, X., Niu, W. and Zhang, Y., 2022. The permeability properties of bedded coal and rock: Review and new insights. *Energy Science & Engineering*, *10*(4), pp.1544-1565.
- Steven, J. (2021). "From Venture Pit to Walker Shore, Coal and Heat and Fathoms of Core': Mine Water Heat Exploitation in Newcastle/Gateshead," in Proceedings 2021 Mine Water Geothermal Energy Symposium, 10th-11th March 2021 (Webinar).
- Su, X., Lin, X., Liu, S., Zhao, M. and Song, Y., 2005. Geology of coalbed methane reservoirs in the Southeast Qinshui Basin of China. *International Journal of Coal Geology*, *62*(4), pp.197-210.
- Todd, F., McDermott, C., Harris, A.F., Bond, A. and Gilfillan, S., 2019. Coupled hydraulic and mechanical model of surface uplift due to mine water rebound: implications for mine water heating and cooling schemes. *Scottish Journal of Geology*, *55*(2), pp.124-133.
- Tucker, M.E., Jones, S.J., 2023. Sedimentary Petrology, 4th Edition.
- Turner, B.R & Richardson 2004. Geological controls on the sulphur content of coal seams in the Northumberland Coalfield, Northeast England. Sedimentary Geology, 60, 169-196.
- Turner, B.R., Smith, D.B., 1995. The Carboniferous and Permian rocks between Tynemouth and Seaton Sluice. In: Scrutton, C.T. (Ed.), Northumbrian Rocks and Landscape: a Field Guide. Yorkshire Geological Society, Ellenbank Press, Maryport, UK, pp. 92–104.

- Verma, D., Kainthola, A., Gupte, S.S. and Singh, T.N., 2013. A finite element approach of stability analysis of internal dump slope in Wardha valley coal field, India, Maharashtra. *American Journal of Mining and Metallurgy*, *1*(1), pp.1-6.
- Walls, D. B., Banks, D., Boyce, A. J., and Burnside, N. M. (2021). A Review of the Performance of Minewater Heating and Cooling Systems. *Energies* 14 (19), 6215. doi:10.3390/en14196215
- Wardell, K. and Wood, J.C., 1966. *Ground instability problems arising from the presence of old, shallow mine workings*. Midland Soil Mechanics and Foundation Engineering Society.
- Warmuzinski, K., 2008. Harnessing methane emissions from coal mining. *Process safety and environmental protection*, *86*(5), pp.315-320.
- Younger PL, Manning DAC, Millward D, et al., 2016. Geothermal exploration in the Fell Sandstone Formation (Mississippian) beneath the city centre of Newcastle upon Tyne, UK: The Newcastle Science Central Deep Geothermal Borehole. *Quart J Eng Geol Hydrol* 2016; 49: 350–363.
- Younger, P., and Robins, N. (2002). Challenges in the Characterization and Prediction of the Hydrogeology and Geochemistry of Mined Ground. *Geol. Soc. Lond. Spec. Publ.* 198, 1–16. doi:10.1144/GSL.SP.2002.198.01.01
- Younger, P.L. and Adams, R., 1999. Predicting mine water rebound.
- Younger, P.L., 1995. Hydrogeochemistry of minewaters flowing from abandoned coal workings in County Durham. *Quarterly Journal of Engineering Geology and Hydrogeology*, *28*(supplement_2), pp.S101-S113.
- Younger, P.L., Manning, D.A., Millward, D., Busby, J.P., Jones, C.R. and Gluyas, J.G., 2016. Geothermal exploration in the Fell Sandstone Formation (Mississippian) beneath the city centre of Newcastle upon Tyne, UK: the Newcastle Science Central deep geothermal borehole. *Quarterly Journal of Engineering Geology and Hydrogeology*, *49*(4), pp.350-363.

- Zalasiewicz, J., Williams, M., Fortey, R., Smith, A., Barry, T.L., Coe, A.L., Bown, P.R., Rawson, P.F., Gale, A., Gibbard, P. and Gregory, F.J., 2011. Stratigraphy of the Anthropocene. *Philosophical Transactions of the Royal Society A: Mathematical, Physical and Engineering Sciences*, *369*(1938), pp.1036-1055.
- Zeng, K., Xu, J., He, P. and Wang, C., 2011. Experimental study on permeability of coal sample subjected to triaxial stresses. *Procedia Engineering*, *26*, pp.1051-1057.
- Zhou, F., Xia, T., Wang, X., Zhang, Y., Sun, Y. and Liu, J., 2016. Recent developments in coal mine methane extraction and utilization in China: a review. *Journal of Natural Gas Science and Engineering*, *31*, pp.437-458.

Appendix

Appendix 1

Matlab script used to convert tri-axial test rig values into permeability values for *in situ* coal sample

```
%% %%% Input information %%%%%%
Experiment_no = 'Dutff00392'; %change experiment number everywhere using  cmd+f co
mmand%
D = 36.0; % sample diameter ( mm)
L=19.2;  % sample length ( mm)
A = ((D/2000)^2)*pi; % initial axial area of the sample (m^2)
Mu= 0.001; % fluid viscosity (Pa*s)
Beta= 4.2*(10^-10); %fluid compressibility (Pa^-1)

%% %%%%%% Extract measured parameters from the raw data file %%%%%%
Dataset = load('DuTff392.txt'); % Load the data
T = Dataset(:,1); % time record in second
Up = Dataset(:,10);% upstream pore pressure in MPa
Dwn= Dataset(:,11);% downstream pore pressure in MPa

%% %%%% Plot Time vs Pore Pressure Graph %%%%%%

figure(1)
plot (T, Dwn, 'LineWidth', .5); hold on; plot (T, Up, 'LineWidth', .5); grid on;
title([' Experiment ', Experiment_no],'FontSize',14);
xlabel('Time(s)','FontSize',14); ylabel('Pore Pressure(MPa)','FontSize',14);
xlim([0 max(T)+100]); ylim([0 max(Up)+10]);
saveas(figure (1),'Pore_Pressure_v_Time_00373_b');

%% %%%%%%%%%%  Start and Stop Points %%%%%%%%%%%%%%%
Start= 206657; % row number at which the permeability test was started
Stop= 208145; % row number at which the permeability test was concluded

%% %%%%%%%%%%%% Zero the measurments at the starting point %%%%%%%%%%%%%%%%%%

T10 = T(Start: Stop)-T(Start); % zero the time from hitpoint
Up10 = Up(Start: Stop);
Dwn10 = Dwn(Start: Stop);

%% %%%%% Sensor Correction %%%%%%
```

```
DPressure= Up10-Dwn10; % Calculates initial pressure difference (MPa)
%%
PressureCorr= 0.58; % Determines value of pressure correction (MPa)
UpCorr10= Up10-PressureCorr; %Corrects the upstream pressure

%% %%%% Plot Test Graph %%%%%%

figure(2)
plot (T10, Dwn10, 'LineWidth', .5); hold on; plot (T10, UpCorr10, 'LineWidth', .5);
grid on;
title([' Experiment ', Experiment_no],'FontSize',14);
xlabel('Time(s)','FontSize',14); ylabel('Pore Pressure(MPa)','FontSize',14);
xlim([0 max(T)+100]); ylim([0 max(Up)+10]);
saveas(figure (2),'PermeabilityTest_00361_b_40MPaEff');


%% %%%%% Inputs for DP vs Time Plot %%%%%%
Pf10= 11.43; % Final pressure (MPa)
DP10= UpCorr10-Dwn10; % Calculates Pressure Difference
UpDiff10= UpCorr10-Pf10; % Calculates P1-Pf
DwnDiff10= Pf10-Dwn10; % Calculates Pf-P2

%% %%%% Plot DP vs Time Graph %%%%%%

figure(3)
plot (T10, DP10, 'LineWidth', .5); hold on; plot (T10, UpDiff10, 'LineWidth', .5); hold
on; plot (T10, DwnDiff10, 'LineWidth', .5); grid on;
title([' Experiment ', Experiment_no],'FontSize',14);
xlabel('Time(s)','FontSize',14); ylabel('Pore Pressure Difference(MPa)','FontSize',14);
xlim([0 max(T)+100]); ylim([0 max(Up)+10]);
saveas(figure (3),'DP_vs_Time_00361_b_40MPaEff');

%% %%%% AlphaR from DP vs Time Graph %%%%%%%%%%

TLinear=T10(1:86); %Defines the linear portion on the time data
DPLinear=DP10(1:86); %Defines the linear portion of the P1-P2 data
lnDP=log(DPLinear); %Takes ln of the linear section of P1-P2
B0=ones(length(TLinear),1); %Creates a column of ones equal in length to TLinear
(Matlab code: https://www.mathworks.com/help/matlab/data_analysis/linear-
regression.html)
TIME=[B0,TLinear]; %Pads TLinear with the column of ones
```

```
Regression=abs(TIME\lnDP); %Takes linear regression
AlphaR=Regression(2,:); %Takes Alpha determined by regression (This is the slope of the regression, or alpha in Brace 1968 eqs 2 and 3)
CR=Regression(1,:); % Takes C determined by regression (C is the y-intercept of the regression, corresponding to the DP((V2/V1)+V2) term of Brace 1968 eq 2

%% %%%% Calculating Cc %%%%%
V1= 2.66182*10^(-6); % in m3
V2= 2.55008*10^(-6); % in m3
DP0=(max(DP10)); % Gets pressure difference at time 0
VFrac=(V2/V1)+V2; % Calculates volume fraction
CC=log(DP0*VFrac); % CC is the DP((V2/V1)+V2) term of Brace 1968 eq 2 that is calculated from known parameters rather than determined from the regression (CR)

%% %%%% Correcting for volumes (if needed) %%%%%%

eCR=exp(CR);
VFraccorr=eCR/DP0; % Calculates the volume fraction based on the experimental result (from the y-intercept of the regression)
%% %%%% Calculating V1 (if needed) %%%%%

V1=V2/(VFraccorr-V2); % VFraccorr can be used to determine one of the reservoir volumes if the other is unknown

%% %%%%% Calculating Permeability (Brace 1968 eq 3) %%%%%%

VSum= (1/V1)+(1/V2); %Calculating volume sum (1/m^3)
k=(AlphaR*Mu*Beta*(L/1000))/(VSum*A); %Gives permeability in m^
```

Appendix 2

Quadrat Counts of Roof Collapse Deposit at Whitley Bay

	Grain size (cm)					
	<1	1<x<4	5<x<9	10<x<14	15<x<19	>20
Left Quadrat	5	27	13	2	2	0
Right Quadrat	4	15	14	5	4	2

	Left Quadrat	
Grain Size (mm)	g	%
>16	24	14.63414634
>8	49	29.87804878
>4	26	15.85365854
>2	22	13.41463415
>1	19	11.58536585
>0.5	9	5.487804878
>0.25	6	3.658536585
>0.125	4	2.43902439
<0.125	5	3.048780488
Total	164	

	Right Quadrat	
Grain Size (mm)	g	%
>16	98	31.61290323
>8	79	25.48387097
>4	45	14.51612903
>2	31	10
>1	23	7.419354839
>0.5	12	3.870967742
>0.25	8	2.580645161
>0.125	4	1.290322581
<0.125	10	3.225806452
Total	310	

Appendix 3

Laser Granulometry for Left Quadrat of Roof Collapse deposit at Whitley Bay

Channel Diameter (Lower) um	Diff. Volume %
0.04	0.00008201
0.0439105	0.00010445
0.0482033	0.00016413
0.0529158	0.00031652
0.0580889	0.00066138
0.0637679	0.00129223
0.070002	0.00219570
0.0768455	0.00320310
0.0843581	0.00429218
0.0926052	0.00553350
0.101658	0.00702982
0.111597	0.00868009
0.122507	0.01042470
0.134483	0.01230220
0.147631	0.01445270
0.162064	0.01685990
0.177907	0.01956870
0.1953	0.02262910
0.214393	0.02625060
0.235353	0.03042840
0.258361	0.03498820
0.283619	0.03970620
0.311346	0.04437210
0.341784	0.04903500
0.375198	0.05373360
0.411878	0.05860430
0.452145	0.06361350
0.496347	0.06875000
0.544872	0.07401590
0.59814	0.07943130
0.656615	0.08503340
0.720807	0.09083450
0.791275	0.09691830
0.868632	0.10335200
0.953552	0.11029500

follow on in next column

Channel Diameter (Lower) um	Diff. Volume %
1.04677	0.11782800
1.14911	0.12608600
1.26145	0.13511700
1.38477	0.14505400
1.52015	0.15589500
1.66876	0.16767000
1.8319	0.18031900
2.011	0.19386300
2.2076	0.20822100
2.42342	0.22322700
2.66033	0.23865400
2.92042	0.25430400
3.20592	0.27010900
3.51934	0.28591700
3.8634	0.30157100
4.2411	0.31683100
4.65572	0.33178500
5.11087	0.34671400
5.61052	0.36205200
6.15902	0.37801100
6.76114	0.39467900
7.42212	0.41231400
8.14773	0.43124200
8.94427	0.45161400
9.81869	0.47233900
10.7786	0.49170000
11.8323	0.50809000
12.9891	0.52254800
14.2589	0.53877400
15.6529	0.56192100
17.1832	0.59564600
18.863	0.63953700
20.7071	0.68961400
22.7315	0.73946000
24.9538	0.78404900

follow on in next column

Channel Diameter (Lower) um	Diff. Volume %
27.3934	0.82095800
30.0714	0.85023000
33.0113	0.87280200
36.2385	0.88838200
39.7813	0.89601300
43.6704	0.89508200
47.9397	0.88737100
52.6264	0.87775900
57.7713	0.87262400
63.4192	0.87752400
69.6192	0.89458300
76.4253	0.92201000
83.8969	0.95598900
92.0988	0.99413200
101.103	1.03878000
110.987	1.09609000
121.837	1.17162000
133.748	1.26359000
146.824	1.36008000
161.177	1.44284000
176.935	1.49742000
194.232	1.52327000
213.221	1.53587000
234.066	1.55921000
256.948	1.61561000
282.068	1.71514000
309.644	1.85372000
339.916	2.01385000
373.147	2.17570000
409.626	2.32240000
449.672	2.44764000
493.633	2.55371000
541.892	2.65991000
594.869	2.78031000
653.025	2.92432000

follow on in next column

Channel Diameter (Lower) um	Diff. Volume %
716.866	3.07381000
786.949	3.21232000
863.883	3.31880000
948.338	3.38041000
1041.05	3.38493000
1142.83	3.36909000
1254.55	3.31859000
1377.2	3.23009000
1511.84	3.02808000
1659.64	2.82595000
1821.89	2.58948000

Appendix 4

Laser Granulometry for Right Quadrat of Roof Collapse deposit at Whitley Bay

Channel Diameter (Lower) um	Diff. Volume %
0.04	0.00034808
0.0439105	0.00042727
0.0482033	0.00063313
0.0529158	0.00118925
0.0580889	0.00251218
0.0637679	0.00491704
0.070002	0.00806749
0.0768455	0.01108620
0.0843581	0.01395260
0.0926052	0.01694310
0.101658	0.02016080
0.111597	0.02328510
0.122507	0.02629950
0.134483	0.02938930
0.147631	0.03239030
0.162064	0.03535630
0.177907	0.03842040
0.1953	0.04183330
0.214393	0.04551140
0.235353	0.04941800
0.258361	0.05343470
0.283619	0.05749850
0.311346	0.06136370
0.341784	0.06509960
0.375198	0.06875390
0.411878	0.07260810
0.452145	0.07652580
0.496347	0.08051890
0.544872	0.08451300
0.59814	0.08876620
0.656615	0.09322790
0.720807	0.09790680
0.791275	0.10276100
0.868632	0.10803800
0.953552	0.11383500

follow on in next column

Channel Diameter (Lower) um	Diff. Volume %
1.04677	0.12018400
1.14911	0.12708700
1.26145	0.13463600
1.38477	0.14293700
1.52015	0.15193300
1.66876	0.16158800
1.8319	0.17181100
2.011	0.18264600
2.2076	0.19400700
2.42342	0.20576700
2.66033	0.21771000
2.92042	0.22973400
3.20592	0.24186300
3.51934	0.25404600
3.8634	0.26620700
4.2411	0.27820500
4.65572	0.29027600
5.11087	0.30280900
5.61052	0.31633600
6.15902	0.33113400
6.76114	0.34740600
7.42212	0.36557500
8.14773	0.38618100
8.94427	0.40958800
9.81869	0.43487800
10.7786	0.46048300
11.8323	0.48477700
12.9891	0.50872000
14.2589	0.53572400
15.6529	0.57059900
17.1832	0.61661600
18.863	0.67303600
20.7071	0.73591000
22.7315	0.79917100
24.9538	0.85859400

follow on in next column

Channel Diameter (Lower) um	Diff. Volume %
27.3934	0.91256700
30.0714	0.96154900
33.0113	1.00620000
36.2385	1.04491000
39.7813	1.07440000
43.6704	1.09084000
47.9397	1.09271000
52.6264	1.08267000
57.7713	1.06720000
63.4192	1.05477000
69.6192	1.05264000
76.4253	1.06478000
83.8969	1.09137000
92.0988	1.13021000
101.103	1.17969000
110.987	1.24018000
121.837	1.31319000
133.748	1.39686000
146.824	1.48195000
161.177	1.55235000
176.935	1.59236000
194.232	1.59797000
213.221	1.58436000
234.066	1.58223000
256.948	1.62635000
282.068	1.73844000
309.644	1.91732000
339.916	2.13338000
373.147	2.34116000
409.626	2.49436000
449.672	2.56917000
493.633	2.56957000
541.892	2.53643000
594.869	2.51061000
653.025	2.52452000

follow on in next column

Channel Diameter (Lower) um	Diff. Volume %
716.866	2.57153000
786.949	2.64406000
863.883	2.72696000
948.338	2.81490000
1041.05	2.89068000
1142.83	2.98525000
1254.55	3.06522000
1377.2	3.11426000
1511.84	3.04985000
1659.64	2.94491000
1821.89	2.84796000

Appendix 5

Dry Sieving results of samples from the Backfill deposit at Whitley Bay

	Low Backfill	
Grain Size (mm)	g	%
>16	34.97	12.05654198
>8	95.77	33.0184451
>4	64.03	22.07550422
>2	48.35	16.66953973
>1	26.17	9.022582313
>0.5	12.31	4.244095846
>0.25	8.23	2.83744182
>0.125	0.2	0.068953629
<0.125	0.02	0.006895363
Total	290.05	

	Mid Backfill	
Grain Size (mm)	g	%
>16	62.51	26.03823885
>8	39.17	16.31607448
>4	50.98	21.23547299
>2	38.84	16.17861457
>1	24.15	10.05956596
>0.5	13.54	5.64002166
>0.25	7.52	3.132419711
>0.125	3.17	1.320448203
<0.125	0.19	0.079143583
Total	240.07	

	Top Backfill	
Grain Size (mm)	g	%
>16	11.23	3.00138978
>8	81.27	21.72065427
>4	117.08	31.29142613
>2	79.39	21.21819542
>1	43.53	11.6340603
>0.5	23.51	6.283408168
>0.25	13.08	3.495830661
>0.125	4.98	1.330981398
<0.125	0.09	0.024053881
Total	374.16	

Appendix 6

Laser Granulometry for Low Backfill deposit sample at Whitley Bay

Channel Diameter (Lower) um	Diff. Volume %
0.04	3.61E-05
0.0439105	5.19E-05
0.0482033	9.96E-05
0.0529158	0.00021669
0.0580889	0.000447269
0.0637679	0.000859613
0.070002	0.00155243
0.0768455	0.00259976
0.0843581	0.00400401
0.0926052	0.00579215
0.101658	0.00812562
0.111597	0.0110004
0.122507	0.0142867
0.134483	0.0178847
0.147631	0.0221909
0.162064	0.0272626
0.177907	0.0331975
0.1953	0.039934
0.214393	0.0480122
0.235353	0.0574639
0.258361	0.0678388
0.283619	0.0783921
0.311346	0.0886352
0.341784	0.0986295
0.375198	0.108442
0.411878	0.118155
0.452145	0.127727
0.496347	0.137097
0.544872	0.146217
0.59814	0.154884
0.656615	0.163116
0.720807	0.170952
0.791275	0.178547
0.868632	0.18588
0.953552	0.193139

follow on in next column

Channel Diameter (Lower) um	Diff. Volume %
1.04677	0.20057
1.14911	0.208581
1.26145	0.217414
1.38477	0.22734
1.52015	0.238532
1.66876	0.251246
1.8319	0.265641
2.011	0.28181
2.2076	0.29965
2.42342	0.31895
2.66033	0.339457
2.92042	0.360841
3.20592	0.382708
3.51934	0.404455
3.8634	0.425515
4.2411	0.445387
4.65572	0.463979
5.11087	0.481433
5.61052	0.498177
6.15902	0.514771
6.76114	0.531973
7.42212	0.550621
8.14773	0.57105
8.94427	0.592561
9.81869	0.612536
10.7786	0.627239
11.8323	0.632745
12.9891	0.627607
14.2589	0.614463
15.6529	0.600589
17.1832	0.595931
18.863	0.608975
20.7071	0.643428
22.7315	0.695311
24.9538	0.753707

follow on in next column

Channel Diameter (Lower) um	Diff. Volume %
27.3934	0.804012
30.0714	0.834189
33.0113	0.840067
36.2385	0.826441
39.7813	0.80459
43.6704	0.786526
47.9397	0.780574
52.6264	0.788975
57.7713	0.808131
63.4192	0.831347
69.6192	0.85151
76.4253	0.864201
83.8969	0.869179
92.0988	0.870464
101.103	0.875719
110.987	0.892773
121.837	0.926514
133.748	0.975153
146.824	1.0301
161.177	1.08002
176.935	1.11717
194.232	1.14349
213.221	1.17051
234.066	1.21483
256.948	1.29291
282.068	1.41351
309.644	1.5762
339.916	1.76791
373.147	1.97027
409.626	2.16268
449.672	2.33137
493.633	2.47243
541.892	2.60364
594.869	2.74237
653.025	2.90401

follow on in next column

Channel Diameter (Lower) um	Diff. Volume %
716.866	3.07405
786.949	3.23837
863.883	3.37629
948.338	3.47577
1041.05	3.52581
1142.83	3.56015
1254.55	3.55528
1377.2	3.49186
1511.84	3.27751
1659.64	3.04771
1821.89	2.75555

Appendix 7

Laser Granulometry for Mid Backfill deposit sample at Whitley Bay

Channel Diameter (Lower) um	Diff. Volume %
0.04	3.39E-05
0.0439105	5.08E-05
0.0482033	0.000103107
0.0529158	0.000231811
0.0580889	0.000478176
0.0637679	0.000914618
0.070002	0.00166557
0.0768455	0.00286781
0.0843581	0.00455036
0.0926052	0.00674991
0.101658	0.00963447
0.111597	0.0132361
0.122507	0.0174072
0.134483	0.0220254
0.147631	0.0275102
0.162064	0.0339828
0.177907	0.0415747
0.1953	0.0502516
0.214393	0.0606038
0.235353	0.072679
0.258361	0.0859084
0.283619	0.0993241
0.311346	0.112289
0.341784	0.124888
0.375198	0.137266
0.411878	0.14948
0.452145	0.161458
0.496347	0.173158
0.544872	0.184601
0.59814	0.195572
0.656615	0.206073
0.720807	0.2162
0.791275	0.22623
0.868632	0.23629
0.953552	0.246632

follow on in next column

Channel Diameter (Lower) um	Diff. Volume %
1.04677	0.257594
1.14911	0.269696
1.26145	0.283341
1.38477	0.298816
1.52015	0.316185
1.66876	0.335566
1.8319	0.357051
2.011	0.380638
2.2076	0.405958
2.42342	0.432397
2.66033	0.459335
2.92042	0.486292
3.20592	0.512816
3.51934	0.53814
3.8634	0.561394
4.2411	0.58192
4.65572	0.599866
5.11087	0.615859
5.61052	0.630662
6.15902	0.644778
6.76114	0.65892
7.42212	0.674345
8.14773	0.692194
8.94427	0.712047
9.81869	0.73036
10.7786	0.741956
11.8323	0.74308
12.9891	0.736127
14.2589	0.729614
15.6529	0.734505
17.1832	0.758131
18.863	0.799776
20.7071	0.851445
22.7315	0.90104
24.9538	0.939106

follow on in next column

Channel Diameter (Lower) um	Diff. Volume %
27.3934	0.962171
30.0714	0.972523
33.0113	0.975124
36.2385	0.973606
39.7813	0.969576
43.6704	0.963277
47.9397	0.95567
52.6264	0.949524
57.7713	0.948203
63.4192	0.95358
69.6192	0.963805
76.4253	0.973385
83.8969	0.976348
92.0988	0.971275
101.103	0.965034
110.987	0.969889
121.837	0.995712
133.748	1.04045
146.824	1.08742
161.177	1.11232
176.935	1.09927
194.232	1.05325
213.221	0.998581
234.066	0.963562
256.948	0.968386
282.068	1.0154
309.644	1.09393
339.916	1.18334
373.147	1.27132
409.626	1.35196
449.672	1.42889
493.633	1.50142
541.892	1.58799
594.869	1.69335
653.025	1.82618

follow on in next column

Channel Diameter (Lower) um	Diff. Volume %
716.866	1.95863
786.949	2.10162
863.883	2.2719
948.338	2.50909
1041.05	2.8169
1142.83	3.26066
1254.55	3.79396
1377.2	4.37165
1511.84	4.77498
1659.64	4.99378
1821.89	5.13826

Appendix 8

Laser Granulometry for Top Backfill deposit sample at Whitley Bay

Channel Diameter (Lower) um	Diff. Volume %
0.04	0
0.0439105	0
0.0482033	0
0.0529158	0
0.0580889	0
0.0637679	0
0.070002	0
0.0768455	1.12E-06
0.0843581	3.17E-05
0.0926052	0.000290594
0.101658	0.00129485
0.111597	0.00359727
0.122507	0.00720595
0.134483	0.012041
0.147631	0.0182615
0.162064	0.0263535
0.177907	0.0365358
0.1953	0.0492255
0.214393	0.0650133
0.235353	0.0842366
0.258361	0.106124
0.283619	0.129286
0.311346	0.152453
0.341784	0.175594
0.375198	0.198833
0.411878	0.222259
0.452145	0.245503
0.496347	0.268377
0.544872	0.290617
0.59814	0.31189
0.656615	0.331828
0.720807	0.350411
0.791275	0.367709
0.868632	0.383852
0.953552	0.398876

follow on in next column

Channel Diameter (Lower) um	Diff. Volume %
1.04677	0.413112
1.14911	0.427236
1.26145	0.442043
1.38477	0.458116
1.52015	0.475737
1.66876	0.495292
1.8319	0.517256
2.011	0.542063
2.2076	0.569589
2.42342	0.599319
2.66033	0.630641
2.92042	0.663156
3.20592	0.696414
3.51934	0.729387
3.8634	0.76069
4.2411	0.789187
4.65572	0.814894
5.11087	0.838588
5.61052	0.861177
6.15902	0.883121
6.76114	0.90519
7.42212	0.929042
8.14773	0.956291
8.94427	0.986039
9.81869	1.01251
10.7786	1.02722
11.8323	1.0243
12.9891	1.00786
14.2589	0.991718
15.6529	0.992554
17.1832	1.01982
18.863	1.06943
20.7071	1.12599
22.7315	1.17009
24.9538	1.18995

follow on in next column

Channel Diameter (Lower) um	Diff. Volume %
27.3934	1.18611
30.0714	1.16807
33.0113	1.14637
36.2385	1.12492
39.7813	1.10047
43.6704	1.06707
47.9397	1.0238
52.6264	0.979844
57.7713	0.951588
63.4192	0.954087
69.6192	0.991165
76.4253	1.04963
83.8969	1.10207
92.0988	1.1212
101.103	1.10032
110.987	1.06117
121.837	1.03994
133.748	1.06167
146.824	1.12403
161.177	1.19758
176.935	1.24451
194.232	1.24685
213.221	1.21998
234.066	1.19967
256.948	1.22028
282.068	1.29648
309.644	1.42256
339.916	1.57562
373.147	1.73153
409.626	1.86995
449.672	1.98021
493.633	2.05456
541.892	2.10277
594.869	2.13004
653.025	2.14605

follow on in next column

Channel Diameter (Lower) um	Diff. Volume %
716.866	2.13665
786.949	2.11175
863.883	2.08337
948.338	2.07921
1041.05	2.10302
1142.83	2.1886
1254.55	2.30833
1377.2	2.17899
1511.84	1.81151
1659.64	1.4172
1821.89	1.33649

Appendix 9

XRD Data for the Roadway section at Whitley Bay

Sample	Illite/Smectite	Illite+Mica	Kaolinite	Chlorite	Quartz	K Feldspar	Plagioclase	Calcite	Dolomite	Siderite	Halite	Pyrite	Jarosite	Anatase	Total
R1	0.1	4.4	16.6	0.0	68.0	3.3	4.3	0.0	3.4	0.0	0.0	0.0	0.0	0.0	100
R5	0.5	12.2	49.1	3.4	26.7	2.9	3.1	0.0	0.0	2.3	0.0	0.0	0.0	0.0	100
R7	0.0	0.0	84.3	0.0	14.9	0.0	0.0	0.0	0.0	0.0	0.8	0.0	0.0	0.0	100
R8	1.2	12.2	56.8	10.9	14.5	2.7	0.0	0.0	0.0	1.2	0.0	0.6	0.0	0.0	100
R10	1.9	13.2	64.8	0.0	18.5	0.0	0.0	0.0	0.0	0.0	0.0	0.0	1.7	0.0	100
R11	0.0	TR	76.4	0.0	4.1	0.0	0.0	0.0	0.0	0.0	0.0	18.2	1.3	0.0	100
R12	7.6	50.4	35.4	0.0	6.7	0.0	0.0	0.0	0.0	0.0	0.0	0.0	TR	TR	100
R13	0.6	6.0	31.1	7.1	41.6	2.8	6.5	0.0	0.0	4.4	0.0	0.0	0.0	0.0	100

Appendix 10

Permeability measurements from Whitley Bay

Pillar Section			
Height from Base (m)	TinyPerm Value	Permeability (mD)	Average Permeability (mD)
0.7	11.00	195.7	
0.7	10.94	260.3	
0.7	10.87	280.7	245.6
1.52	11.05	167.1	
1.52	11.29	96.9	
1.52	11.01	201.1	155.0
3.06	11.09	149.7	
3.06	11.11	160.6	
3.06	11.20	110.6	140.3

Roof Collapse Section			
Height from Base (m)	TinyPerm Value	Permeability (mD)	Average Permeability (mD)
1.1	11.26	97.9	
1.1	11.26	109.8	
1.1	11.32	100.5	102.7
1.85	10.90	257.8	
1.85	10.96	221.5	
1.85	10.87	289.8	256.4
2.95	1.07	478.0	
2.95	10.78	356.0	
2.95	10.88	289.9	374.6

Roadway Section			
Height from Base (m)	TinyPerm Value	Permeability (mD)	Average Permeability (mD)
0.5	10.80	345.4	
0.5	11.04	177.1	
0.5	11.22	172	231.5
1.03	11.28	90.2	
1.03	11.15	146.4	
1.03	11.14	147.6	128.1
1.56	11.22	139.8	
1.56	11.51	78	
1.56	11.33	88.4	102.1
2.08	11.06	173.2	
2.08	10.98	248.4	
2.08	11.15	138.6	186.7
2.54	11.01	258	
2.54	10.86	319.9	
2.54	11.29	141.8	239.9
3.07	10.36	1258.3	
3.07	10.52	1104.7	
3.07	10.57	740.4	1034.5

Appendix 11

ICP-MES and ICP-OES of selected Whitley Bay samples

Inductively Coupled Plasma Mass Spectrometry (ICP-MS)																																								
Location	Sample ID	Be	V	Cr	Co	Ni	Cu	Zn	Ga	Rb	Sr	Y	Zr	Nb	Mo	Sn	Cs	Ba	La	Ce	Pr	Nd	Sm	Eu	Gd	Tb	Dy	Ho	Er	Tm	Yb	Lu	Hf	Ta	W	Tl	Pb	Th	U
		ppm	ppm	ppm	ppm	ppm	ppm	ppm	ppm	ppm	ppm	ppm	ppm	ppm	ppm	ppm	ppm	ppm	ppm	ppm	ppm	ppm	ppm	ppm	ppm	ppm	ppm	ppm	ppm	ppm	ppm	ppm	ppm	ppm	ppm	ppm	ppm	ppm	ppm
	P1	0.75	52.49	74.57	15.27	25.81	10.35	21.30	12.07	46.48	70.13	24.29	550.60	9.90	0.67	1.62	1.71	272.78	46.04	95.03	11.33	41.51	7.42	1.25	6.37	0.87	4.25	0.86	2.32	0.36	2.43	0.37	14.46	0.64	1.23	0.17	6.66	12.64	2.74
	P2	1.05	64.43	75.91	11.19	28.94	11.95	45.54	14.10	54.77	61.10	18.36	257.14	9.35	0.90	1.38	2.26	282.60	31.30	64.57	7.49	28.64	5.17	1.15	4.35	0.65	3.35	0.66	1.70	0.24	1.54	0.24	6.89	0.58	1.12	0.23	6.75	6.70	1.86
	P4	2.01	101.30	137.22	24.26	64.71	34.15	103.61	25.35	103.75	79.09	31.25	392.20	14.28	1.15	2.51	6.22	445.75	51.26	105.75	12.67	47.04	8.46	1.68	7.40	1.08	5.55	1.17	3.18	0.45	3.22	0.50	11.00	0.91	1.43	0.40	16.72	13.69	3.43
	P5	1.23	63.78	71.32	18.18	38.68	17.82	34.95	14.81	68.47	60.66	21.45	196.98	9.07	0.34	1.56	3.16	426.86	22.33	49.66	6.26	24.56	5.06	1.17	4.82	0.71	3.71	0.78	2.01	0.29	1.85	0.27	5.47	0.53	1.22	0.39	12.53	5.59	1.58
	P7	2.08	193.45	151.43	6.91	32.84	30.61	25.23	27.34	79.49	54.25	24.63	106.99	14.11	2.03	2.19	11.15	236.78	57.99	114.60	14.31	52.35	8.93	1.80	7.35	0.97	4.80	0.95	2.57	0.36	2.48	0.36	3.11	0.87	4.16	0.43	2.55	17.62	3.97
	R1	0.46	40.93	75.92	7.07	19.60	10.22	16.32	7.47	27.57	79.14	35.78	987.59	11.36	0.60	1.27	1.36	933.27	52.02	106.41	13.03	49.56	9.14	1.36	8.18	1.17	6.09	1.23	3.60	0.54	3.80	0.59	26.39	0.80	1.41	0.10	4.65	16.96	3.75
	R2	2.22	96.79	147.69	34.75	86.24	34.66	92.38	26.17	111.18	84.57	24.38	285.21	16.07	1.10	2.51	6.77	464.27	44.20	86.49	10.09	34.92	5.96	1.25	5.33	0.77	4.15	0.84	2.38	0.35	2.38	0.36	7.94	1.14	1.66	0.71	22.59	11.51	2.89
	R3	0.59	43.10	61.78	6.27	19.08	13.97	91.58	10.62	42.58	45.65	25.93	498.71	9.27	0.37	1.45	1.58	289.67	31.74	66.71	8.10	30.63	5.78	1.05	5.29	0.80	4.37	0.91	2.65	0.36	2.50	0.40	13.33	0.61	1.19	0.22	11.27	9.81	2.39
	R5	2.80	112.45	147.72	23.20	65.14	59.08	60.59	28.83	110.49	79.17	35.88	298.66	16.10	0.78	2.45	8.22	449.15	50.82	101.78	12.48	45.10	8.59	1.81	7.28	1.15	6.18	1.38	3.69	0.54	3.63	0.53	8.43	1.03	1.63	0.69	17.57	14.59	4.08
	R6	4.02	164.94	112.15	7.63	28.55	97.89	63.82	32.96	230.78	170.95	50.50	151.05	13.03	2.50	2.58	35.27	530.58	83.54	143.08	18.50	66.08	11.15	2.40	10.07	1.56	8.68	1.91	5.34	0.77	5.23	0.77	4.46	0.97	2.57	0.84	10.01	20.54	6.49
	R7	0.77	103.28	11.30	1.08	1.08	18.51	0.85	1.70	3.08	17.35	3.00	6.63	1.08	1.03	0.43	0.42	86.44	2.21	4.23	0.56	2.25	0.45	0.17	0.60	0.09	0.52	0.11	0.28	0.05	0.31	0.04	0.26	0.08	1.46	0.04	0.48	0.89	0.73
	R8	3.22	114.62	150.72	22.80	80.71	52.59	45.19	30.52	112.07	85.37	20.16	86.20	13.82	1.32	2.19	12.68	332.31	42.06	77.38	8.89	30.16	4.88	1.08	4.41	0.60	3.28	0.75	2.15	0.36	2.40	0.35	2.68	1.11	1.73	0.57	10.58	15.89	3.00
	R9	0.98	54.48	68.55	16.52	54.59	20.02	73.91	12.35	50.99	51.47	20.58	267.92	9.09	0.42	1.32	2.22	329.23	28.34	60.87	7.61	28.04	5.28	1.06	4.83	0.68	3.61	0.75	2.07	0.31	2.01	0.33	7.46	0.58	1.10	0.40	14.77	7.75	2.01
	R11	1.08	244.03	14.98	2.76	54.77	34.67	8.21	3.15	4.08	17.19	4.83	11.28	2.69	23.05	0.35	0.42	55.77	3.26	6.21	0.85	3.20	0.69	0.19	0.67	0.13	0.75	0.18	0.49	0.07	0.44	0.06	0.32	0.03	0.67	0.74	0.43	1.12	2.64
	R15	3.18	124.31	150.68	21.38	87.90	52.69	66.55	30.02	107.04	147.58	22.94	96.07	13.32	1.19	1.87	11.34	545.44	54.60	102.15	12.18	42.00	6.69	1.28	5.72	0.73	3.93	0.83	2.39	0.35	2.42	0.35	2.77	0.79	1.69	0.64	6.36	14.59	3.18
	W1	0.60	43.36	56.34	6.99	20.01	14.31	84.94	11.20	44.76	72.60	20.30	311.25	8.26	0.33	1.26	2.08	270.03	26.73	55.10	6.76	25.44	4.57	0.99	4.51	0.63	3.52	0.74	2.00	0.29	1.91	0.29	8.50	0.50	1.25	0.29	10.78	7.03	1.77
	W2	3.04	132.87	165.97	10.14	41.75	30.90	34.31	33.16	103.70	62.88	26.64	148.38	17.50	0.25	2.54	12.83	326.27	47.48	87.81	10.18	34.74	6.02	1.28	5.14	0.82	4.63	1.02	2.78	0.40	2.72	0.42	4.29	1.10	1.89	0.67	9.18	16.53	4.39
	W3	1.98	74.76	11.65	1.27	3.44	31.79	0.80	4.54	6.16	25.50	7.58	6.64	1.06	5.94	0.46	0.74	43.42	3.59	6.17	0.75	2.77	0.62	0.20	1.00	0.18	1.19	0.27	0.74	0.10	0.65	0.10	0.27	0.09	1.66	0.02	0.48	0.95	1.89
	W6	0.81	100.52	6.63	0.82	0.95	32.89	0.15	1.48	1.33	53.70	2.45	3.07	0.53	1.13	0.40	0.14	42.12	11.49	17.73	2.30	7.97	0.94	0.20	0.75	0.09	0.42	0.08	0.27	0.03	0.25	0.03	0.11	0.09	2.05	0.01	0.43	0.96	0.96
	W12	3.47	129.49	140.80	17.84	85.93	57.53	51.15	28.19	102.80	83.40	28.88	73.54	12.24	1.04	2.16	11.42	330.45	42.68	83.65	10.28	38.91	7.22	1.70	6.51	1.00	5.15	1.04	2.74	0.39	2.65	0.39	2.30	0.79	1.65	0.69	50.92	14.18	3.23

Inductively Coupled Optical Emmision Spectrometry (ICP-OES)													
Location	Sample ID	Al2O3	SiO2	TiO2	Fe2O3	MnO	MgO	CaO	Na2O	K2O	P2O5	Total	Sc
		Wt. %	Wt. %	Wt. %	Wt. %	Wt. %	Wt. %	Wt. %	Wt. %	Wt. %	Wt. %	Wt. %	ppm
	P1	10.03	77.91	0.62	3.18	0.05	0.80	1.07	0.96	1.32	0.09	96.02	7.73
	P2	11.15	75.05	0.61	4.93	0.07	1.04	0.85	0.84	1.35	0.10	96.01	8.46
	P4	18.71	59.19	0.97	9.57	0.13	1.76	0.33	0.93	2.23	0.09	93.91	18.36
	P5	14.61	73.52	0.57	4.36	0.04	0.87	0.29	0.91	1.80	0.08	97.06	9.92
	P7	23.50	42.94	0.85	1.93	0.01	0.68	0.33	0.20	1.54	0.05	72.03	18.50
	R1	6.59	67.21	0.77	1.79	0.10	0.71	10.66	0.57	0.81	0.09	89.29	7.38
	R2	17.88	64.25	1.07	5.56	0.07	1.60	0.27	0.85	2.31	0.07	93.92	12.07
	R3	10.43	79.51	0.60	3.26	0.06	0.42	0.47	0.87	1.23	0.08	96.93	7.75
	R5	22.47	58.30	1.01	5.15	0.03	1.51	0.24	0.50	2.36	0.06	91.63	20.89
	R6	25.67	42.07	0.77	2.44	0.01	1.57	0.24	0.53	4.27	0.07	77.65	24.35
	R7	1.09	3.41	0.04	0.36	0.00	0.17	0.29	0.21	0.08	0.01	5.66	0.89
	R8	25.64	50.66	0.91	4.64	0.02	1.41	0.36	0.22	2.19	0.09	86.14	17.17
	R9	10.74	75.23	0.58	5.43	0.08	0.81	0.66	0.86	1.34	0.08	95.80	9.92
	R11	1.49	3.01	0.04	10.56	0.00	0.07	0.14	0.05	0.11	0.01	15.46	3.59
	R15	23.79	48.82	0.83	4.72	0.05	1.32	0.88	0.22	2.07	0.14	82.84	18.94
	W1	10.56	78.36	0.52	2.96	0.06	0.59	1.20	0.86	1.23	0.07	96.43	7.16
	W2	28.16	56.01	1.09	2.35	0.01	1.01	0.30	0.14	2.02	0.04	91.12	23.51
	W3	1.65	3.55	0.04	1.82	0.00	0.10	0.20	0.08	0.13	0.01	7.59	3.69
	W6	0.43	1.89	0.02	0.26	0.00	0.08	0.22	0.12	0.03	0.02	3.07	1.49
	W12	23.58	45.72	0.78	12.08	0.14	1.18	0.32	0.26	1.96	0.23	86.25	22.71

Appendix 12

XRD Data for the EH03B borehole at Bayfield

Well	Depth (m)	Illite+Mica_XRD	Kaolinite_XRD	Chlorite_XRD	Quartz_XRD	K Feldspar_XRD	Plagioclase_XRD	Calcite_XRD	Dolomite_XRD	Siderite_XRD	Pyrite_XRD	Marcasite_XRD	Amorphous_XRD
EH03B	6.00	0.0	7.6	0.0	88.2	4.2	0.0	0.0	TR	0.0	0.0	0.0	0.0
EH03B	9.20	30.5	33.3	9.0	19.1	3.6	2.5	0.0	0.0	2.0	0.0	0.0	0.0
EH03B	12.70	9.2	17.3	1.5	50.8	5.3	3.1	0.0	6.4	6.3	0.0	0.0	0.0
EH03B	14.10	10.4	12.2	0.0	57.9	4.2	3.6	0.0	10.8	0.8	0.0	0.0	0.0
EH03B	14.55	25.0	17.5	1.9	41.7	4.4	4.7	0.0	2.4	2.6	0.0	0.0	0.0
EH03B	16.25	51.0	10.3	8.7	26.4	TR	0.0	0.0	0.0	3.6	0.0	0.0	0.0
EH03B	18.50	48.7	7.8	8.1	33.4	TR	0.0	0.0	0.0	2.0	0.0	0.0	0.0
EH03B	22.10	26.2	28.8	5.4	34.2	4.2	TR	0.0	0.0	1.2	0.0	0.0	0.0
EH03B	23.55	TR	22.0	0.0	72.6	5.5	TR	0.0	0.0	0.0	0.0	0.0	0.0
EH03B	25.90	TR	12.5	0.0	82.1	5.4	0.0	0.0	0.0	0.0	0.0	0.0	0.0
EH03B	28.80	5.3	11.6	0.0	76.6	6.6	0.0	0.0	0.0	0.0	0.0	0.0	0.0
EH03B	31.40	TR	12.5	0.0	80.9	6.6	0.0	0.0	0.0	0.0	0.0	0.0	0.0
EH03B	32.75	5.3	16.0	0.0	70.2	6.5	0.0	0.0	1.9	TR	TR	0.0	0.0
EH03B	33.25	13.2	21.5	0.0	56.7	6.7	1.9	0.0	0.0	TR	0.0	0.0	0.0
EH03B	35.40	TR	12.4	0.0	77.2	5.5	0.0	0.0	2.3	TR	2.7	0.0	0.0
EH03B	36.62	7.1	13.7	0.0	72.2	6.1	0.0	0.0	0.0	TR	0.9	0.0	0.0
EH03B	37.30	6.7	9.4	0.0	44.7	3.2	0.0	0.0	0.0	0.0	35.9	0.0	0.0
EH03B	39.40	0.0	4.4	0.0	1.5	0.0	0.0	0.0	0.0	0.0	2.7	0.6	90.9
EH03B	41.15	44.3	6.7	6.9	33.5	2.4	4.8	0.0	0.0	1.3	TR	0.0	0.0
EH03B	43.00	23.5	5.3	4.0	53.6	2.5	9.6	0.0	0.0	1.4	0.0	0.0	0.0
EH03B	43.45	29.0	5.6	4.5	46.9	2.6	8.9	0.0	0.0	2.5	0.0	0.0	0.0

Appendix 13

Permeability measurements for the EH01 samples

Sample Depth from Surface (m)	TinyPerm II Value	Permeability (mD)	Average Permeability (mD)
	11.25	95.20815317	
22.55	11.2	109.5481801	92.22336951
	11.35	71.91377529	
	10.66	498.4943595	
23.55	10.74	398.2635924	495.5522358
	10.6	589.8987554	
	10.2	1812.281631	
24	10.29	1407.828788	1583.860097
	10.26	1531.469871	
	10.44	924.1804204	
24.25	10.52	738.3582327	814.5059898
	10.5	780.9793163	
	10.85	292.4976286	
24.65	10.79	346.1302697	334.9127451
	10.77	366.110337	
	10.69	458.2491129	
25.45	10.69	458.2491129	496.6915423
	10.61	573.5764011	
	11.06	162.2602123	
26.5	11.06	162.2602123	163.7993672
	11.05	166.8776768	
	10.55	678.747911	
27.55	10.7	445.5694721	515.1901311
	10.72	421.2530102	
	10.63	542.2741025	
28	10.54	698.0631476	673.7721888
	10.5	780.9793163	
	10.58	623.9501455	
28.45	10.66	498.4943595	522.6713257
	10.7	445.5694721	
	10.41	1005.345594	
29.05	10.39	1063.37829	1024.689826
	10.41	1005.345594	
	10.42	977.5279274	
29.55	10.47	849.5680037	822.9339748
	10.57	641.7059934	
	10.88	268.8832407	
29.95	10.78	355.9801535	293.0242097
	10.9	254.2092348	
	10.36	1156.76837	
30.45	10.39	1063.37829	1075.164085
	10.41	1005.345594	
	11.23	100.7039606	
31.5	11.44	55.86454189	76.84291315
	11.34	73.96023696	
	10.8	336.5529298	
31.9	10.83	309.3817986	333.9716273
	10.78	355.9801535	

follow on in next column

Sample Depth from Surface (m)	TinyPerm II Value	Permeability (mD)	Average Permeability (mD)
	10.91	247.1753275	
32.55	10.64	527.2695107	419.7153269
	10.67	484.7011425	
	11.22	103.5697091	
33	11.12	137.1181069	117.7844753
	11.19	112.6656099	
	10.61	573.5764011	
33.1	10.59	606.6855976	590.0535847
	10.6	589.8987554	
	10.76	376.5287967	
33.7	10.59	606.6855976	503.494635
	10.64	527.2695107	
	10.26	1531.469871	
36	10.19	1863.854016	1719.153376
	10.21	1762.136241	
	10.83	309.3817986	
38.65	10.73	409.5970424	322.0513895
	10.91	247.1753275	

Appendix 14

Permeability measurements for the EH02 samples

Sample Depth from Surface (m)	TinyPerm II Value	Permeability (mD)	Average Permeability (mD)
	10.23	1665.969602	
6.15	10.21	1762.136241	1667.718998
	10.25	1575.051151	
	10.66	498.4943595	
6.8	10.7	445.5694721	443.7691893
	10.75	387.2437362	
	10.39	1063.37829	
7.35	10.33	1258.360336	1181.760146
	10.34	1223.541813	
	10.63	542.2741025	
7.75	10.52	738.3582327	666.186792
	10.53	717.9280409	
	10.5	780.9793163	
8.9	10.44	924.1804204	828.7130177
	10.5	780.9793163	
	10.37	1124.760872	
9.8	10.32	1294.169695	1202.872426
	10.35	1189.68671	
	10.18	1916.894004	
11.4	10.19	1863.854016	1831.375461
	10.22	1713.378363	
	11.21	106.5170087	
11.9	11.05	166.8776768	128.6867652
	11.19	112.6656099	
	11.47	51.35439605	
23.2	11.57	38.78962437	65.55367638
	11.21	106.5170087	
	11.61	34.67135008	
24.1	11.41	60.77078655	46.6913875
	11.52	44.63202586	
	11.85	17.6807966	
25	11.85	17.6807966	18.19839572
	11.82	19.23359397	
	11.02	181.5335334	
25.5	11.01	186.6994618	181.58118
	11.03	176.5105449	
	11.2	109.5481801	
25.55	11.17	119.1691338	138.4722586
	11.01	186.6994618	
	11.07	157.7705119	
26.4	11.38	66.10791699	103.8000282
	11.28	87.52165577	
	11.38	66.10791699	
27	11.01	186.6994618	120.7851863
	11.2	109.5481801	
	11.11	141.0200986	
27.35	11.19	112.6656099	130.2679385
	11.12	137.1181069	

follow on in next column

Sample Depth from Surface (m)	TinyPerm II Value	Permeability (mD)	Average Permeability (mD)
	11.39	64.27872709	
28.6	11.11	141.0200986	88.68987074
	11.41	60.77078655	
	11.16	122.5603487	
29.05	11.42	59.08927375	90.55396526
	11.27	90.01227336	
	10.77	366.110337	
29.35	10.95	220.9328512	332.2134102
	10.73	409.5970424	
	10.73	409.5970424	
29.95	10.6	589.8987554	524.3573997
	10.61	573.5764011	
	10.75	387.2437362	
30.7	10.9	254.2092348	335.854436
	10.77	366.110337	
	10.48	826.0606648	
31.75	10.13	2205.612046	1430.011016
	10.33	1258.360336	
	11.1	145.0331298	
31.95	10.94	227.2199723	218.8857976
	10.86	284.4042908	
	10.59	606.6855976	
32.1	10.54	698.0631476	596.4832959
	10.67	484.7011425	
	10.74	398.2635924	
32.9	10.79	346.1302697	366.7913386
	10.78	355.9801535	
	11.18	115.871753	
33.45	11.18	115.871753	126.9679555
	11.09	149.1603605	
	11.4	62.50015043	
34.45	11.52	44.63202586	53.31599084
	11.46	52.81579622	
	11.47	51.35439605	
35.1	11.42	59.08927375	55.96598593
	11.43	57.45428799	
	11.19	112.6656099	
35.5	11.34	73.96023696	81.90504021
	11.42	59.08927375	
	11.29	85.09995296	
36.05	11.29	85.09995296	105.0776786
	11.1	145.0331298	
	10.95	220.9328512	
36.55	10.79	346.1302697	249.5322181
	11.02	181.5335334	
	11.48	49.93343247	
37.2	11.29	85.09995296	68.31910805
	11.36	69.92393872	

follow on in next column

Sample Depth from Surface (m)	TinyPerm II Value	Permeability (mD)	Average Permeability (mD)
	10.95	220.9328512	
37.45	10.89	261.4433072	223.0252068
	11.01	186.6994618	
	10.76	376.5287967	
38.5	10.98	203.0961458	255.4414681
	11.01	186.6994618	
	11.32	78.229527	
39.5	11.19	112.6656099	78.09740185
	11.53	43.39706862	
	11.32	78.229527	
39.9	11.1	145.0331298	140.246394
	10.99	197.4765251	
	11.21	106.5170087	
40.4	11.29	85.09995296	108.3136814
	11.13	133.3240824	

Appendix 15

Permeability measurements for the EH03B samples

Sample Depth from Surface (m)	TinyPerm II Value	Permeability (mD)	Average Permeability (mD)
6	10.16	2027.545035	1672.097392
	10.3	1368.87451	
	10.24	1619.872631	
7.2	10.59	606.6855976	531.5072869
	10.79	346.1302697	
	10.57	641.7059934	
8	10.38	1093.639014	1131.051434
	10.41	1005.345594	
	10.32	1294.169695	
9.2	11.57	38.78962437	37.02226152
	11.47	51.35439605	
	11.79	20.92276414	
9.85	11.88	16.25336215	22.79928664
	11.95	13.35487341	
	11.57	38.78962437	
10.87	11.58	37.71632495	49.38722288
	11.3	82.74525807	
	11.69	27.70008562	
11.7	11.71	26.18838404	28.83205831
	11.78	21.51816654	
	11.57	38.78962437	
13.65	11.36	69.92393872	114.7200509
	11.12	137.1181069	
	11.12	137.1181069	
14.1	11.1	145.0331298	187.8141687
	10.99	197.4765251	
	10.95	220.9328512	
14.55	12.02	10.97327692	8.490369718
	12.21	6.438703703	
	12.13	8.059128526	
15.55	11.68	28.48835133	31.04700002
	11.56	39.89346684	
	11.73	24.7591819	
20.85	11.28	87.52165577	112.3815302
	11.3	82.74525807	
	11.05	166.8776768	
22.1	10.95	220.9328512	234.1206861
	10.94	227.2199723	
	10.9	254.2092348	
23	11.51	45.90212648	89.37197216
	11.2	109.5481801	
	11.19	112.6656099	
23.2	11.47	51.35439605	56.50881267
	11.31	80.45571701	
	11.58	37.71632495	
23.55	10.8	336.5529298	300.1086106
	10.8	336.5529298	
	10.94	227.2199723	

follow on in next column

Sample Depth from Surface (m)	TinyPerm II Value	Permeability (mD)	Average Permeability (mD)
24	10.52	738.3582327	681.781067
	10.46	873.7442946	
	10.71	433.2406737	
24.4	10.61	573.5764011	547.7066714
	10.64	527.2695107	
	10.63	542.2741025	
24.8	10.47	849.5680037	987.8117115
	10.35	1189.68671	
	10.44	924.1804204	
25.6	10.31	1330.998087	1383.696882
	10.31	1330.998087	
	10.27	1489.094474	
25.9	10.57	641.7059934	676.4569691
	10.5	780.9793163	
	10.59	606.6855976	
26.1	10.83	309.3817986	306.6884509
	10.82	318.1859254	
	10.85	292.4976286	
26.45	10.75	387.2437362	501.0314133
	10.63	542.2741025	
	10.61	573.5764011	
26.9	10.39	1063.37829	1106.958325
	10.4	1033.954873	
	10.34	1223.541813	
28	10.64	527.2695107	581.6474385
	10.56	659.9671223	
	10.62	557.7056824	
28.15	10.51	759.3698096	773.9811291
	10.49	803.2037682	
	10.51	759.3698096	
28.8	10.77	366.110337	311.7142864
	10.85	292.4976286	
	10.87	276.5348936	
29.4	10.79	346.1302697	381.5534809
	10.68	471.2895804	
	10.81	327.2405925	
29.5	10.7	445.5694721	506.7231233
	10.6	589.8987554	
	10.67	484.7011425	
29.95	10.61	573.5764011	643.8688903
	10.54	698.0631476	
	10.56	659.9671223	
30.15	10.4	1033.954873	827.0918561
	10.46	873.7442946	
	10.61	573.5764011	
30.55	10.66	498.4943595	417.8152101
	10.83	309.3817986	
	10.7	445.5694721	

follow on in next column

Sample Depth from Surface (m)	TinyPerm II Value	Permeability (mD)	Average Permeability (mD)
31.4	10.21	1762.136241	1526.300782
	10.28	1447.891594	
	10.3	1368.87451	
32.1	10.5	780.9793163	664.7835038
	10.59	606.6855976	
	10.59	606.6855976	
32.5	10.76	376.5287967	459.9346504
	10.7	445.5694721	
	10.62	557.7056824	
32.75	11.43	57.45428799	70.62341399
	11.34	73.96023696	
	11.31	80.45571701	
33.25	11.5	47.20837054	44.33465462
	11.51	45.90212648	
	11.56	39.89346684	
34.35	10.45	898.6085741	907.1325229
	10.44	924.1804204	
	10.45	898.6085741	
35.4	10.75	387.2437362	380.9903495
	10.73	409.5970424	
	10.79	346.1302697	
36.05	11.06	162.2602123	182.1453997
	11.01	186.6994618	
	10.99	197.4765251	
36.62	10.97	208.8756849	206.3574122
	11.03	176.5105449	
	10.93	233.686007	
37.3	11.14	129.6350377	97.37758108
	11.26	92.57376685	
	11.36	69.92393872	
39.75	11.42	59.08927375	65.04037648
	11.36	69.92393872	
	11.38	66.10791699	
40.65	10.89	261.4433072	227.2762587
	11.01	186.6994618	
	10.93	233.686007	
43	11.18	115.871753	145.2984324
	11.01	186.6994618	
	11.13	133.3240824	

Appendix 16

ICPMS and ICPOES data for EH01 borehole at Bayfield

Well	Depth (m	Chemical GR	Al2O3_ICP	SiO2_ICP	TiO2_ICP	Fe2O3_ICP	MnO_ICP	MgO_ICP	CaO_ICP	Na2O_ICP	K2O_ICP	P2O5_ICP	Total_ICP	S_ICP	Be_ICP	Sc_ICP	V_ICP	Cr_ICP	Co_ICP	Ni_ICP	Cu_ICP	Zn_ICP	Ga_ICP	Rb_ICP	Sr_ICP	Y_ICP	Zr_ICP	Nb_ICP	Mo_ICP	Sn_ICP	Cs_ICP	Ba_ICP	La_ICP	Ce_ICP	Pr_ICP	Nd_ICP	Sm_ICP	Eu_ICP	Gd_ICP	Tb_ICP	Dy_ICP	Ho_ICP	Er_ICP	Tm_ICP	Yb_ICP	Lu_ICP	Hf_ICP	Ta_ICP	W_ICP	Tl_ICP	Pb_ICP	Th_ICP	U_ICP
		api	(wt.%)	(wt.%)	(wt.%)	(wt.%)	(wt.%)	(wt.%)	(wt.%)	(wt.%)	(wt.%)	(wt.%)	(wt.%)	(ppm)	(ppm)	(ppm)	(ppm)	(ppm)	(ppm)	(ppm)	(ppm)	(ppm)	(ppm)	(ppm)	(ppm)	(ppm)	(ppm)	(ppm)	(ppm)	(ppm)	(ppm)	(ppm)	(ppm)	(ppm)	(ppm)	(ppm)	(ppm)	(ppm)	(ppm)	(ppm)	(ppm)	(ppm)	(ppm)	(ppm)	(ppm)	(ppm)	(ppm)	(ppm)	(ppm)	(ppm)	(ppm)	(ppm)
EH01	10.00																																																			
EH01	11.20	80.88	21.36	55.68	1.04	6.42	0.07	1.82	0.53	0.44	2.55	0.14	90.03	102.88	2.78	15.30	97.51	144.62	28.10	75.05	33.30	55.76	29.12	128.57	91.14	27.85	248.54	14.72	0.76	2.75	9.48	462.51	50.87	98.45	11.19	40.21	7.00	1.47	5.84	0.84	4.93	0.99	2.79	0.46	2.87	0.43	6.76	1.74	1.45	0.80	10.65	13.76	3.31
EH01	12.20	56.62	11.37	73.29	0.66	4.85	0.08	1.18	0.78	0.43	1.53	0.12	94.27	274.26	0.99	10.01	65.78	76.51	13.08	33.23	12.49	37.78	14.44	63.55	58.22	23.64	396.88	9.16	0.26	1.55	3.12	382.51	35.76	75.14	8.89	33.90	6.26	1.19	5.24	0.73	4.30	0.87	2.36	0.41	2.29	0.34	10.20	1.41	0.98	0.44	6.09	9.85	2.22
EH01	12.55	61.01	14.11	61.20	0.84	7.33	0.10	1.81	0.99	0.52	1.92	0.16	88.96	188.20	1.58	14.80	97.43	110.67	21.58	49.49	20.57	47.48	20.71	93.56	74.99	26.42	350.61	11.19	0.35	2.32	5.43	452.32	41.88	87.42	10.41	39.50	7.35	1.57	6.17	0.90	5.00	0.98	2.62	0.41	2.46	0.37	9.07	1.51	1.15	0.61	6.63	10.17	2.60
EH01	13.10	39.10	10.88	70.56	0.61	5.04	0.10	1.34	2.31	0.43	1.47	0.14	92.89	815.37	0.95	9.61	58.96	68.20	12.63	31.02	13.31	36.09	13.83	63.59	57.76	18.89	282.53	8.56	0.18	1.63	3.19	440.24	28.13	59.16	7.05	26.60	5.00	1.04	4.11	0.60	3.38	0.68	1.80	0.32	1.74	0.27	7.25	1.37	1.03	0.45	5.95	6.75	1.56
EH01	14.05	87.78	23.64	52.57	1.05	6.56	0.09	1.99	0.72	0.17	3.31	0.18	90.27	208.19	3.39	21.92	127.42	143.23	19.61	65.73	41.02	54.33	31.33	166.24	123.32	36.42	129.54	16.19	0.74	2.94	14.15	501.82	53.68	105.07	12.33	45.96	8.41	1.88	7.06	1.06	6.47	1.33	3.68	0.56	3.52	0.51	3.72	1.89	1.90	0.82	5.75	15.53	3.31
EH01	15.00	86.62	22.43	52.38	1.04	6.99	0.10	1.91	0.61	0.27	2.67	0.13	88.53	192.11	2.89	21.49	118.96	145.41	20.77	65.98	40.74	61.96	29.73	140.76	106.88	34.04	212.90	15.52	0.79	2.72	11.25	1770.45	48.53	97.28	11.57	42.74	7.84	1.79	6.43	0.99	6.01	1.25	3.43	0.62	3.32	0.49	5.84	1.79	1.54	0.81	12.93	13.92	3.95
EH01	15.05	84.93	25.53	52.68	0.90	4.25	0.03	1.74	0.63	0.18	3.52	0.10	89.57	294.45	3.65	18.69	112.92	145.71	23.30	78.52	40.33	60.52	30.67	181.90	106.68	20.78	118.28	14.80	0.48	5.28	15.66	562.42	42.54	79.61	9.31	32.94	5.34	1.12	4.24	0.62	3.66	0.79	2.24	0.41	2.29	0.35	3.36	1.82	2.29	1.02	13.29	15.71	2.87
EH01	15.65	44.40	10.07	26.08	0.35	10.80	0.48	6.38	15.62	0.14	2.18	1.00	73.10	611.14	1.82	16.33	71.79	56.55	8.42	31.25	25.70	35.64	12.91	96.23	142.93	59.39	84.51	6.20	0.43	1.52	6.95	1421.90	30.41	65.04	8.98	41.07	10.64	2.88	11.04	1.68	9.76	1.81	4.14	0.55	3.06	0.43	2.29	1.23	1.05	0.45	5.87	5.90	2.62
EH01	16.55	73.20	19.95	53.33	0.81	6.64	0.11	2.06	0.70	0.21	3.91	0.16	87.87	126.01	3.25	20.16	122.28	105.92	20.90	58.52	47.30	96.24	25.68	186.36	107.87	29.80	146.89	14.18	0.87	2.97	15.48	474.79	39.46	79.10	9.48	36.00	6.92	1.51	5.86	0.87	5.30	1.08	2.97	0.47	2.87	0.43	4.19	1.76	1.81	0.86	32.43	11.98	3.23
EH01	17.05	72.02	20.60	54.21	0.82	6.18	0.10	2.05	0.72	0.21	4.01	0.14	89.05	111.70	3.10	21.10	123.69	107.99	18.36	55.88	43.65	75.50	26.42	190.92	108.36	29.71	150.82	14.45	0.59	3.12	15.83	466.67	41.22	81.90	9.71	36.73	6.82	1.52	5.67	0.87	5.24	1.08	2.95	0.47	2.98	0.44	4.24	1.79	1.92	0.90	27.46	12.16	3.00
EH01	17.60	74.22	21.02	55.42	0.87	4.91	0.06	1.81	0.63	0.22	4.09	0.13	89.17	540.85	3.35	17.87	119.77	102.65	26.27	64.88	42.70	62.05	26.78	190.52	107.67	27.05	150.10	15.19	1.10	2.26	16.46	525.59	39.58	77.40	8.91	32.33	5.71	1.25	4.89	0.74	4.59	0.98	2.79	0.47	2.87	0.43	4.25	1.87	2.03	1.03	46.54	12.64	3.04
EH01	19.00	72.92	20.16	54.95	0.83	6.12	0.10	2.01	0.65	0.21	3.98	0.14	89.16	282.18	3.23	20.19	124.10	106.11	22.57	61.30	45.08	61.29	25.90	186.26	109.16	29.87	152.78	14.67	1.35	2.75	15.60	516.68	39.74	79.97	9.55	36.48	6.87	1.55	5.95	0.90	5.39	1.09	3.02	0.47	2.96	0.44	4.26	1.83	2.01	0.86	15.01	12.12	3.13
EH01	20.05	89.89	23.00	58.63	1.06	3.73	0.02	1.47	0.34	0.28	2.55	0.07	91.13	43.22	3.48	19.81	123.69	152.93	22.20	59.71	44.10	71.26	29.53	114.29	90.71	35.29	273.96	15.69	0.57	2.67	9.44	468.75	57.54	116.72	13.62	51.13	9.09	2.01	7.65	1.09	6.42	1.32	3.55	0.54	3.43	0.51	7.33	1.76	1.57	0.60	8.20	15.43	3.62
EH01	20.55	89.97	23.10	58.25	1.04	3.63	0.02	1.45	0.41	0.28	2.56	0.07	90.81	102.55	3.60	19.09	116.85	150.26	19.99	58.76	38.63	56.37	30.16	114.99	95.13	35.24	267.14	15.58	0.62	2.79	9.58	572.52	57.24	116.03	13.55	50.45	9.12	1.93	7.46	1.09	6.42	1.35	3.58	0.55	3.43	0.49	7.26	1.81	1.45	0.67	12.28	15.60	3.55
EH01	20.90	81.41	20.22	59.02	0.96	5.21	0.03	1.22	0.38	0.33	2.39	0.06	89.81	1518.52	2.86	13.20	99.87	133.73	20.27	104.80	29.80	66.41	25.72	103.79	86.62	26.98	322.71	14.11	0.70	1.58	8.27	500.64	48.73	96.27	11.16	39.96	6.98	1.36	5.62	0.81	4.79	0.99	2.76	0.47	2.90	0.44	8.58	1.67	1.36	3.43	8.31	13.84	3.34
EH01	21.50	93.79	27.06	55.42	1.10	3.21	0.02	1.30	0.40	0.15	2.89	0.05	91.60	124.63	5.08	24.79	165.66	175.80	24.38	62.99	38.03	51.51	41.94	131.94	81.82	24.83	174.27	17.22	0.82	3.41	14.02	435.58	48.23	90.33	10.24	36.39	5.99	1.32	4.97	0.74	4.57	0.94	2.65	0.44	2.80	0.42	4.75	1.90	1.46	0.84	12.77	16.42	3.62
EH01	22.10	99.61	22.58	61.06	1.22	2.87	0.02	1.24	0.31	0.27	2.88	0.07	92.52	553.89	3.06	21.62	135.87	172.63	25.54	59.61	29.20	60.59	36.73	125.50	97.89	33.18	406.80	18.18	0.74	2.88	8.97	1872.43	62.34	124.03	14.18	51.91	8.91	1.91	7.26	1.05	6.08	1.23	3.35	0.54	3.41	0.51	10.77	1.93	1.49	0.88	8.63	17.29	3.92
EH01	22.55	22.65	9.54	81.14	0.28	1.27	0.00	0.17	0.25	0.15	1.47	0.02	94.29	254.88	0.66	3.54	42.74	42.63	3.92	11.44	3.38	13.45	11.43	40.13	63.21	9.31	138.73	4.62	0.30	0.92	0.93	366.76	25.62	51.95	5.76	21.43	3.57	0.83	2.48	0.32	1.76	0.35	0.98	0.18	1.02	0.16	3.71	1.12	0.76	0.34	7.34	3.75	0.98
EH01	23.55	15.85	5.42	86.34	0.12	0.76	0.00	0.11	0.22	0.08	1.26	0.02	94.33	216.44	0.40	1.91	18.61	19.05	2.39	6.47	2.37	12.45	6.16	31.76	53.63	8.28	91.63	2.09	0.23	0.59	0.61	447.96	19.25	41.28	4.66	17.75	3.07	0.83	2.36	0.32	1.64	0.32	0.84	0.20	0.78	0.12	2.50	0.97	1.92	0.25	8.64	2.72	0.64
EH01	24.00	12.78	5.26	87.86	0.08	1.22	0.01	0.11	0.19	0.09	1.19	0.02	96.02	184.29	0.29	1.62	17.15	14.54	3.24	7.23	2.43	9.66	5.74	29.22	54.08	7.32	89.37	1.56	0.36	1.49	0.51	388.75	15.21	32.00	3.47	13.24	2.20	0.60	1.70	0.23	1.36	0.27	0.72	0.16	0.69	0.11	2.38	0.93	0.70	0.23	10.81	2.06	0.58
EH01	24.25	15.09	4.57	87.73	0.13	0.79	0.00	0.09	0.18	0.08	1.13	0.02	94.74	238.30	0.29	1.24	15.41	15.06	3.09	8.25	3.02	8.18	4.73	27.26	57.85	7.94	80.59	2.16	0.44	0.57	0.44	358.84	15.21	31.94	3.52	12.89	2.26	0.58	1.76	0.25	1.42	0.29	0.77	0.15	0.73	0.10	2.09	0.97	0.73	0.22	9.21	2.80	0.51
EH01	24.65	25.38	6.03	86.74	0.26	0.65	0.00	0.10	0.22	0.07	1.11	0.02	95.21	250.82	0.35	1.47	24.82	29.81	2.33	5.73	1.76	6.36	6.70	28.01	66.12	6.85	166.21	3.77	0.27	1.02	0.54	323.20	21.43	44.02	4.83	17.52	2.95	0.58	2.17	0.26	1.33	0.26	0.70	0.18	0.71	0.11	4.28	1.08	0.63	0.24	8.96	4.63	0.89
EH01	25.45	11.47	6.04	87.82	0.12	0.35	0.00	0.09	0.16	0.08	1.13	0.02	95.82	138.31	0.26	1.09	17.31	15.29	1.99	6.20	2.21	6.85	5.67	27.48	42.49	5.02	77.49	2.30	0.33	1.03	0.39	293.99	12.48	25.60	2.84	10.62	1.71	0.44	1.29	0.15	0.81	0.16	0.46	0.12	0.43	0.07	2.04	1.11	0.59	0.28	7.73	1.91	0.49
EH01	26.50	17.64	6.58	81.67	0.20	1.18	0.01	0.14	0.18	0.09	1.36	0.03	91.43	192.34	0.38	3.10	30.52	27.82	3.21	8.75	2.50	13.25	7.23	34.50	53.17	6.39	92.28	3.60	0.51	1.11	0.54	371.12	18.29	37.57	4.20	15.21	2.44	0.62	1.80	0.22	1.14	0.23	0.65	0.15	0.67	0.10	2.48	1.04	1.22	0.29	7.38	3.11	0.67
EH01	26.85	16.02	5.05	88.10	0.17	1.38	0.01	0.10	0.20	0.07	0.98	0.03	96.09	281.93	0.33	2.95	18.32	18.32	3.28	9.28	3.20	26.45	4.69	23.88	44.62	5.55	79.75	3.28	0.54	0.94	0.38	296.56	16.32	28.12	3.16	11.48	2.03	0.51	1.57	0.21	1.18	0.24	0.64	0.14	0.63	0.10	2.13	1.07	1.16	0.24	6.93	2.89	0.58
EH01	27.55	19.55	5.31	88.75	0.17	0.58	0.00	0.13	0.26	0.09	1.36	0.03	96.66	263.52	0.31	2.55	18.78	19.32	3.40	7.88	2.91	9.00	5.82	32.55	62.72	5.67	103.71	2.63	0.38	0.87	0.51	367.26	17.48	36.55	3.99	14.64	2.37	0.57	1.69	0.21	1.05	0.22	0.57	0.13	0.59	0.09	2.63	1.02	0.59	0.27	7.99	3.53	0.70
EH01	28.00	19.54	4.86	89.16	0.24	0.55	0.01	0.11	0.28	0.07	1.00	0.02	96.28	239.42	0.27	3.26	18.54	22.87	4.49	8.80	2.94	12.59	4.45	23.30	46.26	6.50	164.56	3.39	0.33	0.59	0.36	288.54	15.52	32.43	3.67	13.57	2.35	0.53	1.74	0.24	1.24	0.25	0.70	0.15	0.77	0.12	4.08	1.28	0.84	0.24	8.60	3.50	0.72
EH01	28.45	13.83	6.65	85.20	0.18	0.84	0.00	0.12	0.17	0.08	1.21	0.03	94.49	166.01	0.39	3.32	28.93	24.61	2.66	6.69	4.81	8.82	6.21	30.38	43.13	4.27	94.72	3.20	0.38	0.72	0.48	308.05	11.49	21.70	2.35	8.44	1.35	0.33	1.07	0.14	0.77	0.16	0.46	0.13	0.51	0.08	2.54	1.11	0.65	0.28	7.89	2.30	0.59
EH01	29.05	11.02	6.69	86.59	0.11	0.47	0.00	0.11	0.20	0.09	1.42	0.02	95.69	317.20	0.35	1.16	17.43	16.19	2.32	5.83	2.29	8.83	5.95	34.06	63.76	3.50	98.75	1.90	0.44	1.03	0.45	376.67	13.68	25.64	2.60	8.84	1.24	0.28	0.99	0.11	0.66	0.12	0.38	0.10	0.43	0.07	2.55	0.97	0.76	0.68	11.40	1.77	0.50
EH01	29.55	41.96	7.14	77.09	0.16	2.60	0.05	0.52	1.92	0.08	1.13	0.06	90.75	2834.61	2.78	10.20	38.76	32.34	11.00	82.91	12.81	198.73	6.13	27.45	59.56	67.92	105.47	2.72	0.39	0.61	0.40	315.08	35.33	100.13	14.06	65.62	17.19	5.59	15.76	2.65	16.11	3.14	8.36	1.28	8.69	1.25	2.72	1.02	0.64	0.40	3.95	6.26	2.15
EH01	29.95	19.95	4.54	85.61	0.20	3.03	0.04	0.12	0.16	0.08	1.04	0.03	94.85	312.34	0.48	3.74	17.28	22.13	10.76	12.39	3.45	44.40	4.45	26.73	44.39	6.70	112.50	3.10	0.42	0.63	0.53	499.45	10.04	20.33	2.30	8.69	1.55	0.41	1.32	0.20	1.21	0.25	0.68	0.14	0.73	0.11	2.91	1.07	0.55	1.81	17.17	3.57	0.73
EH01	30.45	16.79	4.44	87.37	0.11	2.78	0.02	0.09	0.15	0.08	1.02	0.04	96.10	217.36	0.51	4.04	17.50	18.97	9.35	14.08	3.35	47.61	4.02	24.99	42.51	6.32	101.66	1.93	0.44	1.02	0.40	260.71	12.72	26.75	3.01	11.34	2.09	0.54	1.69	0.25	1.41	0.28	0.76	0.17	0.83	0.12	2.72	1.02	0.60	0.32	6.35	2.97	0.63
EH01	31.50	31.60	7.96	83.55	0.40	1.42	0.01	0.15	0.24	0.10	1.29	0.03	95.17	381.87	0.46	3.74	38.80	48.96	4.13	6.43	2.01	25.76	9.06	35.94	69.02	10.19	176.54	6.94	0.42	1.29	1.01	374.98	27.42	56.64	5.65	20.28	3.26	0.68	2.47	0.33	1.79	0.37	1.05	0.20	1.01	0.16	4.66	1.30	1.00	0.41	5.37	5.88	1.05
EH01	31.90	21.90	5.53	89.36	0.34	1.04	0.01	0.13	0.23	0.08	0.91	0.03	97.66	198.29	0.31	2.57	22.48	29.05	3.79	6.12	2.30	15.41	5.23	22.24	40.15	10.47	148.03	5.46	0.31	0.85	0.33	230.71	17.59	36.80	4.04	14.60	2.43	0.56	2.01	0.29	1.81	0.37	1.04	0.20	1.01	0.15	3.83	1.22	0.63	0.16	3.89	4.01	0.76
EH01	32.55	27.93	6.19	87.54	0.52	1.05	0.01	0.11	0.17	0.09	1.09	0.03	96.81	287.81	0.37	2.88	27.31	46.71	5.10	10.40	2.98	27.11	6.04	26.89	46.20	15.90	218.69	7.23	0.36	1.06	0.35	288.34	20.97	43.85	4.99	18.52	3.16	0.72	2.59	0.40	2.58	0.56	1.58	0.29	1.58	0.23	5.59	1.26	0.82	0.19	4.53	5.07	0.99
EH01	33.00	19.03	8.03	84.06	0.24	1.13	0.01	0.14	0.24	0.15	1.32	0.03	95.34	459.83	0.46	4.64	31.98	31.69	4.33	7.92	2.50	24.45	8.27	33.16	49.15	8.92	118.28	3.99	0.34	3.60	0.52	312.70	20.00	42.63	4.71	17.39	2.87	0.68	2.07	0.27	1.54	0.32	0.90	0.18	0.85	0.13	3.05	1.26	0.58	0.25	4.49	3.19	0.81
EH01	33.10	17.01	5.01	88.95	0.11	2.19	0.01	0.11	0.16	0.09	1.28	0.04	97.95	257.90	0.54	6.33	25.65	20.50	7.74	18.83	5.60	41.10	6.34	33.52	66.36	18.56	74.71	1.89	0.72	1.07	0.76	339.24	23.22	54.34	6.14	24.80	5.22	1.57	4.65	0.73	4.22	0.83	2.14	0.35	2.14	0.30	2.00	1.00	0.61	0.22	8.45	2.81	0.74
EH01	33.70	13.50	4.63	88.88	0.12	2.08	0.02	0.08	0.16	0.08	1.09	0.02	97.17	1197.49	0.24	2.03	18.42	15.65	9.06	14.97	2.70	50.94	4.63	26.53	49.15	15.59	80.67	1.91	0.42	0.56	0.38	281.90	15.26	34.32	3.69	14.33	2.60	0.74	2.44	0.38	2.24	0.48	1.27	0.21	1.09	0.16	2.17	0.93	0.47	0.19	5.17	2.21	0.59
EH01	36.00	29.80	7.96	82.74	0.39	2.08	0.02	0.16	0.21	0.18	1.31	0.03	95.07	867.00	0.43	5.15	33.28	43.51	7.31	11.91	3.99	57.27	8.54	33.97	43.05	13.60	206.71	5.88	0.33	0.96	0.80	336.36	23.09	47.50	5.45	20.65	3.60	0.77	2.85	0.42	2.44	0.49	1.33	0.23	1.28	0.19	5.34	1.22	0.70	0.27	3.81	5.19	1.16
EH01	38.65	33.63	7.72	82.12	0.46	1.60	0.01	0.18	0.25	0.16	1.34	0.02	93.88	721.56	0.54	4.64	40.05	50.28	5.11	9.82	4.74	22.86	8.97	39.20	44.99	13.88	232.74	6.91	0.55	1.12	1.99	501.92	24.79	51.67	5.91	22.06	3.84	0.83	2.98	0.41	2.39	0.50	1.39	0.24	1.38	0.21	5.95	1.31	0.85	0.48	6.64	5.78	1.35
EH01	38.80	68.16	15.10	51.49	1.05	9.30	0.03	1.23	0.38	0.18	2.55	0.03	81.34	3890.24	2.07	13.85	93.77	76.54	27.87	60.96	54.68	76.51	18.59	113.90	104.60	25.92	180.98	16.15	4.01	0.32	13.82	6307.46	34.51	69.34	8.10	29.88	5.66	1.39	4.55	0.71	4.56	0.97	2.70	0.67	2.75	0.41	4.93	1.90	2.19	0.97	3.27	11.13	3.02
EH01	40.50	79.84	19.02	61.86	1.08	4.86	0.06	1.93	0.65	0.42	3.64	0.11	93.62	224.24	3.10	19.14	118.56	97.68	20.43	55.70	38.42	67.91	24.66	166.04	105.19	42.82	227.16	18.93	0.49	3.49	14.49	608.76	49.04	101.71	12.08	46.48	8.88	1.99	7.89	1.24	7.57	1.56	4.13	0.66	3.89	0.59	6.19	2.08	2.21	0.78	6.53	13.38	3.37
EH01	41.40	73.05	16.80	58.28	1.01	9.03	0.08	1.70	0.63	0.59	3.24	0.12	91.50	1802.24	2.47	16.08	104.17	85.43	14.75	42.85	41.48	60.69	21.68	141.65	99.45	36.07	204.64	17.41	0.65	1.40	11.04	609.16	44.18	92.33	10.97	42.17	8.18	1.88	7.08	1.09	6.68	1.34	3.59	0.54	3.39	0.51	5.65	2.02	2.41	1.56	2.37	12.38	3.02
EH01	42.85	71.57	13.26	70.99	0.94	4.12	0.07	1.31	0.51	1.11	2.34	0.11	94.75	161.44	1.90	11.13	76.35	71.53	12.41	31.10	18.92	53.41	16.26	96.54	84.29	36.10	448.33	16.52	0.46	3.21	5.83	387.66	41.10	83.29	9.68	36.57	6.95	1.48	5.99	0.97	6.14	1.30	3.59	0.57	3.69	0.55	11.80	1.97	1.88	0.53	5.79	11.93	3.06
EH01	43.55	79.37	16.02	63.35	1.08	6.04	0.10	1.75	0.59	0.90	2.96	0.14	92.93	154.36	2.51	15.38	103.26	89.18	14.60	38.34	26.02	67.97	21.34	130.06	102.42	37.06	314.55	19.04	0.69	3.25	8.74	552.72	46.88	95.56	11.14	41.80	7.66	1.65	6.82	1.05	6.50	1.36	3.74	0.60	3.75	0.55	8.47	2.13	2.18	0.66	7.01	13.26	3.37
EH01	44.50	60.69	12.62	68.20	0.83	6.37	0.12	1.53	0.63	0.93	2.22	0.12	93.57	140.12	1.84	13.13	82.93	66.28	14.47	31.30	19.18	49.31	15.38	93.02	79.99	28.46	269.10	14.39	0.75	2.54	5.60	443.70	34.53	71.11	8.38	32.43	6.22	1.39	5.40	0.82	5.10	1.06	2.89	0.47	2.81	0.43	7.18	1.83	1.63	0.46	5.92	10.08	2.61
EH01	45.00	71.87	14.84	66.46	0.98	5.73	0.10	1.63	0.63	0.96	2.67	0.12	94.12	120.62

Appendix 17

ICPMS and ICPOES data for EH02 borehole at Bayfield

Well	Depth (m)	hemical C	Al2O3_ICI	SiO2_ICP	TiO2_ICP	Fe2O3_IC	MnO_ICP	MgO_ICP	CaO_ICP	Na2O_ICF	K2O_ICP	P2O5_ICF	Total_ICF	S_ICP	Be_ICP	Sc_ICP	V_ICP	Cr_ICP	Co_ICP	Ni_ICP	Cu_ICP	Zn_ICP	Ga_ICP	Rb_ICP	Sr_ICP	Y_ICP	Zr_ICP	Nb_ICP	Mo_ICP	Sn_ICP	Cs_ICP	Ba_ICP	La_ICP	Ce_ICP	Pr_ICP	Nd_ICP	Sm_ICP	Eu_ICP	Gd_ICP	Tb_ICP	Dy_ICP	Ho_ICP	Er_ICP	Tm_ICP	Yb_ICP	Lu_ICP	Hf_ICP	Ta_ICP	W_ICP	Tl_ICP	Pb_ICP	Th_ICP	U_ICP
		api	(wt.%)	(wt.%)	(wt.%)	(wt.%)	(wt.%)	(wt.%)	(wt.%)	(wt.%)	(wt.%)	(wt.%)	(wt.%)	(ppm)	(ppm)	(ppm)	(ppm)	(ppm)	(ppm)	(ppm)	(ppm)	(ppm)	(ppm)	(ppm)	(ppm)	(ppm)	(ppm)	(ppm)	(ppm)	(ppm)	(ppm)	(ppm)	(ppm)	(ppm)	(ppm)	(ppm)	(ppm)	(ppm)	(ppm)	(ppm)	(ppm)	(ppm)	(ppm)	(ppm)	(ppm)	(ppm)	(ppm)	(ppm)	(ppm)	(ppm)	(ppm)	(ppm)
EH02	6.15	24.35	3.60	91.76	0.59	1.49	0.00	0.13	0.20	0.06	0.60	0.02	98.45	103.00	0.20	2.62	25.99	64.63	1.53	1.74	4.31	19.21	3.79	15.95	39.42	8.77	266.40	8.08	0.35	0.91	0.79	394.11	16.39	30.67	3.32	11.52	1.82	0.37	1.53	0.23	1.51	0.32	0.88	0.25	0.90	0.14	6.51	1.92	1.27	0.12	6.28	4.58	0.66
EH02	6.80	12.60	3.39	91.12	0.59	1.97	0.00	0.11	0.15	0.07	0.63	0.02	97.65	96.05	0.22	2.32	23.39	24.49	1.39	1.04	2.34	16.01	3.66	16.31	45.68	5.24	115.08	3.66	0.38	1.52	0.82	488.29	11.08	19.75	2.08	7.27	1.16	0.26	0.92	0.13	0.85	0.19	0.57	0.13	0.68	0.11	2.91	1.12	1.27	0.12	7.14	2.13	0.52
EH02	7.35	11.49	4.39	91.86	0.16	1.19	0.00	0.10	0.15	0.07	0.70	0.01	98.65	73.74	0.15	1.85	17.34	21.68	0.88	0.72	1.88	8.90	3.79	16.40	35.96	3.74	95.07	3.33	0.28	0.41	0.40	422.15	8.60	16.60	1.84	6.68	1.10	0.27	0.88	0.12	0.68	0.13	0.39	0.10	0.41	0.07	2.44	1.07	0.54	0.12	6.10	2.00	0.45
EH02	7.75	14.13	4.75	90.35	0.31	1.65	0.00	0.10	0.16	0.07	0.72	0.01	98.14	58.74	0.17	2.80	20.92	34.10	0.89	0.24	2.38	14.03	4.47	16.17	38.26	4.42	145.05	5.42	0.17	0.69	0.35	369.37	7.27	13.30	1.46	5.28	0.84	0.20	0.72	0.11	0.71	0.16	0.48	0.34	0.56	0.09	3.72	1.23	0.45	0.13	6.07	2.38	0.59
EH02	8.90	20.84	6.80	89.14	0.29	0.42	0.00	0.15	0.17	0.13	1.14	0.02	98.25	41.43	0.30	2.73	25.94	31.99	0.95	2.11	2.49	7.05	7.29	20.69	65.07	8.92	133.67	5.69	0.13	0.85	0.62	351.63	26.17	52.71	5.70	20.54	3.15	0.73	2.48	0.31	1.66	0.32	0.88	0.17	0.85	0.13	3.39	1.32	0.63	0.22	11.66	3.76	0.75
EH02	9.80	14.26	6.15	88.86	0.45	0.69	0.00	0.12	0.16	0.10	0.88	0.02	97.64	72.92	0.31	3.61	28.79	36.07	0.74	0.89	3.17	10.38	7.24	21.45	65.49	6.82	210.01	7.54	0.15	1.02	0.52	254.08	17.54	32.77	3.48	12.22	1.76	0.37	1.32	0.17	1.03	0.24	0.72	0.17	0.91	0.15	5.12	1.74	0.61	0.16	9.93	2.63	0.78
EH02	11.40	10.54	4.03	92.48	0.14	0.45	0.00	0.09	0.16	0.11	0.88	0.01	98.36	100.38	0.11	0.84	9.37	13.60	1.06	1.53	1.41	10.31	3.11	19.27	40.22	3.92	82.59	2.78	0.15	0.57	0.28	256.64	10.54	21.66	2.29	8.16	1.23	0.27	0.96	0.12	0.68	0.14	0.39	0.10	0.42	0.06	2.14	1.25	1.27	0.15	13.70	1.73	0.46
EH02	11.95	76.16	18.27	56.41	1.04	14.36	0.02	0.69	0.34	0.13	2.64	0.06	93.95	107.76	2.03	15.18	139.53	146.91	6.90	29.96	17.13	338.91	29.11	109.90	97.70	20.79	195.07	18.50	1.59	2.82	8.57	646.21	44.42	77.89	8.05	26.34	3.73	0.80	3.14	0.47	3.18	0.74	2.31	0.42	2.67	0.43	5.21	1.97	1.50	1.05	23.70	10.49	4.32
EH02	12.30	86.07	22.62	56.74	1.14	6.43	0.06	2.06	0.45	0.59	2.99	0.13	93.19	296.68	3.29	20.14	134.97	170.40	24.04	77.28	50.48	178.94	29.74	135.58	89.10	33.35	241.13	17.57	0.50	2.39	10.41	744.50	53.53	108.12	12.86	48.57	8.97	2.03	7.56	1.10	6.41	1.28	3.52	0.54	3.46	0.52	6.53	2.04	1.38	0.90	8.61	14.55	3.57
EH02	13.45	66.02	18.43	60.02	0.98	6.61	0.06	1.66	0.42	0.67	2.64	0.13	92.04	200.97	2.25	14.37	107.53	135.95	20.49	59.59	37.26	163.06	23.49	116.30	86.37	26.83	239.98	14.96	0.26	2.01	8.16	2666.08	43.91	88.32	10.40	38.46	6.85	1.59	5.68	0.82	4.85	0.99	2.73	0.44	2.75	0.42	6.33	1.91	1.16	0.67	6.74	10.92	2.86
EH02	14.40	108.81	26.83	46.81	0.96	5.98	0.01	1.36	0.64	0.12	2.89	0.16	95.75	2262.42	4.35	23.84	150.06	162.50	15.67	38.89	25.33	45.59	33.82	140.31	94.64	23.29	99.90	14.04	0.66	1.13	15.04	522.69	59.10	112.19	13.45	49.65	8.66	1.97	6.96	0.96	5.49	1.12	2.98	0.47	2.87	0.43	2.26	1.69	1.27	0.81	6.24	19.67	4.38
EH02	15.45	61.06	14.27	67.53	0.67	7.01	0.12	1.49	0.73	0.50	2.10	0.14	94.56	90.07	1.74	12.72	89.12	90.90	15.49	40.32	24.59	36.94	17.93	83.39	89.33	44.32	234.35	9.16	0.40	2.70	5.34	507.14	51.12	111.13	13.19	51.39	9.96	2.18	8.63	1.22	7.91	1.59	4.21	0.66	3.80	0.53	6.34	1.45	1.18	0.43	9.29	10.37	2.51
EH02	16.85	88.89	25.05	53.59	1.10	5.73	0.05	1.69	0.50	0.29	2.62	0.14	99.75	60.78	3.62	19.30	138.90	162.02	22.85	64.70	43.96	50.78	32.93	131.59	98.50	37.08	155.93	15.43	0.59	3.32	11.25	435.08	56.45	110.03	12.75	47.04	8.72	1.95	7.69	1.14	6.66	1.35	3.71	0.55	3.40	0.49	4.24	1.84	1.60	0.72	6.01	15.39	3.52
EH02	16.50	57.72	12.21	29.87	0.92	11.49	0.14	2.51	1.00	0.23	1.69	0.20	60.26	1002.99	2.48	17.68	144.79	177.21	49.64	93.23	52.49	46.81	24.30	115.59	65.46	37.35	300.25	9.23	0.74	1.66	7.95	409.30	45.46	94.66	10.86	41.20	7.86	1.82	6.97	1.01	6.17	1.33	3.90	0.66	4.52	0.70	6.49	1.46	0.97	0.28	0.01	9.15	2.69
EH02	17.20	51.28	10.96	70.34	0.80	5.78	0.06	1.53	0.91	0.61	2.09	0.13	96.22	135.85	1.36	10.38	76.52	94.49	15.30	40.37	11.32	35.50	17.75	89.47	66.26	24.45	315.17	10.88	0.11	2.68	4.83	530.44	35.91	74.15	8.93	33.13	6.10	1.22	5.23	0.74	4.29	0.87	2.38	0.40	2.32	0.33	6.30	1.54	1.24	0.56	9.67	6.71	2.11
EH02	18.05	85.25	25.25	52.21	1.02	5.24	0.05	1.79	0.54	0.16	3.49	0.12	99.88	525.67	3.47	21.71	126.16	142.76	61.19	97.83	39.50	54.12	30.82	169.33	114.91	28.25	117.90	16.03	0.26	2.67	15.05	478.03	50.52	97.83	11.49	41.90	7.01	1.56	5.73	0.84	5.02	1.06	2.93	0.48	2.89	0.44	3.39	1.93	1.67	0.85	41.63	15.42	3.05
EH02	19.05	88.02	24.84	50.26	1.05	7.15	0.10	2.00	0.71	0.15	3.15	0.17	89.58	154.38	3.51	22.48	122.42	145.23	22.39	59.98	47.06	61.81	30.62	154.97	118.85	32.98	107.87	16.09	0.43	2.65	13.69	1073.80	50.30	98.77	11.53	43.15	7.73	1.81	6.49	0.98	5.92	1.23	3.27	0.51	3.11	0.47	3.10	1.98	1.63	0.84	14.41	15.79	3.21
EH02	20.00	73.82	21.86	55.61	0.79	4.74	0.05	1.93	0.59	0.22	4.41	0.11	90.32	299.68	3.37	19.36	130.11	112.15	20.25	51.92	50.10	56.36	27.90	205.44	113.82	26.30	148.81	13.97	0.66	2.53	17.50	1222.32	40.45	80.11	9.41	35.03	6.11	1.36	4.95	0.74	4.51	0.99	2.72	0.45	2.83	0.41	4.15	1.79	1.84	1.01	28.09	12.28	3.16
EH02	21.10	72.23	18.85	50.38	0.80	9.55	0.17	2.20	0.86	0.19	3.71	0.22	87.53	712.31	2.91	20.35	121.40	104.35	18.16	45.03	43.65	53.22	24.33	174.45	104.05	32.51	145.57	14.21	0.59	2.12	14.63	461.68	37.72	76.67	9.26	36.63	7.77	1.78	6.96	1.08	6.20	1.21	3.21	0.59	2.96	0.43	4.08	1.82	1.69	0.90	24.18	11.74	3.23
EH02	22.05	77.82	21.40	56.63	0.88	4.39	0.05	1.79	0.64	0.22	4.19	0.13	90.38	372.09	3.37	19.88	126.47	106.13	17.66	45.03	46.50	54.45	27.06	189.99	114.02	32.96	153.30	15.49	0.81	2.51	16.88	532.63	43.95	89.33	10.69	41.14	8.06	1.76	6.77	1.03	6.00	1.22	3.25	0.56	3.13	0.47	4.28	1.91	1.93	1.02	17.19	12.99	3.31
EH02	23.20	55.75	14.56	72.69	0.71	2.59	0.02	0.83	0.23	0.51	1.93	0.04	94.21	63.56	1.22	9.29	67.46	83.00	11.59	26.42	13.68	26.11	15.51	72.45	69.33	23.42	363.31	10.29	0.19	3.20	3.75	594.85	37.39	77.74	9.13	33.76	5.65	1.14	4.58	0.67	4.01	0.84	2.31	0.39	2.37	0.35	9.41	1.74	1.10	0.51	6.84	9.38	2.24
EH02	24.10	50.69	12.86	76.22	0.67	2.29	0.02	0.67	0.32	0.48	1.82	0.08	95.44	64.67	1.00	9.35	62.15	80.93	9.59	23.86	10.54	23.90	14.14	63.20	69.72	20.22	351.51	9.60	0.12	1.95	2.76	429.95	33.75	68.11	7.89	29.08	5.09	1.05	4.37	0.62	3.63	0.74	2.00	0.33	1.99	0.30	8.82	1.46	0.81	0.42	27.49	8.69	2.05
EH02	25.00	53.31	13.95	74.11	0.69	2.63	0.04	0.64	0.24	0.46	1.98	0.06	94.78	113.39	1.12	7.61	65.10	82.10	6.59	17.14	7.57	22.56	16.79	64.51	69.07	17.23	333.34	9.57	0.12	1.48	2.60	689.16	33.09	67.82	7.80	29.61	4.82	0.97	3.91	0.54	3.06	0.64	1.77	0.30	1.80	0.27	8.41	1.54	0.95	0.41	5.62	9.05	2.20
EH02	25.50	23.61	6.91	84.40	0.28	1.54	0.04	0.46	0.83	0.27	1.31	0.03	96.07	852.22	0.38	3.78	25.36	37.54	5.46	10.14	3.28	10.89	6.77	33.11	43.63	8.99	185.88	4.51	0.16	0.75	0.66	427.06	20.24	40.78	4.66	16.85	2.78	0.55	2.21	0.29	1.62	0.33	0.89	0.18	0.90	0.14	4.63	1.29	0.55	0.30	6.03	5.43	1.02
EH02	25.95	40.95	7.03	83.88	0.47	1.11	0.03	0.51	0.98	0.16	1.25	0.03	95.47	126.40	0.39	4.18	31.68	52.42	2.89	7.50	2.88	12.47	7.29	32.74	40.45	9.88	299.19	6.79	0.10	0.95	0.64	317.23	26.10	52.81	5.99	21.63	3.53	0.67	2.76	0.34	1.82	0.37	1.06	0.20	1.12	0.18	7.35	1.31	0.65	0.21	4.64	7.78	1.29
EH02	26.40	12.49	4.55	62.82	0.19	2.72	0.07	5.26	9.22	0.19	0.87	0.02	85.84	82.25	0.73	5.74	16.34	19.83	1.82	3.39	1.33	2.36	4.21	22.16	69.13	10.53	64.99	3.12	0.11	0.71	0.58	205.04	8.97	16.35	2.19	8.24	1.58	0.45	1.41	0.24	1.59	0.36	1.03	0.20	1.13	0.17	1.72	1.05	0.59	0.07	1.81	2.20	0.48
EH02	27.00	40.47	8.35	80.47	0.48	1.73	0.05	0.70	1.27	0.28	1.25	0.03	94.62	72.84	0.43	5.72	37.83	53.00	4.74	7.31	4.24	9.92	7.56	32.25	44.46	10.97	327.07	7.02	0.10	1.08	0.68	285.39	25.44	51.82	5.92	21.32	3.56	0.62	2.77	0.36	1.94	0.40	1.16	0.22	1.26	0.20	8.11	1.32	0.67	0.16	3.54	7.42	1.40
EH02	27.35	20.05	6.63	82.99	0.30	2.05	0.07	0.66	1.22	0.25	1.11	0.03	95.31	55.47	0.30	4.71	27.83	33.03	4.56	6.59	1.64	5.73	6.17	27.93	41.78	7.25	139.10	4.64	0.16	0.84	0.57	240.72	15.10	30.16	3.41	12.38	2.01	0.44	1.61	0.23	1.23	0.27	0.76	0.16	0.78	0.12	3.50	1.18	0.58	0.12	2.99	3.59	0.74
EH02	27.95	39.47	10.55	78.34	0.52	3.37	0.06	0.52	0.25	0.40	1.46	0.09	95.56	85.88	0.68	5.76	49.31	59.83	7.18	11.42	4.59	26.55	10.93	43.47	52.88	13.77	284.99	7.59	0.30	1.00	1.54	298.31	28.74	59.56	6.91	25.30	4.35	0.90	3.61	0.47	2.56	0.51	1.38	0.32	1.33	0.21	7.10	1.33	0.76	0.22	3.74	6.88	1.54
EH02	28.60	62.74	23.15	57.68	1.04	4.72	0.05	1.42	0.35	0.30	2.99	0.09	91.80	82.17	3.69	18.31	131.33	164.21	40.74	81.57	42.55	47.35	35.35	132.24	103.36	29.71	221.70	15.56	2.04	2.43	10.80	632.66	55.88	107.52	11.82	41.80	6.80	1.38	5.24	0.70	3.83	0.80	2.32	0.39	2.48	0.40	5.96	1.84	1.84	0.56	5.92	14.58	3.15
EH02	29.05	102.45	26.68	56.25	1.18	3.22	0.03	1.32	0.38	0.16	3.26	0.06	92.54	108.41	4.58	23.24	156.74	173.76	21.53	53.16	41.82	58.26	46.21	142.77	88.72	29.78	228.59	18.24	1.18	2.38	12.66	534.66	59.45	116.05	13.17	47.81	8.08	1.85	6.89	0.99	5.77	1.14	3.15	0.51	3.19	0.49	6.25	1.98	2.11	0.54	3.21	17.84	4.00
EH02	29.35	21.37	9.82	83.28	0.24	0.54	0.00	0.10	0.11	0.16	1.04	0.05	95.35	518.79	0.38	3.66	28.07	28.32	3.17	16.02	3.40	5.60	7.24	27.10	78.67	7.10	116.02	4.52	0.24	0.65	0.70	187.06	11.89	24.85	3.11	12.89	2.68	0.66	1.94	0.27	1.47	0.28	0.70	0.20	0.69	0.10	3.03	1.13	0.52	0.20	1.99	3.88	0.76
EH02	29.95	16.28	4.99	89.02	0.11	1.70	0.02	0.09	0.12	0.09	1.24	0.02	97.39	116.09	0.29	3.06	21.51	19.46	5.28	9.23	4.72	23.25	5.98	31.26	60.40	6.94	94.93	2.01	0.31	0.58	0.74	345.43	17.55	35.65	3.83	13.75	2.22	0.53	1.74	0.23	1.26	0.26	0.70	0.14	0.69	0.11	2.23	0.98	0.42	0.20	6.55	2.73	0.69
EH02	30.70	19.71	4.81	89.69	0.14	1.11	0.01	0.09	0.11	0.08	0.99	0.02	97.05	229.15	0.24	2.18	17.16	15.24	5.04	12.50	2.93	9.54	4.27	24.75	44.26	6.07	95.95	2.56	0.15	0.53	0.60	248.31	15.19	31.24	3.51	12.72	2.04	0.43	1.67	0.22	1.19	0.23	0.61	0.12	0.60	0.09	2.49	1.03	0.44	0.14	3.86	3.71	0.64
EH02	31.75	25.19	5.54	87.19	0.26	0.79	0.02	0.12	0.20	0.08	1.13	0.02	95.36	270.61	0.33	1.99	23.34	33.09	8.79	9.70	3.21	10.07	5.02	26.97	53.84	9.33	190.37	3.34	0.22	0.56	0.49	306.76	22.40	47.11	5.43	20.32	3.46	0.73	2.76	0.34	1.87	0.36	0.98	0.18	0.99	0.15	4.78	1.14	0.41	0.19	2.62	4.58	0.89
EH02	31.95	22.00	5.14	89.47	0.25	0.83	0.01	0.12	0.18	0.07	1.04	0.02	97.32	446.66	0.25	2.19	23.66	33.70	6.14	8.24	3.65	10.52	5.07	24.24	45.95	8.24	142.02	4.76	0.24	0.69	0.33	282.29	19.47	41.19	4.75	17.89	3.09	0.72	2.45	0.32	1.71	0.33	0.90	0.18	0.93	0.14	3.52	1.20	0.51	0.17	3.99	3.87	0.84
EH02	32.10	21.73	6.31	87.26	0.22	1.29	0.01	0.10	0.20	0.08	1.16	0.02	96.66	701.43	0.50	3.52	24.25	25.40	11.00	19.55	1.57	21.38	5.99	29.02	44.01	10.11	135.65	3.43	0.21	1.15	0.51	285.17	19.17	40.68	4.75	18.07	3.23	0.76	2.73	0.37	2.13	0.42	1.11	0.22	1.12	0.17	3.48	1.32	0.53	0.19	2.98	3.90	0.79
EH02	32.95	24.75	5.32	82.47	0.25	1.34	0.01	0.11	0.21	0.11	1.26	0.03	91.12	226.91	0.26	1.99	25.85	29.43	8.29	13.14	2.26	9.17	5.45	28.83	59.85	8.39	170.11	3.20	0.32	1.01	0.44	308.68	21.34	43.73	4.88	17.92	2.93	0.61	2.26	0.28	1.46	0.30	0.94	0.18	0.99	0.15	4.14	1.44	0.38	0.61	6.25	4.45	0.90
EH02	33.45	43.74	6.67	84.38	0.46	1.91	0.08	0.23	0.19	0.13	1.17	0.05	95.27	244.32	0.48	4.47	37.49	52.21	7.10	9.27	3.00	14.94	7.43	30.23	49.33	17.04	260.97	6.37	0.42	3.56	0.50	271.60	35.01	75.92	8.86	33.38	5.70	1.20	4.40	0.60	3.22	0.65	1.69	0.28	1.54	0.24	6.50	1.29	0.56	0.23	5.57	8.20	1.42
EH02	33.90	45.44	7.84	83.66	0.71	1.17	0.03	0.21	0.18	0.17	1.30	0.05	95.32	230.92	0.54	5.54	45.71	71.41	5.72	10.01	1.91	11.49	9.05	33.77	53.58	20.95	399.31	10.71	0.37	1.09	0.61	274.92	32.69	69.45	7.90	29.57	5.12	1.08	4.26	0.61	3.63	0.75	2.10	0.36	2.03	0.31	9.76	1.62	0.79	0.24	6.14	8.20	1.63
EH02	34.45	43.15	9.57	74.89	0.66	5.30	0.21	0.47	0.28	0.14	1.29	0.08	92.90	71.69	0.53	5.07	56.18	80.48	15.49	22.56	4.05	14.77	12.32	35.97	48.91	19.33	440.48	9.24	1.10	3.80	0.83	260.92	29.20	59.99	7.03	26.86	4.83	1.08	4.20	0.60	3.40	0.68	1.87	0.32	1.86	0.29	10.97	1.61	0.98	0.29	6.16	6.98	1.95
EH02	35.10	39.42	9.01	76.52	0.57	1.68	0.05	0.97	1.90	0.20	1.65	0.08	92.62	328.80	0.63	11.93	67.12	78.48	15.86	21.62	4.78	19.82	12.84	47.90	63.09	16.49	223.58	8.47	0.99	1.30	1.33	444.05	36.71	80.30	9.11	34.69	6.02	1.44	4.80	0.61	3.23	0.63	1.66	0.27	1.49	0.22	5.62	1.48	0.87	0.36	6.07	6.24	1.85
EH02	35.50	27.24	8.68	79.40	0.43	1.38	0.04	0.86	1.66	0.21	1.52	0.08	94.27	280.13	0.60	7.88	53.45	52.82	7.79	13.07	4.32	13.00	10.24	39.93	54.96	14.81	191.10	6.55	0.41	2.03	1.01	600.58	25.96	56.73	6.69	25.92	4.95	1.31	4.14	0.57	2.95	0.56	1.45	0.44	1.35	0.20	4.73	1.37	1.02	0.27	6.14	4.51	1.18
EH02	36.05	28.05	8.33	78.71	0.46	1.45	0.05	1.00	1.87	0.22	1.54	0.04	93.67	350.30	0.52	9.62	54.11	64.07	5.54	9.40	3.47	9.09	11.24	41.81	53.66	13.72	165.31	7.29	0.22	1.14	1.00	379.41	30.50	67.35	7.79	29.77	5.22	1.27	4.04	0.52	2.74	0.51	1.35	0.23	1.31	0.20	4.21	1.30	0.74	0.30	6.20	4.74	1.16
EH02	36.55	33.97	7.25	76.52	0.61	1.69	0.05	1.52	3.02	0.28	1.93	0.04	92.01	827.18	0.53	5.02	35.37	64.77	9.49	15.84	4.66	16.91	7.53	27.12	47.48	14.80	324.77	8.78	0.32	0.85	0.54	220.74	19.73	40.35	4.60	17.48	3.26	0.65	2.73	0.42	2.65	0.55	1.56	0.28	1.55	0.24	7.98	1.46	0.98	0.33	4.82	6.08	1.25
EH02	37.20	25.42	8.17	52.05	0.55	4.47	0.15	4.91	9.21	0.39	1.61	0.08	92.59	274.91	1.38	14.05	62.35	70.52	15.91	27.16	8.32	23.96	14.86	53.75	103.95	26.87	137.32	8.38	0.51	1.60	1.76	849.43	31.16	69.14	8.01	31.05	5.96	1.63	5.32	0.81	4.77	0.95	2.53	0.39	2.22	0.33	3.48	1.41	0.72	0.36	5.70	4.20	1.23
EH02	37.45	14.36	7.10	42.77	0.26	4.45	0.15	7.62	13.10	0.40	1.37	0.04	77.25	308.12	1.33	5.46	34.76	33.74	6.88	12.83	3.09	12.03	8.90	38.89	90.60	12

Appendix 18

ICPMS and ICPOES data for EH03B borehole at Bayfield

Vell	Depth (m)	hemical C	Al2O3_ICI	SiO2_ICP	TiO2_ICP	Fe2O3_IC	MnO_ICP	MgO_ICP	CaO_ICP	Na2O_ICF	K2O_ICP	P2O5_ICF	Total_ICF	S_ICP	Be_ICP	Sc_ICP	V_ICP	Cr_ICP	Co_ICP	Ni_ICP	Cu_ICP	Zn_ICP	Ga_ICP	Rb_ICP	Sr_ICP	Y_ICP	Zr_ICP	Nb_ICP	Mo_ICP	Sn_ICP	Cs_ICP	Ba_ICP	La_ICP	Ce_ICP	Pr_ICP	Nd_ICP	Sm_ICP	Eu_ICP	Gd_ICP	Tb_ICP	Dy_ICP	Ho_ICP	Er_ICP	Tm_ICP	Yb_ICP	Lu_ICP	Hf_ICP	Ta_ICP	W_ICP	Tl_ICP	Pb_ICP	Th_ICP	U_ICP
		api	(wt.%)	(wt.%)	(wt.%)	(wt.%)	(wt.%)	(wt.%)	(wt.%)	(wt.%)	(wt.%)	(wt.%)	(wt.%)	(ppm)	(ppm)	(ppm)	(ppm)	(ppm)	(ppm)	(ppm)	(ppm)	(ppm)	(ppm)	(ppm)	(ppm)	(ppm)	(ppm)	(ppm)	(ppm)	(ppm)	(ppm)	(ppm)	(ppm)	(ppm)	(ppm)	(ppm)	(ppm)	(ppm)	(ppm)	(ppm)	(ppm)	(ppm)	(ppm)	(ppm)	(ppm)	(ppm)	(ppm)	(ppm)	(ppm)	(ppm)	(ppm)	(ppm)
EH03B	6.00	10.65	3.36	93.43	0.12	0.18	0.00	0.07	0.13	0.07	0.69	0.01	99.07	2.75	0.24	0.75	9.75	15.00	0.99	0.07	0.07	6.61	2.92	14.76	45.83	5.35	63.95	2.76	0.08	0.16	0.27	259.61	13.94	27.29	3.03	10.86	1.90	0.38	1.40	0.17	0.99	0.19	0.53	0.12	0.51	0.08	1.92	1.08	0.65	0.12	4.40	1.91	0.39
EH03B	7.20	22.25	5.45	87.63	0.55	0.26	0.00	0.09	0.13	0.08	0.80	0.03	95.02	6.42	0.32	2.26	23.34	51.45	1.28	3.03	0.62	8.47	4.55	20.30	40.56	8.20	286.50	8.49	0.20	0.24	0.57	232.55	19.85	38.92	4.23	15.00	2.46	0.48	1.83	0.25	1.42	0.29	0.87	0.16	0.88	0.14	6.94	1.49	1.31	0.29	20.34	3.95	0.83
EH03B	8.00	28.30	4.39	87.80	0.61	0.63	0.00	0.09	0.15	0.07	0.61	0.03	94.40	4.82	0.34	2.03	25.17	56.70	1.38	3.11	3.25	20.28	3.86	15.04	36.95	11.96	223.96	9.30	0.34	0.73	0.36	202.94	29.56	62.21	6.83	24.89	4.08	0.87	2.89	0.38	2.09	0.42	1.16	0.22	1.14	0.18	5.46	1.65	1.92	0.16	33.49	5.32	0.91
EH03B	9.20	94.51	23.98	49.08	1.02	7.47	0.13	1.95	0.58	0.21	2.93	0.15	87.51	83.80	4.03	26.22	145.70	168.44	27.64	77.58	54.59	105.32	30.26	138.37	88.72	38.53	133.98	16.27	0.85	2.36	12.01	407.45	51.00	100.63	12.17	45.77	8.58	2.10	7.95	1.18	6.94	1.40	3.80	0.58	3.55	0.54	3.65	1.96	1.45	1.03	11.74	16.00	3.92
EH03B	9.85	62.41	16.34	59.16	1.03	7.17	0.09	2.09	0.83	0.88	2.57	0.15	90.31	67.11	2.04	14.57	107.64	138.22	22.50	64.40	33.27	63.90	23.08	119.58	87.58	30.90	247.15	15.54	0.47	2.47	7.90	523.14	42.94	84.75	9.68	36.14	6.85	1.46	5.86	0.85	5.14	1.11	2.99	0.49	2.98	0.46	6.51	1.92	1.47	0.74	7.31	10.21	2.76
EH03B	10.67	81.15	20.22	56.97	1.05	5.97	0.06	1.95	0.59	0.64	2.69	0.12	90.26	51.74	2.47	19.33	125.45	152.53	18.68	60.69	46.19	67.01	26.28	128.13	95.26	33.45	250.16	16.48	0.74	2.21	9.26	524.91	52.92	109.44	13.26	49.47	8.89	1.91	7.36	1.08	6.38	1.25	3.44	0.52	3.36	0.49	6.70	2.59	1.87	0.80	8.21	13.07	3.69
EH03B	11.70	76.21	21.57	58.00	1.05	5.10	0.02	1.66	0.32	0.40	2.42	0.04	90.57	128.75	2.73	19.59	194.37	147.22	23.83	59.79	30.92	71.15	28.47	106.26	90.45	34.23	231.00	15.01	0.27	2.46	8.73	1413.73	50.44	101.03	11.95	44.89	7.57	1.62	6.56	0.99	5.78	1.25	3.39	0.58	3.42	0.53	6.25	1.94	1.46	0.81	12.38	12.41	3.40
EH03B	12.70	62.55	13.51	63.99	0.58	7.62	0.19	1.70	1.52	0.41	1.82	0.11	91.46	61.23	1.47	13.10	88.62	81.90	18.61	38.89	20.97	59.73	15.67	66.08	84.38	34.98	277.70	8.35	0.54	1.28	3.74	365.39	52.44	112.44	13.12	49.95	8.79	1.84	7.28	1.08	6.28	1.24	3.37	0.52	3.31	0.48	7.30	1.52	1.00	0.50	20.77	10.87	2.46
EH03B	13.65	44.76	15.27	60.11	0.88	8.89	0.11	2.17	0.79	0.60	2.31	0.20	91.31	86.55	1.82	14.67	101.35	109.99	24.33	54.10	18.77	66.92	23.03	117.20	77.94	23.73	215.99	11.44	0.38	2.27	6.77	451.38	37.27	77.89	8.87	33.88	6.34	1.38	5.47	0.78	4.35	0.84	2.34	0.36	1.94	0.30	5.59	1.84	1.07	0.78	9.08	7.61	1.84
EH03B	14.10	14.61	6.50	71.64	0.20	3.39	0.20	2.10	5.26	0.37	0.93	0.03	90.63	71.51	0.37	3.95	19.81	20.26	4.14	4.35	1.54	9.72	5.07	25.89	46.36	13.85	100.50	3.37	0.20	0.30	0.73	283.53	16.47	21.72	2.65	10.01	1.94	0.56	2.07	0.31	2.14	0.48	1.32	0.25	1.46	0.21	2.65	1.22	0.75	0.19	4.16	2.58	0.58
EH03B	14.55	44.55	15.25	66.22	0.78	6.23	0.08	1.71	0.91	0.63	2.22	0.15	94.17	93.51	1.44	11.76	85.45	94.49	16.45	39.64	11.52	53.37	20.64	90.52	69.43	20.04	264.76	11.31	0.10	1.99	5.44	632.16	34.02	70.71	8.17	31.50	5.74	1.29	4.84	0.68	3.79	0.76	1.89	0.30	1.75	0.27	6.90	1.75	1.18	0.72	9.78	7.66	1.79
EH03B	15.55	92.30	24.94	51.05	1.14	5.50	0.07	1.79	0.63	0.18	3.01	0.16	88.47	86.89	3.46	22.56	128.40	159.64	30.62	73.36	43.71	62.04	32.39	150.30	122.59	36.66	141.23	17.77	0.80	2.92	12.82	885.10	56.81	116.84	13.29	49.92	8.41	1.97	7.42	1.06	6.52	1.34	3.71	0.57	3.49	0.53	3.88	2.13	1.76	0.86	14.67	16.41	3.44
EH03B	16.25	81.01	23.17	53.08	0.94	5.93	0.07	2.16	0.61	0.21	4.36	0.14	90.66	58.57	3.61	22.30	131.76	123.20	21.11	56.68	30.48	69.42	31.04	204.18	141.66	31.07	131.29	15.71	0.33	2.73	16.61	482.94	52.31	102.04	12.18	44.71	7.72	1.53	5.96	0.88	5.33	1.16	3.20	0.55	3.37	0.50	3.73	2.42	1.89	1.01	8.89	14.61	2.92
EH03B	17.20	71.31	21.05	53.08	0.79	6.54	0.10	2.15	0.92	0.23	4.21	0.16	89.24	106.95	3.19	20.15	125.35	109.39	16.73	52.99	37.05	62.45	26.59	199.11	110.60	25.57	148.48	13.27	0.57	2.24	16.13	469.22	38.38	75.92	8.80	32.27	5.88	1.31	5.25	0.75	4.42	0.96	2.65	0.44	2.72	0.41	4.20	1.88	1.74	0.74	14.54	12.04	2.97
EH03B	18.05	74.90	21.62	55.18	0.84	4.91	0.06	1.94	0.62	0.23	4.24	0.13	89.76	101.46	3.28	19.46	123.42	109.09	18.59	55.16	43.37	162.51	27.14	197.42	108.53	27.17	160.59	14.53	0.60	2.92	16.08	474.51	40.02	79.09	9.31	34.18	6.19	1.24	5.19	0.77	4.69	0.97	2.73	0.45	2.73	0.44	4.46	2.04	1.94	0.72	17.79	12.65	3.12
EH03B	19.50	76.45	21.45	56.14	0.86	4.77	0.05	1.85	0.57	0.21	4.04	0.13	90.09	136.95	3.21	19.20	122.40	108.09	15.83	49.75	41.52	75.64	27.21	191.45	109.81	28.41	153.24	14.57	0.44	2.56	15.97	462.65	41.05	81.70	9.58	35.52	6.47	1.36	5.20	0.77	4.90	1.02	2.92	0.48	3.00	0.47	4.26	2.00	2.01	0.82	23.96	13.13	3.08
EH03B	19.95	77.63	20.95	58.13	0.86	4.42	0.05	1.81	0.54	0.22	4.01	0.15	91.15	97.04	3.08	18.00	123.11	104.59	14.23	47.53	47.31	69.66	26.76	189.27	111.48	29.94	163.49	14.98	0.49	4.65	15.83	539.71	40.63	82.02	9.63	35.59	6.39	1.51	5.67	0.86	5.28	1.07	3.02	0.46	2.99	0.47	4.56	2.09	2.02	0.87	24.21	12.71	3.42
EH03B	19.95	78.13	21.37	57.01	0.89	4.66	0.06	1.82	0.68	0.23	4.07	0.17	90.96	133.07	3.04	18.49	119.35	101.09	13.59	39.87	38.89	61.73	26.76	189.66	112.27	29.55	159.45	15.18	0.45	2.52	16.21	528.92	41.25	81.11	9.56	35.22	6.38	1.39	5.56	0.81	5.21	1.06	2.95	0.51	3.06	0.45	4.45	2.12	2.10	0.90	11.09	13.33	3.19
EH03B	20.40	N																																																			
EH03B	20.85	91.29	22.90	59.21	1.06	4.58	0.02	1.37	0.27	0.18	2.36	0.05	92.00	717.31	2.93	20.86	122.30	149.83	27.61	73.42	35.88	89.07	28.58	195.07	77.90	37.00	277.18	15.62	0.43	1.55	9.32	470.89	57.86	116.34	13.73	51.07	9.30	1.99	7.97	1.20	6.99	1.41	3.79	0.58	3.49	0.52	7.62	2.05	1.56	0.63	5.55	15.69	3.67
EH03B	22.10	87.28	24.03	57.57	1.06	4.07	0.02	1.47	0.30	0.22	2.58	0.06	91.39	41.44	3.65	20.28	124.33	152.63	26.43	78.26	38.09	79.58	31.83	119.48	86.06	29.28	294.06	15.89	1.18	5.80	9.93	588.73	51.69	102.04	11.93	44.18	7.53	1.69	6.18	0.89	5.32	1.09	3.01	0.48	3.02	0.47	5.76	2.06	1.96	0.86	7.19	15.01	3.50
EH03B	23.00	93.08	24.00	58.68	1.10	4.09	0.04	1.27	0.33	0.22	2.66	0.07	92.45	126.56	3.63	20.92	126.98	156.33	29.68	68.34	32.69	69.77	33.56	117.30	89.49	34.12	278.53	16.71	1.00	2.26	10.12	694.81	55.43	112.64	13.05	49.40	8.59	1.82	7.03	1.03	6.20	1.26	3.42	0.57	3.42	0.53	7.62	2.05	1.46	0.72	7.25	16.04	3.72
EH03B	23.20	87.13	21.22	63.53	1.02	3.36	0.04	1.12	0.28	0.30	2.51	0.08	93.45	74.38	3.00	18.88	110.19	138.72	28.01	68.12	26.09	62.45	30.75	106.86	99.78	31.37	379.27	14.96	0.62	2.23	7.40	543.34	52.10	104.84	12.34	46.63	8.31	1.84	6.84	1.01	5.76	1.16	3.20	0.51	3.18	0.50	10.17	1.92	1.28	0.65	7.53	15.03	3.47
EH03B	23.55	34.86	9.34	84.95	0.50	0.35	0.00	0.11	0.19	0.17	0.93	0.02	96.56	466.56	0.38	2.85	35.68	47.15	1.41	2.82	1.26	9.56	8.07	27.71	47.49	11.81	322.01	7.89	0.18	0.48	1.02	3251.00	20.06	39.82	4.59	16.94	2.86	0.48	2.39	0.34	2.01	0.41	1.15	0.22	1.19	0.19	8.16	1.46	0.71	1.02	3.99	6.19	1.30
EH03B	24.00	22.26	5.93	88.73	0.32	1.11	0.00	0.11	0.15	0.08	1.13	0.02	97.57	211.03	0.51	2.59	24.88	38.50	2.25	4.72	4.59	21.21	6.38	31.07	45.29	10.85	149.00	5.02	0.30	0.35	0.90	435.98	21.13	44.11	5.09	18.63	3.24	0.77	2.35	0.33	1.84	0.38	1.02	0.18	0.93	0.15	3.89	1.26	0.76	0.29	8.36	3.92	0.85
EH03B	24.40	21.29	5.35	88.63	0.25	1.50	0.00	0.10	0.17	0.08	1.03	0.03	97.16	293.06	0.36	2.28	21.29	28.56	2.81	6.04	5.64	18.94	5.61	28.32	43.45	9.22	137.19	4.26	0.37	0.43	0.87	615.40	18.30	37.70	4.29	15.70	2.62	0.65	2.05	0.29	1.67	0.33	0.86	0.16	0.83	0.12	3.60	1.24	0.73	0.29	8.71	3.97	0.75
EH03B	24.80	16.45	4.96	91.15	0.17	1.00	0.00	0.08	0.12	0.07	0.83	0.02	98.39	102.51	0.27	1.65	16.06	15.25	1.43	2.08	1.79	11.07	4.58	22.41	37.00	7.95	81.20	3.08	0.15	0.42	0.63	280.88	15.26	29.82	3.40	12.44	2.30	0.54	1.67	0.26	1.48	0.28	0.77	0.14	0.71	0.10	2.17	1.11	0.52	0.18	6.83	3.08	0.54
EH03B	25.60	22.10	5.27	89.19	0.23	0.50	0.00	0.12	0.20	0.09	1.35	0.03	96.99	206.86	0.38	2.30	20.44	23.67	1.90	2.19	1.56	14.71	6.18	33.73	65.13	9.91	133.98	3.62	0.22	0.94	0.67	499.51	19.74	39.93	4.29	15.54	2.54	0.58	2.08	0.28	1.76	0.35	0.93	0.20	0.92	0.14	3.57	1.29	0.63	0.26	11.47	3.89	0.84
EH03B	25.90	13.66	4.80	90.87	0.62	0.58	0.00	0.11	0.12	0.07	0.86	0.02	98.06	106.07	0.34	2.60	22.82	49.22	2.07	2.71	1.88	9.39	4.42	22.19	36.47	10.24	152.00	9.02	0.21	0.60	0.62	275.88	13.69	28.35	3.21	11.76	2.01	0.52	1.88	0.27	1.82	0.37	1.01	0.20	0.98	0.14	3.98	3.00	0.69	0.17	6.93	3.24	0.86
EH03B	26.10	20.71	5.24	90.83	0.15	0.73	0.00	0.10	0.11	0.08	1.15	0.02	98.41	161.75	0.41	1.93	20.39	20.43	2.22	3.57	0.22	11.76	6.06	30.23	62.06	6.93	96.29	2.43	0.27	0.98	0.83	351.28	19.13	39.12	4.12	15.01	2.34	0.45	1.82	0.22	1.30	0.25	0.70	0.15	0.68	0.11	2.54	1.14	0.65	0.23	10.17	3.78	0.72
EH03B	26.45	13.15	4.79	92.17	0.13	0.62	0.00	0.11	0.13	0.08	0.95	0.01	98.97	168.14	0.20	1.48	14.29	13.30	2.19	1.30	1.98	6.77	4.36	24.12	39.61	6.09	67.27	2.44	0.12	0.83	0.61	290.46	13.24	27.64	3.00	11.49	1.88	0.44	1.48	0.20	1.17	0.18	0.57	0.14	0.59	0.09	2.43	1.10	0.54	0.19	6.43	2.29	0.52
EH03B	26.90	23.01	5.57	89.96	0.42	1.12	0.01	0.11	0.14	0.09	1.05	0.03	98.50	146.89	0.50	2.98	23.17	36.97	4.94	8.77	2.49	23.19	5.21	26.23	45.47	12.62	200.73	5.62	0.31	0.77	0.59	275.35	16.76	37.81	4.28	15.73	2.73	0.61	2.29	0.35	2.07	0.38	1.36	0.27	1.34	0.20	5.11	1.61	0.63	0.26	13.85	4.00	0.90
EH03B	28.00	23.01	7.01	90.13	0.32	0.23	0.00	0.12	0.13	0.09	1.25	0.01	99.29	61.69	0.43	1.39	25.99	35.55	1.32	0.11	1.00	4.73	7.22	31.99	47.31	7.33	156.07	5.17	0.12	0.67	0.82	288.55	20.39	41.44	4.65	16.92	2.64	0.54	1.76	0.23	1.25	0.21	0.75	0.17	0.79	0.12	3.95	1.30	0.76	0.27	6.43	4.03	0.89
EH03B	28.15	18.82	4.93	92.17	0.25	0.28	0.00	0.10	0.13	0.08	0.99	0.01	98.94	70.83	0.24	1.00	14.93	24.97	1.24	1.27	1.17	5.26	4.49	23.76	41.69	5.02	170.03	4.33	0.23	0.71	0.41	293.35	14.59	28.97	3.12	10.90	1.71	0.33	1.33	0.17	0.90	0.15	0.50	0.17	0.61	0.09	4.35	1.21	1.18	1.24	11.32	3.33	0.71
EH03B	28.80	22.55	5.52	90.44	0.34	0.52	0.00	0.10	0.13	0.08	1.19	0.01	98.34	73.61	0.24	1.29	18.91	31.96	1.99	1.21	0.40	5.29	5.41	28.85	52.12	6.43	194.77	5.03	0.19	0.55	0.42	332.75	18.08	36.62	4.08	14.49	2.37	0.47	1.60	0.21	1.13	0.19	0.74	0.14	0.71	0.12	4.94	1.32	0.74	0.29	6.62	4.06	0.82
EH03B	29.40	15.34	6.09	91.00	0.13	0.56	0.00	0.10	0.13	0.09	1.32	0.02	99.45	70.73	0.28	2.31	20.62	18.64	2.88	3.04	0.58	8.51	5.77	31.24	59.70	4.16	103.80	2.35	0.20	0.82	0.46	376.56	16.20	32.29	3.48	12.98	1.73	0.43	1.35	0.15	0.77	0.13	0.49	0.22	0.49	0.08	2.76	1.06	0.58	0.32	7.37	2.63	0.62
EH03B	29.50	14.34	4.43	91.01	0.16	0.30	0.00	0.09	0.12	0.09	1.05	0.01	97.26	63.67	0.29	1.15	11.71	16.26	1.76	0.25	0.49	6.80	4.05	25.51	47.04	4.12	90.18	2.85	0.15	0.85	0.52	256.94	14.39	28.86	3.12	11.29	1.61	0.35	1.22	0.15	0.83	0.12	0.42	0.12	0.44	0.06	2.49	1.09	0.55	0.25	6.32	2.54	0.54
EH03B	29.95	25.20	5.19	85.93	0.32	1.55	0.01	0.13	0.13	0.10	1.29	0.02	94.67	88.23	0.44	3.61	30.69	40.79	7.96	10.00	6.49	15.19	7.26	33.26	58.09	7.88	150.21	4.59	0.64	2.03	0.68	297.75	23.55	49.05	5.39	20.03	3.27	0.77	2.33	0.29	1.59	0.25	0.84	0.18	0.89	0.15	3.90	1.22	1.22	0.40	11.44	3.97	1.19
EH03B	30.15	11.45	4.58	91.33	0.09	1.58	0.02	0.07	0.10	0.08	0.99	0.01	98.86	129.78	0.27	1.74	15.22	12.25	5.69	8.46	0.94	10.15	4.14	23.15	48.07	5.24	79.08	2.07	0.64	0.98	0.32	261.44	12.44	25.94	2.82	10.62	1.80	0.41	1.32	0.18	1.02	0.15	0.54	0.13	0.58	0.08	2.04	1.02	0.96	0.20	6.55	1.99	0.45
EH03B	30.55	27.80	4.81	91.18	0.33	1.04	0.01	0.12	0.14	0.09	1.13	0.03	98.88	186.77	0.34	3.65	23.84	34.46	4.45	4.28	1.44	11.18	5.47	29.16	48.57	10.79	195.80	4.72	0.23	0.71	0.78	272.74	21.67	43.93	4.81	17.47	2.96	0.58	2.26	0.33	1.86	0.33	1.07	0.24	1.12	0.17	4.86	1.33	0.56	0.30	6.90	5.01	1.00
EH03B	31.40	13.79	4.95	88.73	0.09	2.52	0.02	0.09	0.12	0.11	1.47	0.01	98.11	180.42	0.39	2.63	14.18	12.67	8.10	12.38	4.84	53.73	4.95	35.49	67.41	8.78	97.47	1.54	0.32	0.83	0.90	360.06	15.54	32.26	3.63	13.45	2.55	0.72	2.10	0.32	1.93	0.30	0.98	0.19	1.01	0.14	2.76	1.02	0.67	0.34	10.14	2.30	0.59
EH03B	32.10	16.36	5.35	87.90	0.25	1.40	0.06	0.27	0.68	0.09	1.04	0.03	97.06	897.13	0.41	4.96	23.37	28.98	12.43	18.61	1.45	37.39	5.03	25.42	45.48	19.32	131.32	3.88	0.20	0.52	0.55	257.34	16.36	41.73	5.05	20.19	4.27	1.32	4.52	0.68	3.95	0.63	2.09	0.34	1.84	0.28	3.37	1.19	0.56	0.23	4.20	3.39	0.70
EH03B	32.50	28.61	4.91	87.76	0.25	1.40	0.04	0.18	0.44	0.08	1.21	0.03	96.32	671.17	0.38	3.31	28.17	34.71	12.83	17.51	1.88	19.18	6.26	31.87	56.03	16.81	249.19	3.86	0.18	0.57	0.92	301.55	27.79	58.40	6.54	24.66	4.06	0.92	3.53	0.47	2.65	0.43	1.38	0.25	1.23	0.20	6.24	1.20	0.54	0.30	5.68	4.78	1.21
EH03B	32.75	24.49	8.49	83.01	0.32	1.17	0.03	0.19	0.35	0.11	1.34	0.04	95.06	536.98	0.52	5.14	41.49	51.15	10.46	14.63	1.24	15.22	9.10	36.14	49.94	14.75	148.26	5.14	0.38	0.93	0.97	321.05	21.92	46.87	5.29	20.22	3.49	0.86	2.77	0.41	2.39	0.43	1.53	0.29	1.75	0.27	3.79	1.24	0.61	0.47	3.97	3.96	1.10
EH03B	33.25	96.44	17.92	70.35	1.45	0.97	0.01	0.56	0.32	0.28	2.64	0.14	94.62	149.60	1.50	9.49	164.36	188.71	5.59	11.87	0.22	17.07	28.06	85.44	105.70	38.04	931.46	22.10	0.35	2.33	3.09	466.88	67.56	134.42	15.25	55.52	9.72	2.01	8.31	1.14	6.16	1.05	3.61	0.58	3.74	0.59	22.88	2.50	1.25	0.61	6.35	16.25	4.03
EH03B	34.35	15.36	4.17	85.40	0.14	3.30	0.16	0.18	0.33	0.08	0.93	0.02	94.73	2159.06	0.29	1.74	13.97	14.22	17.17	20.50	2.22	40.51	3.81	24.34	41.12	10.64	81.15	2.60	0.77	0.51	0.73	239.14	14.67	32.24	3.65	14.15	2.53	0.65	2.28	0.33	1.84	0.30	0.99	0.18	0.88	0.14	2.30	1.14	0.57	0.34	13.20	2.86	0.58
EH03B	35.40	16.52	4.27	87.36	0.15	2.67	0.09	0.42	0.79	0.08	0.90	0.01	96.74	2291.39	0.33	1.95	14.38	17.14	12.26	17.69	5.76	23.51	3.83	22.82	42.55	12.00	94.08	2.55	0.34	0.47	0.60	233.84	13.49	29.62	3.26	12.37	2.49	0.51	2.18	0.32	1.99	0.35	1.16	0.23	1.12	0.16	2.33	1.15	0.61	0.25	7.46	3.36	0.76
EH03B	36.05	60.54	7.74	84.88	0.65	1.52	0.04	0.16	0.17	0.10	1.16	0.04	96.46	1816.29